Hot Corrosion of Wrought and Weld Overlay Alloy 625 in Molten Salts Environments

by

Ehsan Mohammadi Zahrani

A THESIS SUBMITTED IN PARTIAL FULFILLMENT OF
THE REQUIREMENTS FOR THE DEGREE OF
DOCTOR OF PHILOSOPHY

in

THE FACULTY OF GRADUATE AND POSTDOCTORAL STUDIES

(Materials Engineering)

THE UNIVERSITY OF BRITISH COLUMBIA
(Vancouver)

November 2013

Abstract

KIVCET smelter is a modern direct smelting process which has been used to replace conventional sinter/blast furnace technology in pyrometallurgical process of lead and zinc. Although heavy metals including Cd, Pb, Zn, Fe as well as S, O and Cl, are the main elements playing a leading role in the formation of molten phase on the waterwall tubes of the KIVCET waste heat boiler, hot corrosion behavior and electrochemical properties of weld overlay and wrought alloy 625 have not been studied yet in the molten salt environments containing the above-mentioned elements. The present study was carried out to study hot corrosion behavior of the weld overlay and wrought alloy 625 as well as failure mechanism of the weld overlay alloy 625 under the corrosive conditions of the radiant boiler in the KIVCET smelter.

It was found that the deposited salt mixtures on the waterwall tubes of the radiant boiler had a strong tendency to form a molten phase at the operating temperature range of the radiant boiler. Presence of the deposited salt mixtures and the formation of the molten phase led to the occurrence of the hot corrosion attack in the waterwall and the ultimate failure of the weld overlay. The dilution and, consequently, the presence of a significant amount of Fe in the weldment composition were the key issues in the alloy 625 weld overlay. High concentrations of sulfur and oxygen in the grain boundaries of the wrought alloy 625 are to blame for the occurrence of the intergranular corrosion together with the internal attack. An electrochemical model (a porous and non-protective barrier layer model) was used to explain the corrosion/electrochemical behavior of the wrought alloy which fit into the obtained EIS data well.

Preface

This dissertation is an original, independent work by the author, Ehsan Mohammadi Zahrani. The following papers were extracted from the research work presented in this dissertation.

Journal Papers

1. **E. Mohammadi Zahrani**, A. Alfantazi, "Hot corrosion and electrochemical behavior of Inconel 625 weld overlay in $PbSO_4$-Pb_3O_4-$PbCl_2$-ZnO-CdO molten salt medium", Submitted.
2. **E. Mohammadi Zahrani**, A. Alfantazi, "Hot corrosion failure of overlay weld cladding in radiant boiler of a KIVCET flash lead smelter", Metallurgical and Materials Transaction: A, 44 (2013) 4671-4699.
3. **E. Mohammadi Zahrani**, A. Alfantazi, "Molten salt induced corrosion of Inconel 625 superalloy in $PbSO_4$-Pb_3O_4-$PbCl_2$-Fe_2O_3-ZnO environment", Corrosion Science, 65 (2012) 340-359.
4. **E. Mohammadi Zahrani**, A. Alfantazi, "Corrosion behaviour of alloy 625 in $PbSO_4$-Pb_3O_4-$PbCl_2$-ZnO-10 wt. % CdO molten salt medium", Metallurgical and Materials Transaction: A, 43 (2012) 2857-2868.
5. **E. Mohammadi Zahrani**, C. Cuevas-Arteaga, D. Verhelst, A. Alfantazi "High temperature corrosion of 625 supperalloy under Iron-Zinc-Lead Oxide/Sulfate/ Chloride salt mixtures", Electrochemical Society Transaction, 28(24) (2010) 171-185.

Conferences

1. **E. Mohammadi Zahrani**, A. Alfantazi, "Hot corrosion of weld overlay alloy 625 in KIVCET smelter off-gas environment, Materials Science and Technology 2013 (MS&T 2013) Conference, 27-31 October 2013, Montreal, QC, Canada (Oral Presentation).
2. **E. Mohammadi Zahrani**, A. Alfantazi, "Characterization of anodic layer formed on alloy 625, in 47 $PbSO_4$-13 Pb_3O_4-7 $PbCl_2$- 23 ZnO-10 Fe_2O_3 (wt. %) molten salt mixture at 800 and 700^oC", Conference of Metallurgist 2011 (COM 2011), 2-5 October 2011, Montreal, QC, Canada (Poster Presentation).
3. **E. Mohammadi Zahrani**, A. Alfantazi, "Hot corrosion and electrochemical behavior of alloy 625 beneath $PbSO_4$-Pb_3O_5-PbCl-ZnO-5%CdO molten salt mixture at 800, 700 and 600^oC", 219th Electrochemical Society Meeting, 1-6 May 2011, Montreal, QC, Canada (Oral Presentation).
4. **E. Mohammadi Zahrani**, A. Alfantazi, "Effect of temperature on the corrosion behavior of 625 supperalloy in $PbSO_4$-Pb_3O_5-PbCl-ZnO molten salt system with 10 wt. % CdO", TMS 2011: Fatigue and Corrosion Damage in Metallic Materials, 27th Feb. - 3rd Mar. 2011, San Diego, CA, USA (Oral Presentation).
5. **E. Mohammadi Zahrani,** A. Alfantazi, D. Verhelst, "High temperature corrosion of 625 superalloy under iron-zinc oxide/lead sulfate salt mixture", 217th Electrochemical Society Meeting, 25-30 April 2010, Vancouver, BC, Canada (Oral Presentation).

Table of Contents

List of Tables

List of Figures

Acknowledgements

First of all, I am sincerely thankful to my dear God (Allah: the Almighty, Creator and Sustainer of the Universe) for blessing me with a loving family, fatherly PhD supervisor, kind friends as well as health and strength to educate up to this level.

I am deeply grateful to dear Professor Akram Alfantazi (my PhD supervisor) for opening the door of opportunity and prosperity for me with providing critical advice, helpful guidelines, and strong fatherly support over the course of my PhD study. Dear Professor Alfantazi's outstanding guidance, valuable feedback, and thoughtful comments on my research activities as well as his strong support have had a significant positive effect on my accomplishment over the past four years at UBC. Undoubtedly, without his great encouragement and critical comments, excellent scientific guidance, and dedicated support, it would not have been possible for the author to fulfill his academic dreams. The author is truly proud of having this world-class professor and outstanding scientific scholar as his supervisor during his PhD.

Furthermore, financial support from the Natural Sciences and Engineering Research Council of Canada (NSERC) and Teck Metals Ltd. is gratefully acknowledged. The author would like to express his gratitude toward the Federal Government of Canada for providing the prestigious Vanier Canada Graduate Scholarship, the University of British Columbia for providing the Killam Doctoral Fellowship and the Four Years Doctoral Fellowship, and the Metallurgy & Materials Society of the Canadian Institute of Mining, Metallurgy and Petroleum (MetSoc of CIM) for providing MetSoc Doctoral Scholarship to him.

The author is also grateful to Mr. Dominic Verhelst (Technical Specialist Furnaces, Teck Metals Ltd.) for valuable and constructive technical discussion on the different aspects of corrosion issue in the KIVCET boiler over the course of this project.

Special thanks to Mr. Jacob Kabel (SEM Technician) for facilitating the access of the author to the electron microscopy laboratory over the course of this project.

My gratitude is extended to Mr. Ross Mcleod and his dear colleagues, Mr. Carl Ng and Mr. David Torok, for being patient and supportive in cutting the weld overlay alloy 625 specimens from the waterwall tubes.

At the end, I am deeply grateful to my friends and whoever has supported me over the four years of study at UBC.

To:

My Dedicated Father

and

My kind-hearted Mother

1 Introduction

Teck Metals Ltd. (Teck) is an integrated mining and metals company with principal activities in mineral exploration, mining, smelting, and refining. Teck, as one of the largest lead and zinc producers in the world, operates a KIVCET flash lead smelter in Trail, BC. A large radiant shaft boiler and subsequent convection boiler to cool the off-gas of the smelter are two parts of this plant. The original boiler tubes were constructed of carbon steel, which experienced unacceptably high corrosion rates. Because of a successful application of Inconel 625 (UNS N06625) superalloy in Waste-To-Energy (WTE) boilers and low corrosion rates of this alloy in this specific application, alloy 625 weld overlay was applied on the waterwall tubes of the radiant boiler to reduce corrosion rate of the carbon steel tubes. However, even after performing this overlay, the corrosion rate of the weld overlay alloy 625, as well as the corrosion rate of the boiler tubes, are still unacceptably high, leading to the ultimate failure of the weld overlaid boiler tubes.

The company is now faced with a question as to whether alloy 625 weld overlay is the best choice for tube protection in this boiler. In this system, a range of heavy metal salts such as $PbCl_2$, ZnO, TlCl, Tl_2SO_4, and $PbSO_4$, to name just a few, deposited on the boiler tubes in the operating condition of the boiler. Heavy metal elements such as Pb, Cd, Zn, Tl, Br, and Fe together with S, Cl, and O enter the boiler from the reaction shaft in the gas phase. As the gas is cooled in the radiant section of the boiler, the mentioned compounds would condense on the boiler tubes, consequently causing the formation of deposited salt mixtures on the boiler tubes. The precipitation of the salts on the surface of the weld overlay alloy 625 caused the formation of phases with a low melting point. Low melting point molten phases play the main role in 1) dissolving protective layers of the alloy, 2) the occurrence of hot corrosion attack, also called molten salt-induced corrosion, and 3) the ultimate failure of the weld overlaid tubes.

It is worthwhile to mention that, based on the released statistics, 5-10% of the operating costs of such types of plants are attributed to the hot corrosion failure and related maintenance costs. However, because of strict economical considerations, the costs related to the maintenance of the plant (corrosion failure costs included) and related downtime and periodic shutdowns have to be reduced as much as possible, which is why focusing on this research topic and developing a better understanding of the high temperature corrosion phenomenon in this plant is of high importance, economical value and interest, particularly for industrial sectors. The corrosive environment of the radiant boiler in the KIVCET smelter is unique and no report can be found in the literature on this issue. Consequently, lack of knowledge in dealing with this costly industrial issue is evident which can justify the importance and originality of the present study.

Summarizing the key points in the reviewed literature, a high-temperature protecting system must meet several criteria; it should provide adequate resistance against the corrosive environment, be chemically and mechanically compatible with the substrate, be practically applicable, reliable, and economically viable. The Inconel 625 superalloy is one of the most important members of high Cr, high Mo-Ni-base superalloys. This alloy has been widely used in the form of bulk, weld overlay, or plasma-sprayed coatings for high temperature corrosion applications due to its oxidation resistance, even though alloy 625 presents vulnerability to suffering certain corrosion types under severe corrosive conditions. High concentrations of Cr and Mo and the presence of Nb and Si, which causes the formation of a Cr_2O_3 protective film together with NiO, Nb_2O_3, and $NbCrO_4$ and, in some cases, a Cr-Mo- and Nb-rich layer, are the most important compositional and microstructural features of alloy 625. More details on the properties and applications of this grade of superalloy will be described in chapter 2. Despite the fact that superalloys have been developed for high-temperature applications, it should be noted that they are not always able to meet simultaneous high-temperature strength and high-temperature corrosion resistance requirements in most applications. Historically, when gas turbine engines in military aircraft

were faced with severe corrosion attack and short-time failure during Vietnam conflict as a result of working over sea water, hot corrosion became a topic of scientific interest and importance in the late 1960s. Hot corrosion is the most prevalent mode of attack at high temperatures, in particular where the surface of the alloy is covered by a layer of deposited salt mixtures. A porous, non-protective, and poorly adhered scale forms on the surface of the alloy when hot corrosion occurs.

In summary, in the present project, a thorough failure analysis of the weld overlaid boiler tubes of KIVCET smelter was carried out to 1) identify the root cause of the failure, 2) characterize the corrosive environment of the boiler, and 3) study the interaction of the weld overlaid tubes with the molten salt deposits. This failure analysis also assisted in understanding the corrosion mechanism. In addition, electrochemical behavior and corrosion performance of the Inconel 625 superalloy in the form of wrought and weld overlay beneath simulated molten salt mixture were investigated. Based on the electrochemical studies and characteristics of the developed scale on the surface of the alloy, compatible electrochemical models were postulated to explain the corrosion phenomena and the nature of the developed scales in this system.

2 Literature review

2.1 KIVCET smelter and radiant boiler

In comparison with conventional sinter/blast furnace technology in the pyrometallurgical process of lead and zinc, the KIVCET smelter, as a modern direct smelting process, has several inherent advantages such as lower energy usage and operational costs and lower amounts of emissions (SO_2 as an example) which leads to improved environmental performance [1], suitability for smelting of a mixed lead concentrate and zinc plant residue charges, and finally effective reduction of lead from the slag [2-4]. Hence a number of industrial units around the world have replaced their previous sinter/blast furnace technology with modern KIVCET furnaces. The schematic of the KIVCET furnace, showing different areas of this furnace and its 30 m tall radiant boiler and a section of the weld overlaid carbon steel tubes, is presented in Figure 2-1 [5]. This KIVCET smelter has been in service in the Trail operation of Teck since 1997. High pressure water flows inside the tubes to extract heat from the high temperature off-gas of the smelter. Off-gas is in contact with the fireside (hot side) of the tubes. A large radiant shaft boiler and subsequent convection boiler to cool the off-gas are two parts of the smelter (see Figure 2-1).

As can be seen in Figure 2-1, the off-gas from the reaction shaft at 1375°C enters a 717 m^2 vertical radiant boiler of a membrane wall construction by means of an uptake shaft, constructed with water-cooled copper elements. In the radiant section of the boiler, the off-gas is cooled to 800-830°C prior to entering the downcoming section of the boiler. Based on the plants experience, actual boiler heat transfers are 11-16 kcal/ (m^2h °C) in the radiant section which depends on the feed composition. The total surface area of the downcoming section of the boiler is about 486 m^2 and the temperature of the gas decreased to 600-630°C in this section. Afterwards, the off-gas enters the convection section of the boiler with a total area of 1012 m^2 reduces the final gas temperature to 325-350°C. Final stages of

cooling occurred in the adiabatic-sprayed tower and cooling tower, where the temperature of the gas lowered to 65 and 18°C, respectively [5]. Because of the severely aggressive conditions in the boiler environment, the conventional waterwall tube materials, such as carbon steels and chromium-molybdenum steels, require some sort of corrosion protection. The current prevailing method of protection for the furnace waterwall is the use of alloy 625 weld overlay or cladding applied by the automatic gas metal arc welding (GMAW) process on the surface of the carbon steel tubes.

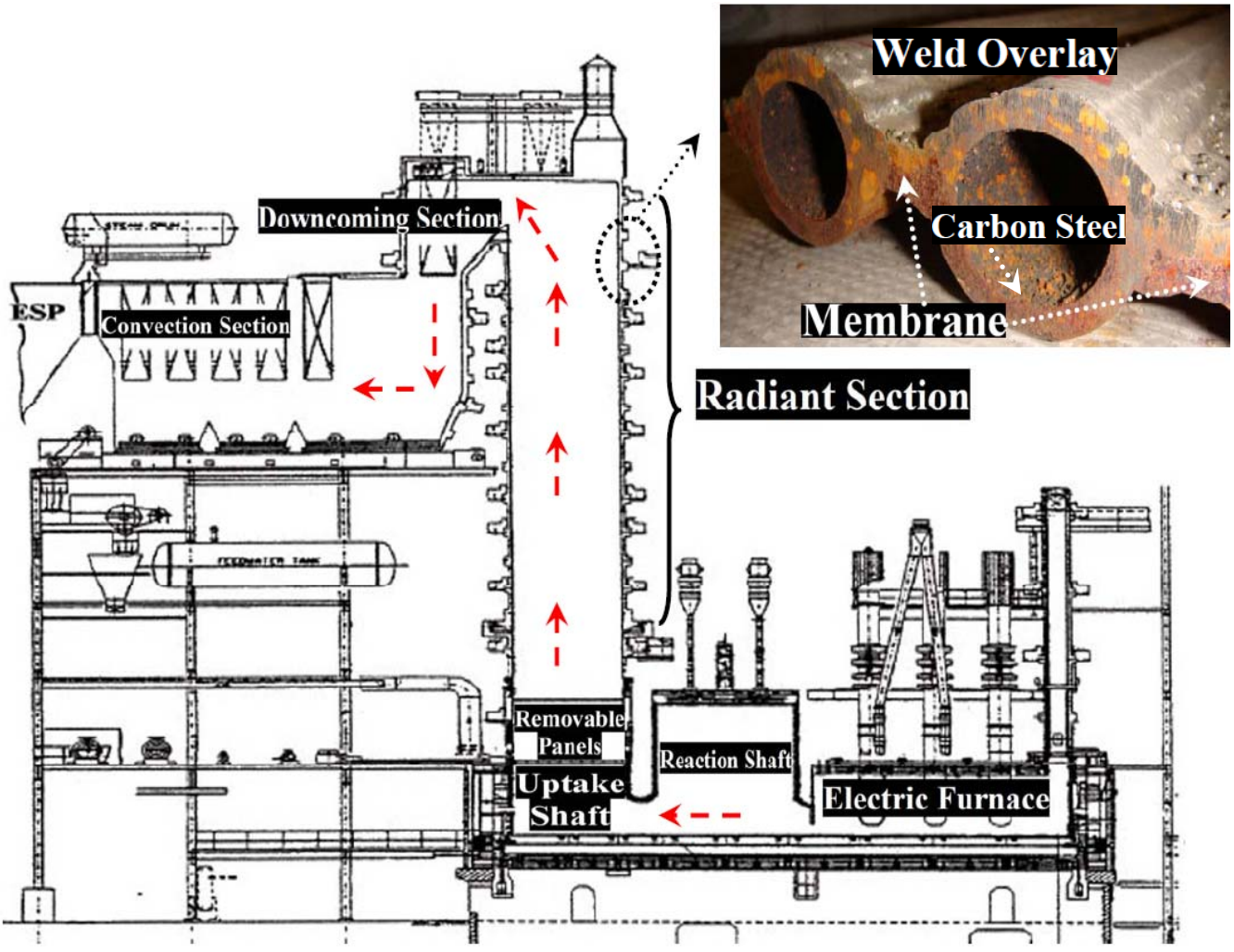

Figure 2-1- Schematic image of the KIVCET waste heat boiler and an image of the weld overlaid waterwall tubes in the radiant section of the boiler [5].

A section of the weld overlaid carbon steel tubes can be seen in Figure 2-1. The overlay cladding is typically performed on-site in the boiler. It should be mentioned that, in the radiant section of the Teck's KIVCET waste heat boiler, the original boiler tubes were constructed of carbon steel, which were experiencing unacceptably high corrosion rates because of the severely aggressive working conditions in the boiler environment. Consequently, a significant wall-thinning occurred in the tubes. Strength and structure integrity of carbon steel tubes, resistance of the tubes to high temperature and high pressure water and steam (used in heat transfer), and relatively low cost of the carbon steel are the key benefits of using carbon steel in manufacturing the waterwall tubes [6]. However, carbon steel does not have satisfactory resistance to corrosion at elevated temperatures in this environment. Hence, an alloy 625 weld overlay was applied on the waterwall tubes of the radiant boiler to control the corrosion rate.

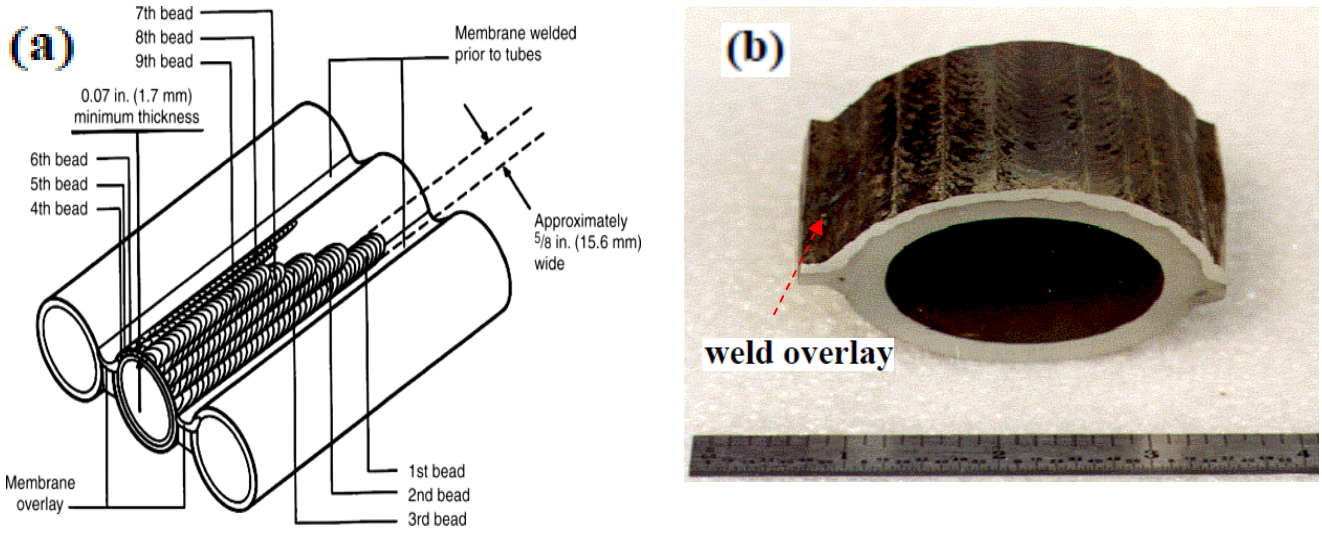

Figure 2-2- a) Schematic image showing the weld bead sequence in overlaying waterwall of a boiler, b) Cross section of a type 309 stainless steel overlay boiler tube sample, which was obtained from a recovery boiler waterwall [7] .

Figure 2-2 shows a schematic for the application of overlay cladding on the waterwall, consisting of membranes and tubes [7]. Alloy 625, developed primarily for high temperature turbine applications [8],

has good resistance to wear [9, 10] and corrosion [8, 11]. For these inherent properties, it has been mainly used as a weld overlay on carbon steel and chromium-molybdenum steel parts, which are in service under harsh corrosive environments.

2.2 Superalloys for high temperature application

Satisfactory resistance to mechanical (fatigue and creep) and chemical degradation at temperatures near their melting point is the main characteristic of superalloys [15]. They are nickel-based alloys, containing significant amounts of other alloying elements including chromium, molybdenum, and aluminum [12, 13, 15]. Nickel-based alloys are chosen for high temperature applications because nickel has a face-centered cubic (FCC) crystal structure which makes it ductile and tough. FCC metals have high symmetry [15]. Moreover, they contain four distinct (non-parallel) close-packed slip planes of the form {111} and three close-packed slip directions of the form <110> within each plane, giving a total of 12 slip systems. Accordingly, there is a wide choice of slip systems when an FCC metal undergoes deformation and at least one slip system is favourably oriented for slip to occur at low applied stresses, causing FCC metals to have high ductility and toughness [16-18]. Furthermore, nickel is stable in an FCC crystallographic structure at ambient temperature up to its melting point, as a result, no contraction/expansion can occur due to the phase transformation. Moreover, nickel has a moderate cost and low rate of thermally-activated creep, the latter being a crucial characteristic for turbine blade application [15]. These characteristics of nickel could justify the use of this element as a solvent for high temperature-resistant alloys [15]. It is worthwhile to mention that in the HCP transition metals, only cobalt is comparable with nickel to be used as solvent in temperature-resistant alloys. Hence, cobalt-based superalloys are used for high temperature applications although they tend to be more expensive than the nickel-based superalloys [14, 15]. The nominal chemical composition (wt. %) of some common wrought superalloys can be seen in Table 2-1 [15, 19].

Table 2-1- Chemical composition (wt. %) of some common wrought superalloys, which have been used for high temperature, corrosive environments (for all alloys, the balance is Ni) [15, 19].

	Cr	Co	Mo	W	Nb	Al	Ti	Fe	C	B	Zr
Inconel 617	22.0	12.5	9.0	-	-	1.0	0.3	-	0.07	-	-
Inconel 625	21.5	-	9.0	-	3.6	0.2	0.2	2.5	0.05	-	-
Inconel 740	25.0	20.0	0.5	-	2.0	0.9	1.8	0.7	0.03	-	-
Haynes 230	22.0	-	2.0	14.0	-	0.3	-	-	0.1	-	-
Nimonic 263	20.0	20.0	5.9	-	-	0.5	2.1	-	0.06	0.001	0.02

From a physical metallurgy point of view, the microstructure of a typical superalloy consists of different phases as described below [15, 20, 21]:

1- The gamma phase (γ) with FCC crystallographic structure forms a continuous matrix. Other available phases in microstructure of superalloy reside in this continuous γ matrix. Cobalt, chromium, molybdenum, ruthenium, and rhenium are the elements which can be found in the γ phase [22].
2- Precipitate phase of Ni_3 (Al, Ta, Ti) compound, called gamma prime precipitate (γ′), which is usually coherent with γ matrix. γ′ phase is rich in aluminum, titanium, and tantalum.
3- Carbides and borides: carbon concentrations in the microstructure of a superalloy is up to 0.2 wt. %. This element tends to combine with titanium, tantalum, and hafnium to form MC carbide. Carbides are often found in interdendritic or intergranular regions. Where a superalloy is utilized in a service temperature of about 750°C, decomposition of MC carbides to $M_{23}C_6$ and M_6C occurs. These carbide species prefer to form on the γ grain boundaries. $M_{23}C_6$ and M_6C carbides are rich in chromium, molybdenum, and tungsten. Borides form because boron tends to combine with chromium or molybdenum. The γ-grain boundaries are preferred sites for the residing of borides in the microstructure of the superalloy.

Alloy 625 is one of the most important members of high Cr, high Mo-Ni-based superalloys, which has been used in the form of bulk, weld-overlay or plasma-sprayed coatings for applications at high temperature, harsh corrosive environments due to its satisfactory oxidation resistance [15]. It is worth mentioning that weld cladding has been widely used in WTE boilers in the waste incinerator industry to protect boiler tubes against the harsh corrosive working environment of the boiler although it is very costly, ~ €2,000-€2,500 per square meter [38]. However, alloy 625 presents vulnerability to certain corrosion types under severe applications [23, 24]. Alloy 625 as a thermally-sprayed coating, as an alloyed material, or a weld overlay has been used to prevent high temperature oxidation and hot corrosion at elevated temperatures in gas turbines and waste-fired boilers [25]. High concentrations of Cr and Mo as well as the presence of Nb, which causes the formation of a Cr_2O_3 protective film together with NiO, Nb_2O_3, and $NbCrO_4$ and, in some cases, a Cr- Mo- and Nb-rich layer, are the most important compositional and microstructural features of alloy 625 [26].

The high content of nickel in alloy 625 has given satisfactory results in the mechanical performance of the alloy, and it has been observed that when the chromium oxide layer is dissolved by a corrosive environment, a NiO film is developed together with other metallic oxides [27, 28]. Its high content of chromium provides good resistance to oxidation and corrosion in molten salts at high temperatures mainly due to the formation of a Cr-rich protective oxide layer. Chromium is one of the most effective alloying elements to act against corrosion and is required to be between 18 and 24 wt. % to optimize its effectiveness [29-31]. The significant content of molybdenum makes the alloy 625 resistant to pitting and crevice corrosion, whereas a combined nickel and molybdenum content makes the alloy resistant to a non-oxidizing environment and crevice corrosion [32]. Alloying with niobium has stabilized it against sensitization during welding, thereby preventing subsequent intergranular attack [33, 34]. Niobium and tantalum stabilization makes the alloy suitable for corrosion service in as-welded condition. Furthermore, it has excellent resistance to chloride corrosion cracking [29].

With regard to Table 2-1, it is worthwhile to mention that Inconel 740 has been developed on the base of Nimonic 263 by Special Metal Corporation in the USA to be used at temperatures above 750°C as boiler superheater and reheater materials [15]. The highest stress-rupture strength for 10^5 h at 750°C amongst today's commercial superalloys as well as excellent oxidation and corrosion resistance at high temperature are two main characteristics of Inconel 740, which is why it is considered to be used in Europe for the most advanced fossil power plant at the steam temperatures above 700°C [35, 36]. Inconel alloy 617 is also one of the alloys selected as a candidate for cladding or structural material in new generation of nuclear power plants due to its good combination of high temperature strength and corrosion/oxidation resistance. Alloy 617 and 625 are solid solution- strengthened alloys. These two alloys are strengthened by the precipitation of carbides such as MC, M_6C, (rich in Ni, Nb, and Mo), and $M_{23}C_6$ (rich in Cr). Intermetallic phases formed when subjecting the alloys to aging treatment at intermediate temperatures. As was mentioned previously, the γ′ phase such as Ni_3 (Al, Ti) is a common intermetallic precipitate in Ni-based alloys and has been observed in alloy 617 as well [14, 15].

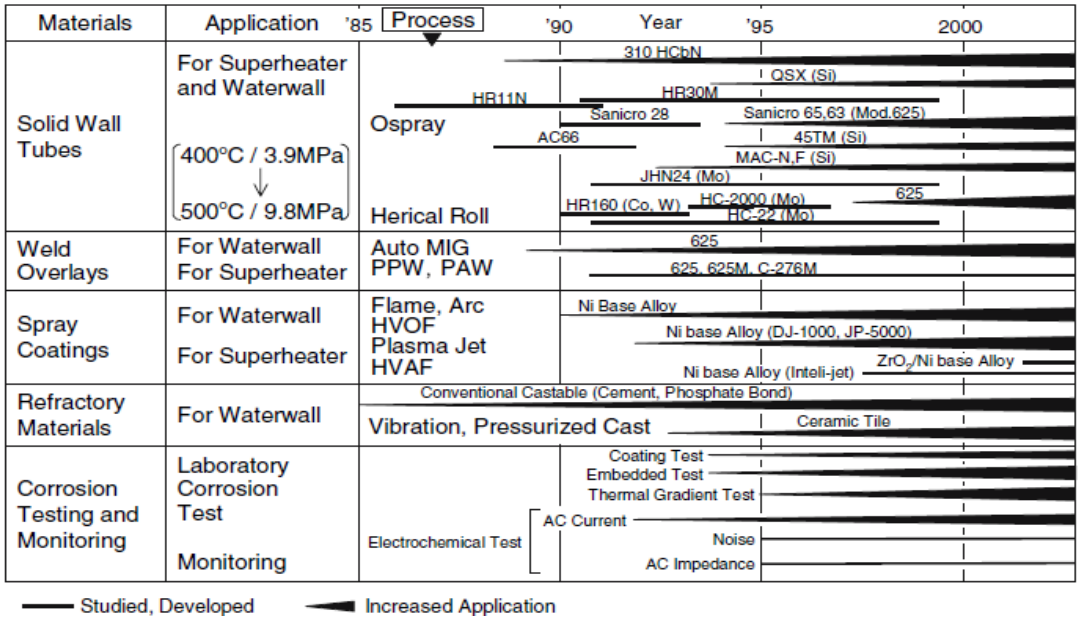

Figure 2-3- Development and application of different techniques to protect waterwall tubes of boilers against severe corrosive environments at high temperatures [37].

2.3 Corrosion protection at high temperature

Because of the severity of corrosive conditions in a boiler's environment, development and application of new corrosion-resistant materials and coatings have been extensively discussed in literature. Protecting metals and alloys at high temperature, especially where molten salt phases formed in the system, is challenging. According to Figure 2-3 [37], numerous techniques have been developed for dealing with high temperature corrosion issues in different types of boilers including: 1) development of solid-wall tubes with a higher resistance to corrosive environments, 2) use of weld overlay or spraying techniques such as high velocity, oxy-fuel spraying (HVOF) or air plasma spraying (APS) for depositing a thick layer of a material with strong resistance to high-temperature corrosion on the surface of the waterwall tubes in the boiler and, 3) application of refractory tiles on the surface of the waterwall tubes.

A general overview of these three protective techniques can be seen in Figure 2-4. Each of the above-mentioned techniques has its own advantages and limitations. As an example, the degradation of an alloy's mechanical properties and increasing the general costs of plants are the two most important drawbacks for the use of composite tubes or developing alloys with higher contents of alloying elements and higher resistance to high-temperature corrosion. These shortcomings justify the focus of researchers on the weld overlaying or spraying techniques for performing high temperature-resistant overlays and coatings on the waterwall tubes [38].

Furthermore, thermal conductivity of alloy 625 weld overlay is higher than refractory materials such as refractory tiles. This characteristic of alloy 625 weld overlay lead to a reduction of gas temperature in the first gas pass [52]. Alloy 625 is more expensive than refractory materials. However, the price of alloy 625 is partly compensated by avoiding the cost of refractory maintenance, as mentioned by Lee et al. [52]. A coating is protective if it prevents outward diffusion of metal cations and inward diffusion of

elements that could react with the substrate material. However, interconnected porosity, oxide-containing splat boundaries, and compositional inhomogeneities, which are created by coating processes, limit the corrosion resistance of the applied coatings [39].

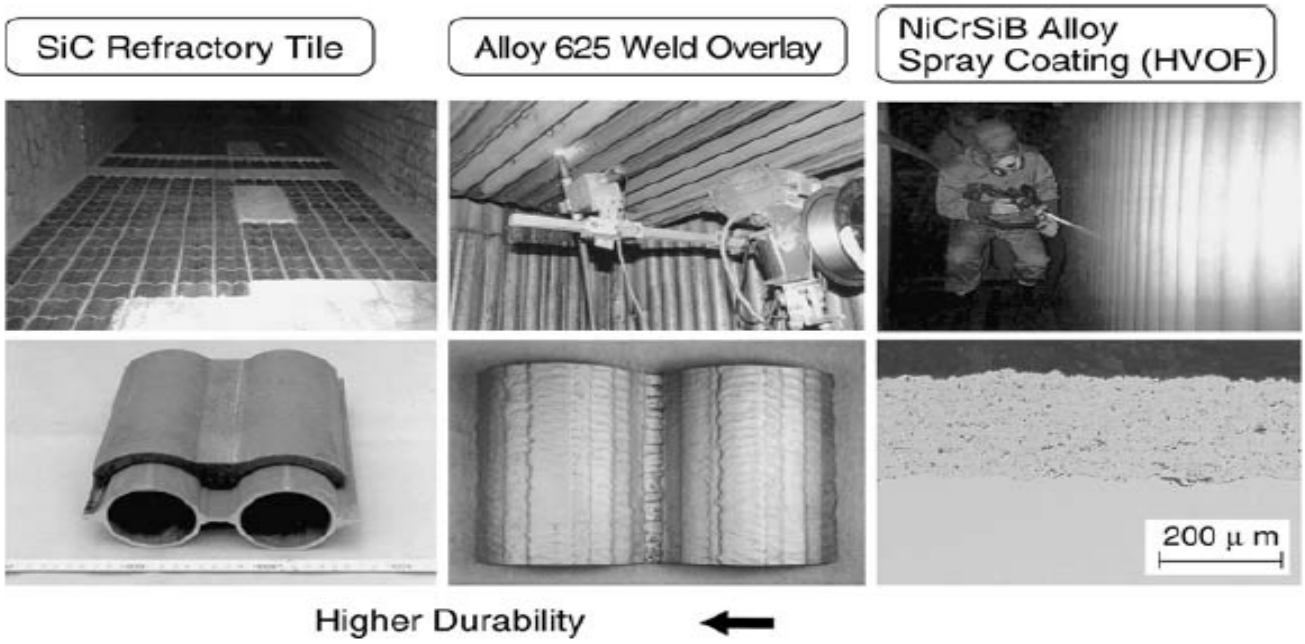

Figure 2-4- Application of corrosion-resistant materials to the waterwall tubes of the boilers [37].

2.4 Thermally sprayed protective coatings

Thermal spraying processes such as HVOF have been used to deposit protective overlay coatings onto the surfaces of engineering components, such as boiler waterwall tubes [40]. Protective coatings allow the engineering components to function well under extremely corrosive conditions [40-42]. With the advent of this process, thermal-sprayed coatings, which previously had limited usefulness as corrosion protection coatings due to the presence of interconnected porosity in the structure, have now gained popularity and are being studied extensively for their corrosion-resistant properties [42]. The metal spray of corrosion-resistance coatings with a thickness of about 150-500 μm (see Figure 2-4) can be applied on-site at low cost and relatively fast. Workability, severity of corrosive environment, required lifetime, and cost are the main considerations in the selection of a spray coating system for a specific

application [43, 44]. High density, increased thickness capability, smoother surface finish, lower oxide levels and porosities, less effect on the environment during the spray process, and having better corrosion, wear, and fatigue resistance properties, are all the characteristics of HVOF coatings [45-47]. According to Uusitalo et al. [48] and Ahmed et al. [41], a laser-melted HVOF coating does not suffer from any corrosion damage because laser remelting efficiently eliminates interconnected network of voids at splat boundaries of the HVOF coating and localized region of materials depleted in Cr. As-sprayed coating is penetrated by corrosive species because interconnected porosities compromise the effectiveness of the coating as a barrier to corrosive species [41]. The weak adherence of the deposited coating to the substrate, the presence of porosities, which typically range from 3-5% in plasma spray coatings and 1% in HVOF process, and the limitation in the maximum achievable coating thickness, which is about $500\,\mu m$, are the main shortcomings of the spray technology for providing a protective layer on engineering compounds [49, 50].

2.5 Solidification and weldability of alloy 625 weld overlay

Alloy 625 weld overlays possess an excellent corrosion resistance and welding workability [51, 52]. Weld overlaying is known as a technique with the capability of performing a dense coating layer, which is chemically bonded with a base metal, and its thickness is about several millimetres. The durability of weld overlay, which might be about 10 years or longer in certain applications, is significantly higher than the durability of thermally-sprayed coatings [37]. The major concern, associated with the weld overlay technique, is that repeated applications at the same area causes embrittlement of the old overlay, accelerating the process of crack initiation. Initiated cracks propagate into the overlaid tubes and ultimately lead to reducing the lifetime of the overlay [52, 53]. Furthermore, it is not possible to carefully predict the lifetime of weld overlay alloy 625 because lifetime is highly dependent on the corrosive nature of the boiler environment and deposited corrosive salts on the

overlaid tubes [52]; it may last as much as several years, or as little as a few months, which is completely dependent on the working condition and interaction of the weld layer with the corrosive medium. For the KIVCET waste heat boiler, there is absolutely no report and knowledge of the characteristics and nature of the existent corrosive environment in the boiler or lifetime of the weld overlay alloy 625 in this environment, which makes the situation more complicated and worthy of investigation.

In order to evaluate high temperature corrosion behavior of the alloy 625 weld overlay on waterwall tubes, having information about the effects of the welding process on the microstructure and properties of the weld overlay alloy is of high value. The first point, which should be considered with regard to this subject, is the solidification of the alloy and microstructural evolution during the welding process. This factor is important because microstructural changes during welding have a direct effect on the corrosion behavior of the weld overlay alloy. Solidification behavior of alloy 625 and dissimilar metal weld between alloy 625 (weld overlay) and Cr-Mo steel (GMAW process) were extensively studied by Cieslak et al. [54, 55] and DuPont [8], respectively. In the studies of Cieslak et al. [54, 55], the effects of variation in the amounts of Nb, Si, and C on the solidification behavior of wrought alloy 625 were evaluated. Results showed that the addition of Nb, Si, and C minor elements increased the melting and solidification temperature range of the alloy. Weldability (solidification cracking resistance) decreased with increasing the total minor element (Nb + Si + C) content, which is attributed to the increased solidification temperature range and tendency to form secondary phases at terminal stages of solidification [54, 55]. The most detrimental effect, which promotes susceptibility of the weld overlay to solidification cracking, belongs to Nb because Nb-bearing alloys terminate solidification by a eutectic-type reaction between γ and various Nb-rich phases such as NbC [54, 55]. Furthermore, with increasing the temperature range of solidification and formation of terminal secondary constituents in small quantities, the cracking tendency of weld metal increases [56]. However, cracking susceptibility

can often decrease because of the backfilling of hot cracks with the formation of large quantities of interdendritic liquid during the solidification process [57, 58].

Element	1	2	3	4	5	Average
Iron	17.6	19.5	17.7	17.8	17.6	18.0 ± 0.8
Nickel	30.0	29.4	30.7	29.4	31.3	30.2 ± 0.8
Chromium	11.7	11.6	11.6	11.6	11.4	11.6 ± 0.1
Molybdenum	16.9	15.4	16.7	17.4	17.3	16.7 ± 0.8
Niobium	22.5	22.6	22.1	22.1	21.1	22.1 ± 0.6
Silicon	1.1	1.2	1.0	1.4	1.0	1.1 ± 0.2

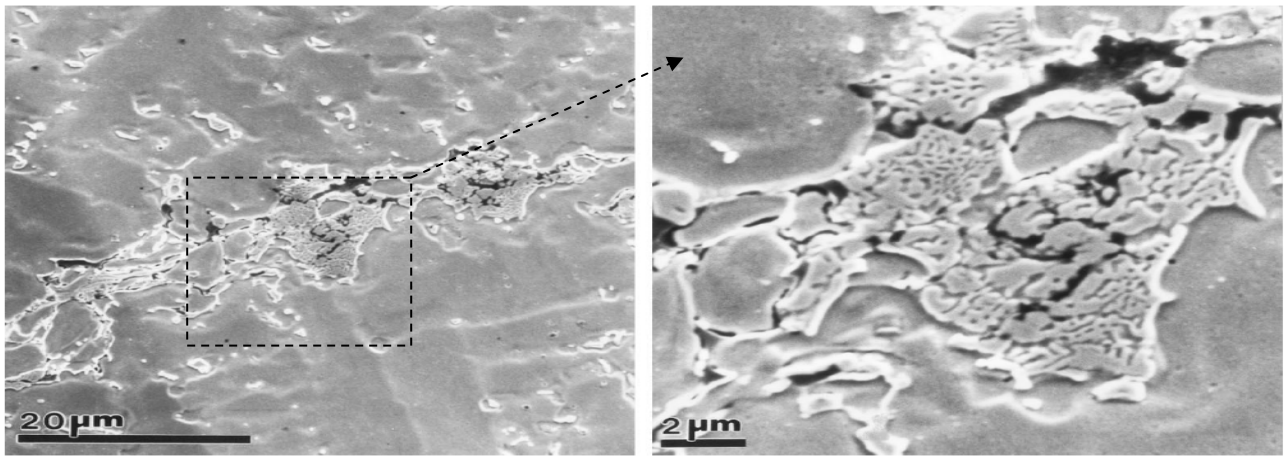

Figure 2-5- SEM photomicrographs of developed solidification cracks in weld overlay alloy 625 and chemical composition of secondary constituents (Laves phase) [8].

During the solidification process of alloy 625 overlays, microsegregation of some elements (most notably Nb and to a lesser extent Mo and Si) from dendrite cores to the liquid phase occurs and causes widening of the solidification temperature range and secondary phase formation [8]. The mentioned phenomena have a deleterious effect on the weldability of alloy 625 [8]. Segregation of Mo and Nb into interdendritic regions was also reported by Kalivodova et al. [38] and Ahmed et al. [41]. According to DuPont's report [8], formation of hot cracks in the alloy 625 overlay on Cr-Mo steel occurs due to the wide solidification range of this alloy (~ 170°C) and 1.3-2.2 vol.% of interdendritic constituents. As can be seen in Figure 2-5 [8], solidification cracks are always associated with this constituent and secondary constituents (Laves phase) are highly enriched in Mo, Nb, Si, and Fe and depleted in Ni and

Cr. However, the presence of solidification cracks does not completely prevent the application of alloy 625 as an overlay for protection of carbon and Cr-Mo steels [8]. Technically, a selection of filler alloys and substrate composition with relatively high C and low Fe and Si contents, along with reduction in dilution (transferring of Fe from substrate to overlay) through control of processing parameters (for example maximizing the filler metal feed rate to arc power ratio) may serve to reduce the solidification cracking problem [59, 60]. It is worthwhile to mention that reducing the crack susceptibility of alloy 625 weld overlays is of importance since the presence of any crack, which is open to the overlay surface, acts as a penetration path for molten salt into the overlay; it exacerbates the high temperature degradation of the overlay and results in ultimate failure.

2.6 Hot corrosion

2.6.1 Industrial significance

Historically, when gas turbine engines in military aircraft faced with severe corrosion attack and short-time failure during the Vietnam conflict, as a result of working over sea water, hot corrosion became a topic of scientific interest and importance in the late 1960s [70]. Hot corrosion is the most prevalent mode of attack at high temperatures, in particular where the surface of the alloy is covered by a layer of deposited salt mixtures [64, 70]. Reportedly, 5-10% of the operating costs of power generation plants, such as waste heat boilers, are attributed to the hot corrosion failure and related maintenance costs [52, 65]. Figure 2-6 shows the contribution of maintenance costs to the overall cost of a German WTE facility compared to the overall revenue [52, 65]. As can be seen in Figure 2-6, around 60% and 15% of the annual cost in the WTE facility is respectively allocated to the capital costs and maintenance costs [52, 65]. Typically, 30-35% of the maintenance cost should be allocated to dealing with corrosion issues, particularly hot corrosion in the boiler facilities; hence, corrosion issues cost a WTE boiler about 5% of its yearly total cost [52, 65].

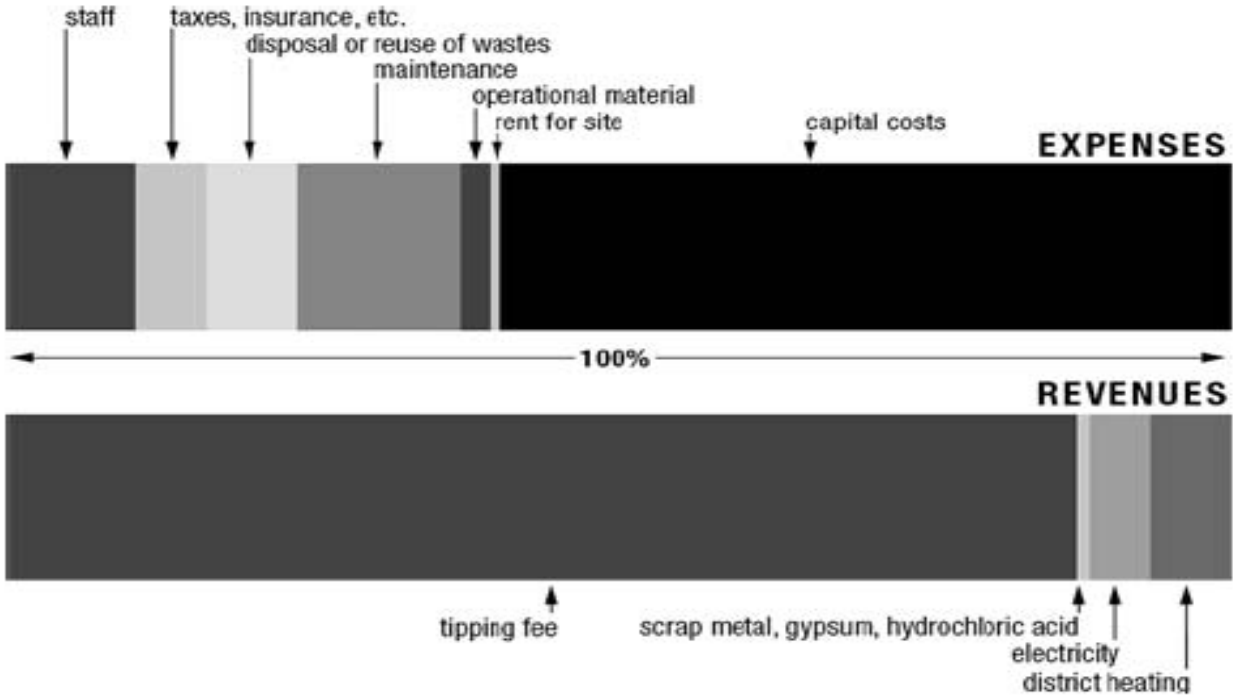

Figure 2-6- Contribution of maintenance cost to the overall cost of a German WTE facility compared to the overall revenue [52, 65].

Considering shutdowns of the facility for maintenance as a consequence of corrosion problems, the actual cost of corrosion issues in a boiler plant will be higher than the value estimated above. Because the present study was focused on the molten salt-induced corrosion in the radiant boiler of the KIVCET smelters, having a vision toward basic definition of this phenomenon and relevant variables is essential.

2.6.2 Definition and characteristics

Alloys used in practical environments such as power generation machines, gas turbines, waste-to-energy boilers and industrial waste incinerators, pulp and paper industries, coal-fired boilers, oil-fired boilers and furnaces, and black liquor recovery boilers sometimes undergo an aggressive mode of corrosion attack associated with the formation of salt deposits on their surfaces at elevated temperatures. This deposit-induced accelerated degradation is called “hot corrosion” [61]. For an occurrence of a severe hot corrosion attack, formation of a molten salt deposit is generally necessary

although in some cases having only a thick and dense solid deposit is enough for occurrence of a considerable hot corrosion attack [62]. Numerous variables, including composition and amount of deposits, gas composition, temperature, temperature cycling, erosion, alloy composition, and alloy microstructure, directly affect the severity of hot corrosion [63]. As a consequence of this corrosion phenomenon, a porous oxide scale is formed on the surface of the attacked alloy, which does not have acceptable capability to protect the substrate against harsh corrosive conditions [64].

Hot corrosion is explained as a two-stage process; at the beginning of the phenomenon, named as the initiation stage, the presence of solid or molten salt deposits do not have any considerable effect on the corrosion behavior of the alloy and corrosion rate is slow. It should be noted that during the initiation stage, alloy and deposit undergo some changes including: 1) depletion of the element which is responsible for the formation of the protective scale on the alloy's surface, 2) incorporation of a component such as sulfur or oxygen from the deposit into the alloy, and 3) dissolution of oxides into the salt or development of cracks or channels into the scale. The mentioned changes, which occur during the initiation stage of hot corrosion, make the alloy susceptible to rapid corrosion attack and degradation at the second stage of hot corrosion, named as the propagation stage [25, 63, 66-68].

Reportedly, local penetration of molten salt through the scale and subsequent spreading along the scale-alloy interface can occur at the end of the initiation stage. Consequently, molten salt can reach the sites with low oxygen activity and the Cr-depleted zones, when the alloy is a Ni- or Co-based superalloy containing a high percentage of Cr, which facilitates a rapid propagation stage. At the initiation stage of hot corrosion, the oxidation of alloying elements causes the electron transfer from metallic atoms to the reducible species. Oxygen acts as a reducible species in the environment, which comes from atmosphere and molten salt composition. In the second stage of hot corrosion (propagation stage), the protective nature of oxide scales is drastically reduced because oxide scales become porous and, subsequently, the alloy experiences rapid corrosion and ultimate failure [25, 63, 66-70]. The

transferring of sulfur from Na_2SO_4 to the alloy can occur during the propagation stage of Na_2SO_4-induced hot corrosion in combustion systems of energy generation plants [69]. In this type of plant, the use of residual fuel oil is common because it is cheaper than high-grade fuel [71]. In such cases, oxidation of these transferred sulfides could be known as another effective factor on degradation and could be considered as a propagation mode.

2.6.3 Classification of hot corrosion attacks

At an elevated temperature, a salt deposit can be a liquid phase from the beginning of exposure, or it could be solid and then becomes a liquid phase by reacting with the alloy and reaction with the environment. These two types of hot corrosion are named as “High Temperature Hot Corrosion” or “Type (I)” and “Low Temperature Hot Corrosion” or “Type (II)” [72-74]. This classification is important because the morphology and mode of attack in each type of hot corrosion is predictable. At the first type of hot corrosion (Type (I)), the temperature is higher than the melting point of the deposited salt, and it happens mainly in the temperature range of about 850-950°C. When a superalloy faces this mode of hot corrosion, after the formation of the Cr-depleted area on the surface of the alloy (initiation stage), oxidation and sulfidation of the base material accelerate; consequently, a porous and non-protective oxide layer forms on the surface of the alloy (propagation stage) [75, 76].

Type (II) of hot corrosion occurs well below the melting point of the deposited salt, where formation of low melting point eutectic salt phases between salt species and corrosion products causes localized attack and pitting. Localized/pitting corrosion occurs as a consequence of the localized breakdown of the protective oxide layer through the chemical reaction with the molten phase. In this type of hot corrosion, neither microscopic sulfidation nor Cr-depletion can be detected [75, 77]. Reportedly, the morphology of Type (II) hot corrosion consists of non-uniform attack with pits of different sizes

growing into the metal, which is why measuring the rate of this mode of hot corrosion through electrochemical techniques or weight-loss measurements is difficult and unreliable [78].

2.7 High temperature corrosion and failure of weld overlay alloy 625

The failure of alloy 625 weld clad boiler tubes in a supercritical, pulverized, coal-fired boiler, which extensively cracked and corroded after less than 24 months of service, was studied by Luer et al. [79]. The reason for the overlay cracking was identified as corrosion-fatigue. In the weld overlay, cracks initiated at the preferentially corroded Mo- and Nb-depleted dendrite cores, then propagated further along the main axis of the columnar dendrite in the valley of the weld ripples [79]. Preferentially corroded dendrite cores acted as microscopic stress concentration and crack initiation sites.

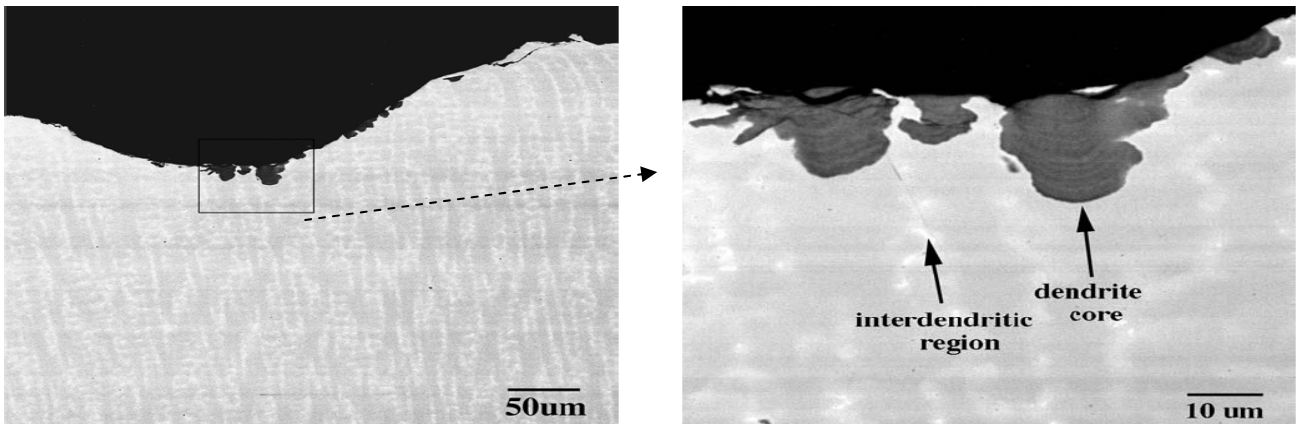

Figure 2-7- Preferential corrosion of Mo- and Nb-depleted dendrite cores in the weld overlay alloy 625, acted as microscopic stress concentration and crack initiation sites [79].

Figure 2-7 presents the dendritic microstructure and microsegregation of Mo and Nb. Preferential corrosion occurred in the dendrite cores of the weld overlay alloy 625 [79]. The lighter shaded areas in the weld metal are enriched with Mo and Nb and depleted in Cr. Oxidation and sulfidation were the main corrosion mechanisms that caused the formation of Cr-based oxide or oxide-sulfide phases together with Ni-based sulfide. Not discussed in this study are characteristics of the deposited salt mixture on the waterwall, the role of welding defects and solidification cracking on molten salt

penetration into the weld layer, ultimate failure of the overlay, and source of thermal stresses, which leads to thermal fatigue. The corrosion of alloy 625 welds was studied by Kalivodova et al. [38] in simulated waste combustion flue gas (2000 ppm HCl, 360 h, 600°C).

Similar to the findings of Luer et al. [79], localized corrosion, segregation of Mo and Nb in the weld metal and the formation of a Cr-depleted layer under the developed (Cr and Fe)-rich oxide layer on the surface of the weld metal were also reported by Kalivodova et al. [38]. Furthermore, the developed cracks along the (Nb and Mo)-rich interdendritic regions acted as pathways for the penetration of the corrosive species into the weld overlay [38]. Details can be seen in Figure 2-8 [38].

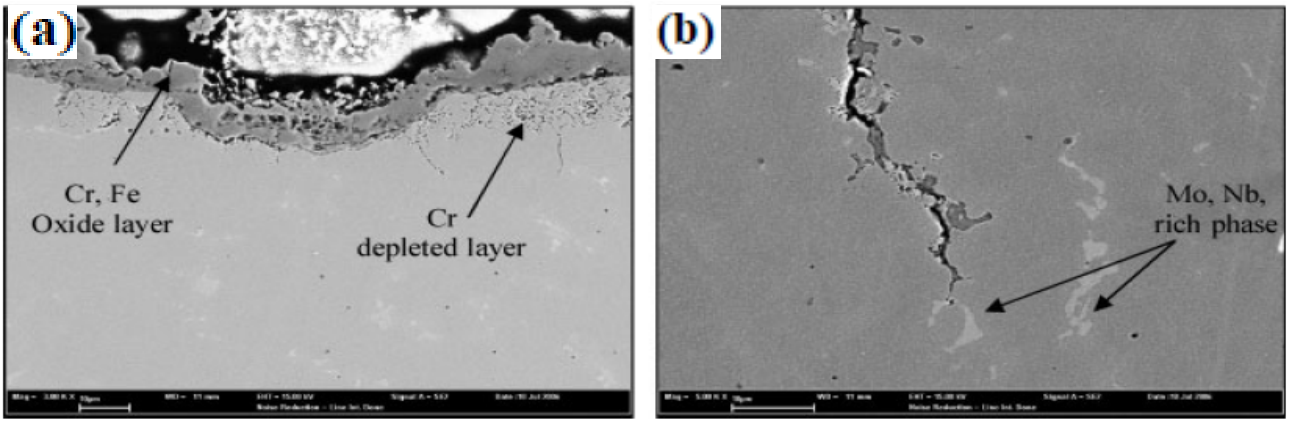

Figure 2-8- a) Cross sectional micrograph of oxidized surface of weld metal alloy 625 after exposure to simulated waste combustion flue gas (2000 ppm HCl, 360 h, 600°C), b) details of the crack in the weld metal alloy 625 after the exposure [38].

Montgomery et al. [80] reported severe corrosion of the weld overlay alloy 625 at a relatively low temperature of 300°C in waste incinerator and biomass plants, because of the presence of high levels of heavy metals together with chlorine in the system. The identified corrosion mechanisms under these conditions were pitting and dendritic corrosion. Under these conditions heavy metal chlorides posed the greatest threat with respect to corrosion attack due to their low melting points. Another point with regard to the welding structure is the segregation of Mo and Nb to the interdendritic regions [80], as

was also reported by Luer et al. [79]. Consequently, the galvanic effect between interdendritic regions and dendrite cores facilitated the occurrence of preferential corrosion.

The electrochemical impedance spectroscopy technique was used to study the corrosion behavior of alloy 625 in $ZnCl_2$- KCl salt mixture at 650°C for up to 200 hr by Perez et al. [81]. Nyquist plots were composed of two capacitance loops, a small semi-circle at high frequency and a large semi-circle at low frequency. The corrosion process was controlled by the transition of ions in the oxide scale. Because of Zn and Nb diffusion from molten salt and alloy respectively, both $ZnCr_2O_4$ and $NbCrO_4$ were found as corrosion products in this system [81]. In this study, EIS profiles fit to a protective scale model before 100 hr of exposure and to a porous scale model afterwards [81]. The effect of temperature fluctuation as well as gas temperature on corrosion behavior of the alloy 625 weld overlay on surface of SA 213 steel in WTE plants was evaluated by Kawahara et al. [82]. Findings of this study confirmed that localized corrosion attack occurred at a low metal temperature of 300°C and that the diffusion of alloying elements is very slow without the presence of molten salt [82]. This kind of corrosion was accelerated by a breakdown of the protective oxide layer due to thermal stress that resulted from differences in thermal expansion rates of the substrate and its weld metal [82]. The severity of corrosion environments at the interface of metal/molten salt was influenced by the penetration depth of the corrosive species through scales [83]. Accordingly, it was reported that the protective effects of oxide films, derived from alloying elements, played an important role in preventing corrosion attack.

In a WTE environment, when the molten phase contains chlorine and sulfur, formation of corrosion products with a lamellar structure on the alloy 625 weld overlay was observed [83]. Furthermore, the occurrence of oxidation, sulfidation, and chlorination was confirmed at the alloy/scale interface under a low P_{O2}–high P_{Cl2} condition [83]. In another study, Ishitsuka and Nose [84] reported that in molten chloride and chloride/sulfate mixture, Cr_2O_3 dissolved rapidly as a hexavalent chromium ion. In fact, in molten chloride environments, which mainly forms in WTE boilers, the dissolution of protective Cr_2O_3

films occurred through the chemical formation of CrO_4^{2-} [84]. Analysis of severely corroded tube samples, which were obtained from different waste-fired steam boilers in the USA, showed that Cl, Zn, Pb, Cd, Na, K, and S, along with major alloying elements from the tube (Fe in steel tubes or Cr, Ni, and Mo when the tube was coated by an alloy 625 overlay) can be detected in deposits and corrosion products [85]. Deposited salts on the severely corroded waterwall tubes contained 10-30 % chloride, 33-47% Pb, 3-13% Zn, 3-14% Na, and 2-11% (wt.%) K and chloride salts played the main role in the corrosion mechanism [85]. In some cases, the morphology of the corroded weld overlay alloy 625 involved general metal wastage followed by an internal corrosion penetration along dendrites of the weld overlay as also reported by Luer et al. [79]. This internal corrosion penetration through the dendrites in weld overlay is very similar to the internal oxidation attack within the alloy matrix or intergranular oxidation attack following general oxidation for wrought alloys [85].

2.8 Pseudo-reference electrode selection for molten salt-induced corrosion studies

The application of platinum as a counter electrode and as a pseudo-reference electrode has been widely reported in literature, particularly under molten salt corrosive conditions, some much harsher than that in the present study. This fact confirms that platinum has been known a reliable pseudo-reference electrode to be utilized in molten salt-induced corrosion studies. Considering the importance of selecting a suitable pseudo-reference electrode in a molten salt-induced corrosion study, some of the relevant manuscripts are reviewed in this section. Barraza-Fierro et al. [86] reported the utilization of platinum wire as a pseudo-reference electrode which was immersed directly in a molten LiCl-55 wt. % KCl electrolyte medium in order to study the electrochemical behavior of Fe-40 at.% Al intermetallic compound at 450, 550, and 600°C. However, the reduction/oxidation (redox) electrochemical couple was not identified [86]. Zeng et al. [87] used a three-electrode electrochemical cell arrangement and a platinum foil as a counter electrode to study the corrosion behavior of FeAl and Ni_3Al in (0.62 % mol.

Li, 0.38 % mol. K)$_2CO_3$ at 650°C and (0.36 % mol. Li, 0.64 % mol. (Na, K))$_2SO_4$ at 700°C under air atmosphere after 24 hr of exposure to a molten salt medium.

The use of platinum foil as a counter electrode was also reported for an electrochemical impedance spectroscopy study by Tristancho-Reyes et al. [88]. Tristancho-Reyes et al. studied the hot corrosion behavior of Ni-19Cr-18Fe-5Nb-3Mo-1Ti-0.5Al plasma-sprayed coating on a SAE213-T22 alloy, which is commonly used in thermal power generation plants, in molten 80% Na_2SO_4-20% V_2O_5 and 80% K_2SO_4-20% V_2O_5 mixtures at 700°C under static air atmosphere. In this study, the corrosion cell was a three-electrode arrangement and a high-purity platinum wire was used as a pseudo-reference and counter electrode in polarization and EIS studies [88]. Corrosion resistance of a 12CrMoV alloy in 52% $PbCl_2$-48% KCl (% mol.) molten salt mixture at 450, 500, and 550°C was studied by Otero et al. [89]. In this study, platinum was used as both a counter and pseudo-reference electrode in a three-electrode cell arrangement during polarization and EIS studies. The use of platinum wire as a pseudo-reference and counter electrode was also reported by Espinosa-Medina et al. [90] in a three-electrode cell design for potentiodynamic polarization and EIS studies. In this report, molten $NaVO_3$ salt at 700°C was selected as an electrolyte [90].

Corrosion behavior of a Ni_3Al intermetallic compound in molten 52% $LiCO_3$-48% K_2CO_3 (% mol.) at 650°C was studied through potentiodynamic and linear polarization, EIS, and electrochemical noise techniques by Gonzalez-Rodriguez et al. [91]. In this study, the pseudo-reference and counter electrode was made of a 0.5 mm diameter platinum wire inside a mullite tube and filled with refractory ceramic cement [91]. In another report, published by Martinez-Villafane et al. [92], the electrochemical behavior of SA213-T22 and SA213-TP347H, which are widely used in power generation boilers, was studied in 80% V_2O_5-20% Na_2SO_4 (% mol.) in the temperature range of 540°C to 680°C in a three-electrode electrochemical cell design utilizing platinum wire as a pseudo-reference and counter electrode for performing potentiodynamic polarization tests. In this report, it was emphasized that

several other pseudo-reference electrode systems were tested; because platinum gave the best results, it was selected as the pseudo-reference and counter electrode during electrochemical tests [92].

In a report published by Cuevas-Arteaga et al. [93], high temperature corrosion of alloy 800 in 80% Na_2SO_4-20% V_2O_5 (% mol.) molten salt mixture was studied at 700 and 900°C utilizing potentiodynamic and linear polarization tests during 10 days of exposure. Platinum wire was used as a pseudo-reference and counter electrode in a three-electrode electrochemical cell in this research work [93]. The application of platinum wire as a pseudo-reference and counter electrode was also reported for corrosion behavior evaluation of alloy 800 in 20% Na_2SO_4-80% V_2O_5 (% mol.) molten salt mixture at 700 and 900°C utilizing potentiodynamic polarization and electrochemical noise techniques [94]. In these two reports [93, 94], the successful application of platinum wire as a pseudo-reference and counter electrode for performing electrochemical tests at 900°C under highly corrosive condition (high sulfate content of the salt mixture intensifies the corrosivity of the molten salt medium) for 10 days is an indication to support the reliability of platinum as a pseudo-reference and counter electrode in molten salt-induced corrosion studies. In two other reports of Cuevas-Arteaga et al. [95, 96], the corrosion behavior of HK-40m alloy in 80% Na_2SO_4-20% V_2O_5 and 20% Na_2SO_4-80% V_2O_5 (% mol.) molten salt mixtures was investigated via electrochemical noise technique [95] and the linear polarization resistance method [96] at 700°C over a maximum exposure time of 10 days. In these two reports, the application of platinum wire as pseudo-reference and counter electrode was also reported.

Espinosa et al. reported the stability of a platinum electrode as a pseudo-reference in molten Na_2SO_4 at 900 and 1000°C [97] and molten $NaVO_3$ at 700°C [98]. In this study, in order to check the stability of platinum wire, two platinum electrodes were immersed in the working salt and the potential of the first electrode was monitored with time once the temperature was stabilized [97, 98]. Reportedly, after 40-50 min of immersion in the molten salt, the potential difference was very stable, having a fluctuation of ± 2 mV [97, 98].

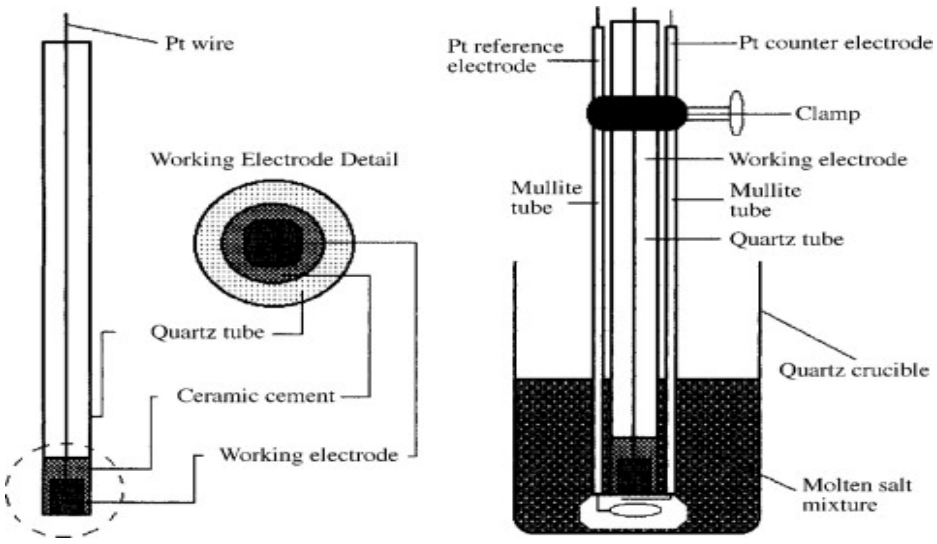

Figure 2-9- Schematic diagram of the electrochemical three-electrode cell used by Martinez et al. [99].

Figure 2-9 shows the scheme of the three-electrode cell of the experimental setup utilized by Maritnez et al. [99] to study hot corrosion behavior of Fe-40 at.% Al, Fe40Al-0.1B and Fe40Al-0.1B-10Al_2O_3 intermetallic materials in molten $NaVO_3$ at 625 and 700°C using polarization curves and linear polarization resistance measurements. In this study, two platinum wires were used as a pseudo-reference and counter electrode and each one was inserted in a mullite tube for electrical isolation, as can be seen in Figure 2-9 [99]. Successful application of the platinum electrode for a high temperature, molten salt-induced corrosion study was also mentioned by Gao et al. [100] and Farrell et al. [101, 102].

3 Objectives

Although heavy metals including Cd, Pb, Zn, Fe as well as S, O, and Cl are the main elements playing a leading role in the formation of molten phase on the waterwall tubes of the KIVCET waste heat boiler, hot corrosion behavior and electrochemical properties of the weld overlay and wrought alloy 625 have not previously been studied. Furthermore, there is still a question as to whether alloy 625 is the best choice for tube protection in the KIVCET waste heat boilers, although alloy 625 weld overlay has been a successful choice in protecting waterwall tubes of WTE boilers against corrosion in WTE corrosive environments.

The objective of this project was to develop a better fundamental understanding of the molten salt-induced corrosion/hot corrosion of alloy 625, in the form of weld overlay and wrought alloy, beneath the molten salt mediums containing the above elements. The following steps were followed toward the objective of the project:

A. To conduct a detailed failure analysis on the failed overlaid tubes waterwall of a KIVCET waste heat boiler to identify the root cause and mechanism of the failure and to propose technical recommendations to minimize the risk of failure in future applications.
B. To characterize the deposited salt mixtures on the waterwall tubes of the KIVCET waste heat boiler for designing a simulated salt mixture to be utilized as an electrolyte in the laboratory-scale hot corrosion studies.
C. To prepare a reliable hot temperature electrochemical test setup for conducting electrochemical tests in the simulated molten salt mixture at high temperatures.
D. To study electrochemical and hot corrosion behavior of weld overlay and wrought alloy 625 in the simulated molten salt mixture of the KIVCET waste heat boiler.

4 Experimental procedure

4.1 Deposited salts mixture characterization

Salt mixtures deposited on the waterwall tubes of the radiant boiler were characterized to determine chemical composition, phase structure, morphology, and thermal behavior. The deposits were gathered from the surfaces of the waterwall tubes during one of the periodical shutdowns of the plant. The morphology and physical condition of the deposits can be seen in Figure 4-1. Based on the physical condition and morphology, the deposited mixture in Figure 4-1a was split into four groups of samples (Samples 1-4) and each sample was separately characterized. Samples 1, 2, 3, and 4 can be seen in Figures 4-1b, c, d, and e, respectively.

Phase analysis of the deposits was studied by the x-ray diffraction technique (XRD: Rigaku MultiFlex, Tokyo, Japan) and by using Ni filtered Cu Kα ($\lambda_{Cu\ K\alpha}$ = 0.154186 nm, radiation at 40 kV and 20 mA) over the 2θ range of 10-80° (scan speed: 2° per minute, and step size: 0.04°). Obtained XRD patterns were compared to the standards compiled by the "Joint Committee on Powder Diffraction and Standards" (JCPDS) to identify phases. Chemical composition of the deposits was determined by inductively coupled plasma/atomic absorption spectroscopy (ICP/AAS: Inspectorate-International Plasma Laboratory, IPL, BC, Canada). Microstructure and morphology of the deposited salts were also studied by a scanning electron microscope with light-metal, energy-dispersive x-ray spectroscope (SEM/EDX: Hitachi S-3000N, Tokyo, Japan). For this purpose, the deposited salts were mounted in a cold-epoxy resin. The mounted samples were ground on 600, 1200, and 2400-grit silicon carbide papers followed by polishing on 6, 1, and 0.5 μm polishing pads. The deposits were examined by differential thermal analysis (DTA: Linseis L70 / 2171, Linseis Inc., Selb, Germany) in an air atmosphere from ambient temperature up to 1200°C at a heating rate of 10°C min^{-1} to evaluate thermal behavior of the mixtures and to determine the liquidus temperature of each mixture. Characterization of

the deposits was important for designing a simulated salt mixture used as an electrolyte in electrochemical tests to study hot corrosion resistance of the weld overlay.

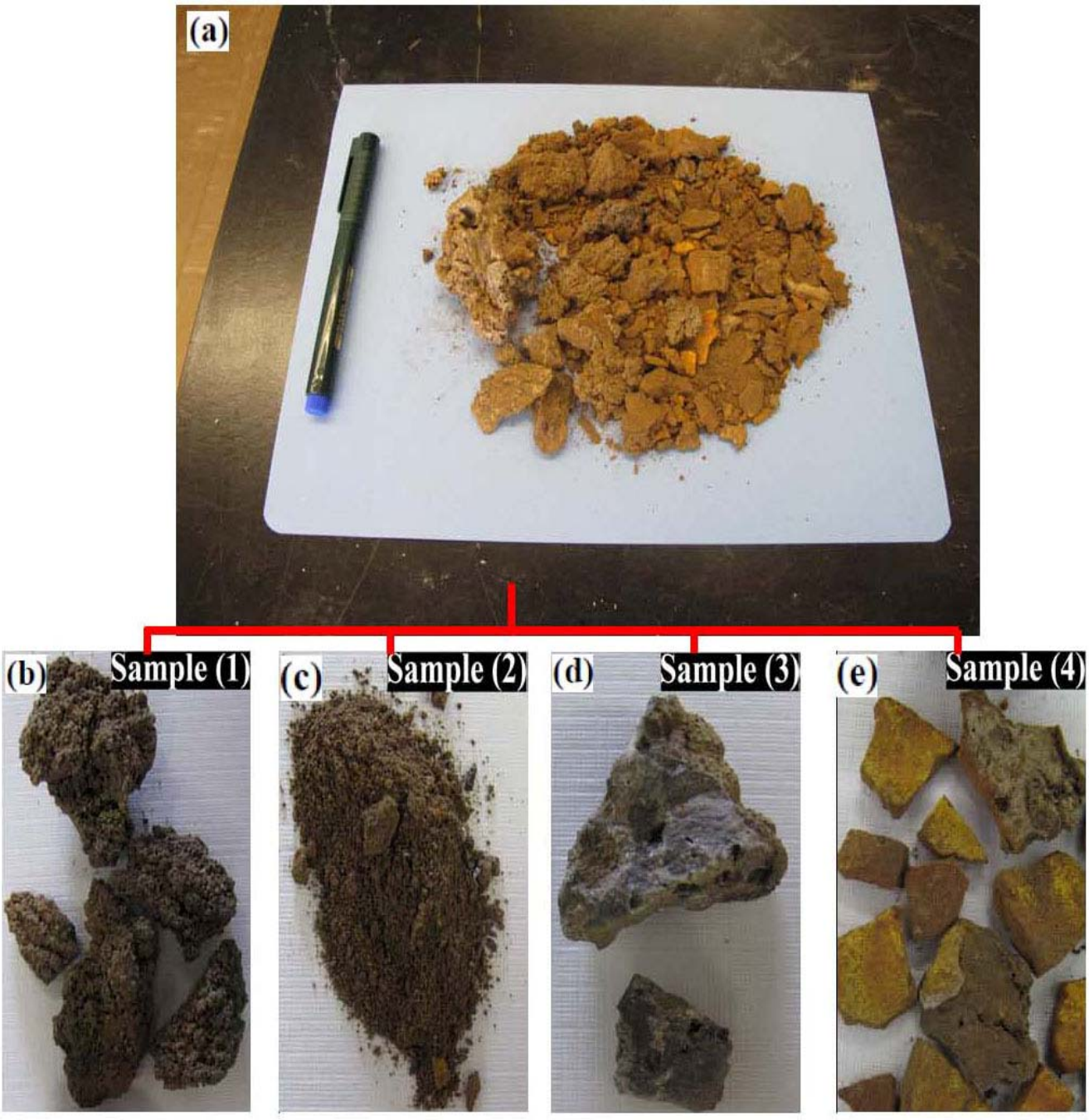

Figure 4-1- a) Morphology and physical condition of the actual deposited salt mixtures on the waterwall of the boiler; b), c), d), and e) show different groups of the samples selected from the actual salt mixture in (a), for characterization purpose.

4.2 Failure analysis study

A part of the failed waterwall was cut to investigate the condition of the weld overlay and the substrate. This part was partially covered by the deposited salt mixtures during service in the boiler. It was cleaned from the deposited salts and corrosion products. The methodology for characterization of the deposited salts was explained in section 4-1. This part of the failed waterwall was a window portion, containing five tubes. This sample can be seen in Figure 4-2.

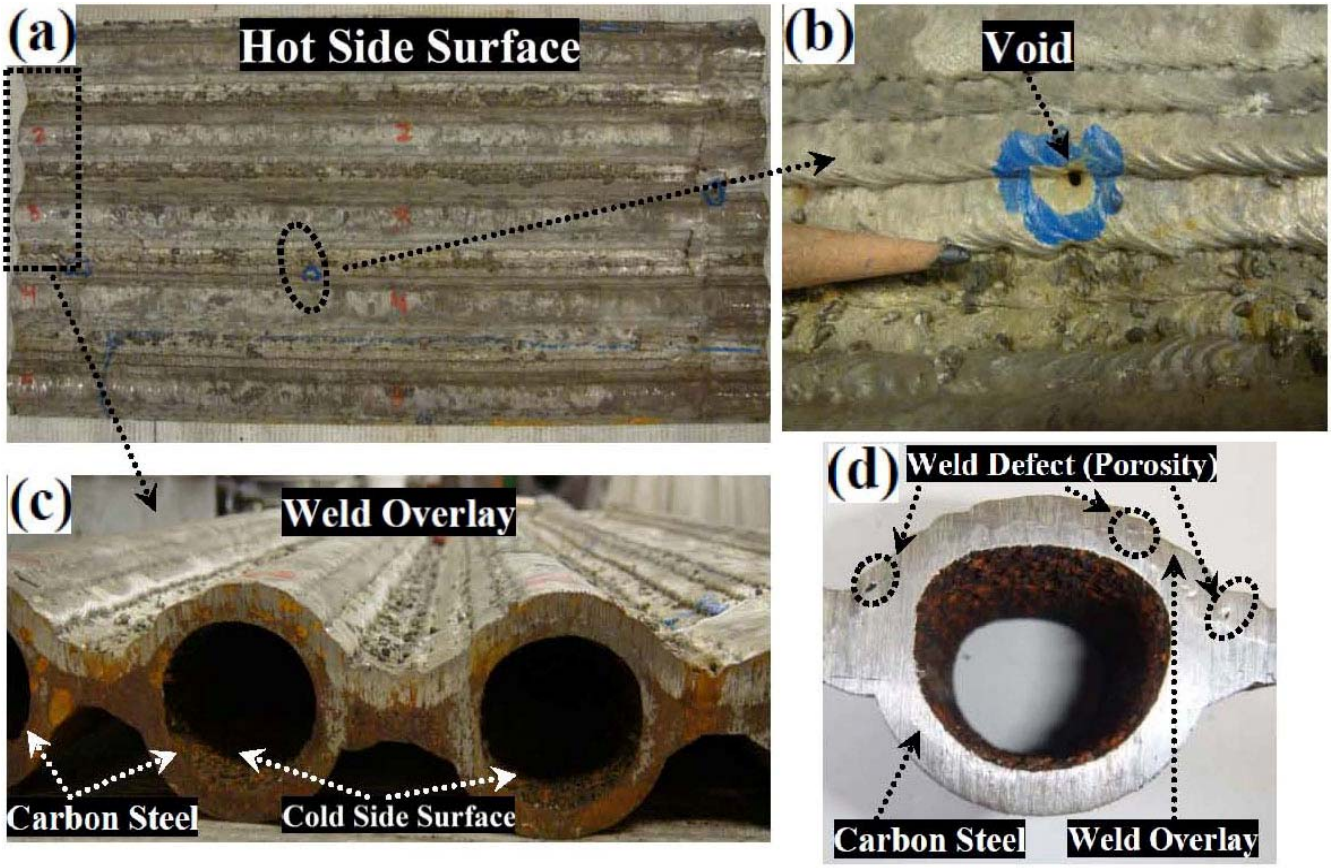

Figure 4-2- a) and c) A sample of the failed waterwall, coated by the weld overlay alloy 625, b) A well-developed cavity formed in the weld overlay in the boundary of two weld beads, and d) A cross section of the failed tube after grounding, showing the presence of porosities in the weld overlay.

The sample had two sides, including the front side covered with the weld overlay alloy 625 and facing the hot off-gas of the smelter (hot side surface: HSS), and the back side (cold side surface: CSS). HSS is the surface exposed to the deposited salts during service in the radiant boiler environment. After visual inspection, dye penetrant and fluorescent dye penetrant tests were conducted on the HSS in this part of the failed waterwall. Afterwards, several groups of samples were cut from different locations in this part of the failed waterwall for metallographic examination. Locations of the samples were selected based on the results of visual examinations, fluorescent dye penetrant tests, and conducted SEM studies on the surface of the weld overlay. For a cross sectional metallographic study, the mounted samples were ground with silicon carbide (grit range of 80-4000) and subsequently diamond polished down to 6, 1, and finally 0.05μm. The polished samples were studied by an optical microscope and SEM/EDX. Preparation of the specimens for the metallographic study was done based on the ASTM E3-11 [103]. ISO/DIS 26146 standard was also considered for the metallographic examination of the samples [104]. To observe the microstructure of the alloy 625 weld overlay on the failed tubes, polished samples of the weld overlay were etched in a solution containing 5 mL H_2SO_4, 3 mL HNO_3, and 92 mL HCl [105].

4.3 High temperature electrochemical study

4.3.1 Preparation of working electrode

Weld overlay and wrought alloy 625 working electrodes had a rectangular shape with dimensions of 20 × 10 × 2 mm. Chemical composition of the weld overlay and wrought alloy 625 was determined by ICP/AAS. To observe the microstructure of the wrought alloy 625 in as-received condition, one sample was polished and then etched in a solution containing 5 mL H_2SO_4, 3 mL HNO_3 and 92 mL HCl for 35 seconds [105]. The etched sample was examined by an optical microscope and SEM/EDX. Preparation of specimens for metallographic study was done based on ASTM E3-11 [103]. Mean grain size of the wrought alloy 625 was measured by a lineal intersection method based on ASTM E112 – 10 [106].

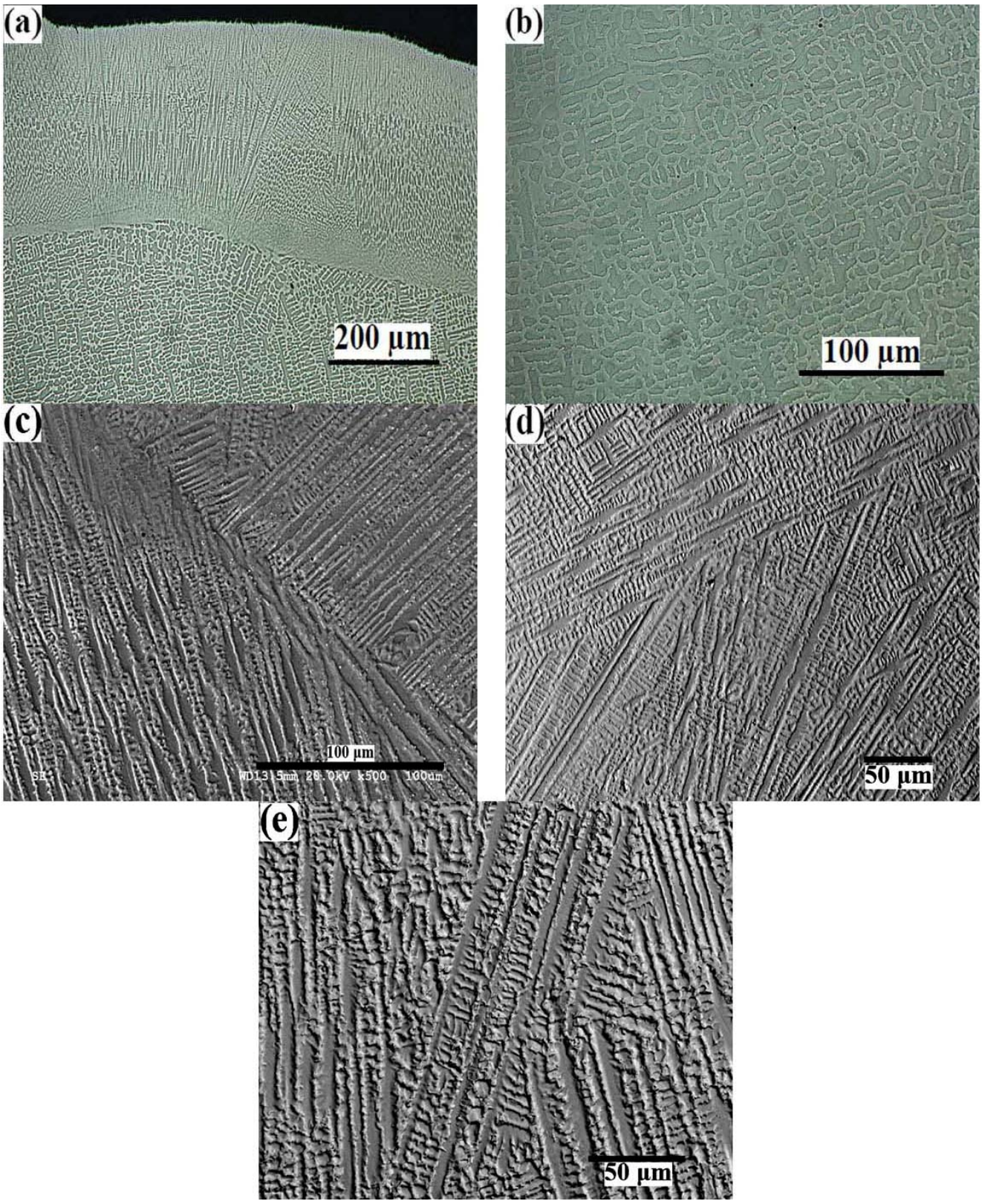

Figure 4-3- a) and b) Optical, c), d), and e) SEM photomicrographs of the weld overlay alloy 625, showing the microstructure and the dendritic solidification in the weld overlay.

On a laboratory scale, it was not technically possible to produce an alloy 625 weld overlay with characteristics exactly similar to the weld overlay alloy 625 in the radiant boiler. For this reason, weld overlay samples were carefully cut from specific locations of the waterwall in the radiant boiler, which were in sound condition. In these locations, no macroscopic or microscopic signs of corrosion attack were observed in the weld overlay. These samples of the weld overlay alloy 625 were used to prepare the working electrodes for conducting the hot corrosion electrochemical studies. Microstructure of the weld overlay alloy 625 working electrode prior to the test can be seen in Figure 4-3. The chemical composition of the weld overlay alloy 625 was determined by ICP/AAS analysis.

For preparation of the working electrodes, the rectangular pieces of the weld overlay and wrought alloy 625 were ground to 600-grit silicon carbide paper, rinsed with distilled water, ultrasonically degreased with acetone, and dried under a warm air stream. A wire made of 80Cr-20Ni (wt. %) was spot welded to each sample to provide an electrical connection between the working electrode and potentiostat. Alumina tubes were used to isolate the 80Cr-20Ni wire and gap between the alumina tube and the wire was filled with refractory cement (Ceramabond: Aremco Products, Inc., NY, USA). Use of specimens ground to 1200 and/or 4000-grit [107-110] silicon carbide paper and even polishing with a diamond paste (6 and/or 1 μm) [111, 112] were reported in corrosion studies, in particular molten salt-induced corrosion and high temperature oxidation. In fact, there are no specific standard instructions for the grounding and preparation of specimens for a molten salt-induced corrosion study.

4.3.2 Molten salt electrolyte medium

Analytical-grade $PbSO_4$, CdO, and Fe_2O_3 (Sigma-Aldrich, MO, USA), Pb_3O_4 (Alfa Aesar, MA, USA), $PbCl_2$ (Anachemia, QC, Canada), and ZnO (Fisher Scientific, NH, USA) were used to prepare the simulated salt mixtures. For preparation of the simulated salt mixtures, the measured amounts of the necessary chemical compounds (Table 4-1) were milled to ensure homogeneity of the final mixture.

Because of the serious safety concerns associated with Tl and Br, these two elements and their compounds were not examined in this project for preparation of the salt mixtures. Tl and Br compounds tend to form relatively low melting point molten phases with Pb, Cd, and Zn at a temperature as low as 200-300^{o}C. The focus of the present study is on the hot corrosion of the weld overlay alloy 625 in the regions of the radiant boiler where the concentration of Tl and Br in the deposited salt is negligible.

Table 4-1- Chemical composition (wt. %) of the prepared simulated salt mixtures.

	$PbSO_4$	$PbCl_2$	Pb_3O_4	ZnO	Fe_2O_3	CdO
Salt Mixture (1)	47	7	13	23	10	0
Salt Mixture (2)	47	7	13	23	0	5
Salt Mixture (3)	47	7	13	23	0	10

Elemental analysis of the simulated salt mixtures is presented in Table 4-2. The composition of the simulated salt mixture was selected based on the chemical composition of the corrosive salt mixtures deposited on the waterwall tubes of the radiant boilers in the KIVCET lead and zinc smelter.

Table 4-2- Elemental analysis (wt. %) of the prepared simulated salt mixtures.

	Pb	Cl	S	Zn	Fe	Cd
Salt Mixture (1)	48.1	1.7	5	18.6	3.5	0
Salt Mixture (2)	48.1	1.7	5	18.6	0	4.4
Salt Mixture (3)	48.1	1.7	5	18.6	0	8.8

4.3.3 Platinum pseudo-reference electrode

The electrochemical cell was constituted by the working electrode and two 1.2 mm diameter/500 mm long platinum wires as auxiliary and pseudo-reference electrodes which were immersed directly in the molten salt medium. The platinum wires were woven together to produce a mesh-like counter electrode. Redox electrochemical couple of the platinum pseudo-reference electrode was not identified. The mesh-like counter electrode (CE) to the working electrode (WE) surface ratio was equal to 5

(CE:WE = 5:1). The platinum electrodes were cleaned and abraded using 600-grit silicon carbide paper, ultrasonically washed in ethanol and then in acetone, and dried under a warm air stream before being isolated in the alumina tubes and sealed with the refractory cement, leaving a 25 mm-long free length to make direct contact with the molten salt medium. The alumina tubes, which were used for preparation of the pseudo-reference, the counter and working electrodes, were replaced after each test. All the potentials cited in the text are given versus pure platinum as the pseudo-reference electrode.

It should be noted that selection of a correct reference electrode has always been a major issue in a molten salt-induced corrosion study [86]. Particularly in the present study, finding a suitable candidate that can successfully serve as a reference and counter electrode was very challenging due to the extreme harshness, toxicity, and novelty of the molten salt medium. Because of the novelty of the corrosive medium, there were no prior experiences or knowledge about a suitable reference and counter electrode that can demonstrate acceptable performance, stability, and durability. Hence, a number of reference electrode systems were tested such as pure silver, pure platinum, platinum - 30 wt. % iridium, and platinum - 10 wt. % ruthenium. However, pure platinum demonstrated the best response, stability, and durability. The stability of the pure platinum wire as a pseudo-reference electrode in the molten salt mixture was confirmed by ICP/AAS, SEM/EDX, and XRD techniques as well as weight-loss measurement method. Reportedly, the platinum pseudo-reference electrode satisfies three conditions including fast kinetic, well-known redox couple and constant potential [86]. Furthermore, application of pure platinum as a counter and reference electrode has been widely reported in literature, which was reviewed in section 2.8.

Silver wire dipped into molten salt-containing silver cations (Ag^{+}) such as silver chloride (AgCl) was another candidate to be used as a reference electrode [86, 113]. Ag^{+}-containing salt must be separated from the molten salt medium by a conductive membrane to have ionic continuity with it [86]. Two potential membrane materials, which were considered to create this electrode, were yttria-stabilized

zirconia and alumina. However, none of them can demonstrate acceptable performance, stability, and appropriate durability in the $PbSO_4$-ZnO-Pb_3O_4-Fe_2O_3-$PbCl_2$-CdO molten salt system which was used as an electrolyte in the present study. Because of the inhomogeneous nature of the molten salt medium, pores of the porous membrane would be blocked at high temperature and the membrane could not successfully play its role in such an inhomogeneous system. The molten salt system was inhomogeneous because it did not have a specific melting point and it melted in a wide temperature range. Furthermore, the conductive membranes must be manufactured in a laboratory because they are not commercially available [86]. Because of these technical limitations, this type of reference electrode was not examined in the present study.

4.3.4 Electrochemical techniques and weight-loss measurement

The specific amounts of the simulated salt mixture (15 g cm^{-2} of the initial area of the specimen) were introduced into a 30 mL alumina crucible to give a melt depth of about 3.5 cm. The crucible was then set inside a vertical electrical furnace to reach the test temperature, which was measured constantly during the tests using a type K thermocouple under a dynamic air atmosphere (flow rate: 200 $mLmin^{-1}$). The crucible and the solid corrosive salt mixture were replaced for each experiment. The potentiostat used in the electrochemical experiments was a Princeton Applied Research (PAR) model 273A with M352 analysis software (see Figure 4-4a).

Open-circuit potential (OCP) measurement, potentiodynamic polarization tests, and electrochemical impedance spectroscopy (EIS) were conducted in the molten salt medium at 600, 700, and 800°C in the three-electrode electrochemical cell arrangement. Each test was repeated at least twice to ensure reproducibility of obtained results. Once the crucible containing the simulated salt mixture was set into the electrical tube furnace, the electrochemical cell was introduced inside the crucible and the

corresponding wires of the potentiostat were connected to the electrochemical cell (see Figure 4-4b). The OCP was recorded during the first 24 hr of immersion.

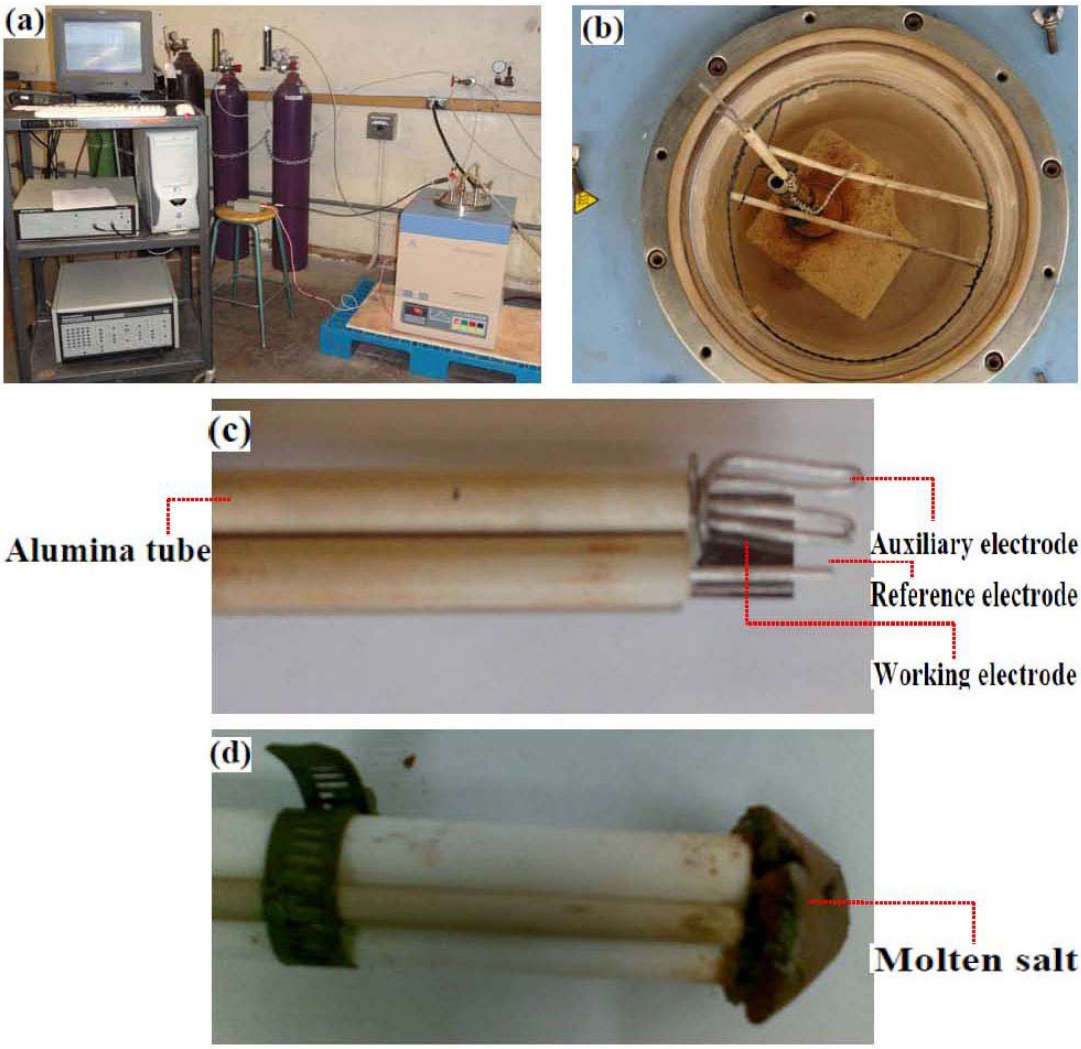

Figure 4-4- a) and b) Experimental arrangements, c) Electrochemical cell design, and d) Formation of molten salt around the electrode tip after conducting high temperature corrosion test.

Before performing the potentiodynamic polarization and EIS tests, the OCP of the cell must reach a stable value and the system should be at an equilibrium condition. Afterwards, impedance measurements were carried out in a frequency range of 50 kHz to 1 mHz with the AC voltage amplitude of ± 10mV with respect to the OCP. In the potentiodynamic polarization test, the potential of

the working electrode was continuously increased from -200 to +1200 mV with respect to the OCP at a scan rate of 0.166 mV/s.

Selection of the potential sweep rate of 0.6 V/h (0.166 mV/s) for performing the polarization test was based on the requirements of ASTM G59-97 [114] and ASTM G5-94 [115]. It should be noted that a different fresh working electrode was used for each electrochemical test. Electrochemical determination of the corrosion current density (i_{corr}) as well as the anodic and the cathodic Tafel slopes (β_a and β_c) by the Tafel extrapolation technique was not possible because the obtained potentiodynamic polarization curves, in log representation, did not show a decade of linearity (Tafel region), even in the cathodic branch. Weight-loss measurement has been widely used as the most accurate and precise method for corrosion rate determination [116]. In this method, a relatively simple procedure and easy experimentation reduce the probability of introducing systematic errors into the obtained results [116]. In order to examine the corrosion rate of alloy 625 through the standard weight-loss measurement (gravimetric) method, an embedded test was carried out under the same experimental conditions as that for the electrochemical tests, considering the standard procedure presented in ASTM G1-03 [117] and ASTM G31-72 [118]. The schematic of the embedded test was reported by Kawahara [83]. Once the initial weights and dimensions of the specimens were measured and the samples were ultrasonically washed in acetone, the samples were exposed to the molten salt mixture in a 30 mL alumina crucible. At each temperature, three specimens were tested in different crucibles, under identical conditions, to control the precision of the final weight-loss measurement data. After 24 hr of exposure to the molten salt medium at 600, 700, and 800°C, the corroded samples were taken out of the furnace and cooled down in static air. All the tests were conducted at 600, 700 and 800°C because molten phase did not form in the simulated salt mixtures at temperatures below 600°C.

In order to measure the weight-loss of the corroded samples after the embedded test, it is essential to completely remove the scales and corrosion products from the corroded surfaces. Accordingly, the

corroded samples were scraped using a wire brush, mechanically cleaned under a compressed air stream, washed in boiling distilled water, and ultrasonically cleaned in the alcohol to remove loose and bulky corrosion products and deposits. The corrosion products and scales strongly adhered to the corroded samples. Consequently, it was not possible to remove all the corrosion products and the scales from the surface of the corroded sample through a physical technique. Therefore, the rest of scales were chemically removed according to the standard methodology presented in ASTM G1-03 [117]. After being cleaned and dried, the corroded specimens were weighed by an electronic balance with a sensitivity of 10^{-4} g. The corrosion mass loss (ΔW) was determined by subtracting the mass of the corroded specimen after removal of the scales and corrosion products from the initial mass of the specimen. The corrosion rate was reported as a millimeter per year (mm/year), calculated by using the following equation [117]:

$$\text{Corrosion Rate (mm/year)} = K \left(\frac{\Delta W}{DAT} \right) \tag{4-1}$$

where K = 87,600 (a constant), T = time of exposure (hr), A = surface area (cm^2), ΔW = mass loss (g), D = density = 8.44 g cm^{-3} (for alloy 625).

4.4 Characterization techniques

At the end of the EIS test, the working electrode had been taken out of the furnace before it was characterized by SEM/EDX. The SEM was used to study the surfaces and cross section of the corroded samples after the EIS test in which it can be considered just a slight potential perturbation, which means almost free corrosion condition. In order to study the morphology and chemical composition of the scales and corrosion products, the corroded sample is immediately placed in the SEM chamber to be analyzed after the EIS test. It should be noted that for determining the type and mechanism of the corrosion attack, the scales and corrosion products must be removed from the corroded surfaces. For

this purpose, the corroded sample was physically cleaned under the compressed air stream and washed in boiling distilled water for 30 minutes, followed by the ultrasonic cleaning in a bath of the alcohol for one hour to remove the loose and bulky corrosion products and deposits. Then the standard methodology presented in ASTM G1-03 [117] was followed to chemically remove the rest of the scales. This standard methodology was carefully followed to ensure that the corroded sample was cleaned from corrosion products and the scales. This must be done to observe the surface directly exposed to the molten salt medium through the SEM, determining the type and the mechanism of the corrosion attack.

For cross sectional SEM analysis, the cross section of the corroded sample, taken after the EIS test (no prior treatment on the corroded sample or de-scaling), was mounted in a cold-epoxy resin. The mounted sample was ground on 600, 1200, and 2400-grit silicon carbide papers, followed by polishing on 6, 1, and 0.5 μm polishing pads. The ISO/DIS 26146 standard was considered for a metallographic examination of the samples after exposure to the molten salt medium [104]. The use of this standard was also mentioned by Firouzi and Shirvani [119]. Phase analysis of the corrosion products and scales on the surface of the attacked specimens were studied by x-ray diffraction technique (XRD: Rigaku MultiFlex, Tokyo, Japan) and using Ni filtered Cu Kα ($\lambda_{Cu\ K\alpha}$ = 0.154186 nm, radiation at 40 kV and 20 mA) over the 2θ range of 10-80° (scan speed: 2° per minute, and step size: 0.04°). For phase analysis, the XRD patterns were compared to the standards compiled by the "Joint Committee on Powder Diffraction and Standards" (JCPDS) to identify the phases. The amounts of the dissolved alloying elements in the molten salt electrolyte were quantitatively measured using the ICP/AAS analysis.

5 Failure analysis of the weld overlay alloy 625 in the KIVCET waste heat boiler[1]

5.1 Background

An alloy 625 (UNS N06625) was applied as a weld overlay on the waterwall tubes of the radiant boiler in the KIVCET flash lead smelter by an automatic gas metal arc welding (GMAW) process to control/reduce the corrosion rate of the carbon steel tubes. This process was done on-site in the boiler. In order to achieve a uniform coverage of the waterwall (*i.e.*, membranes and tubes), the weld beads were deposited by the GMAW technique in a vertical down mode starting from the membrane and then moving to the tube section based on a pre-programed weld bead sequence. Multiple welding passes were performed to fully cover the surface of the waterwall with a single layer of the weld deposit. The schematic diagram of the process can be seen in Figure 2-2a. The wire transfer mode was either sprayed or pulsed sprayed during welding. A single-layer GMAW overlay was followed by a gas tungsten arc welding (GTAW) wash pass. The GTAW wash pass remelted the GMAW deposit without any filler addition. The technical details of the GMAW technique were as follows: Type of Polarity: DC Reverse (DCEP); Amperage Range: 190-225 A; Voltage Range: 21-27.5 V; Minimum Travel Speed: 0.01 m/s (25 inches per minute, IPM), and Maximum Heat Input Rate: 593,622 J/m (15,078 Joule per Inch, J/In). GTAW parameters were selected as follows: Type of Polarity: DC Straight (DCEN, Non-Pulsed); Amperage Range: 350-435 A; Voltage Range: 12-16.5 V; Minimum Travel Speed: 0.01 m/s (25 IPM), and Maximum Heat Input Rate: 687,559 J/m (17,464 J/In). In both GMAW and GTAW techniques, amperage, voltage, and travel speed were carefully controlled in the mentioned ranges to assure that maximum heat input did not exceed the specified maximum heat input rates at any time during welding. Heat input was calculated by multiplying welding voltage × welding amperage × 60 and dividing the results by travel speed (in inches per minute: IPM). The resultant value was heat

[1] A version of this section is published: E. Mohammadi Zahrani, A. M. Alfantazi, "Hot corrosion failure of overlay weld cladding in radiant boiler of a KIVCET flash lead smelter", Metallurgical and Materials Transaction: A, 44 (2013) 4671-4699.

input, measured in Joules per inch (J/In). According to the presented images of the waterwall in Figure 2-1 and Figure 4-2, each of the weld beads was overlapped by the subsequent weld bead to ensure full coverage with no missing spots. The average thickness of the weld overlay was about 3.38 ± 0.5 mm, determined by cross-sectional SEM analysis of the overlaid tubes.

The application of alloy 625 weld overlay or cladding applied by the GMAW process is known as the current prevailing cost-effective and long-term protection method for providing life extension for boilers in a diverse range of corrosive environments [6]. Reportedly, the weld overlaying technique can provide a dense coating layer which is chemically bonded to the base metal with a thickness of several millimetres [37]. A wide range of reports on the successful application of weld overlay alloy 625 in the waste incinerator industry and WTE boilers to mitigate the corrosion issue was the main reason to select this strategy for protecting the waterwall tubes of the radiant boiler in the KIVCET smelter against corrosion attack. However, in the radiant shaft boiler, the corrosion rate of the alloy 625 weld overlay and the boiler tubes are still unacceptably high. Deposition of salt mixtures on the waterwall tubes occurred in the radiant boiler environment. Presence of these deposits seems to be an important factor in exacerbating the corrosivity of the boiler environment and accelerating the degradation of the weld overlay and tubes. A mechanical hammer was periodically used in the radiant boiler to hit the waterwall, which caused the physical removal of the deposited salt on the waterwall, to facilitate the heat transfer through the tubes. A sample of the overlaid tubes from the KIVCET waste heat boiler, received for evaluation and failure analysis study, can be seen in Figure 4-2.

Prior to the use of the GMAW technique for applying the weld overlay alloy 625 in this boiler, the plasma spray (APS) technique had been utilized to perform an alloy 625 coating on a limited section of the waterwall tubes of the boiler for protection purposes. However, the plasma-sprayed coating was not able to act as an effective barrier layer to protect the tubes against the corrosive environment and its long-term performance was not acceptable. Because of the weak bond strength of the plasma-sprayed

coating and its relatively thin thickness, the plasma-sprayed alloy 625 coating did not demonstrate an appropriate durability in this application. Consequently, ultimate failure of the plasma-sprayed alloy 625 coating happened after several months of being in service. This can justify the selection of the GMAW technique for performing the alloy 625 protective layer on the waterwall tubes of the radiant boiler in the KIVCET smelter.

Preventing high temperature oxidation and hot corrosion at elevated temperatures due to oxidation resistance of alloy 625 is the main purpose for this broad range of applications of this alloy in the form of weld overlay or plasma-sprayed coatings for high temperature protection applications in many corrosive environments such as gas turbines, waste-fired boilers, as well as in pulp and paper industries [25]. Despite the wide range of weld overlay Inconel 625 application to protect waterwall tubes in different types of boilers and to reduce corrosion rates of boiler tubes in energy production applications, there is no systematic study on investigating failure of the weld overlay alloy 625 at high temperatures in the presence of deposited salt mixtures. In particular, the corrosive environment of the radiant boiler in the KIVCET flash lead smelter is unique due to the presence of deposited salts containing heavy metals such as lead, zinc, and cadmium, together with chlorine, oxygen, and sulfur. The hot corrosion failure mechanism of the weld overlay alloy 625 in this environment when deposited salts exist, as well as characteristics of the deposited salts are not well understood, yet. The purpose of this chapter is to discuss the results of a conducted detailed failure analysis on the failed overlaid tubes waterwall in the KIVCET waste heat boiler to identify the root cause and mechanism of the failure and to propose technical recommendations to minimize the risk of failure in the future applications. Furthermore, corrosion behavior and electrochemical properties of the weld overlay in 47 $PbSO_4$-23 ZnO-13 Pb_3O_4-7 $PbCl_2$-5 CdO (wt. %) molten salt medium are assessed in laboratory scale.

5.2 Deposited salt mixture characterization

Due to the importance of the salt mixtures deposited on the waterwall tubes on degradation of the weld overlay alloy 625, having detailed information about phase structure and chemistry of the deposits is essential for developing a better understanding of the root cause of the degradation in the weld overlay and the role of the deposited salts in this phenomenon [28]. XRD patterns of samples 1-4, which are deposited on the waterwall tubes, were presented in Figure 5-1. The general appearance of samples 1-4 of the deposited salt mixtures can be seen in Figure 4-1. Based on the XRD results, $PbSO_4$ (anglesite), $PbO_{1.55}$, PbS (galena), and $Pb_2(SO_4)O$ (lanarkite) [$Pb(SO_4)$ + PbO] phases were the main Pb-containing phases in the structure of samples 1, 2, and 3. The strongest intensity of the diffraction peaks in the XRD patterns of samples 1, 2, and 3 belonged to the characteristic peaks of $PbSO_4$ and $Pb_2(SO_4)O$ phases.

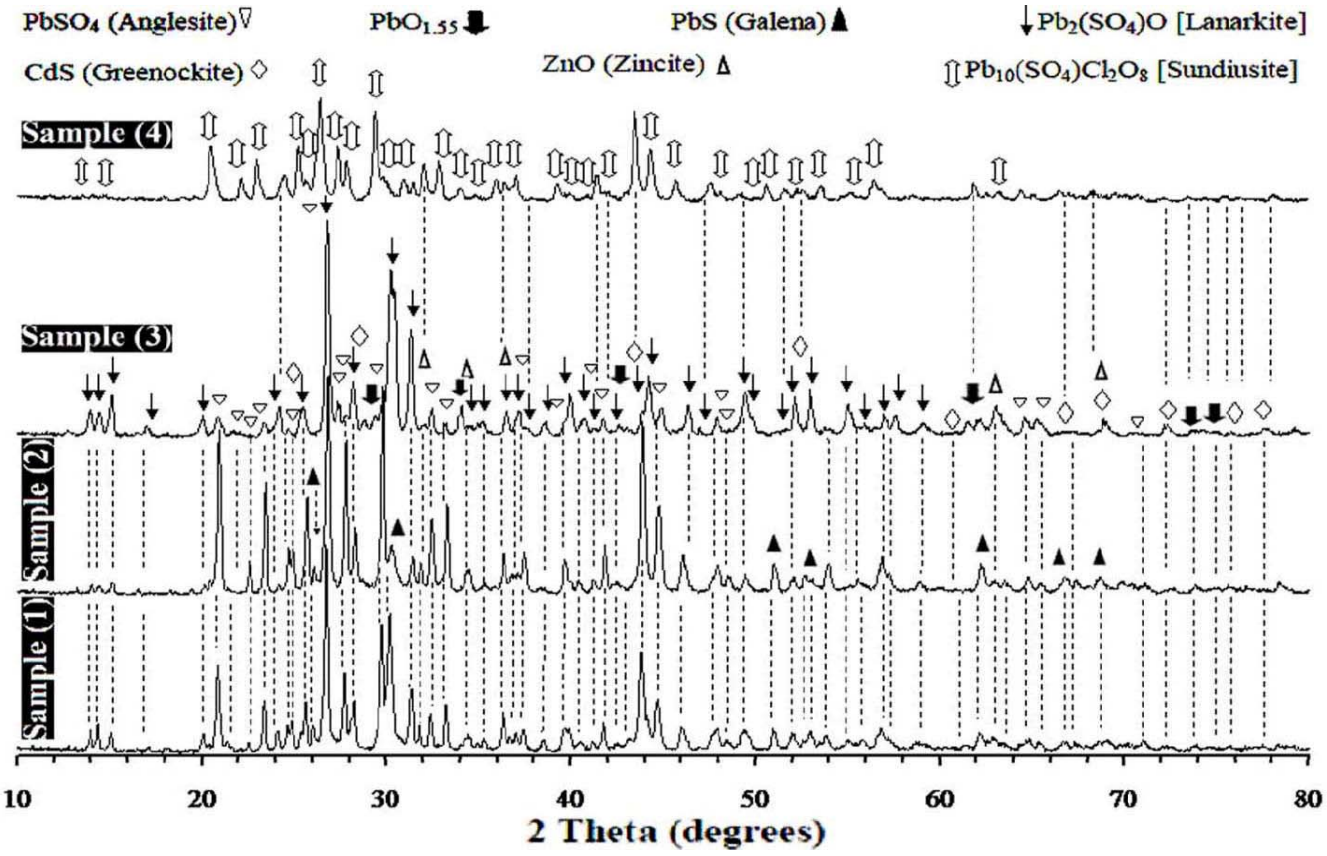

Figure 5-1- XRD patterns of the deposited salt mixtures on the waterwall tubes (HSS).

In addition to $Pb_2(SO_4)O$, the characteristic peaks of $Pb_{10}(SO_4)Cl_2O_8$ [$Pb(SO_4)$ + $PbCl_2$ + 8 PbO] phase were identified in the XRD pattern of sample 4. The presence of Cl ions in the structure of $Pb_{10}(SO_4)Cl_2O_8$ phase caused a shift in the major diffraction peaks to the left-hand side of the XRD pattern of sample 4 compared to the major diffraction peaks of $Pb(SO_4)$ and $Pb_2(SO_4)O$ phases in the other XRD patterns. CdS and ZnO were identified in all samples as Cd- and Zn-containing phases, respectively. SEM photomicrographs of the deposited salt mixtures in Figure 5-2 (a, b, c, d) showed the morphology of the different available phases in samples 1, 2, 3, and 4, respectively. Spatial distribution of Zn, Pb, O, and Cd in the sample 2 can be seen in Figure 5-2 (e, f). X-ray mapping, EDX analysis and ICP/AAS (Table 5-1) results confirmed the presence of Fe in all the samples although no Fe-containing phases were detected in the XRD patterns (Figure 5-1). Based on the EDX analysis results, Fe mainly dissolved in the Zn-rich regions. For example, in Figure 5-2e, the Zn-rich regions contained 4.22 wt. % Fe in addition to 62.46 wt. % Zn, 8.65 wt. % Pb, 23.91 wt. % O, and 0.76 wt. % Cd. The Pb-rich regions in the same Figure contained: 63.44 wt. % Pb, 7.94 wt. % Zn, 1.52 wt. % Fe, 7.30 wt. % As, 3.01 wt. % Cd, 4.60 wt. % S, and 12.19 wt. % O.

Table 5-1- Chemical composition (wt. %) of the deposited salt mixtures on the waterwall tubes.

	Sample 1	Sample 2	Sample 3	Sample 4
Pb	48.93	44.26	52.01	39.91
Zn	11.56	10.94	8.74	10.05
Cd	8.54	11.58	4.13	14.14
Fe	2.65	2.00	3.70	1.24
K	0.41	0.49	0.19	0.44
Na	0.10	0.12	0.07	0.09
Ag	0.2	0.16	0.08	0.15
Cu	0.2	0.16	0.35	0.12
As	0.86	0.69	0.69	0.35
Sb	0.18	0.16	0.32	0.12
Cl	1.02	2.27	1.51	2.50
S	5.98	6.98	5.28	7.61
Si	1.76	1.31	2.88	1.05
Sn	0.25	0.19	0.13	0.11
In	0.15	0.13	0.14	0.06

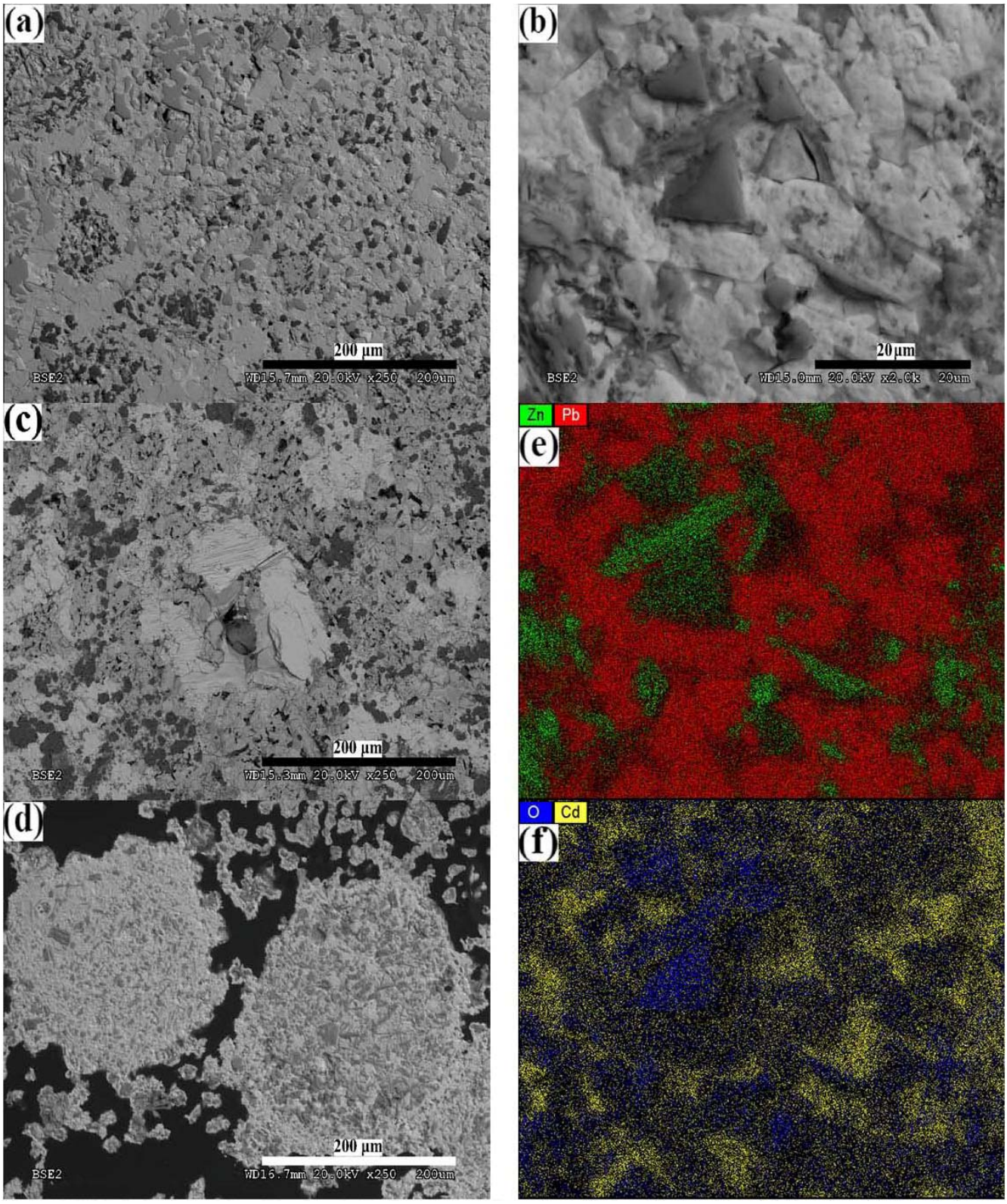

Figure 5-2- SEM photomicrographs of the deposited salt mixtures on the waterwall tubes, a) Sample 1, b) Sample 2, c) Sample 3, and d) Sample 4 as well as X-ray mapping of e) Zn and Pb, and f) Cd and O, in Sample 2.

DTA curves of samples 1-4 are presented in Figure 5-3. Except for the DTA curve of sample 1, a broad endothermic peak in the temperature ranges of 640-730°C, 650-700°C, and 640-736°C was distinguishable in the DTA curves of samples 2, 3, and 4, respectively. These broad endothermic peaks were caused by heat adsorption due to the formation of a molten phase in the salt mixture. Accordingly, the formation of the molten phase occurred in the temperature range of 600-700°C for samples 2, 3, and 4. Therefore, the molten phase formed on the waterwall at the operating temperature of the radiant boiler (700-830°C) due to the deposition of the salt mixtures.

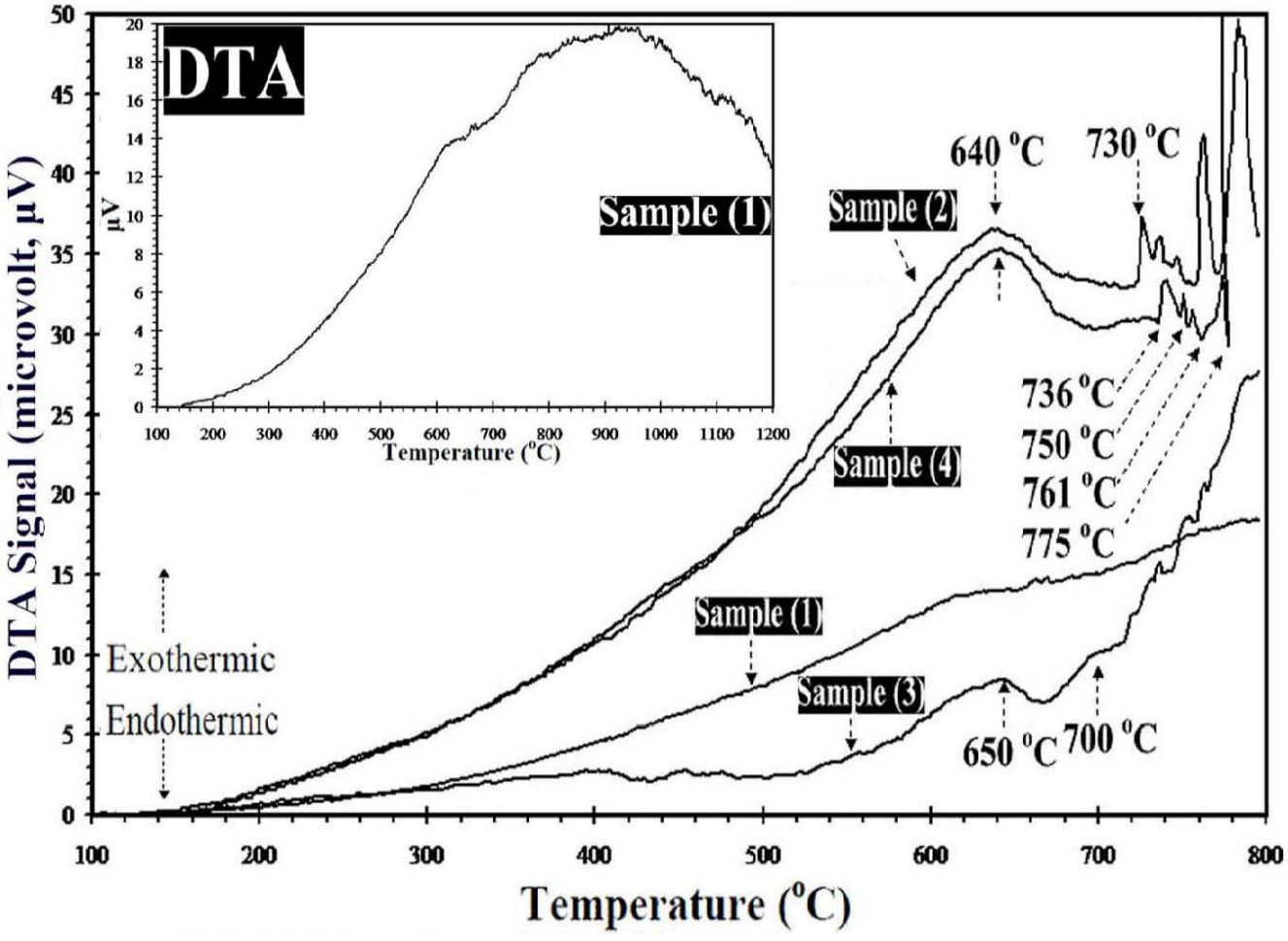

Figure 5-3- DTA curves of the deposited salt mixtures on the waterwall in the radiant boiler.

For sample 1, the DTA test was continued up to 1200°C. The presence of a few small endothermic peaks in the DTA curve of sample 1 in the temperature range of 1000-1200°C indicated that the sample

did not melt at temperatures below 1000°C. Therefore, this sample did not contribute to the formation of the molten phase on the waterwall, but it can still act as a thermal barrier against the heat transfer from the hot off-gas to the tubes. In the DTA curves of samples 2, 3, and 4, the inhomogeneous nature of the deposited salt mixtures caused the presence of several small endothermic peaks at temperatures higher than 700°C. Furthermore, the physical appearance of the salt mixture after DTA test confirmed the formation of the molten phase for samples 2, 3, and 4. The presented DTA results clearly confirmed that the deposited salt mixtures have a strong tendency to form a molten phase at the operating temperature range of the radiant boiler. The fact of the matter is that precipitation of the molten salt phase on the waterwall tubes was an important factor in exacerbating the corrosivity of the environment and accelerating the degradation of the tubes and the weld overlay alloy 625. The presence of the deposited salt mixtures, which caused the formation of the molten phase, can lead to the occurrence of the molten salt-induced corrosion, also known as “hot corrosion”, in the waterwall (alloy 625 weld overlay + carbon steel tubes) of the radiant boiler. A reduction in the performance and reliability of the boiler during the operation is another consequence of the salt mixture deposition on the waterwall because these deposited salt mixtures have a thermal insulation effect and can act as a thermal barrier against heat transfer between the hot off-gas and the tubes, as was mentioned previously.

It should be noted that the phase and the chemical characteristics of the actual deposits, gathered from the surface of the waterwall, were considered to prepare the simulated salt mixtures for conducting a hot corrosion study on the weld overlay alloy 625 in the laboratory scale. The main purposes of the laboratory-scale hot corrosion study were to assess the susceptibility of the weld overlay alloy 625 to the hot corrosion and to study the hot corrosion attack mechanism. It was not possible to use the actual deposits in the laboratory-scale hot corrosion study due to 1) safety concerns associated with the potential health effects of the deposits (for example, the presence of As and Tl together with the high

concentration of CdS in the composition of the deposited salt mixtures based on Table 5-1), 2) the inhomogeneous nature of the deposited salts, and 3) limitation in the amount of the available deposits. Therefore, it was essential to design the simulated salt mixtures to be used as electrolyte in the electrochemical tests. The phase and the chemical composition as well as the melting point of the simulated salt mixture were close to the characteristics of the actual deposits gathered from the surface of the waterwall. As a result, the prepared salt mixtures in Table 4-1 can simulate the corrosive condition of the boiler in the laboratory-scale hot corrosion tests to assess the susceptibility of the unfailed weld overlay alloy 625 to the hot corrosion attack in a laboratory-scale study.

5.3 Microstructural assessments

The microstructure of the alloy 625 in as-welded conditions can be seen in Figure 4-3, page 32. Weld overlay alloy 625 exhibited a well-defined anisotropic, dendritic structure. A bright structure in the interdendritic regions pertained to Laves phase. Prior to the visual inspection and the dye/fluorescent dye penetrant tests, the surface of the sample (HSS) was cleaned from the deposits and carefully washed. During the visual examination, many cavities (pinholes) were observed on the HSS of the sample. These cavities were mainly detected in the boundaries of the deposited weld beads, as can be seen in Figure 4-2b, page 30.

Except for the signs of the general corrosion (rust formation) which caused the reddish color of the CSS, there were no signs of failure or any abnormal features on the CSS constructed with the carbon steel. The occurrence of general corrosion on the CSS was expected due to the weak corrosion resistance of carbon steel. Welding defects such as excessive spatter, undercut and porosity on the surface, and cross section of the weld layer were detectable during the visual inspection of the weld overlay (see Figure 4-2d and Figure 5-4). Based on the morphology of the porosities in Figure 5-4 (a, b, c, f, g), porosities formed because the shielding gas (Argon) was trapped inside the fused zone.

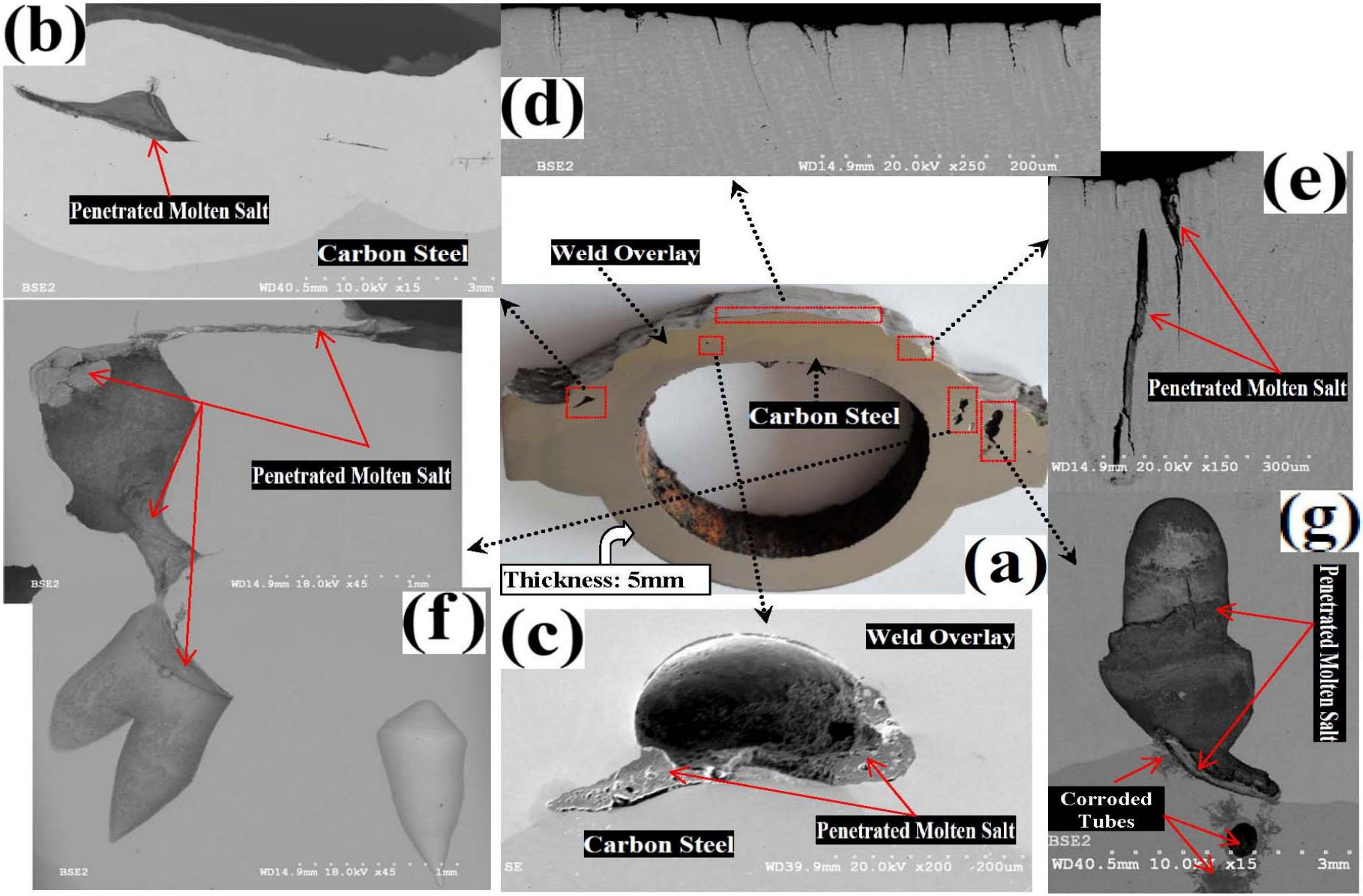

Figure 5-4- Cross-sectional SEM photomicrographs from a section of the overlaid tubes after grounding and polishing.

The flow rate of the shielding gas during welding was 15.6-16.5 liters per minute (33-35 cubic foot per hour, CFH). The excessive spatter and the undercut defects can be formed due to high heat input to the welding pool during the welding process [120]. The high heat input is a consequence of improper selection of arc power parameters (voltage and current) or low deposition rate of the weld metal (low filler metal feed rate). In Figure 5-4 (c, e, f, g), because of the molten salt penetration into the weld defect, carbon steel substrate is directly exposed to the molten phase and the occurrence of the hot corrosion attack (sulfidation and oxidation of Fe, based on the EDX results in Figure 5-11) in the carbon steel tube can be observed. Further details will be discussed in Figures 5-11 and 5-12.

Table 5-2- Chemical composition (wt. %) of weld overlay alloy 625, carbon steel tube (substrate) and alloy 625 consumable electrode (filler metal).

	Ni	**Cr**	**Mo**	**Fe**	**Nb**	**Ti**	**Co**
Weld Overlay	bal.	17.02	6.00	23.64	2.85	0. 25	<0.0001
Base Metal	0.01	0.06	0.01	bal.	-	<0.01	0.0013
Filler Metal	64.50	22.19	8.67	0.383	3.61	0.201	0.044
	Zn	**Al**	**C**	**S**	**Si**	**Mn**	**Zr**
Weld Overlay	0.25	0.35	0.05	0.01	0.30	0.17	1.9
Base Metal	0.001	0.03	0.16	0.02	0.39	0.39	0.08
Filler Metal	-	0.095	0.008	0.001	0.072	0.042	-

The chemical composition of the weld overlay, carbon steel tube substrate, and filler metal, determined by the ICP/AAS, is presented in Table 5-2. The dilution level was determined based on the concentration of Fe in the weld overlay, the filler metal, and the carbon steel tube (base metal). For simplification, it can be assumed that the fusion zone was fully mixed. Accordingly, the final weld composition will be a mixture of the carbon steel substrate and the filler metal, which can be calculated by applying the following equation [59, 60]:

$$C_{fz} = C_{fm}\,(1 - D_{Fe}) + C_s(D_{Fe}) \;\Rightarrow D_{Fe} = \frac{C_{fz} - C_{fm}}{C_S - C_{fm}} \tag{5-1}$$

where C_{fz}, C_{fm}, and C_s are the concentration of Fe in the fusion zone, the filler metal, and the carbon steel substrate, respectively, and D_{Fe} is the dilution level of Fe. Based on equation (5-1), the dilution level of Fe was equal to 23.62%. The thickness of the tubes in CSS (no weld overlay on this surface) was equal to 5 mm, the same as the thickness of the tubes originally used for construction of the waterwall. The thickness of the tubes was reduced to 2.12 ± 0.3 mm in the HSS. As a result, the total reduction in the tube thickness in the HSS was about 2.88 mm. Based on equation (5-2) [59, 60], for geometric dilution calculation, 1.04 mm of the reduction in the thickness of the tube was attributed to the dilution and the rest of the reduction in the thickness (~ 1.84 mm) was attributed to the degradation of the tubes prior to applying the weld overlay alloy 625 for protection. A good agreement and consistency between the obtained dilution levels through the geometric measurements and the chemical analysis method was reported in the literature [59, 60]. Equation (5-2) is as follows:

$$D_{Fe} = \frac{A_s}{A_s + A_{fm}} \tag{5-2}$$

where A_s and A_{fm} are the area of the melted substrate and the melted filler metal, respectively, and D_{Fe} is the dilution level of Fe. When a section of the weld overlaid tube is considered to have a width of one unit of length (cm or mm), the section of the weld overlay will be rectangular in shape. Under this condition, equation (5-2) will be the ratio of the melted substrate thickness (T_s) to the total melted cross-sectional thickness from the filler metal and substrate ($T_s + T_{fm}$). The cross-sectional thickness of the filler metal was equal to 3.38 mm (T_{fm} = average thickness of the weld overlay).

An increase in the dilution, due to the high heat input and the arc power, caused a significant decrease in the thickness of the substrate (tube) because the tube metal (carbon steel) melted at the welding temperature (see Figure 4-2d and Figure 5-4a). In Figures 4-2d and 5-4a, the observed considerable distortion (plastic deformation) in the tube wall under the weld layer clearly confirmed the excessive

heat input to the base metal during the depositing of the weld overlay by the GMAW technique; consequently, a significant amount of Fe was transferred to the weld overlay from the carbon steel tube. Although the concentration of Fe in the alloy 625 consumable electrode, used for deposition of the weld overlay through the GMAW technique, was 0.383 wt. %, the concentration of Fe in the weld overlay chemical composition was significantly higher, 23.64 wt. % (Table 5-2), as a direct consequence of the dilution phenomenon and the high heat input/arc power. The concentration of C and Si in the alloy 625 consumable electrode (filler metal) was equal to 0.008 and 0.072 wt. %, respectively, but the dilution from the carbon steel substrate caused an increase in the C and Si content of the weld overlay. The amount of C and Si in the weld overlay alloy 625 was equal to 0.05 and 0.3 wt. %, respectively (Table 5-2). These amounts of C and Si in the weld overlay alloy 625 can significantly increase the susceptibility of the weld alloy to the occurrence of fusion zone solidification cracking during the welding process [8, 54, 55, 121]. Reportedly, solidification cracking susceptibility of the weld overlay alloy 625 increases with increasing the dilution level [59]. Other studies confirmed that the content of Fe in the weld overlay alloy should be kept to less than 6-7% to minimize the adverse effects of Fe on the properties of the deposited weld layer and its corrosion resistance [122, 123]. Based on the studies of Adamiec [123], for alloy 625 weld overlay on the tubes of 1.0305 steel with a GMAW process, a heat input rate (linear energy of pad welding) less than 300 kJ/m is required in order to keep the Fe concentration in the weldment less than 7% by controlling the dilution. However, in the case of the present study, the maximum heat input rates for the GMAW process and the GTAW wash pass were about 600 and 700 kJ/m, respectively. These values were significantly higher than the optimum heat input rate suggested by Adamiec [123]. This is an evidence to confirm the adverse effect of inappropriate selection of the heat input rate in the GMAW process on the dilution and high concentration of Fe in the weldment. Shielding gas flow rate in the GMAW process, applied in a radiant boiler, (15.6-16.5 liter per minute), was almost the same as the value reported by Adamiec (18 liters per minute) [123].

Overall, two factors including: 1) the solidification temperature range, the range over which the solidification cracking occurs, and 2) the amount of the secondary phase, which forms at the terminal stage of solidification, control the relationship between the dilution phenomenon and the solidification cracking susceptibility [8]. It has been well established that higher contents of C, Si, and particularly Nb, in alloy 625 simultaneously increase the solidification temperature range of the alloy and reduce its liquidus/solidus temperature. These two factors raise the susceptibility of the weld overlay alloy 625 to the solidification cracking during welding and reduce the weldability (resistance to solidification cracking) of the alloy [8, 54]. Furthermore, excessive amounts of C, Si, and Nb in alloy 625 can promote the termination of the solidification process by a eutectic-like reaction between the gamma phase (γ) with FCC crystallographic structure and various Nb-rich phases and/or Laves. It causes further increase in the solidification temperature range and, thus, raises the tendency for the fusion zone solidification cracking in the alloy 625 weld overlays [8, 55, 59]. According to Dupont et al. [59], for weld overlay alloy 625, higher content of Mo and Nb-rich secondary phases, Laves, in the interdendritic regions means that higher amounts of Mo and Nb-rich liquid phase formed at the final stage of solidification of the weld overlay, which wet the grain boundaries as a continuous film. Consequently, shrinkage strain across the boundaries, which cannot be accommodated, causes the separation of the boundaries, which results in the formation of the cracks as terminal eutectic liquid solidifying [59, 124, 125]. Cross-sectional SEM photomicrographs of the weld overlay samples can be seen in Figure 5-5 (a, b, c, d). Based on the EDX results, the white areas (Laves) were rich in Mo and Nb. Greater concentration of Mo and Nb in the Laves phase, compared to the bulk composition or γ matrix, was also reported by Maguire and Michael [124]. These areas appear in the interdendritic regions. The chemical composition as well as the spatial distribution of Mo, Nb, and Ni in this region will be discussed in Figure 5-6 and Table 5-3 based on the EDX and X-ray mapping results. The formation of solidification cracks and cavities along these regions and interdendritic nature of solidification cracking are evident in Figure 5-5 (c, d).

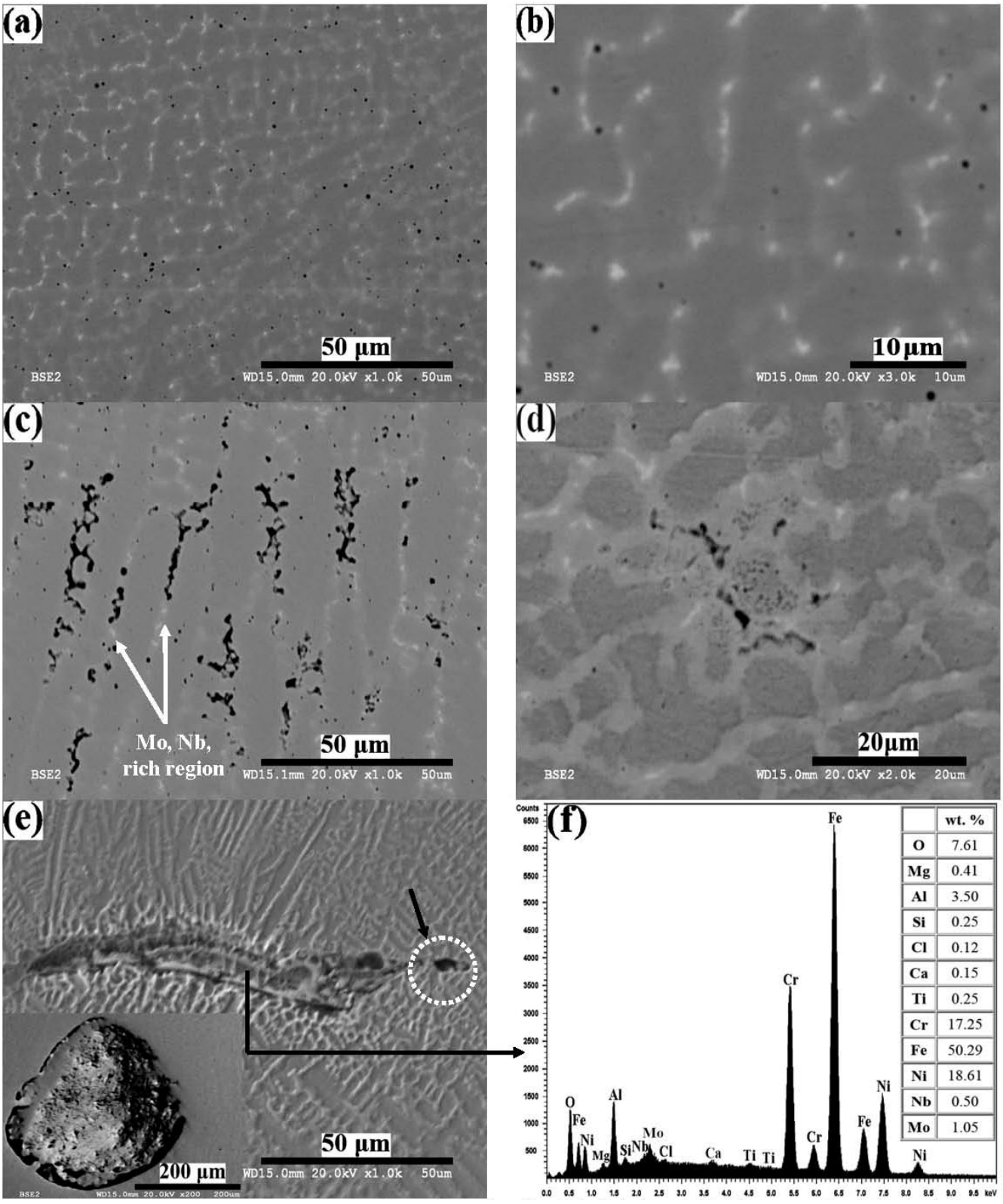

Figure 5-5- Cross-sectional SEM photomicrographs of the weld overlay alloy 625 which show a) and b) Microsegregation in the dendritic regions and formation of the Laves, c) and d) Solidification cracking, e) Fe-rich inclusion, and f) EDX elemental analysis of the Fe-rich inclusion.

The pores can act as stress-raiser zones to facilitate the crack formation in the weld layer during service or the pathways for penetration of corrosive species well inside the layer to accelerate the degradation of the alloy. This confirms that the interdendritic regions are susceptible to the solidification cracking. Solidification cracks are found to be associated with these regions in the weld overlay alloy 625 mainly due to the segregation of Mo and Nb into these regions and formation of the Laves constituent during solidification. Formation of pores in the interdendritic regions of the weld overlay alloy 625 and direct effect of porosities on the crack formation and subsequent enhanced corrosion penetration into the alloy were also reported by Kalivodova et al. [38]. The mechanism of solidification crack formation in interdendritic regions of weld overlay alloy 625 has been clearly described elsewhere [59]. Formation of solidification cracks in Mo- and Nb-rich interdendritic regions was also reported by Dupont [8].

The SEM photomicrograph, in Figure 5-5e, shows the presence of large inclusions in the microstructure of the weld layer. EDX elemental analysis in Figure 5-5f indicates that the inclusions are rich in Fe, Ni, Cr, and O. The concentration of Fe, Ni, Cr, and O in the inclusions is about 50.29, 18.61, 17.25, and 7.61 wt. %, respectively. High concentration of Fe in the inclusions was due to dilution. Based on this, inclusions were susceptible to corrosion and dissolution when the weld overlay was exposed to the corrosive environment. In Figure 5-5e, a microcrack, initiating from the edge of the inclusion, is shown by an arrow. Inclusions can act as stress-raiser zones to accelerate the initiation and propagation of the cracks in the weld overlay during service. As was mentioned previously, a mechanical hammer was periodically used in the radiant boiler to hit the waterwalls, which caused the physical removal of the deposited salt on the waterwalls to facilitate the heat transfer through the tubes. Crack initiation and propagation in the weld overlay can be facilitated by this externally applied stress. Moreover, the role of the deposited salts on the waterwalls in inducing the thermal stresses in the weld layer should be considered. Deposited salts on the waterwalls insulated the hot off-gas from the water coolant circulating inside the tubes. A thick layer of the deposited salts acted as a thermal-resistant

barrier against the heat transfer in the tube's wall; consequently, thermal stresses were induced in the weld layer. In fact, non-uniform distribution of the temperature on the waterwalls and formation of hot and cold zones on the weld overlay, due to the partial deposition of a thick layer of the salt mixtures, caused expansion and contraction of the weld overlay, which can directly contribute to inducing the thermal stresses. These sources of stress in the weld overlay can contribute to facilitating the crack initiation and propagation in the weld layer, in particular from the zones which acted as stress raisers such as cavities and inclusions. Studies confirmed that the thermal expansion coefficient of alloy 625 is very close to that of carbon steel, which keeps the weld layer well-adhered to the tubes even after being in service for a long time [126]. Furthermore, weld overlay is found to be under compressive stress, lower than the alloy's yield stress, during a normal operating temperature transient in the boiler [127]. Because of these two factors, alloy 625 is highly resistant to stress corrosion cracking (SCC) and thermal fatigue under the normal working conditions of the boiler [126]. SEM/EDX and X-ray mapping results in Figure 5-6 clearly showed the microsegregation of Mo and Nb into the interdendritic region of the weld overlay and formation of the Laves constituent during non-equilibrium solidification of the weldment.

Table 5-3- EDX elemental analysis (wt. %) from the dendrite cores and the interdendritic regions of the weld overlay alloy 625.

	Dendrite Core	Interdendritic Region
Nb	1.91 ± 0.70	12.11 ± 0.95
Mo	5.51 ± 1.10	11.88 ± 0.67
Ni	54.89 ± 2.11	45.61 ± 1.14
Cr	18.94 ± 0.61	16.86 ± 0.37
Fe	16.19 ± 3.24	10.02 ± 0.52
Ti	0.19 ± 0.09	0.33 ± 0.14
Si	0.22 ± 0.18	0.77 ± 0.08
Al	0.11 ± 0.05	0.12 ± 0.02
O	2.05 ± 0.59	2.41 ± 0.15

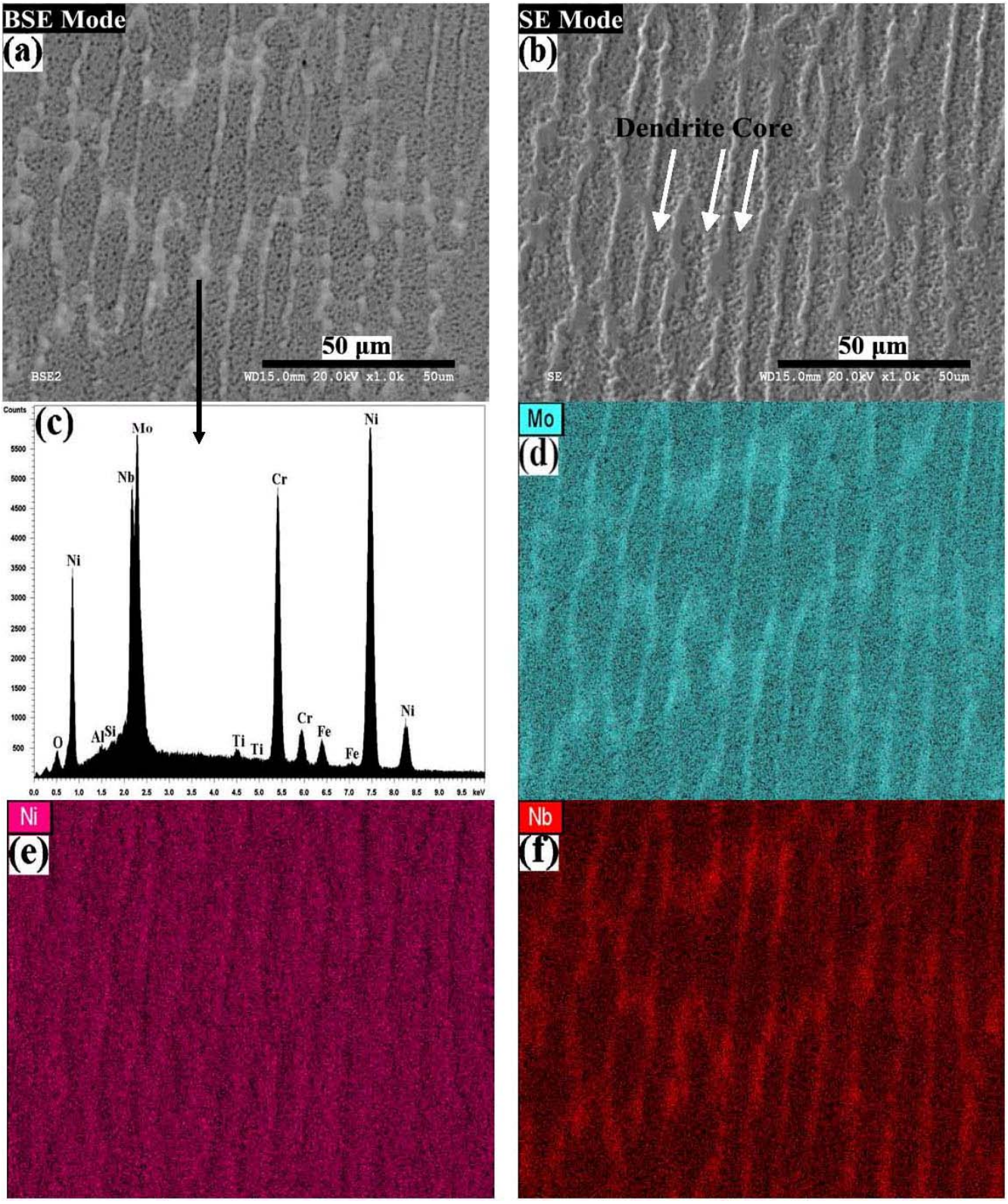

Figure 5-6- Cross-sectional SEM photomicrographs of the weld overlay alloy 625 in a) BSE and, b) SE mode as well as c) EDX elemental analysis of the Laves phase and X-ray mapping of d) Molybdenum, e) Nickel, and f) Niobium in the dendritic structure.

X-ray mapping results showed the depletion of Mo (5.51 ± 1.10 wt. %) and Nb (1.91 ± 0.70 wt. %) in the dendrite cores, compared to the Mo (11.88 ± 0.67 wt. %) and Nb (12.11 ± 0.95 wt. %) content of the interdendritic regions. EDX elemental analysis of the dendrite cores and interdendritic regions in Table 5-3 confirmed the excessive amounts of Mo and Nb in the interdendritic regions. Compared to Cr, Mo, Fe, and Si elements, the strongest tendency to partition to the interdendritic regions pertained to Nb. Based on the EDX results and X-ray mapping of Ni in Figure 5-6, dendrite cores were enriched with Ni and Fe. The EDX results shown in Table 5-3 confirmed that Cr concentration in the dendrite cores (18.94 ± 0.61 wt. %) is higher than interdendritic regions (16.86 ± 0.37). This confirmed the tendency of Cr for microsegregation in the weld overlay dendritic structure. The tendency of Si for microsegregation to the interdendritic regions was evident based on the results presented in Table 5-3. Si is known as an element that strongly promotes the Laves formation [121]. Therefore, rejection of Si from the solidified γ phase dendrites to the interdendritic liquid phase during the solidification process of the weld overlay alloy 625 can promote the formation of the Laves in the interdendritic regions. Furthermore, high concentration of Fe in the weld overlay, as a consequence of dilution, can exacerbate the problem and increase the tendency for the Laves formation, thereby promoting the γ/Laves constituent. The measured concentration of Si in the Laves was 0.77 ± 0.08 wt. % (see Table 5-3). These findings are in agreement with the findings of the previous studies [8, 59, 121]. Cr is one of the most effective alloying elements in alloy 625 to act against corrosion, necessitating at least 18 to 24 wt. % to optimize its effectiveness [29-31]. Therefore, determined concentrations of Cr (16.86 ± 0.37) in the interdendritic regions of the weld overlay were slightly below the acceptable range and this can adversely affect the corrosion resistance of the weld overlay. Dupont et al. reported that the tendency of Mo and Nb to segregate increases as a consequence of transferring Fe to the fusion zone due to the dilution, which means that the solubility of Mo and Nb in gamma phase (γ) decreases with increasing the dilution level of Fe [8, 59, 121]. Accordingly, more Mo and Nb are rejected from the solidified γ phase to the liquid phase during solidification. When this solute-rich liquid solidifies between the

dendrites, microsegregation occurs in the interdendritic regions [8, 59, 121]. Based on these findings, in the present study, segregation of Mo and Nb into the interdendritic region of the weld overlay during solidification can be justified considering the excessive content of Fe (23.64 wt. %) in the weld overlay. This can justify why the dendrite cores were depleted in Nb and Mo while they contained a higher concentration of Fe compared to the interdendritic regions. The segregation phenomenon plays an important role when weldability and solidification of weldment are concerned. Because of the segregation phenomenon, the core of the dendrite arms contained less solute than the interdendritic regions in the weld overlay alloy 625, which caused the higher solidus temperature of the dendrite arms. Segregation can also have a detrimental effect on the mechanical properties of the weldment [128]. The morphology of the Laves phase in Figures 5-5 and 5-6 can show that the solute-rich liquid, which solidified at the terminal stage of solidification, had a propensity to spread out as a continuous thin film between the dendrites because of having a low surface tension [129].

When Mo and Nb segregate from the solidified phase to the liquid phase during welding solidification, low diffusion rate of these two elements in the γ phase prohibits them from diffusing back to the dendrite cores [59, 121, 130]. In other words, solid-state diffusion of substitutional alloy elements, such as Mo and Nb, in alloys with FCC crystallographic structure, such as alloy 625, is negligible under typical cooling rates of arc welding [59, 121, 131]. For this reason, it is plausible to claim that the determined concentrations of substitutional alloying elements in Table 5-3 are very close to the concentration of the alloying elements at the onset of solidification of the weld overlay. In addition to the Cr and Ni concentration gradient, a concentration gradient of Mo and Nb between the dendrite cores and the interdendritic regions also formed, confirmed by X-ray mapping (Figure 5-6) and EDX results (Table 5-3). The concentration gradient of Mo and Nb adversely affected the corrosion resistance of the weld overlay and made the weld alloy susceptible to the preferential corrosion in the Mo- and Nb-depleted dendrite cores due to the galvanic effect. Based on the literature [38, 79], poor

resistance to localized corrosion in the weld metal, due to the segregation of Mo and Nb alloying elements, can lead to the failure of the weld overlay alloy during service in power plants. It should be noted that the role of Mo in alloy 625 is to make the alloy resistant to crevice and pitting corrosion when it is uniformly distributed in the alloy [132]. From a corrosion perspective, depletion of Cr and Ni in the Mo- and Nb-rich interdendritic regions can reduce the resistance of these regions to corrosion attack. As was mentioned earlier, increasing the dilution level and the concentration of Fe in the weld overlay exacerbated the microsegregation of Mo and Nb in the dendritic structure of the weld overlay [59]; consequently, the concentration gradient of Mo and Nb and the susceptibility of the dendrite cores to the preferential corrosion increased. Dupont et al. [59] mentioned that segregation potential of Nb and Mo in the weld overlay, which depends on the Fe concentration, is indirectly affected by the arc power and volumetric filler metal feed rate because these welding parameters control the dilution level and chemical composition of the weld layer, in particular the concentration of Fe in the weld overlay. The direct effect of processing parameters of arc power and volumetric filler metal feed rate on the dilution level was also investigated by Banovic et al. [60]; it was found that an increase in the volumetric filler metal feed rate and/or a decrease in the arc power can reduce the volumetric melting rate of the substrate and, thus, the resultant weld-metal dilution level.

The solidification sequence of an alloy 625 weld overlay deposited on 2.25Cr-1Mo steel by GMAW was explained elsewhere in detail [8]. In summary, γ dendrites form at the early stage of solidification, and depletion of Mo and Nb occurs at the dendrite cores due to the low solubility of these two elements in γ phase (particularly in the presence of Fe) while Fe, Ni, and Cr segregate to the solidifying γ dendrites [8]. By continuation of the solidification, the concentrations of Mo and Nb increase at the interdendritic liquid phase until the final stage of the solidification in which termination of solidification occurs by a eutectic-like reaction between γ phase and Laves [8]. Based on this report, the presence of Fe and Si promotes the formation of Laves phase during solidification of weld overlay

alloy 625 [8]. This mechanism was consistent with the results presented in Figures 5-5 and 5-6 and Table 5-3. NbC or other Nb-containing carbides were not detected in the weld overlay microstructure in the current study, which can be justified considering the low concentration of C in the weld overlay (see Table 5-2). This observation can confirm that the eutectic reaction between γ phase and the Laves is the terminal stage of solidification in the alloy 625 weld overlay.

The measured microhardness values of the weld overlay alloy 625 samples were in the range of 325-369 HV100. This range of microhardness values means that no annealing or age hardening occurred in the weld during service in the boiler environment [133]. Cortial et al. [133] reported that heat treatment for 8 hr at 1000°C causes the concentration gradient and heterogeneity between the interdendritic regions and dendrite cores to vanish in alloy 625 weld overlay on A533 steel plates by means of the TIG welding process. In other words, this heat treatment procedure can make the welding structure fully homogenized and dissolve the detrimental Laves phase; thereby improving the corrosion resistance of the weld overlay [133]. However, this approach, heat treating the weld overlay at 1000°C for 8 hr, is not practical in solving the issue of concentration gradient of Ni, Cr, Mo, Nb, Fe, and Si in the weld overlay alloy 625, where the welding procedure is done on-site in the boiler.

Overall, the dilution and, consequently, the presence of a significant amount of Fe in the chemical composition of the weld overlay alloy 625 are the key issues in the waterwalls. Dilution is the root cause of exacerbating the susceptibility of the weld layer to solidification cracking. It also makes the dendritic structure of the weld layer susceptible to preferential corrosion due to the microsegregation of Mo and Nb from the dendrite cores to the interdendritic regions, causing the formation of Mo- and Nb-depleted zones and Laves phase. Therefore, it is critical to pay attention to the relation between the dilution and the welding parameters to understand how the welding parameters should be optimized to minimize the dilution, reducing the solidification cracking susceptibility. Processing parameters of arc power (current and voltage) and filler metal feed rate control the volumetric melting rates of the filler

metal and substrate and, thus, weld metal dilution [59, 60]. In fact, by decreasing the arc power/heat input and increasing the volumetric filler metal feed rate (deposition rate), which means maximizing filler metal feed rate-to-arc power ratio, the dilution level and Fe content in the overlay will be minimized. This can ultimately lead to improving the cracking resistance of the weld overlay and its corrosion resistance and avoid the formation of undesirable phases and inclusions [8, 38, 60, 134]. An optimum heat input is important not only to reduce the dilution and segregation level of the major alloying elements of the alloy but also for providing sufficient wetting for a good weld to be preceded [38]. Reportedly, in addition to minimizing the heat input, a high weld metal cooling rate has to be used to decrease the Nb segregation and amount of detrimental Laves phase, thereby reducing the susceptibility of the occurrence of the solidification cracking [125, 128]. A direct current with reverse polarity (DCEP) was used in the GMAW process to apply the weld overlay on the waterwalls of the radiant boiler. However, studies showed that the use of a pulsating current with a stable power voltage can provide a higher quality weld layer [123]. The use of the pulsing technique in welding is a beneficial strategy to reduce the heat build-up during process [128]. Accordingly, it is recommended to use a pulsating direct current for applying weld overlay to control segregation and dilution phenomena in the weldment, thereby reducing the susceptibility to the solidification cracking. Compared to the straight direct current, residual stress and distortion are reduced due to the lower heat input by applying a DC pulsating current [135].

The relatively large dendritic arm spacing of the weldment in Figure 4-3 (c, d, e) can be evidence of the slow weld cooling rate of the weldment during applying the weld overlay alloy 625 by the GMAW technique. The weld cooling rate can strongly affect the segregation because it is a time-dependent phenomenon [128]. Studies by Radhakrishna and Prasad-Rao [128] have shown that coarse dendritic spacing provides congenial/preferential sites for segregation during solidification of the weld metal. Circulating water inside the tubes during the deposition of the weld layer is an effective option to

increase the cooling rate of the weldment and to reduce the microsegregation and Laves formation. This is an important technical consideration where applying weld overlay on the waterwalls of a boiler is concerned. Studies confirmed that forced internal cooling of the tubes can ensure appropriate weld layer quality and appropriate Fe content on the surface of the weld layer [123].

Selecting a filler metal with a relatively high content of C and low content of Si and Fe to promote the formation of γ/NbC at the terminal stage of the overlay solidification at the expense of the γ/Laves is another precaution for decreasing the solidification temperature range and, therefore, reducing the cracking susceptibility [8, 54]. Based on the literature [128, 136], it is generally believed that Laves is a phase in the form of $(Ni, Fe, Cr)_2(Nb, Mo, Ti, Si)$ with a hexagonally close packed crystallographic structure. The inherent brittle nature of the intermetallic Laves phase causes them to act as preferential sites for crack initiation and propagation in the weld overlay structure [128, 136], as confirmed by Figure 5-5. It is pertinent to mention here that, based on the presented results in Table 5-2, the effect of Fe and the dilution on making the overlay susceptible to the solidification cracking is predominant in the case of the current study. Accordingly, maximizing filler metal feed rate-to-arc power ratio looks to be more effective for reducing the cracking susceptibility.

5.4 Molten phase penetration into the weld overlay

After visual inspection, dye penetrant and fluorescent dye penetrant tests were conducted on the HSS of the waterwall to reveal cracks and discontinuities which are open to the HSS. These defects might not be detectable through a normal visual inspection. In the boiler environment, the weld layer was partially covered by the deposited salt mixtures, characterized in section 5.2. The results of the dye penetrant and fluorescent dye penetrant tests can be seen in Figure 5-7. In Figure 5-7 (a, b, c), dye penetrant test reveals the presence of the cavities (pinholes) with various diameters as well as many discontinuities between the weld beads. The cavities mainly appeared in the boundaries of the weld

beads. As can be seen in Figure 5-7c, the dye penetrant test did not reveal the presence of any cracks on top of the deposited weld bead, on the crown of the tube, but results of the fluorescent dye penetrant test confirmed the presence of the cracks in this area.

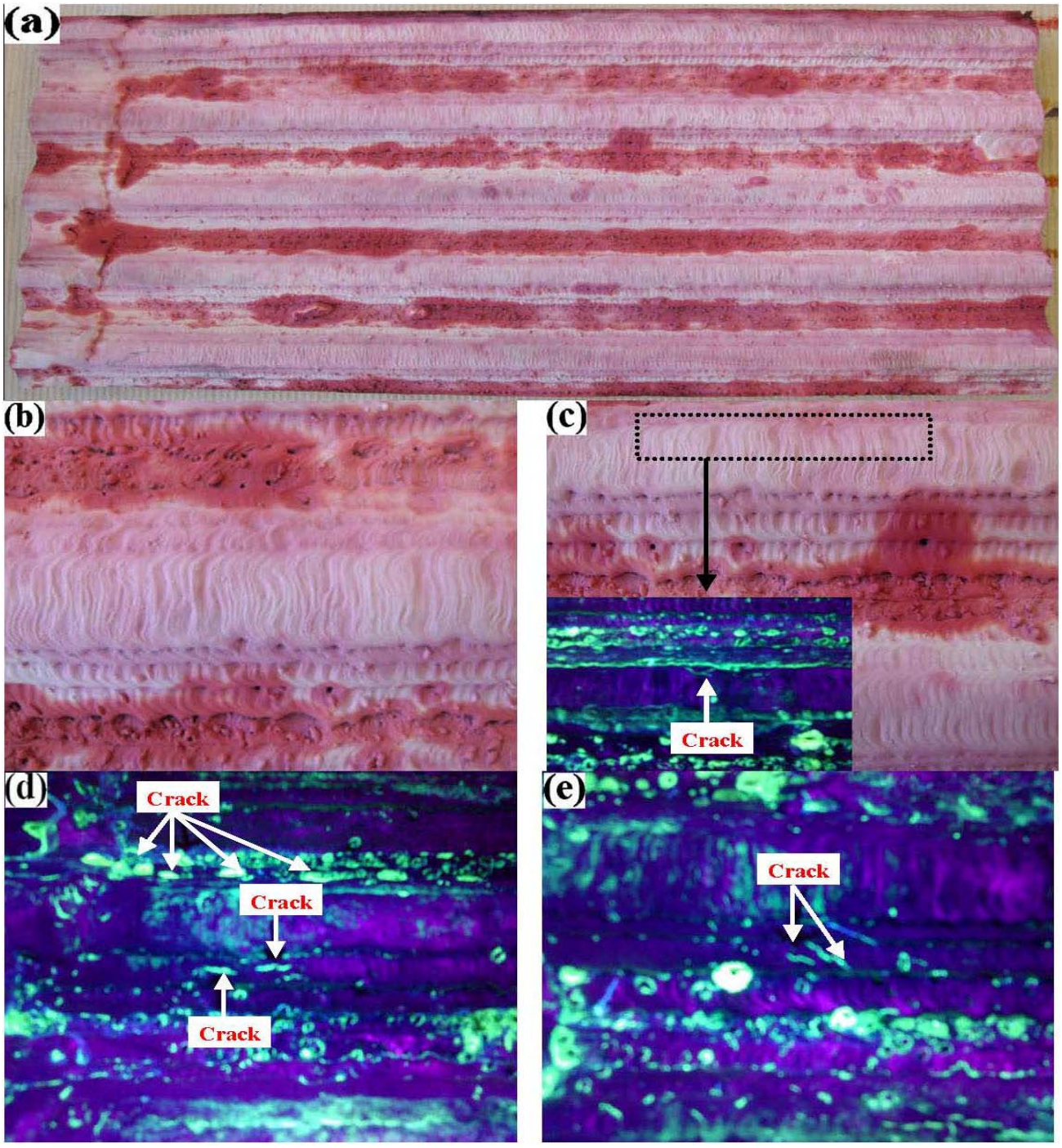

Figure 5-7- a), b), and c) The surface of the weld overlay after applying dye penetrant as well as fluorescent dye penetrant test (d, e).

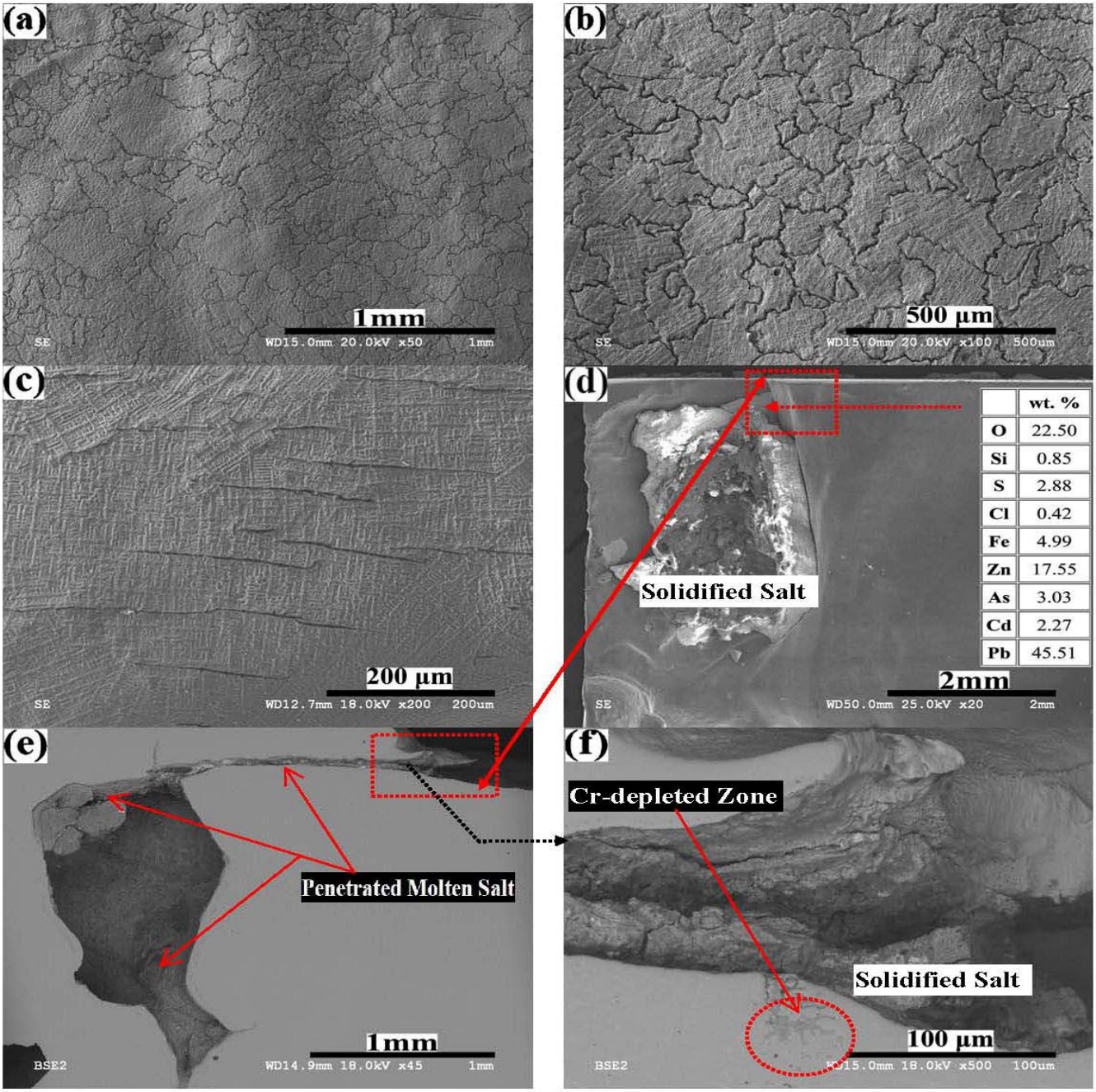

Figure 5-8- a), b), c) A network of well-developed circumferential cracks across the HSS of the weld overlay, d) External view of a single well-developed, straight and unbranched circumferential crack, which was located adjacent to the membrane and covered by the deposited salts and EDX elemental analysis of the deposits, plus e) and f) Cross-sectional view of the crack in (d), which shows the penetration of the molten phase into the weld layer through the crack, and subsequent degradation and Cr-depletion in the weldment.

The dye penetrant test did not successfully reveal the presence of such cracks in other regions of the weld overlay because of the limitation of the discontinuities and crack sizes, which can be detected by the dye penetrant test. For more accurate results, a fluorescent dye penetrant test, as a more sensitive test for crack detection, was conducted on the HSS. The results were presented in Figure 5-7 (c, d, e). As was expected, the fluorescent dye penetrant test revealed the presence of some cracks which were not identifiable by the dye penetrant test. Conducting visual inspection and dye/fluorescent dye penetrant tests assisted in determining the suitable locations for cutting the metallographic samples. Despite the fact that the fluorescent dye penetrant test is more accurate than the dye penetrant test, it is not still precise enough to reveal all surface cracks. For this reason, the entire surface of the weld overlay was also studied by SEM.

In Figure 5-8 (a, b, c), the presence of a network of well-developed circumferential cracks across the HSS of the weld overlay was evident. During the SEM study, in some locations, it was clear that the subsurface region of the weld layer flaked off. A single well-developed, straight, and unbranched circumferential crack, which was located adjacent to the membrane and covered by the deposited salts, can be seen in Figure 5-8 (d, e, f) from two different directions, external (Figure 5-8d) and cross-sectional (Figure 5-8e, f) views. The EDX elemental analysis of the solidified salt that covered the crack was presented in Figure 5-8d. The deposited salt was rich in Pb, Zn, and O. The depth of the crack and the initiation of the crack from the interface of the two weld beads as well as the penetration of the molten salt into the crack were apparent in the cross-sectional view of the crack in Figures 5-8e and f. It should be noted that Figure 5-8e was part of Figure 5-4f, which was shown again for clarifying the penetration depth of the molten salt into the cracks and the size of the crack. Obviously, this well-developed crack was deep enough to be connected to the porosities inside the weld overlay, facilitating the penetration of the molten phase and corrosive species inside the weld layer. This is an obvious example to show how a combination of defects such as cracks and porosities as well as molten salt

penetration can lead to the degradation of the weld overlay. These findings indicated that the viscosity of the molten phase had been low enough to easily penetrate inside the deep cracks, as observed in Figure 5-8 (d, e, f).

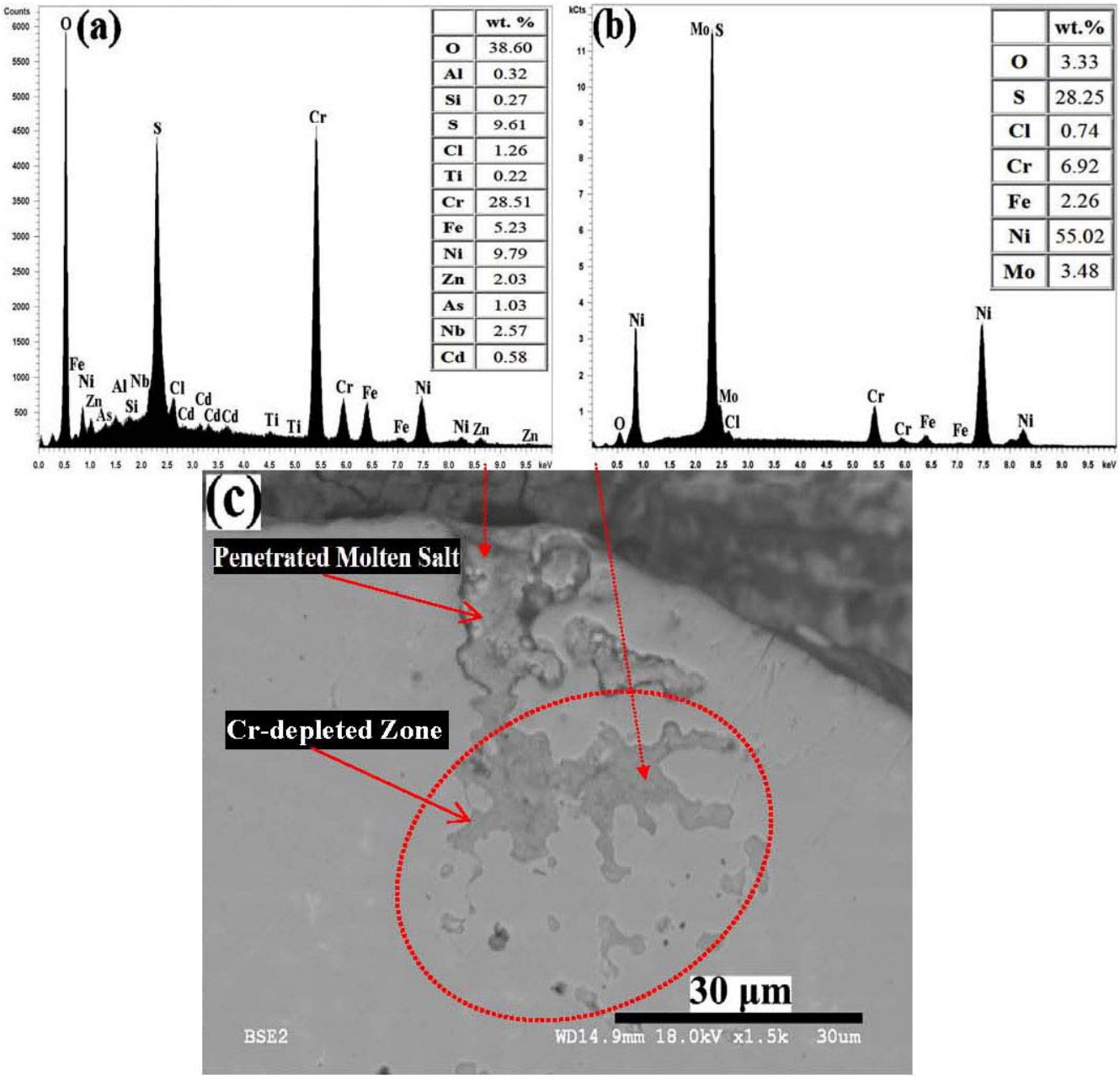

Figure 5-9- a) EDX elemental analysis of locally penetrated molten phase into a region close to the Cr-depleted zone, and b) Cr-depleted zone; c) Cross-sectional SEM photomicrograph showing occurrence of Cr-depletion in the weldment, exposed to the penetrated molten phase.

A Cr-depleted zone in the weld layer can be seen in Figure 5-8f. More details of this Cr-depleted zone were shown in Figure 5-9c at a higher magnification. The chemical analysis of the penetrated molten salt and the Cr-depleted zone were presented in Figures 5-9a and 5-9b, respectively. Based on the EDX spectrum in Figure 5-9a, dissolution of the alloying elements (Cr, Ni, Nb, Ti, and Fe) of the weld overlay alloy 625 into the penetrated molten phase was evident. Compared to the other alloy elements, particularly Ni, a high percentage of Cr in the penetrated molten phase (28.51 wt. % Cr vs. 9.79 wt. % Ni) confirmed the highest tendency of Cr to dissolution when the weld overlay was exposed to the molten phase. The concentration of Cr in the Cr-depleted zone (6.92 wt. %) in the EDX spectrum of Figure 5-9b, compared to the Cr concentration in the weld overlay (17.02 wt. % Cr, see Table 5-2), is another evidence to confirm the strong tendency of Cr for dissolution in the molten phase. Selective oxidation of Cr can be mentioned as the main mechanism for the dissolution of Cr in the molten phase due to the presence of 38.60 wt. % O in the EDX spectrum of Figure 5-9a. Nb was not detected in the Cr-depleted zone because it fully dissolved and diffused into the molten phase, as can be observed in the EDX spectrum of Figure 5-9a. Mo in the weld overlay was also prone to dissolution because its concentration in the Cr-depleted zone (3.48 wt. %) is less than the concentration of Mo in the weld overlay (6.00 wt. %, see Table 5-2). Based on the EDX results, Cr-depleted zone was enriched with S; accordingly, internal sulfidation was the mode of corrosion attack in the weld overlay alloy 625. The presence of 3.33 wt. % O in the EDX analysis of the Cr-depleted zone showed that internal oxidation can act as another mode of corrosion attack. In the presence of the molten phase, oxidation and sulfidation of the alloy accelerate after the depletion of Cr during the initiation stage of hot corrosion attack [75, 76]. Local penetration of the molten salt into the sites with low oxygen activity and Cr depletion in the weld alloy during the initiation stage of hot corrosion can easily occur when no external oxide forms on the surface. These factors are the main parameters to facilitate a rapid hot corrosion attack and ultimate failure of the weld layer at the propagation stage of hot corrosion, known also as the second stage of hot corrosion.

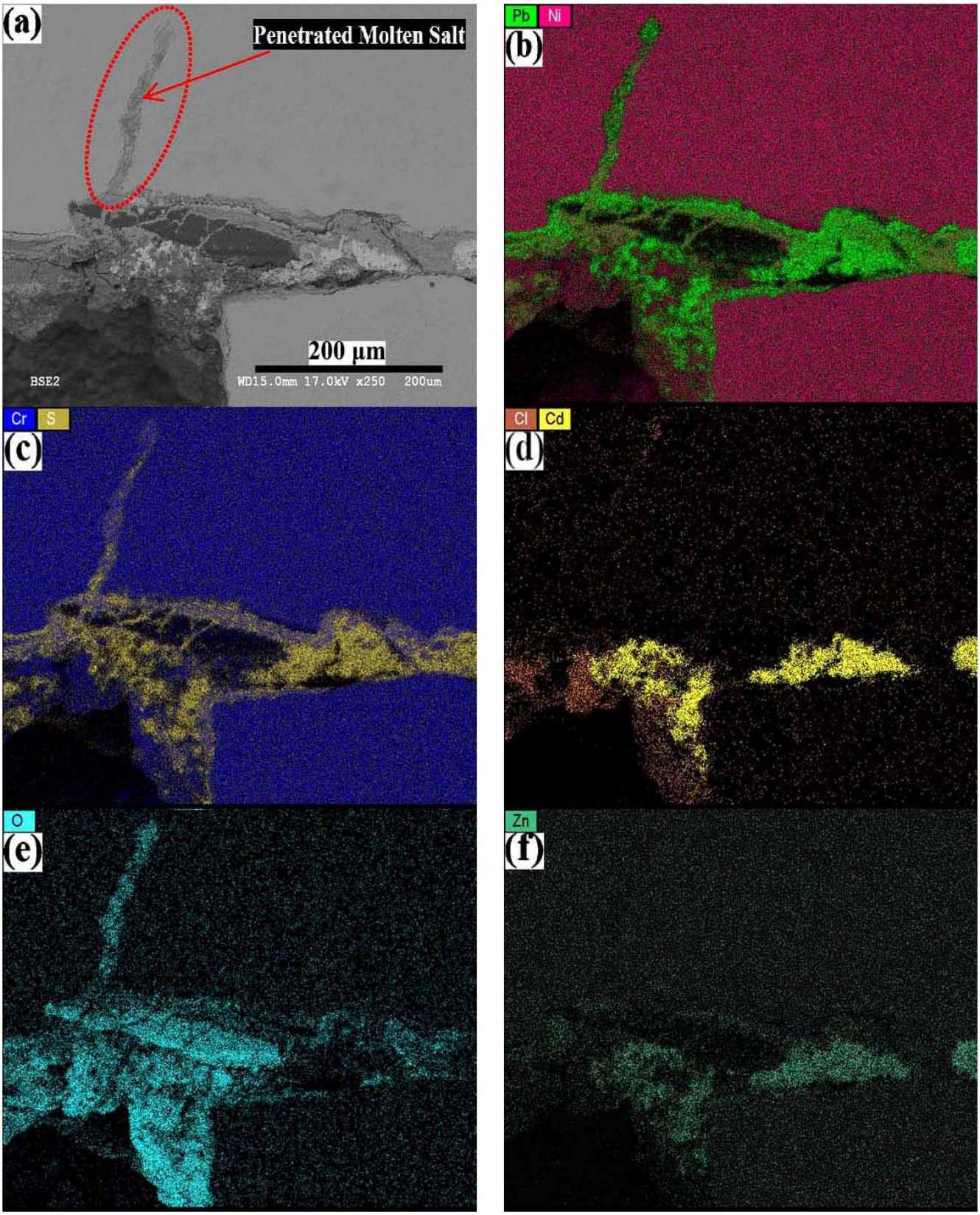

Figure 5-10- X-ray mapping and spatial distribution of Pb, Zn, Cd, Ni, Cr, Cl, S, and O in the penetrated molten phase into the weld layer through a deep crack.

X-ray mapping and spatial distribution of Pb, Zn, Cd, Ni, Cr, Cl, S, and O in the penetrated molten phase into the weld layer through a deep crack can be seen in Figure 5-10. At the root of the crack, a well-developed channel provided a pathway for further penetration of the molten phase into the weld layer (Figure 5-10a). Penetration of the aggressive species (O, S, and Cl) into the channel was obvious in the relevant X-ray maps. The formation of such kind of channel is a direct consequence of the molten phase penetration into the weld layer through open cracks and defects, accelerating the degradation of the weld layer. Based on the X-ray mapping of S, Pb, Zn, and Cd, the penetrated S-rich phase is also rich in Pb, Zn, and Cd. X-ray mapping of Ni and Cr illustrated the dissolution of these two key alloying elements of the weld layer in the penetrated molten phase through sulfidation, oxidation, and chlorination mechanisms.

In Figure 5-11, an open crack to the HSS is shown. This crack propagated through the entire weld overlay thickness, and it is the most alarming type of crack. The presence of such cracks can preclude the use of alloy 625 as a weld overlay for protecting carbon steel tubes. This type of crack can lead to pitting corrosion and ultimate failure of the carbon steel tube, which allows water to leak onto the smelt bed. Unfortunately, detecting such a type of crack is not always possible during a regular boiler inspection. The observed crack was straight and unbranched at the beginning but after penetration some distance into the weld layer, signs of branching appeared. The occurred changes in the crack growth direction caused stepped crack morphology. This deep crack acted as a suitable pathway for the molten phase and the aggressive species to penetrate inside the weld overlay, reach the underlying substrate, and ultimately spread along the weld layer/tube interface. This caused further degradation of the tube and the weld layer. The crack was widened due to the action of the penetrated molten phase. EDX elemental analysis confirmed the presence of the penetrated molten salt inside the crack and in the locations close to the weld layer/substrate interface.

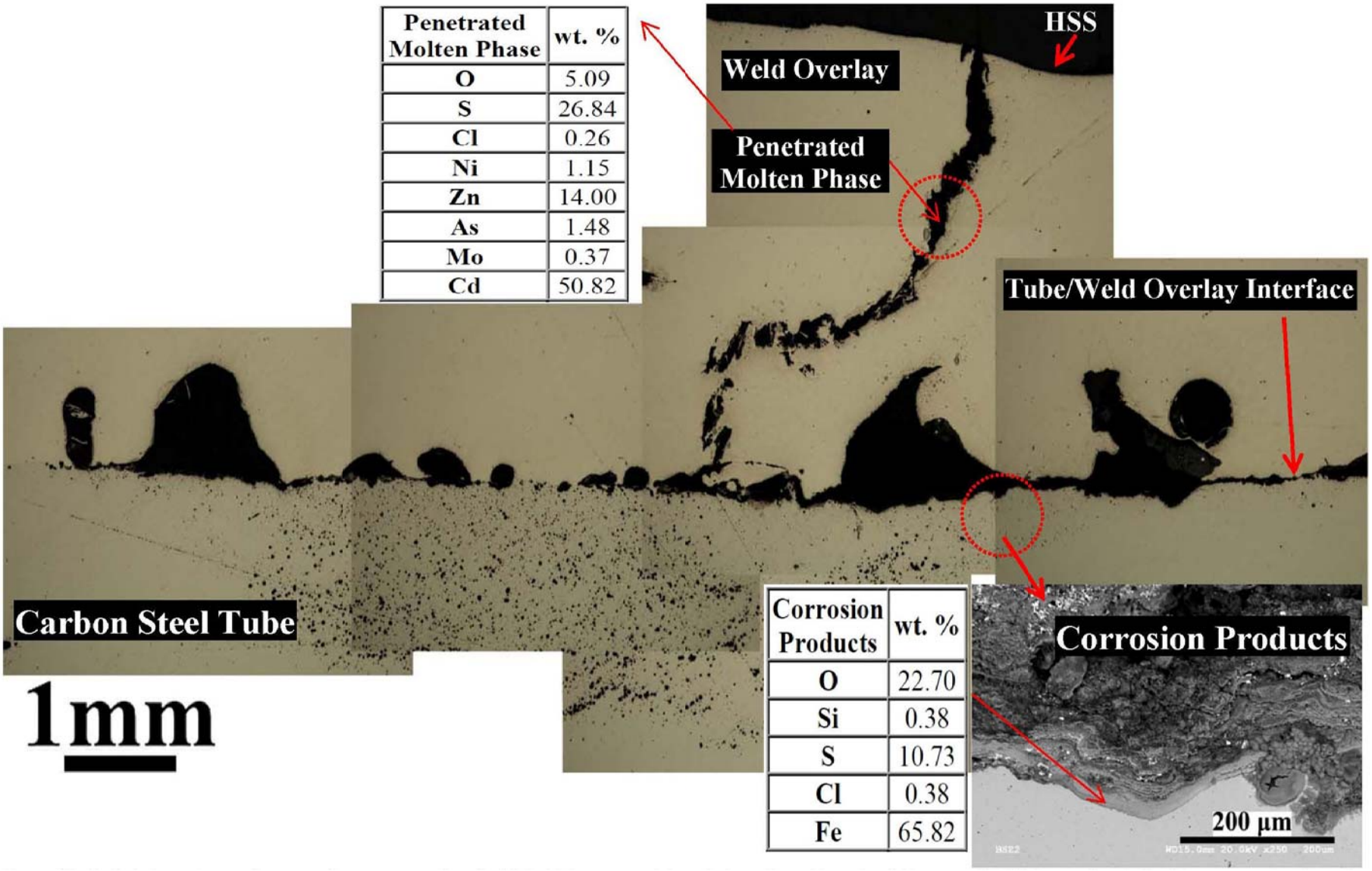

Figure 5-11- Optical photomicrographs, presenting an open crack to the HSS which propagated through the entire weld overlay thickness, and EDX elemental analysis of the penetrated molten salt into the crack and corrosion products of the carbon steel tube.

A relatively poor correlation was observed between the analyses of the deposited salt mixture (Table 5-1) and the penetrated molten salt inside the cracks because of the inhomogeneous nature and layered structure of the deposited salts. When the crack reached the interface, because of the occurrence of hot corrosion attack along the weld layer/carbon steel tube interface, both weld layer and carbon steel tube significantly corroded and a large quantity of corrosion products accumulated in this region, as can be seen in the presented SEM image in Figure 5-11. Pitting corrosion in the carbon steel tube was a direct consequence of the molten salt penetration into the interface and hot corrosion attack. Oxidation and sulfidation of Fe were the main mechanisms of the carbon steel tube corrosion, as confirmed by EDX elemental analysis of the resultant corrosion products in Figure 5-11. The irregular shape and width of this crack and thorough SEM/EDX analysis of the crack pathway indicated that the growth of this crack gradually occurred due to the penetration of the molten phase into a circumferential crack or a surface defect in the early stage of degradation of the weld overlay.

Details of the propagation path of a branched crack, traversed through the entire thickness of the weld layer and intersected the weld layer/carbon steel interface, are presented in Figure 5-12 (a, b, c). Accumulation of a significant amount of (Fe, O, S)-rich corrosion products at the interface of the weld layer/carbon steel tube indicated that more severe damage was caused by this type of crack propagated through the entire thickness of the weld layer. Many branched cracks, similar to those reported in Figures 5-11 and 5-12, are observed during the cross-sectional SEM study of the waterwall. The branches were usually finer than the original crack. In some areas, signs of further branching observed in the cracks and a multi-branched morphology, also called the “river-delta pattern” [137], were exhibited. Based on the EDX elemental analysis of the (Cr, Ti, O)-rich corrosion products in Figure 5-12a, internal oxidation was the predominant mechanism for the dissolution of Cr and Ti alloying elements of the weld overlay alloy 625.

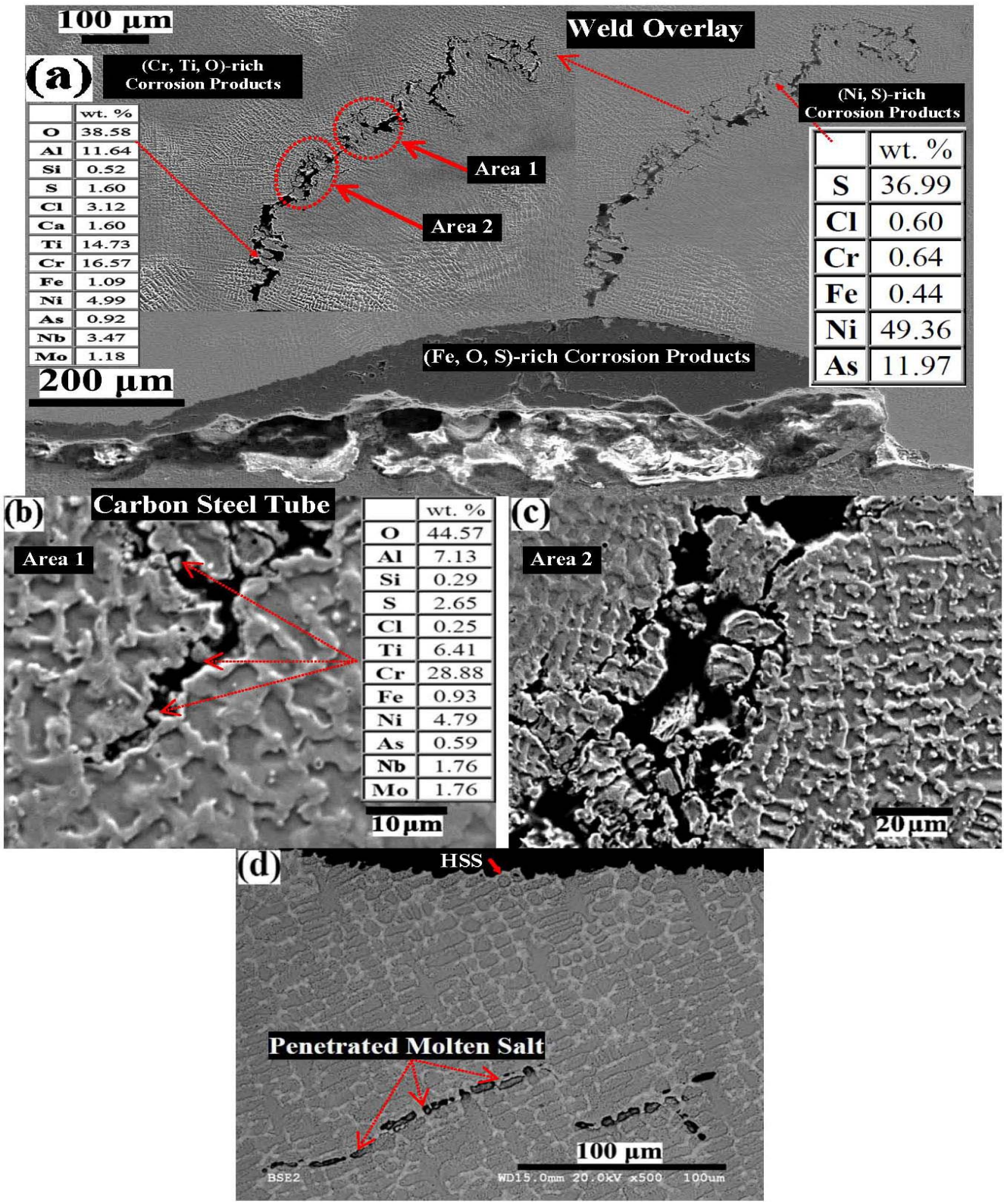

Figure 5-12- Cross-sectional SEM photomicrographs of the weld overlay, showing propagation paths of a branched crack, which traversed through the entire thickness of the weld layer and intersected the weld layer/carbon steel interface as well as EDX elemental analysis of the corrosion products.

Dissolution of Ni through internal sulfidation mechanism was confirmed because of the presence of 49.36 wt. % Ni and 36.99 wt. % S in the EDX elemental analysis of (Ni, S)-rich corrosion products in Figure 5-12a. According to Figure 5-12 (b, c, d), the dendrite cores are the preferential pathways for penetration of the molten salts and the crack branching. As was discussed before, the dendrite cores were depleted in Mo and Nb but enriched with Fe, and appeared as a consequence of mixing of the weld overlay alloy 625 and the base metal/carbon steel. For these reasons, dendrite cores acted as preferential pathways for the molten salt penetration, which consequently facilitated crack growth and crack branching. This is in agreement with the findings of other studies which reported that corrosion occurs preliminary in the dendrite cores rather than the interdendritic regions [80, 122, 138].

In Figure 5-12b, high concentration of O and S in the dendrite cores, compared to the interdendritic regions, indicated the tendency of aggressive species (O and S) to diffuse inward mainly through the dendrite cores in the weld overlay, which caused the occurrence of internal oxidation and sulfidation. Internal oxidation plays a detrimental role in a significant percentage of high-temperature corrosion failure cases and it is known as a very destructive process in industrial applications [139]. Embrittlement and dilation of the alloy subsurface region might occur due to the presence of internally precipitated reaction products, which can cause the affected zone to flake off [132]. Internal oxidation and sulfidation are rapid because both phenomena are supported by diffusion of interstitial species (dissolved O and S) into the alloy dendritic microstructure [139]. Internal sulfidation was also identified as a destructive mode of corrosion attack in hot corrosion failure of the wrought alloy 625 in a corrosive molten salt environment containing lead, zinc, iron, as well as sulfur, oxygen, and chlorine at 600, 700, and 800°C and grain boundaries were the preferential pathways for diffusion of O and S into the alloy during the occurrence of the hot corrosion phenomenon [132]. As can be seen in Figure 5-12d and 5-13, the non-uniform nature of the corrosion on the HSS of the waterwall caused the roughening of the weld overlay surface.

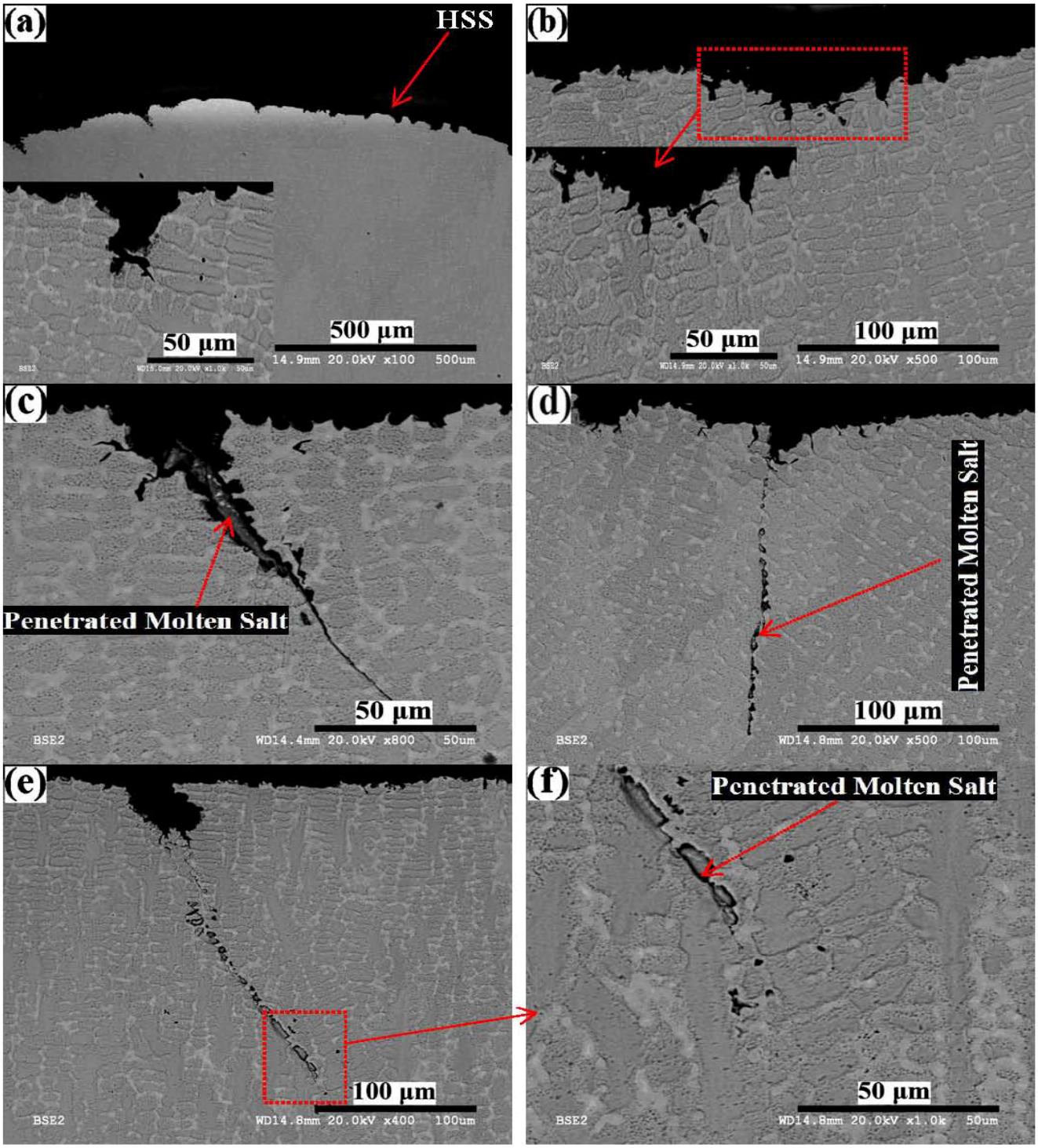

Figure 5-13- a), b), c) and d) Cross-sectional SEM photomicrographs of the weld overlay surface layer showing roughening of the HSS due to the occurrence of non-uniform preferential corrosion on the HSS, and the initiation of the cracks from the HSS, as well as e) and f) the molten salt penetration into the initiated cracks along the dendrite cores.

Microsegregation of alloying elements in the dendritic structure of the weld layer, discussed in section 5.3, was the main reason for the occurrence of the preferential corrosion on the HSS and consequent roughening of the weld layer. Preferentially corroded zones can act as crack initiation sites, as was observed in Figures 5-13a and b. The conducted cross-sectional SEM studies on the HSS confirmed that cracks mainly initiated from the preferentially corroded, and (Mo, Nb)-depleted dendritic cores on the HSS. The presence of the molten phase inside the developed surface cracks indicated that the penetration of the molten phase into the initiated surface cracks accelerated the propagation of the cracks mainly through the dendrite cores and further crack branching or caused the cracks to be widened. The outcome of this phenomenon was the development of some cracks like those reported in Figures 5-11 and 5-12. Initiation of the cracks from the dendrite cores of alloy 625 weld cladding was also reported by Luer et al. [79]. As was extensively discussed in section 5.3, the weld layer was highly susceptible to solidification cracking along the Laves phase, (Mo, Nb)-rich regions. Solidification cracks, which are open to the surface, can also act as potential sites for penetration of the molten phase into the weld layer and gradual development of the cracks which intersect the weld layer/tube interface. An important point in Figure 5-13d was the formation of pores in the (Mo, Nb)-rich interdendritic regions, adjacent to the crack tip. Some pores were still at their early stage of development. Formation of pores in interdendritic regions, as a sign of internal hot corrosion attack, was a consequence of the aggressive species' (O and S) diffusion into the interdendritic regions [132].

5.5 Hot corrosion study and weight-loss measurement in 47 $PbSO_4$-23 ZnO-13 Pb_3O_4-7 $PbCl_2$-5 CdO (wt. %) molten salt medium

Figure 5-14 shows the OCP curves of the weld overlay alloy 625 working electrodes at 600, 700, and 800°C. Despite the potential fluctuations, the OCP curves demonstrated an overall upward trend at the beginning of the exposure to the molten salt medium. Ultimately, the OCP of the working electrode

reached a stable value after almost 24 hr. The OCP of the weld overlay alloy 625 working electrode was equal to 16, 15, and 14 mV at 600, 700 and 800°C, respectively.

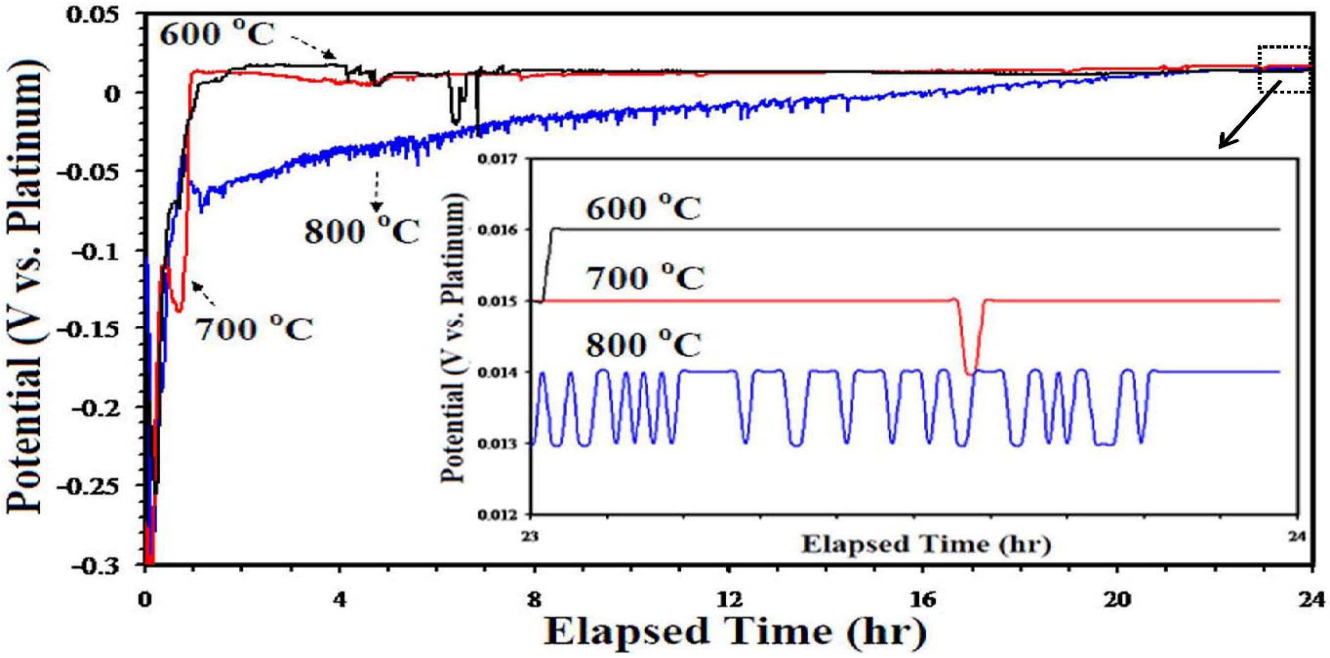

Figure 5-14- OCP curves of the weld overlay alloy 625 electrodes, exposed to the molten salt mixture.

Rapid increase in the OCP of the working electrode upon exposure to the molten salt was attributed to the spontaneous growth of an anodic film on the surfaces of the electrode. The potential fluctuations in the OCP curve of the weld overlay at 800°C were an evidence of unstable nature of the formed anodic film on the surface of the working electrode. The OCP curves at 600 and 700°C reached a reasonably stable value after almost 8 hr of exposure; this means that a reasonably stable anodic film was formed on the surface of the working electrode at these two temperatures.

Potentiodynamic polarization curves of the weld overlay alloy 625 at 600, 700, and 800°C, after 24 hrs of exposure to the molten salt when the OCP curve reached a steady-state potential, are presented in Figure 5-15. In Figure 5-15, it is observed that anodic current density increased rapidly when the potential shifted in the noble direction; consequently, the weld overlay alloy 625 exhibited an active dissolution behavior at 600, 700, and 800°C and passivation of the alloy did not occur. This confirmed

that the anodic film, which formed on the surface of the alloy, was a corrosion product layer, not an effective protective film/passive layer. The shape of the curves in Figure 5-15 is similar to those previously reported for wrought alloy 625 [132].

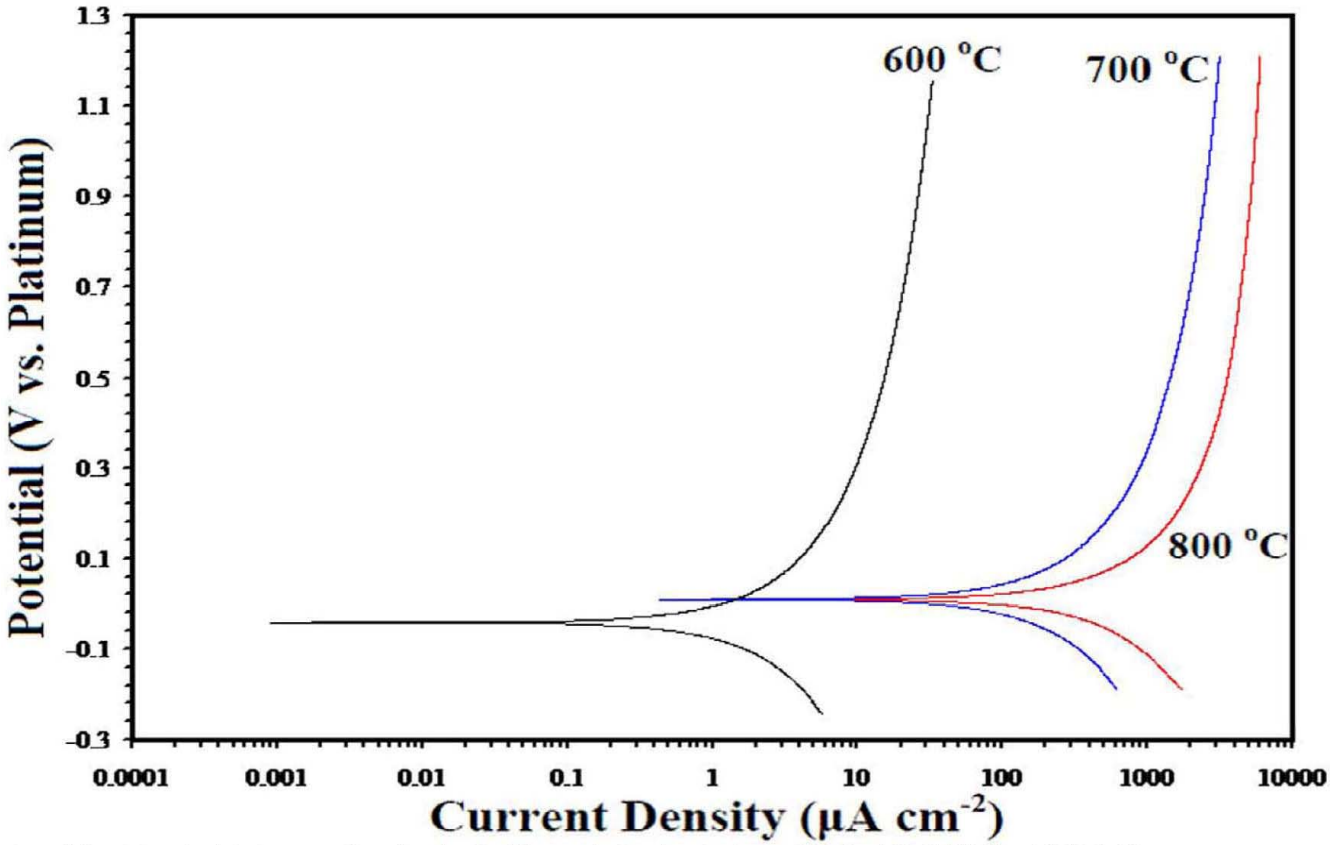

Figure 5-15- Potentiodynamic polarization curves of the weld overlay alloy 625, exposed to the molten salt mixture at 600, 700 and 800°C for 24 hr.

Table 5-4- Obtained corrosion potential from the potentiodynamic polarization curves, and the calculated corrosion rate through weight-loss measurement technique for weld overlay alloy 625, exposed to the molten salt mixture at 600, 700, and 800°C for 24 hr.

	800°C	700°C	600°C
E_{corr} (mV vs. Platium)	9.0	9.5	- 41.5
Corr. Rate (mm/year)	22.75	17.03	1.69

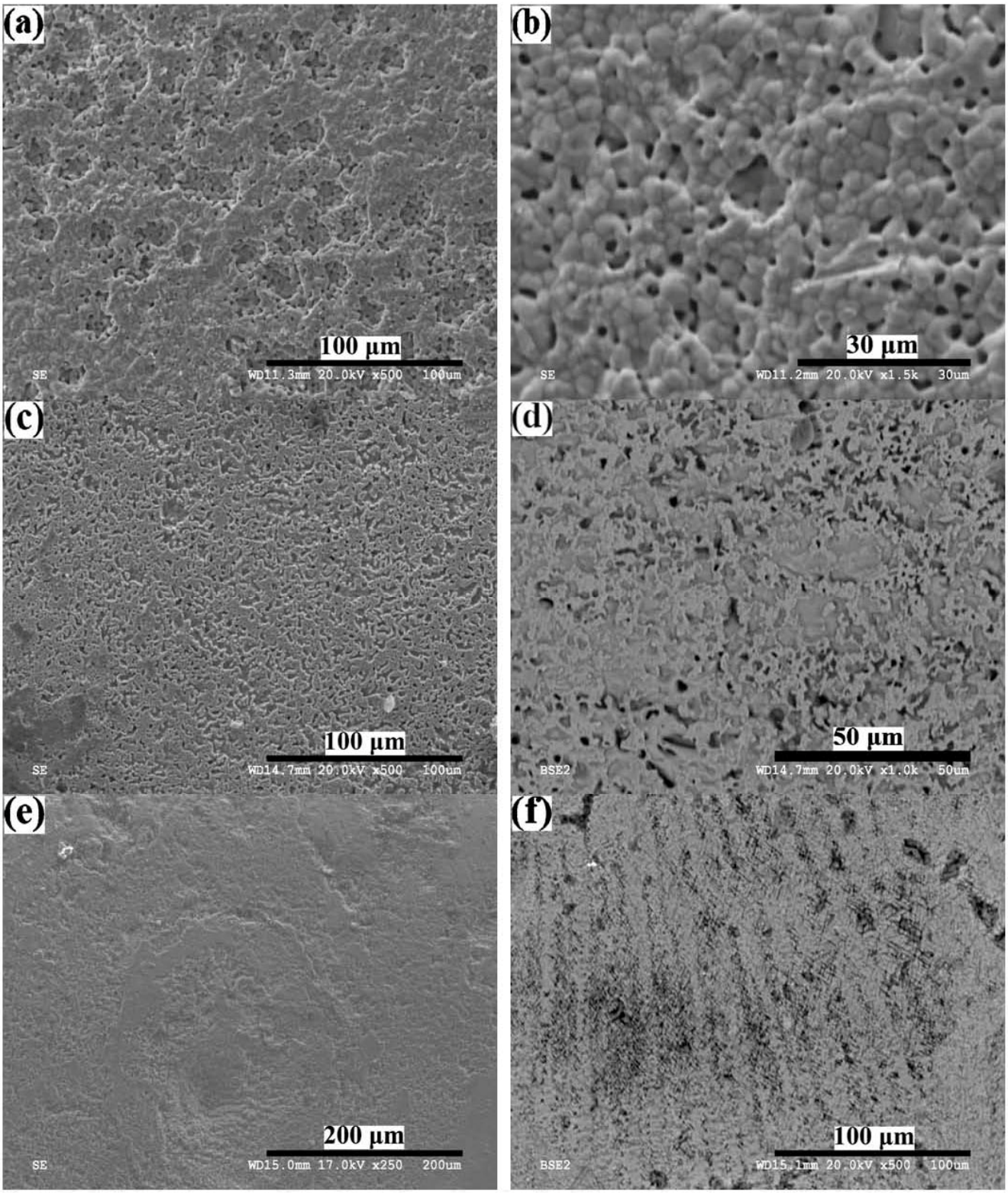

Figure 5-16- SEM photomicrographs of the surfaces of the weld overlay alloy 625 corroded specimens at a) and b) 800°C; c) and d) 700°C, e) and f) 600°C, which show the morphology of the attacked surfaces after cleaning and removing the corrosion products and the scales according to ASTM G1-03.

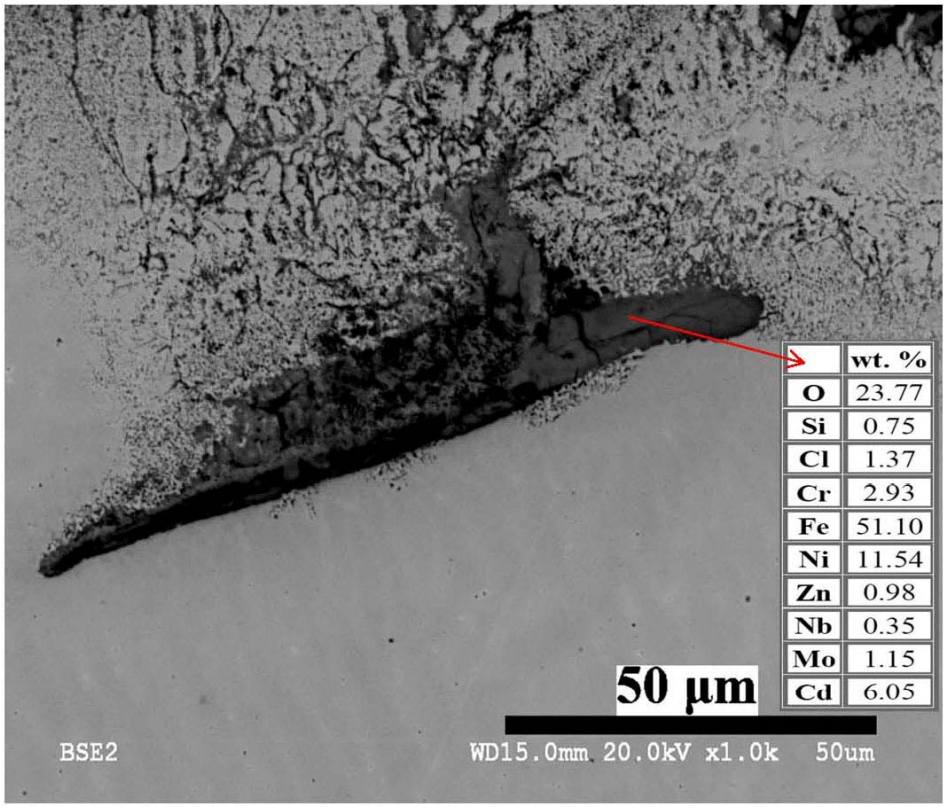

Figure 5-17- Cross-sectional SEM photomicrographs of the weld overlay alloy 625 corroded specimen at 600°C, which show the penetration of molten phase to the subsurface region of the weld layer through the developed channels and cracks and oxidation of an Fe-rich inclusion, located close to the surface layer.

Corrosion potential (E_{corr}), determined from the potentiodynamic polarization curves and the calculated corrosion rate through the weight-loss measurement technique are presented in Table 5-4. As can be seen, the corrosion rate of the weld overlay in the molten salt medium increased at higher temperatures.

In Figure 5-16, SEM photomicrographs show the morphology of the attacked surface of the weld overlay alloy 625, after 24 hr of exposure to the molten salt mixture at 600, 700, and 800°C. In addition to the general surface corrosion at all the investigated temperatures, the weld overlay was susceptible to the localized corrosion attack at 700 and 800°C. This is why a network of pores formed on the attacked surface at these two temperatures, as can be seen in Figure 5-16 (a, b, c, d). The susceptibility of the

weld overlay to the formation of pores and pitting corrosion can justify the presence of many cavities on the surface of the weld layer, as was observed in Figure 5-4. At 600°C, the signs of general surface corrosion (Figure 5-16e) and preferential corrosion along the dendrite cores (Figure 5-16f) were observed on the attacked surface of the weld overlay. High percentage of Fe and depletion of Mo and Nb in the dendrite cores (based on Table 5-3) made these regions susceptible to preferential corrosion attack, as was also mentioned before when the results in Figure 5-12 were discussed.

Figure 5-17 shows cross-sectional SEM photomicrographs of the weld overlay alloy 625 corroded specimen at 600°C. Penetration of the molten phase and the aggressive species through the developed channels/cracks and pathways across the subsurface regions of the overlay was evident. Oxidation of Fe in a Fe-rich inclusion, located in the subsurface regions of the overlay, was also noticeable in this image. Making a comparison between Figure 5-17 and Figure 5-5 (e, f) confirmed that the presence of Fe-rich inclusions in the weld overlay due to the dilution of Fe reduced the resistance of the weld overlay to the hot corrosion attack.

Chemical composition of the attacked surface of the weld overlay was determined by EDX elemental analysis, and the results are presented in Table 5-5. Compared to the chemical composition of the weld overlay alloy 625 in Table 5-2 (prior to high temperature electrochemical tests), the attacked surface of the weld overlay was depleted in Cr and Nb. This result was in agreement with the formation of Cr- and Nb-depleted zones in weld overlay, as was observed in Figure 5-9. In the Cr-depleted surface at 700 and 800°C, the concentration of Cr decreased to 6.30 and 1.94 wt. %, respectively, which were significantly lower than the concentration of Cr in the weld overlay in Table 5-2 (Cr: 17.02 wt.%). However, after 24 hr of exposure to the molten salt at 873 K (600°C), the concentration of Cr (17.31 wt. %) was very close to the original composition of the weld overlay (17.02 wt. %). Based on this evidence, chromium is very prone to dissolution in molten salt during the exposure of the weld overlay

alloy 625 to the molten salt at 700 and 800°C. Dissolution of Cr occurs during the initiation stage of hot corrosion.

Table 5-5- EDX elemental analysis (wt. %) from the attacked surface of the weld overlay alloy 625 corroded samples, exposed to the molten salt mixture at 600, 700, and 800°C for 24 hr.

Attacked Surface of Weld Overlay Alloy 625			
	800°C	700°C	600°C
Ni	70.32 ± 3.06	70.26 ± 2.16	61.79 ± 4.06
Cr	1.94 ± 0.31	6.30 ± 1.90	17.31 ± 2.01
Mo	11.20 ± 0.92	14.17 ± 1.93	9.73 ± 1.61
Nb	0.71 ± 0.96	1.26 ± 0.27	1.97 ± 0.41
Ti	0	0	0.24 ± 0.14
O	14.00 ± 1.81	6.64 ± 1.32	3.71 ± 2.64
Fe	1.32 ± 0.16	0	0.63 ± 0.17
Al	0.18 ± 0.10	0.44 ± 0.17	0.18 ± 0.10
Si	0.12 ± 0.08	0.52 ± 0.20	0.14 ± 0.09
Cl	0.17 ± 0.07	0.41 ± 0.20	2.63 ± 2.51

Despite the fact that Cr is known as the most important alloying element in protecting wrought alloy 625 against corrosive environments at ambient temperature through the formation of the protective chromium-nickel oxide, this element cannot play an effective role in providing protection for the weld overlay alloy 625 in the molten salt medium at high temperature working conditions of the boiler. This is why the corrosion rate of the weld overlay in molten salt medium of the present study at 600, 700 and 800°C was too high. At all the investigated temperatures, the concentration of Fe was significantly lower than the original concentration of Fe in the weld overlay alloy 625 (23.64 wt. %, reported in Table 5-2). This showed that Fe content of the weld overlay was almost fully dissolved in the molten salt, confirming low resistance of the Fe element to the hot corrosion attack. Therefore, the presence of Fe in the weld overlay alloy 625, mainly through the carbon steel dilution during welding, reduced the overall resistance of the weld overlay to the hot corrosion attack in the molten salt medium. The attacked surface of the weld overlay was rich in Ni and Mo at all the investigated temperatures. The concentrations of Ni and Mo in the weld overlay prior to the exposure to the molten salt were around

47.46 and 6.00 wt. %, respectively. The concentration of (Ni, Mo) in the surface layer increased to (61.79, 9.73), (70.26, 14.17), and (70.32, 11.2) wt. %, after 24 hr of exposure to the molten salt at 600, 700 and 800°C, respectively, which was considerably higher than the concentration of Ni and Mo in the weld overlay prior to the exposure. Considering the depletion of Cr in the surface layer of the attacked weld overlay and high concentration of Ni and Mo in this layer, it can be concluded that after 24 hr of exposure to the molten salt, a (Ni, Mo)-rich layer formed on the surface. This layer was also rich in oxygen particularly at 800°C as reported in Table 5-5. However, this (Ni, Mo, O)-rich layer was highly porous and was not able to act as an effective barrier layer to protect the weld overlay against the hot corrosion attack. This is consistent with the high corrosion rate of the weld overlay, determined through weight-loss measurement technique and tabulated in Table 5-4, and SEM results in Figures 5-16 and 5-17. The concentration of the dissolved Mo in the molten salt mixture, measured by means of the ICP/AAS technique, was less than 1 ppm (lower than the detection limit of ICP/AAS) at all the investigated temperatures. The amounts of the dissolved chromium and nickel in the molten salt mixture were determined as Ni, 34, 28, and 31 ppm at 800, 700, and 600°C, respectively, and Cr, 61, 37, and 15 at 800, 700 and 600°C, respectively.

The XRD patterns of the scales and corrosion products, which formed on the attacked surface of the corroded specimens at 800, 700 and 600°C, are presented in Figures 5-18, 5-19 and 5-20. Each XRD pattern was compared with the standard XRD patterns (JCPDS file) of the major identified phases to show the phase match. The identified phases in these XRD patterns are tabulated in Table 5-6. XRD results confirm that nickel, chromium, molybdenum, niobium, titanium and iron are the major elements in the chemical composition of the corrosion products and scales which show the susceptibility of these elements to be dissolved in the molten salt mixture. Obviously, sulfidation and oxidation of chromium occurred at all the investigated temperatures. In addition to sulfidation and oxidation, chlorination of chromium is also observed at 700 and 600°C where $CrCl_2$ and CrOCl are identified, respectively.

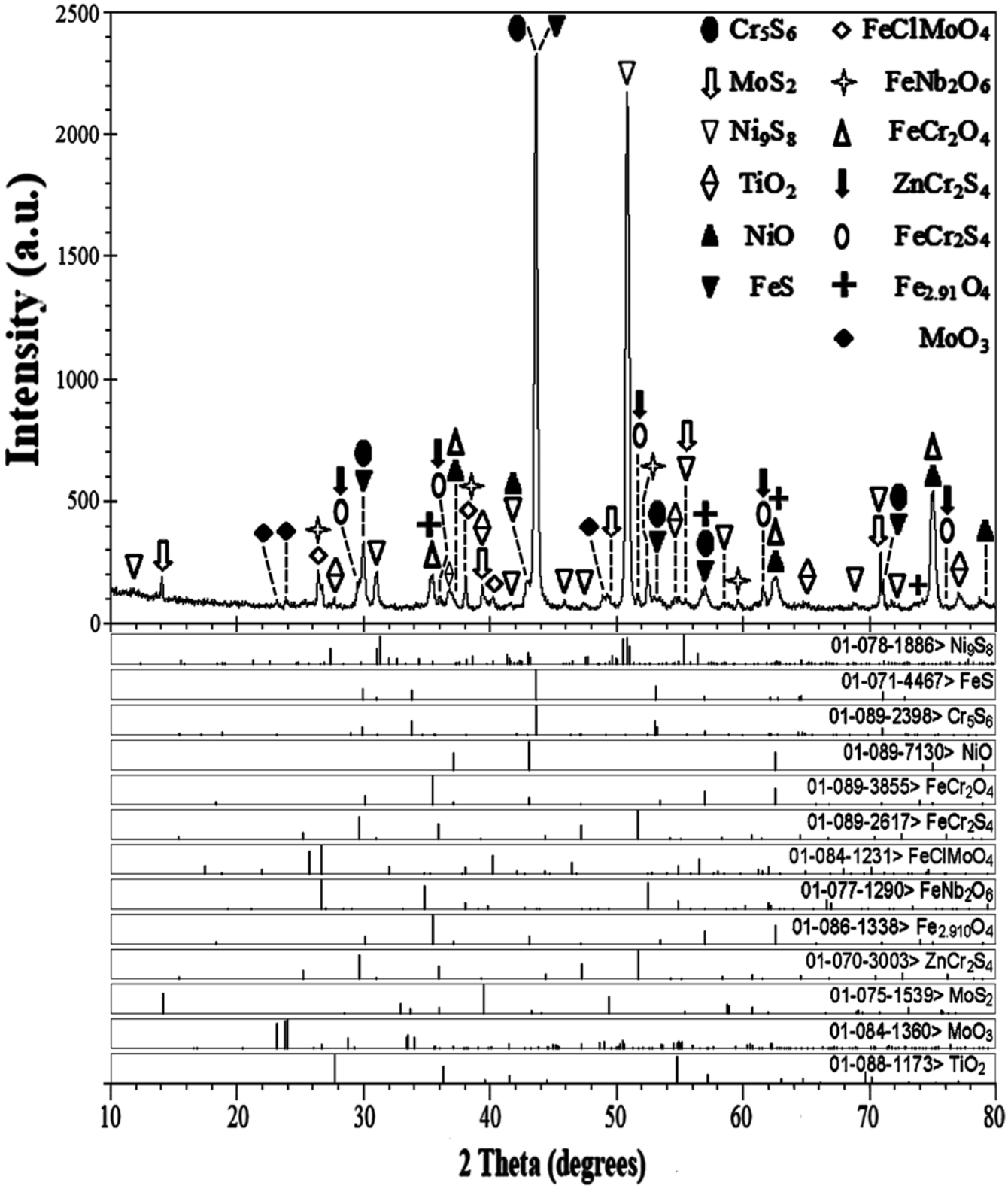

Figure 5-18- X-ray diffraction (XRD) pattern of attacked surface of the weld overlay alloy 625 at 800°C (prior to descaling) in comparison with the standard XRD patterns of the identified components, compiled by JCPDS.

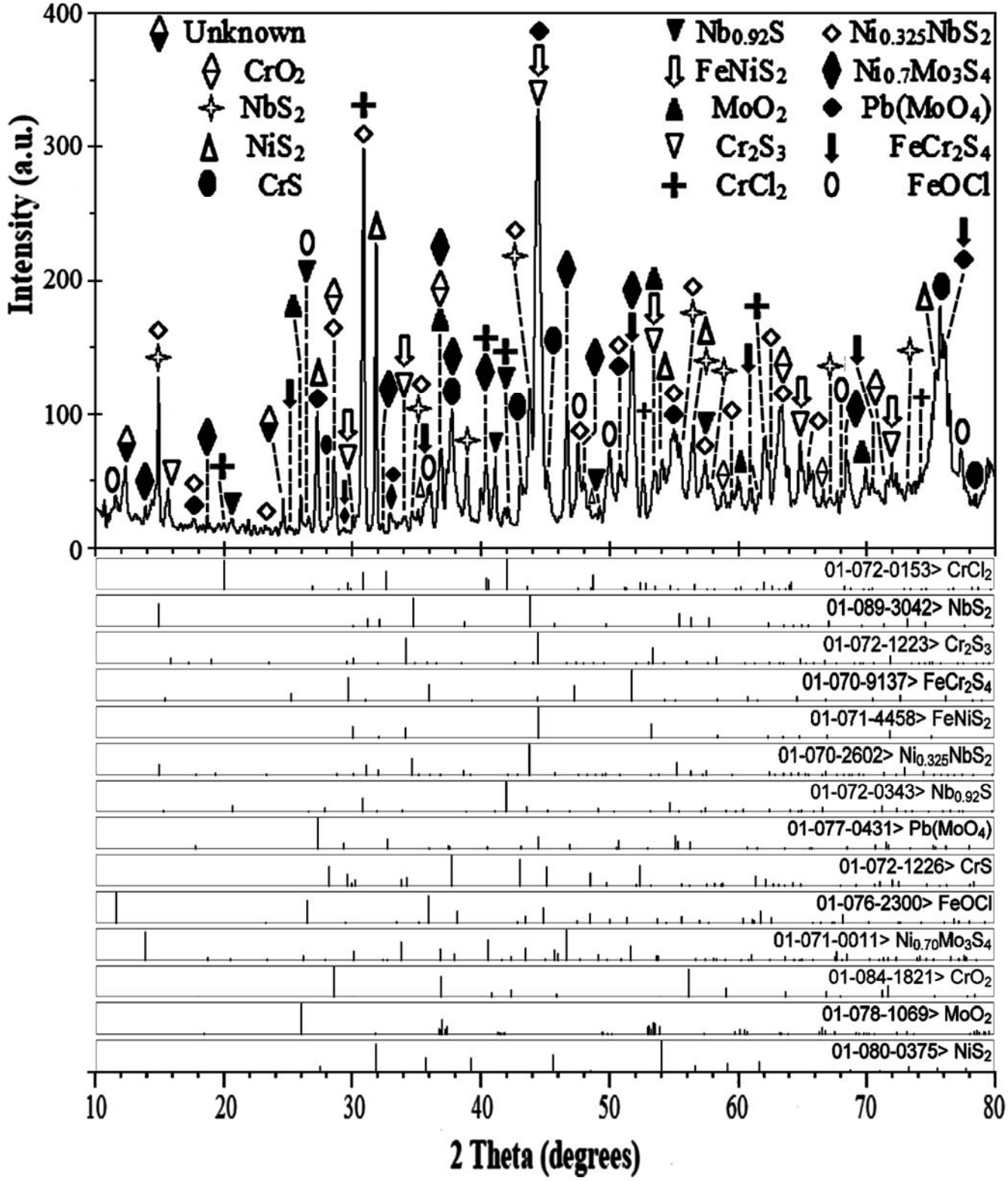

Figure 5-19- X-ray diffraction (XRD) pattern of attacked surface of the weld overlay alloy 625 at 700°C (prior to descaling) in comparison with the standard XRD patterns of the identified components, compiled by JCPDS.

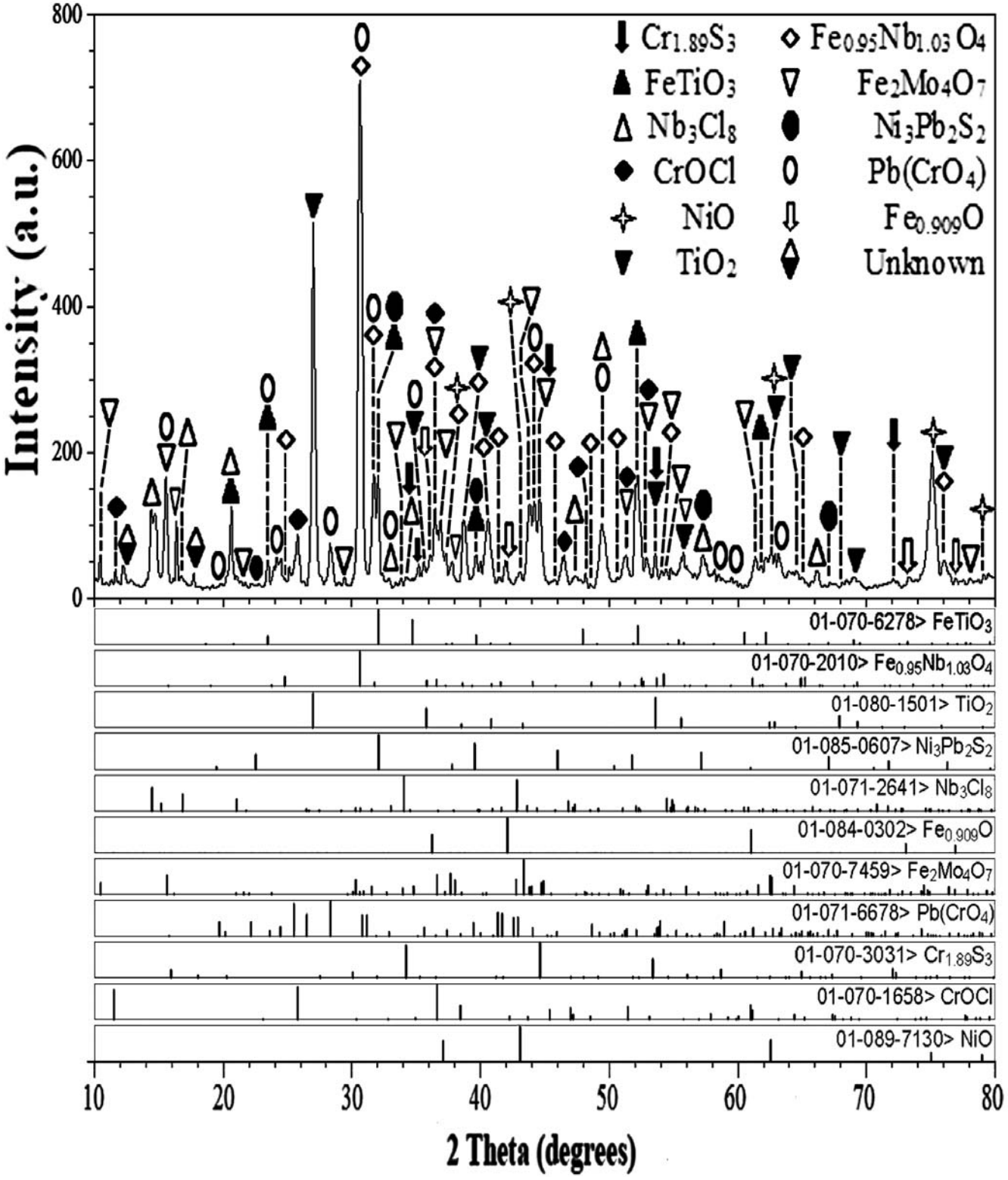

Figure 5-20- X-ray diffraction (XRD) pattern of attacked surface of the weld overlay alloy 625 at 600°C (prior to descaling) in comparison with the standard XRD patterns of the identified components, compiled by JCPDS.

Table 5-6- Identified corrosion products in the scales, extracted from Figures 5-18, 5-19 and 5-20.

	800°C	700°C	600°C
Ni	NiO, Ni_9S_8	NiS_2, $FeNiS_2$, $Ni_{0.7}Mo_3S_4$, $Ni_{0.325}NbS_2$	NiO, $Ni_3Pb_2S_2$
Cr	Cr_5S_6, $FeCr_2O_4$, $ZnCr_2S_4$, $FeCr_2S_4$	CrS, CrO_2, Cr_2S_3, $CrCl_2$, $FeCr_2S_4$	CrOCl, $Cr_{1.89}S_3$, $Pb(CrO_4)$
Mo	MoS_2, MoO_3, $FeClMoO_4$	MoO_2, $PbMoO_4$, $Ni_{0.7}Mo_3S_4$	$Fe_2Mo_4O_7$
Fe	FeS, $FeCr_2S_4$, $FeCr_2O_4$, $Fe_{2.91}O_4$, $FeNb_2O_6$, $FeClMoO_4$	FeOCl, $FeNiS_2$, $FeCr_2S_4$	$FeTiO_3$, $Fe_{0.909}O$, $Fe_2Mo_4O_7$, $Fe_{0.95}Nb_{1.03}O_4$
Nb	$FeNb_2O_6$	NbS_2, $Nb_{0.92}S$, $Ni_{0.325}NbS_2$	Nb_3Cl_8, $Fe_{0.95}Nb_{1.03}O_4$
Ti	TiO_2	-	TiO_2, $FeTiO_3$

The morphology of the scales and corrosion products as well as solidified molten salt mixture on the external surface of the corroded specimens can be seen in Figure 5-21. The scales consist of a number of phases which were thoroughly analysed by XRD technique and the results were discussed. EDX elemental analysis confirms that scales are rich in Fe, Cr and O. Underneath the scales, there is an internal attacked area, Ni-rich region, which is clearly detectable in Figures 5-21b, d, and f. Cross-sectional morphology of the scales and internal attacked area is presented in Figure 5-22. The scales are considered as corrosion products not effective barrier layers to protect the substrate against corrosive species. Developed channels and discontinuities as well as pores in the structure of the scales act as the effective pathways for corrosive species (O, S, Cl) to reach the surface of the weld overlay. Penetration of the corrosive species into the weld overlay through the surface cracks is visible in Figures 5-22c and d. In order to reveal the microstructure of the corroded specimens after being exposed to the simulated molten salt mixture, the corroded specimens were etched for 10 minutes in a solution containing 5 mL H_2SO_4, 3 mL HNO_3, and 92 mL HCl and the microstructure of the etched specimens can be seen in Figure 5-23. Obviously, weld overlay alloy 625 is susceptible to interdendritic corrosion. The developed channels are potential pathways for the penetration of the corrosive species into the weld overlay and development of the internal attacked areas.

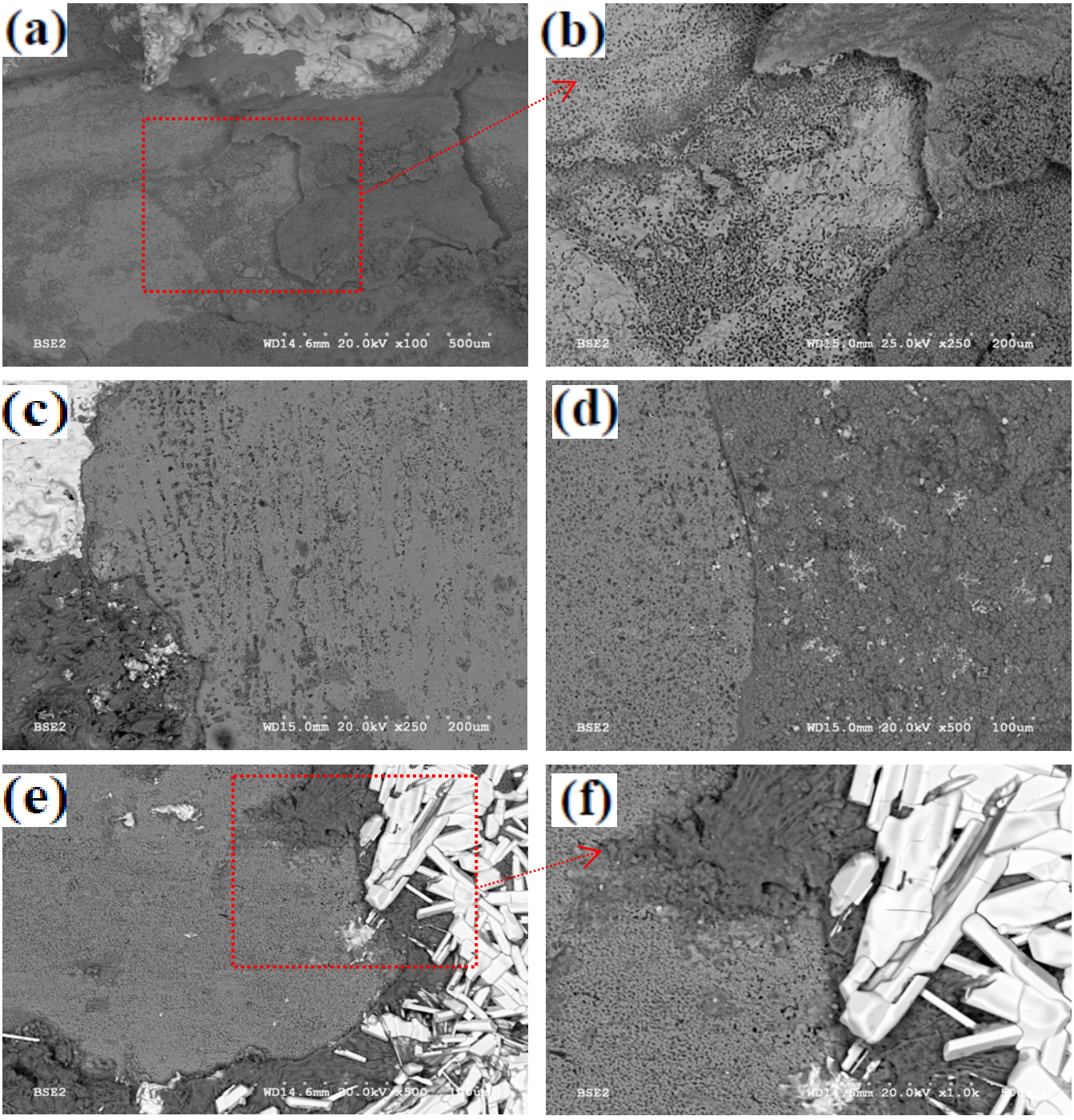

Figure 5-21- SEM photomicrographs of the surface of the weld overlay alloy 625 substrates, exposed to the molten salt mixtures at a) and b) 800°C, c) and d) 700°C, plus e) and f) 600°C which show the morphology of the scales and solidified Pb-rich molten salt (white regions).

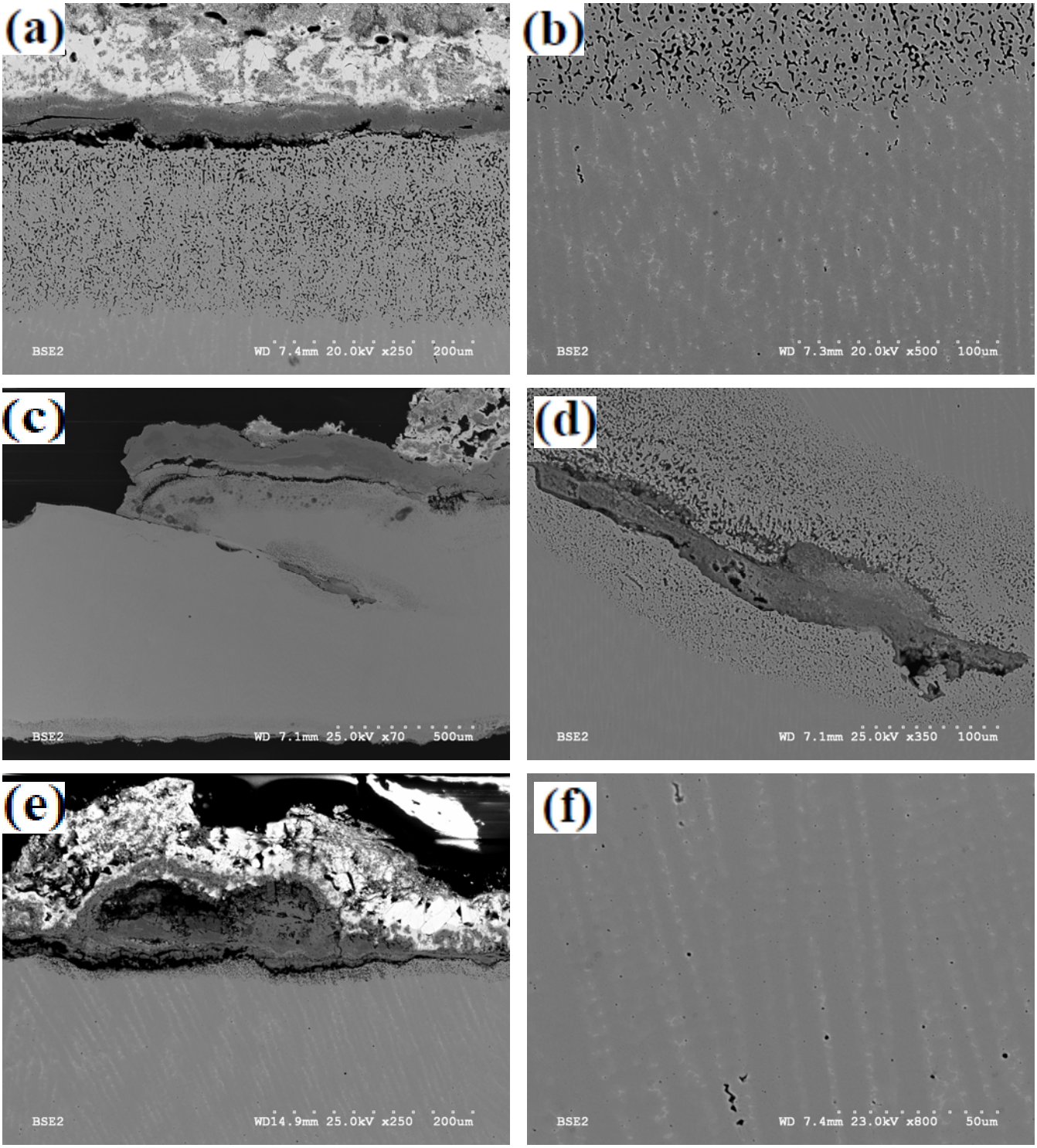

Figure 5-22- Cross-sectional SEM photomicrographs of the weld overlay alloy 625 substrates, exposed to the molten salt mixtures at a) and b) 800°C, c) and d) 700°C, plus e) and f) 600°C which show the morphology of the scales and solidified Pb-rich molten salt (white regions).

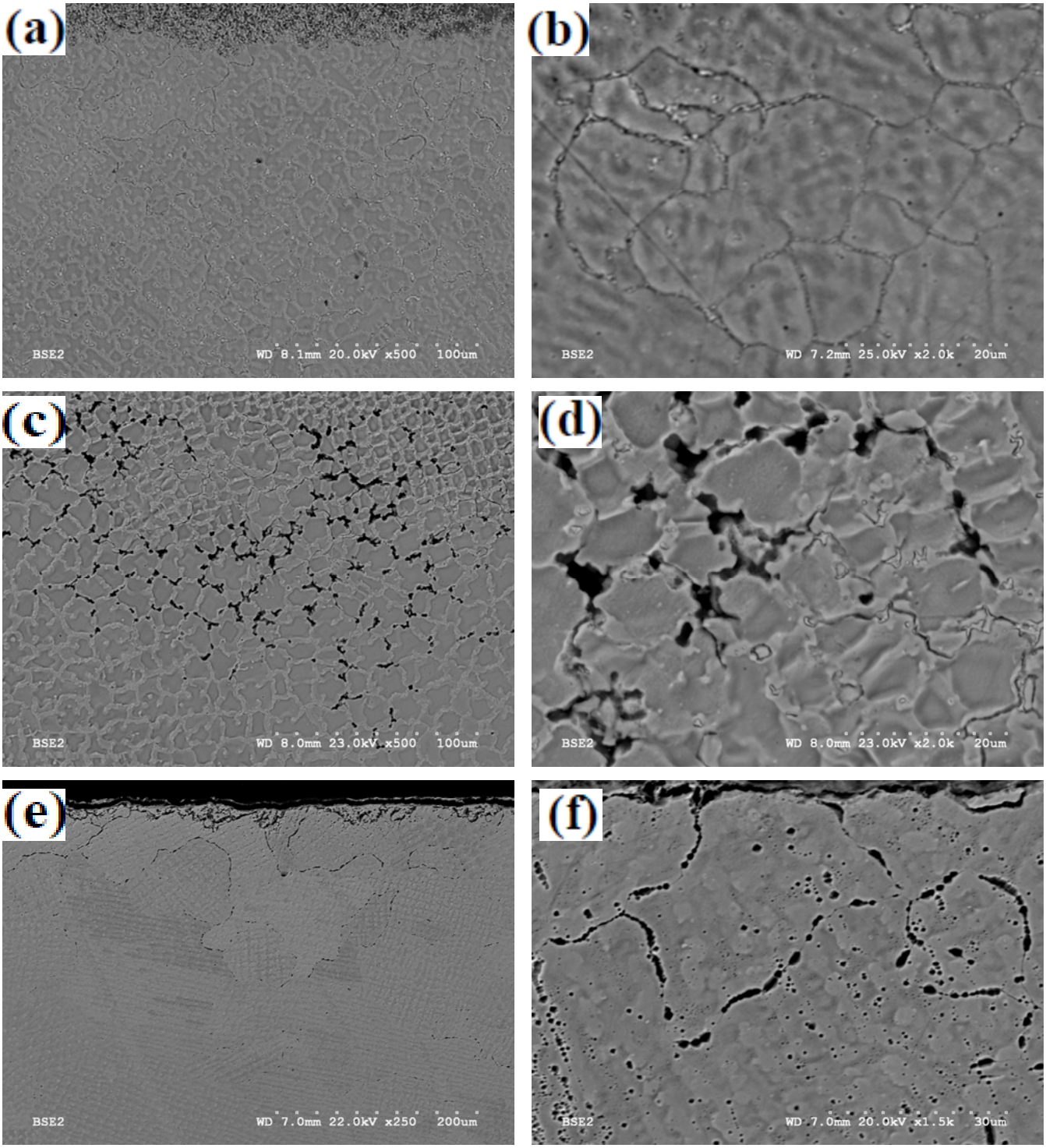

Figure 5-23- Cross-sectional SEM photomicrographs of the weld overlay alloy 625 substrates, exposed to the molten salt mixtures at a) and b) 800°C, c) and d) 700°C, plus e) and f) 600°C. Samples were etched in a solution containing 5 mL H_2SO_4, 3 mL HNO_3, and 92 mL HCl for 10 minutes.

5.6 Recommendations

Considering the conducted studies on the weld overlay alloy 625 and the reviewed literature, the following recommendations are presented to minimize the risk of hot corrosion failure in the radiant boiler of the KIVCET smelter:

5.6.1 Optimizing the parameters of the welding process

- The content of Fe in the weld overlay alloy should be kept to less than 6-7% to minimize the adverse effects of Fe on the properties of the deposited weld layer. The dilution level of Fe can be controlled by controlling the heat input.
- By decreasing the arc power/heat input and increasing the volumetric filler metal feed rate (deposition rate), which means maximizing the filler metal feed rate-to-arc power ratio, the dilution level and Fe content in the overlay will be minimized. This can ultimately lead to improving the cracking and corrosion resistance of the weld overlay and avoid the formation of undesirable phases and inclusions, such as Fe-rich inclusions. Further study on the welding process is necessary to be carried out for optimizing the filler metal feed rate-to-arc power ratio.
- It is recommended to use a pulsating direct current for applying weld overlay to control the segregation and dilution phenomena in the weldment and to reduce heat build-up, residual stress, and distortion during the welding process.
- In addition to minimizing the heat input, a high weld metal cooling rate has to be used to decrease the Nb segregation and amount of detrimental Laves phase, thereby reducing the susceptibility to the occurrence of the solidification cracking. Circulating water inside the tubes during deposition of the weld layer is an effective option to increase the cooling rate of the weldment and to reduce the microsegregation and Laves formation when applying the weld overlay on the waterwalls.

5.6.2 Modifying/altering the chemical composition of the filler metal

- Selecting an alloy 625 filler metal with relatively high content of C and low content of Si and Fe to promote the formation of γ/NbC at the terminal stage of the overlay solidification at the expense of the γ/Laves is another precaution for decreasing the solidification temperature range and, therefore, reducing the cracking susceptibility.
- All the above-mentioned recommendations ultimately reduce the risk of solidification cracking and the formation of inclusions in the weld overlay alloy 625 microstructure. Considering the proven contribution of cracks and inclusions to the ultimate hot corrosion failure of the weld overlay, these recommendations are expected to extend the lifetime of the weld overlay and to delay the failure. Moreover, the vulnerability of the weld overlay alloy 625 to hot corrosion and interdendritic attack in the molten salt environment of the KIVCET radiant boiler has been established in practice. Therefore, it is recommended to find an alternative candidate to replace the weld overlay alloy 625 in this application.
- Based on the findings, Mo and Ni showed the highest resistance to hot corrosion and dissolution in the molten salt environment of the KIVCET radiant boiler compared to other alloying elements in the wrought or weld alloy 625. From this perspective, it is recommended to investigate the possibility of applying Inconel 622, Inconel 686, or Inconel 59 as weld overlay instead of alloy 625, due to (a) the presence of higher concentration of Mo, and (b) replacement of Nb with W in these alloys, compared to Inconel 625. It has to be considered that the hot corrosion behavior of Inconel 622 and Inconel 686 and Inconel 59 is not yet well understood. Therefore, further study on the hot corrosion behavior of the wrought and/or weld overly Inconel 622, Inconel 686, and Inconel 59 in the molten salt environment of the KIVCET waste heat boiler is required to prove the suitability of these three potential candidates to replace the weld overlay alloy 625 in this application.

5.7 Summary

The purpose of this chapter was to discuss the results of the detailed failure analysis conducted on the failed overlaid tubes waterwall in the KIVCET waste heat boiler. The root causes and mechanisms of the failure were identified. The technical recommendations were proposed to minimize the risk of failure in the future applications. Furthermore, corrosion behavior and electrochemical properties of the weld overlay in 47 $PbSO_4$-23 ZnO-13 Pb_3O_4-7 $PbCl_2$-5 CdO (wt. %) molten salt medium were assessed in a laboratory scale.

The deposited salt mixtures on the waterwall had a strong tendency to form a molten phase at the operating temperature range of the radiant boiler. The presence of the deposited salt mixtures and the formation of the molten phase led to the hot corrosion attack in the waterwall and the degradation of the weld overlay. The weld overlay alloy 625 exhibited a well-defined anisotropic, dendritic structure. A bright/white structure in the interdendritic regions pertained to the Laves phase. The white areas (Laves) were rich in Mo and Nb. The dendrite cores were depleted in Nb and Mo, while they contained higher concentration of Fe, Ni, and Cr, compared to the interdendritic regions. The high heat input caused an increase in the dilution level of Fe because the carbon steel substrate melted in the weld pool temperature. The dilution level was determined based on the concentration of Fe in the weld overlay, the filler metal, and the carbon steel tube (base metal). The cracks, which initiated from the HSS and traversed through the entire thickness of the weld layer and ultimately intersected the weld layer/carbon steel interface, were the most alarming type of cracks.

6 Hot corrosion behavior of wrought alloy 625 in 47 $PbSO_4$-23 ZnO-13 Pb_3O_4-10 Fe_2O_3-7 $PbCl_2$ (wt. %) molten salt mixture[1]

Corrosion behavior of alloy 625 was studied in a molten salt consisting of 47 $PbSO_4$-23 ZnO-13 Pb_3O_4-10 Fe_2O_3-7 $PbCl_2$ (wt. %), molten salt mixture (1), under air atmosphere at 600, 700 and 800°C, utilizing OCP measurement, potentiodynamic polarization, EIS and weight-loss measurement techniques. Phase structure, morphology and chemical analysis of corrosion products and scales were characterized by means of XRD, SEM/EDX, and ICP/AAS.

6.1 Microstructural study

Optical and SEM photomicrographs in Figure 6-1 show the microstructure of the as-received wrought alloy 625. The mean grain size was 10.23 ± 2.63 μm. The chemical composition of the alloy can be seen in Table 6-1.

Table 6-1- Chemical composition (wt. %) of the as-received wrought alloy 625.

Ni	Cr	Mo	Fe	Nb	Ti	Sb	Zn	Al	C	S	Si	Mn	Zr
55.08	20.97	8.30	4.50	2.80	0.16	0.20	0.25	0.44	0.15	0.02	0.31	0.05	0.01

The alloy 625 exhibited the anisotropic microstructure including the annealed twin structures (Figures 6-1a, b) after solid-solution treatment and the micron-sized carbides, distributed along the inter/intra-granular areas (Figure 6-1c). EDX spectrum of the micron-sized carbides can be seen in Figure 6-1d. These carbides are rich in niobium and titanium. From a physical metallurgy point of view, alloy 625 consists of a continuous FCC austenitic matrix (gamma phase: γ) in which other phases reside, including Ni_3 (Al, Ti) intermetallic compound (gamma prime precipitate: γ′) and carbides [20, 21]. The

[1] A version of this section is published: E. Mohammadi Zahrani, A.M. Alfantazi, "Molten salt induced corrosion of Inconel 625 superalloy in $PbSO_4$-Pb_3O_4-$PbCl_2$-Fe_2O_3-ZnO environment", Corrosion Science, 65 (2012) 340-359.

gamma phase contains significant concentrations of chromium and molybdenum [22]. The gamma prime, which forms as a precipitate phase, often coherent with the γ-matrix, is rich in aluminum and titanium. Carbon, presents in the wrought alloy 625 at 0.15 wt. % (Table 6-1), combines with titanium and/or niobium to form the micron-sized carbides. These carbides can be mainly found in the γ-grain boundaries (Figure 6-1c, d). Inconel 625 is a solid solution alloy which is strengthened by precipitation of carbides such as MC, M_6C, and $M_{23}C_6$, as well as intermetallic phases such as the γ′ phase [14, 15].

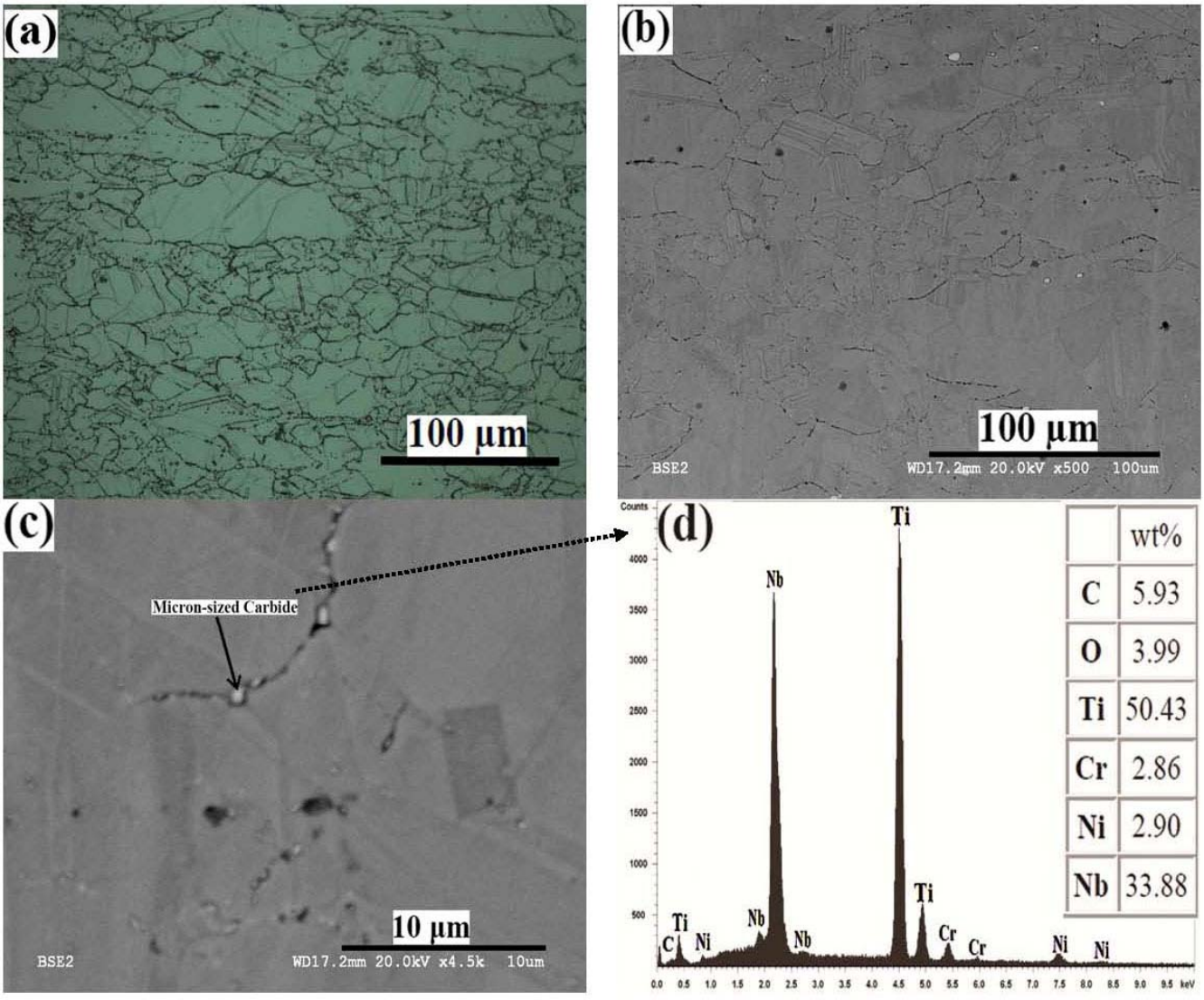

Figure 6-1- Optical photomicrograph at a) 500 times magnification, b) and c) SEM photomicrographs, which show the microstructure of the wrought alloy 625, as well as d) EDX spectrum of the micron-sized carbides.

6.2 DTA analysis

The DTA curve of the prepared salt mixture can be seen in Figure 6-2. A broad endothermic peak in the temperature range of 550 to 700°C is distinguishable in the curve. This broad endothermic peak was caused by the heat adsorption due to the formation of the molten phase. There are no other obvious peaks in the DTA curve. Accordingly, the formation of the molten phase occurred in the temperature range of 550-700°C. Also, the physical appearance and the visual monitoring of the salt mixture during the experiments at 600, 700 and 800°C confirmed the presence of the molten phase at all the investigated temperatures.

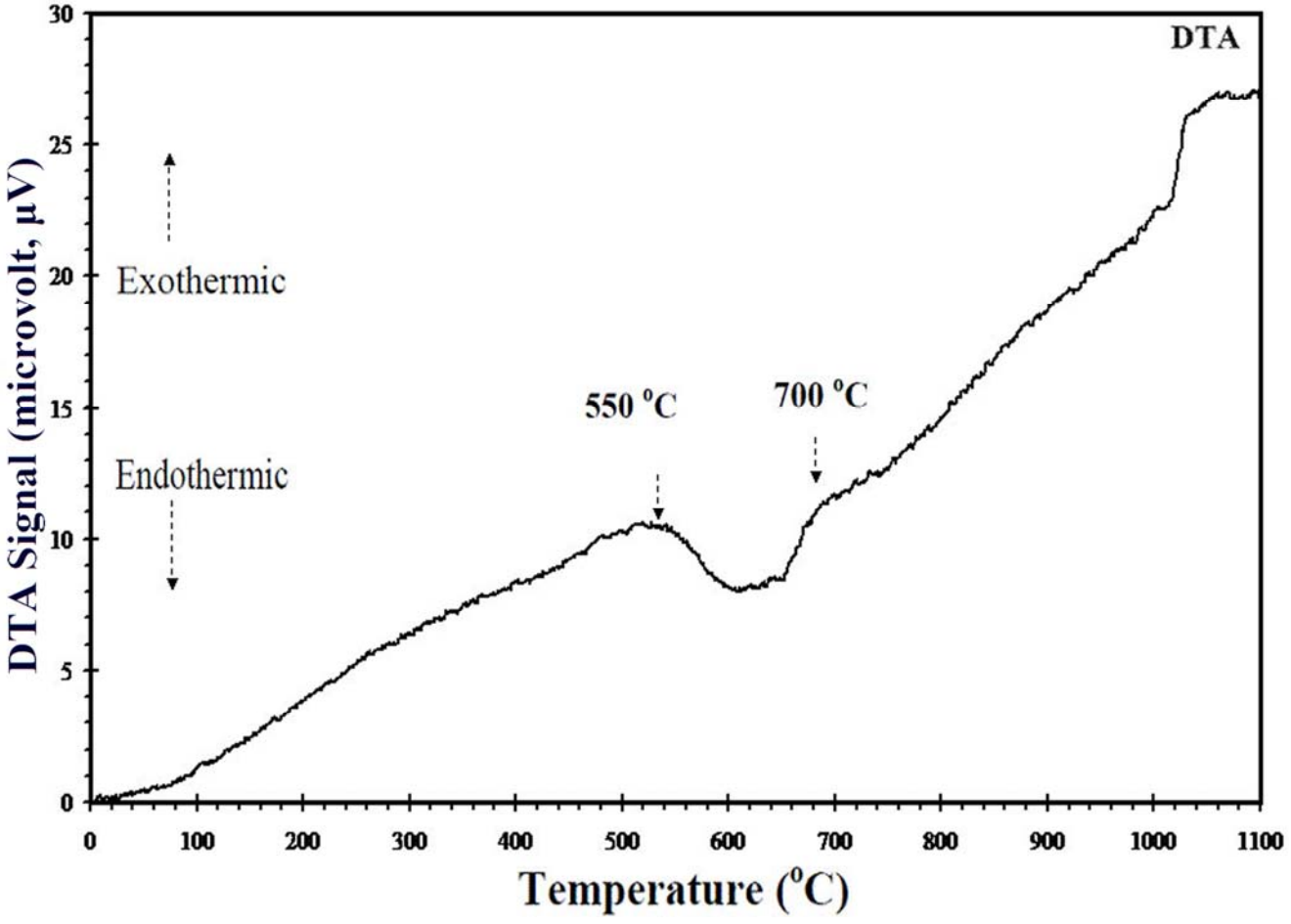

Figure 6-2- DTA curve of the as-prepared simulated salt mixture (1), 47 $PbSO_4$-23 ZnO-13 Pb_3O_4-10 Fe_2O_3-7 $PbCl_2$ (wt. %).

6.3 OCP measurements

OCP curves of the alloy 625 at 600, 700 and 800°C are presented in Figure 6-3. At the beginning of the exposure, potential of the electrode increased, and then reached a steady value. The time (t_s), which the electrode needed to reach the steady-state OCP and steady-state OCP of the electrode are mentioned in Figure 6-3.

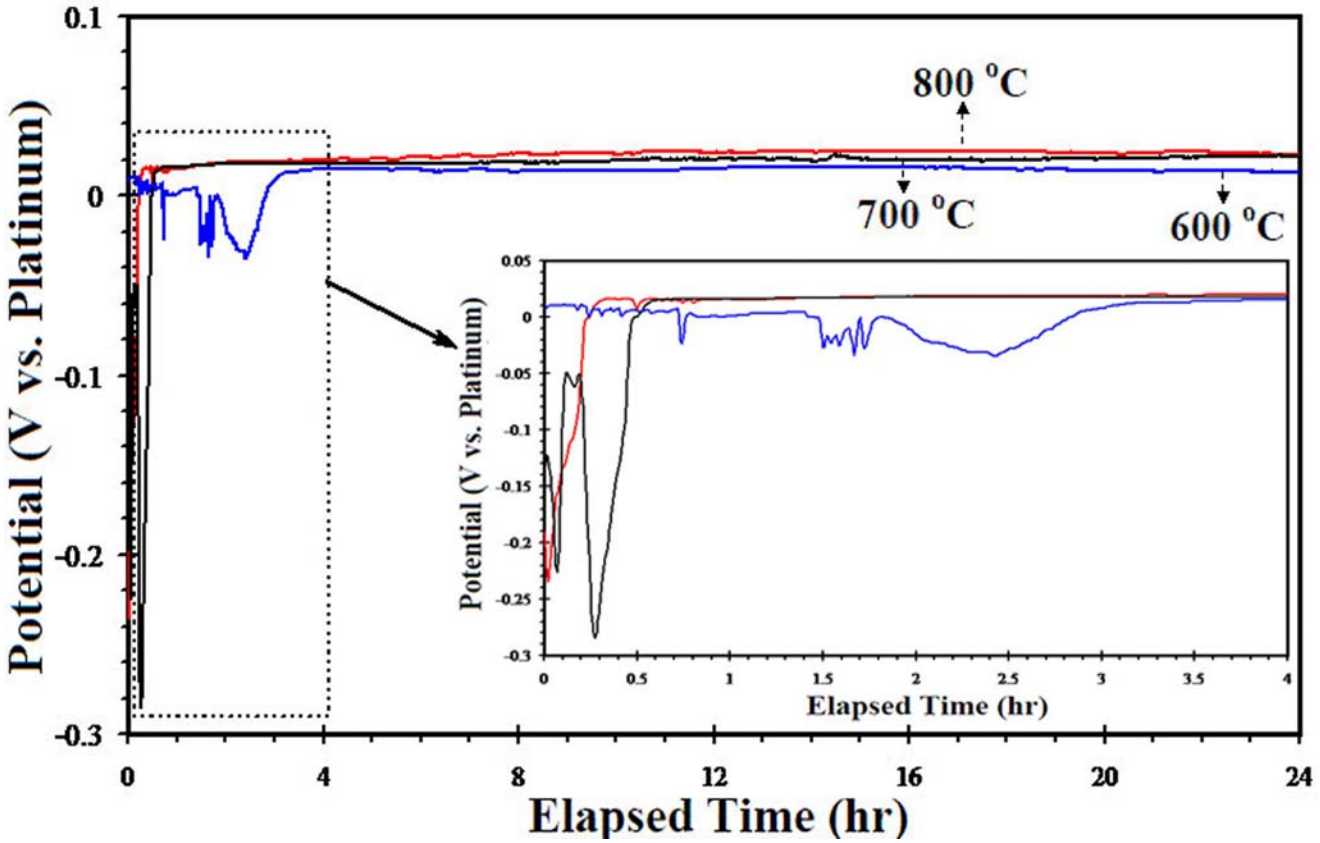

	800°C	700°C	600°C
OCP (mV vs. Platinum)	23.4	22.1	13.5
t_S (hr)	0.96	0.61	3.06

Figure 6-3- OCP of the alloy 625 electrode exposed to the molten salt mixture (1) at 600, 700 and 800°C, as well as the time (t_s) which the electrode needed to reach a steady-state OCP.

At 700 and 800°C, rapid increase in the potential of the electrode upon exposure to the molten salt is attributed to the spontaneous growth of an anodic film on surfaces of the electrode. The lowest t_s value

occurs at 700°C, which confirms the fastest growth rate of the anodic film at this temperature. Observed fluctuation in the OCP curves at the beginning of the exposure can be attributed to the unstable nature of the anodic film.

6.4 Potentiodynamic polarization study and weight-loss measurement

Figure 6-4 shows potentiodynamic polarization curves of the alloy 625, exposed to the molten salt mixture at 600, 700 and 800°C for 24 hr, when the OCP reached a stable value.

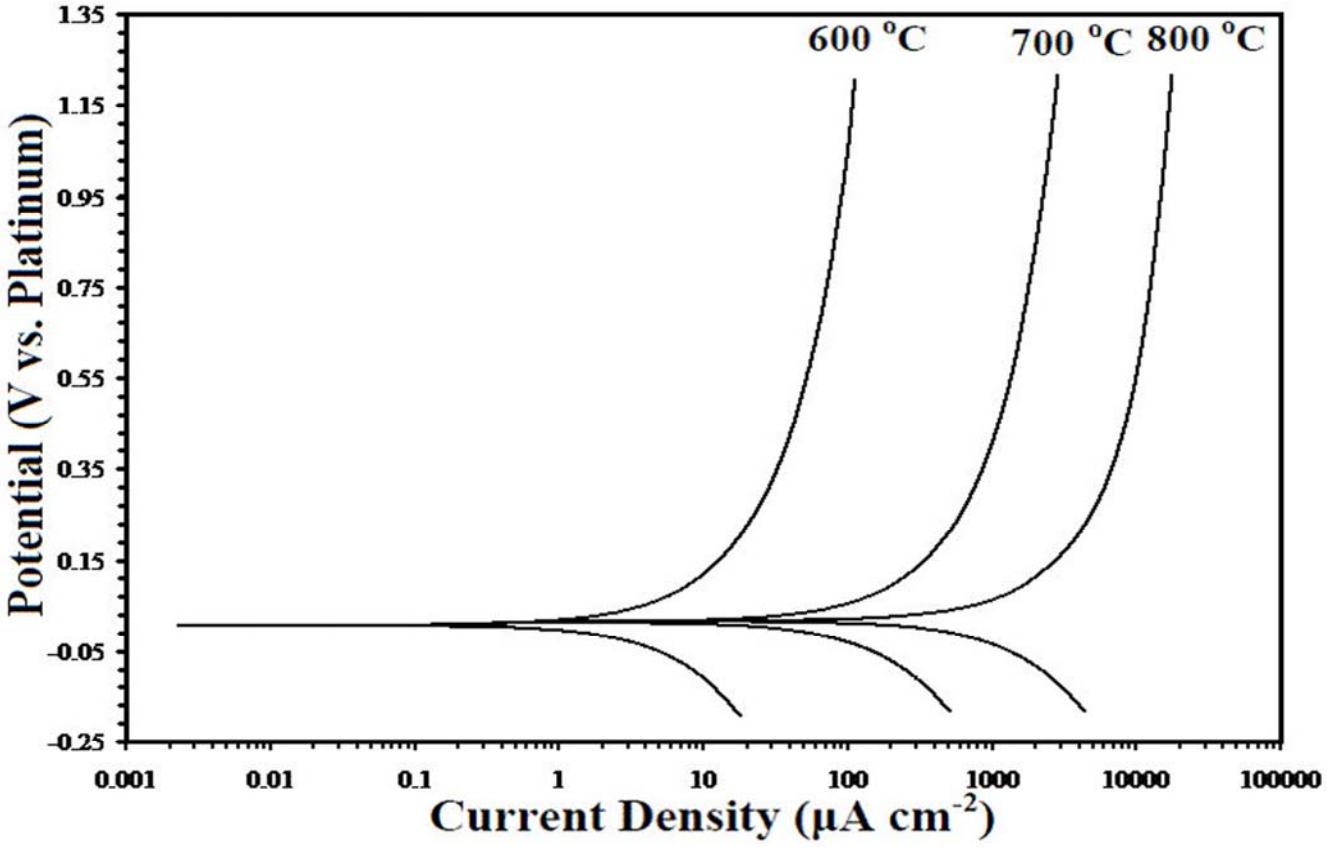

Figure 6-4- Potentiodynamic polarization curves of alloy 625, exposed to the molten salt mixture (1) at 600, 700 and 800°C for 24 hr.

For the polarization curves in Figure 6-4, it is not possible to apply the Tafel extrapolation technique to obtain the anodic and the cathodic Tafel slopes and the corrosion current density because a linear Tafel

region, almost a decade of linearity, cannot be observed in the polarization curves, even in the cathodic branch of the curves. Consequently, calculation of the electrochemically measured corrosion rate is not possible. Potentiodynamic polarization curves are very useful to determine some corrosion mechanisms: active dissolution, passivation and pitting potentials, to name just a few. The alloy 625 exhibited the active dissolution behavior at all the investigated temperatures. The potentiodynamic polarization curves in Figure 6-4 are similar to those reported by Martínez-Villafañe et al. [92] for SAE213-T22 steel exposed to 80% V_2O_5 -20% Na_2SO_4 molten salt mixture, Espinosa-Medina et al. for Fe-40Al-0.1B-10Al_2O_3 alloy exposed to $NaVO_3$ molten salt at 700°C [90] and Farrell and Stott [102]. Farrell and Stott explained that the shape of the curves is attributed to ohmic resistance of the molten salt. Despite the fact that molten salt is an ionic conductor, it can develop ohmic resistance due to dissolution of metal and metal oxides into the medium [102]. In the current study, the dissolution of the metal oxides into the molten salt medium was confirmed by XRD and ICP results (section 6.7).

Based on the results of the potentiodynamic polarization test and the OCP measurement, the alloy 625 has the capability to form the anodic film at all the investigated temperatures in the molten salt medium. Morphology as well as chemical and phase analysis of the anodic films will be extensively discussed in sections 6.5 and 6.7. At all the investigated temperatures, the anodic film is a non-protective layer/corrosion product film, which cannot provide an appropriate protection for the alloy against the corrosive medium. This is because the anodic current density increased rapidly when the potential shifted in the noble direction, exhibiting the active dissolution behavior. Obviously, passivation of the alloy did not occur because the current densities are too high at all the investigated temperatures. According to Figure 6-4, the potentiodynamic polarization curves show neither the passivation behavior nor a pitting potential, indicating that the alloy 625 is not susceptible to suffer from the pitting corrosion. Metal dissolution occurred by transport through a porous and non-protective oxide scale/anodic film. Formation of the non-protective porous anodic film was also confirmed by

SEM and EIS results which will be discussed in sections 6.5 and 6.6. Obtained corrosion potential (E_{corr}) from the potentiodynamic polarization curves and the calculated corrosion rate from equation (4-1), based on the weight-loss measurement technique, are presented in Table 6-2. By increasing the temperature, a rise in the mass fraction of the molten phase (Figure 6-2) and other factors, such as solubility of protective scale, caused the corrosion rate to increase.

Table 6-2- Corrosion potential obtained from the potentiodynamic polarization curves, and the calculated corrosion rate from equation (4-1) for the alloy 625 samples, exposed to the molten salt mixture (1) at 600, 700 and 800°C for 24 hr.

	800°C	700°C	600°C
E_{corr} (mV vs. Platium)	16	13.5	7
Corr. Rate (mm/year)	26.54 ± 1.69	14.25 ± 2.01	1.80 ± 0.33

6.5 SEM/EDX analysis

Figure 6-5 shows morphology of the alloy 625 surfaces immediately after the EIS test in as-tested condition (Figures 6-5a, c, e) and the attacked surfaces (Figures 6-5b, d, f), cleaned from the corrosion products and the scales. The cleaning procedure was based on the standard methodology presented in ASTM G1-03 [117]. It was necessary to clean the samples for observing the surfaces directly exposed to the molten salt medium. The corrosion products, a thick chromium-rich scale and lead-rich solidified salts can be seen in Figure 6-5 (a, c, e). Moreover, voids, a network of pores (internal attacked area) and intergranular attacked regions are clearly identifiable on the surface of the corroded alloy in Figure 6-5 (b, d, f). X-ray maps of oxygen, nickel, and chromium on the surface, as well as EDX elemental analysis (obtained through the cross-sectional SEM study), are presented in Figure 6-6 and Table 6-3, respectively, which show the elemental distribution, particularly for Cr, Ni, Nb, Mo, S and Cl, in the scale and the corroded surface of the alloy.

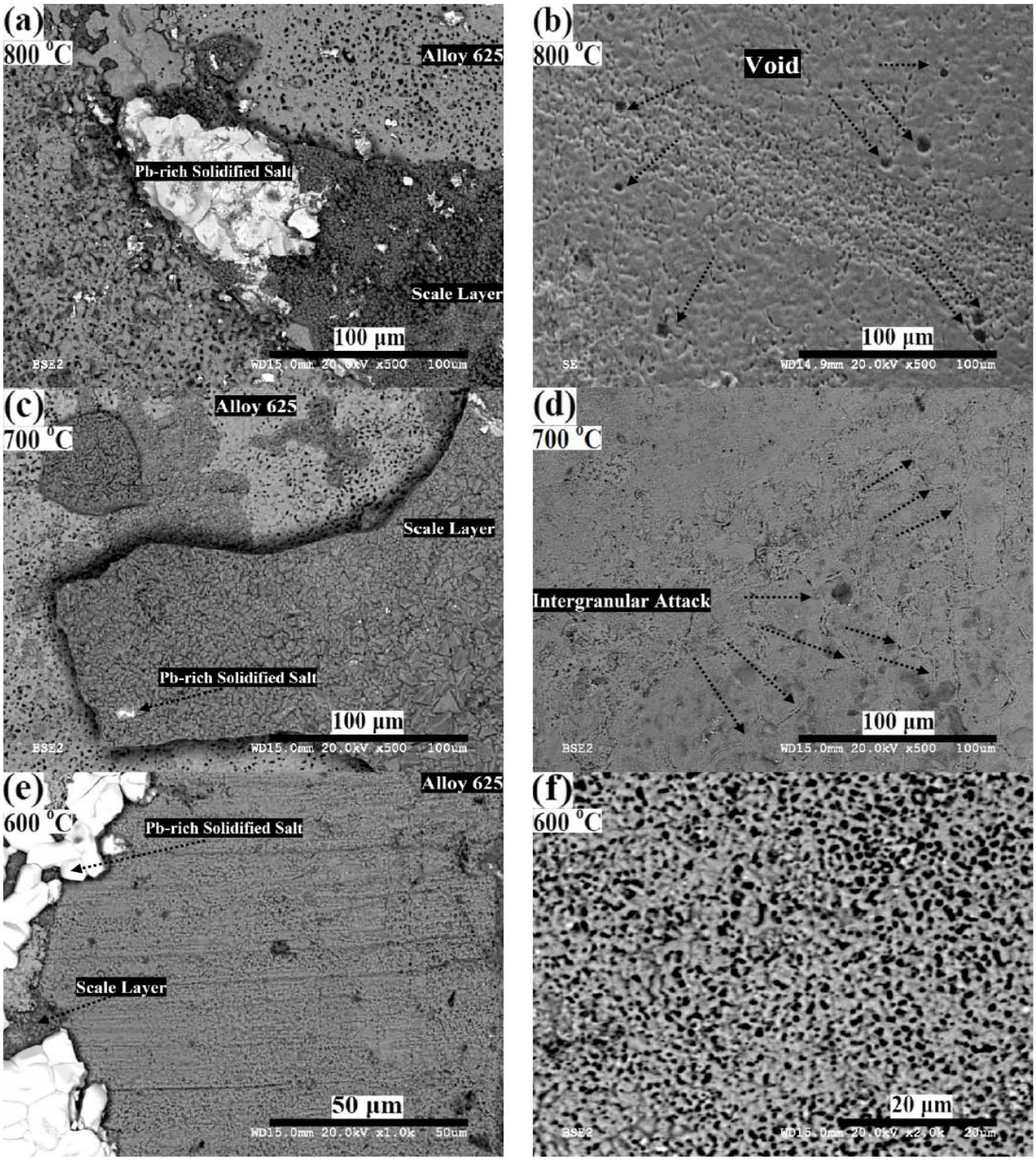

Figure 6-5- SEM photomicrographs of surfaces of the alloy 625 corroded specimens: a), c), and e) immediately after the EIS test, which show morphology of scales and corrosion products, b), d), and f) attacked surfaces after cleaning and removing the corrosion products and the scales according to ASTM G1-03.

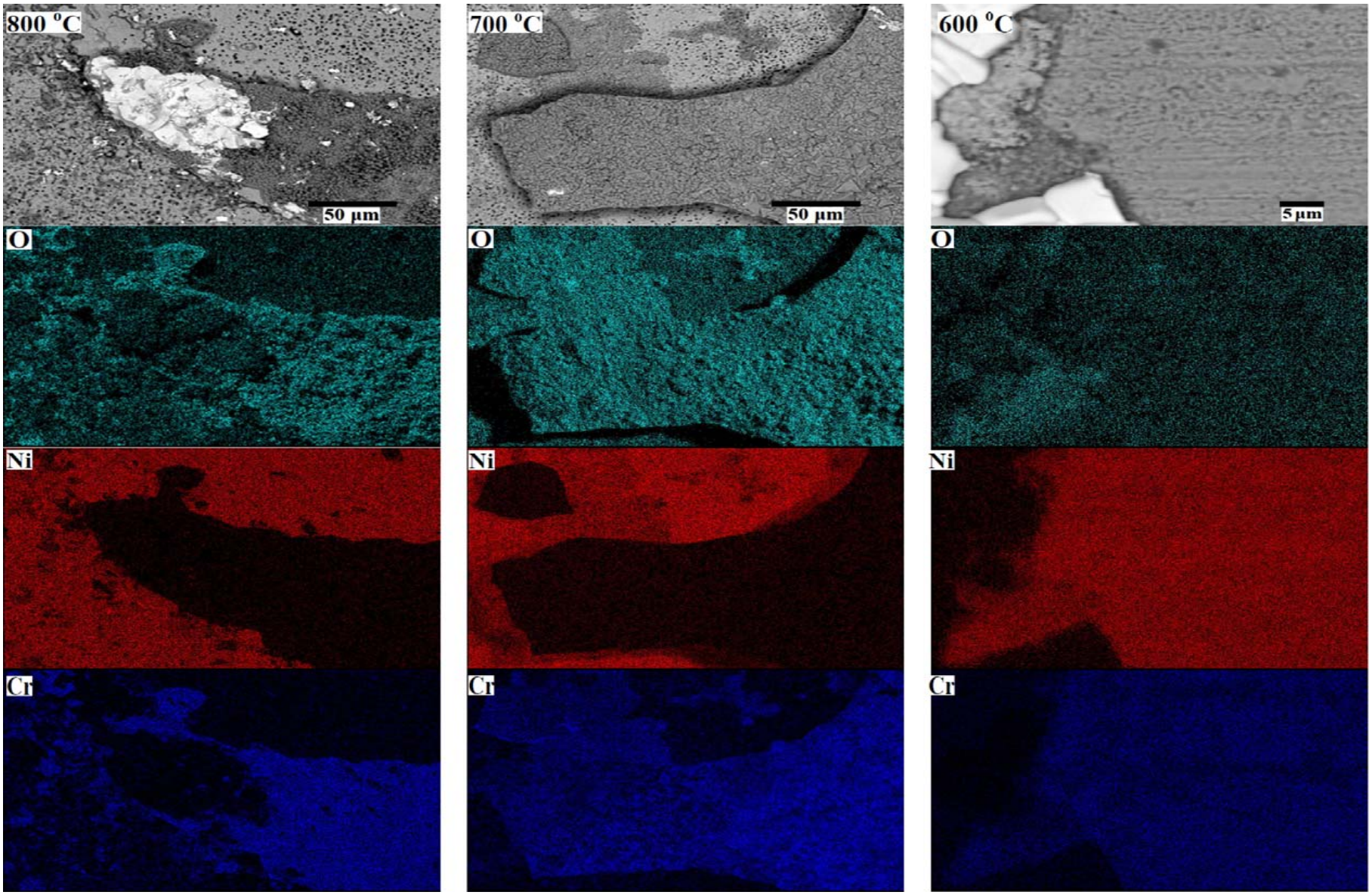

Figure 6-6- X-ray mapping of oxygen, nickel and chromium on attacked surface of alloy 625, exposed to the molten salt mixture (1) for 24 hr.

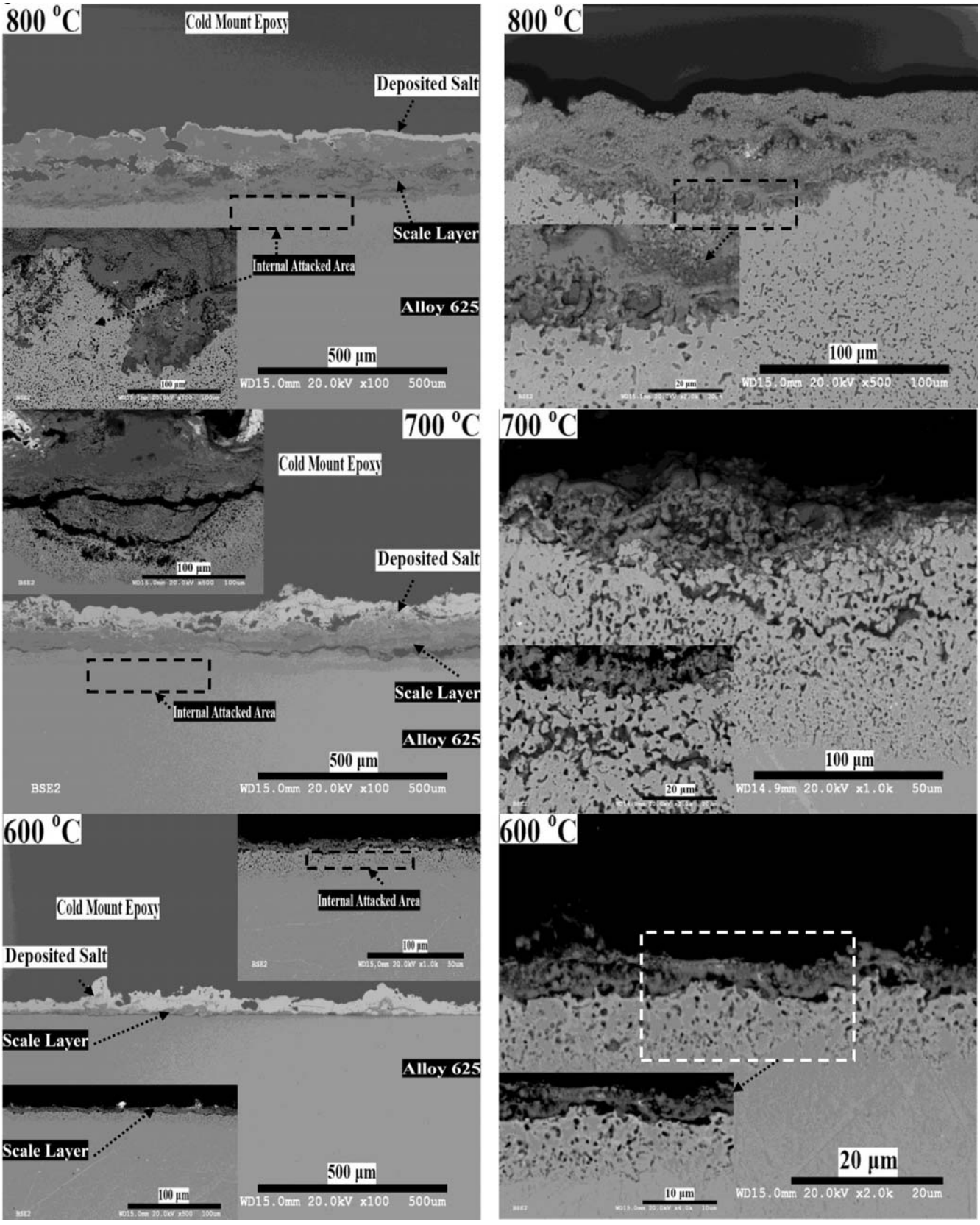

Figure 6-7- Cross-sectional SEM photomicrographs of the attacked alloy 625 samples, exposed to the molten salt mixture (1) for 24 hr.

According to the X-ray mapping results in Figure 6-6 and EDX elemental analysis in Table 6-3, the corrosion product layer (anodic film/scale) mainly consists of chromium, oxygen, and nickel and no molybdenum was detected. Phase analysis of the scale will be discussed in section 3.7. At 800 and 700°C, underneath the chromium-rich corrosion product layer, there is a chromium-depleted zone, which is shown by a well-defined film of nickel-rich compound (Figure 6-6) and it is also rich in oxygen. It confirms that the growth of the chromium-rich external scale was accompanied by the depletion of chromium within the subsurface region of the alloy. In the chromium-depleted zone, underneath the chromium-rich corrosion product layer, the concentration of chromium significantly decreases to 3.5 wt.%, 9.5 wt.% and 11.5 wt.% for 800, 700 and 600°C, respectively, which are considerably lower than the concentration of chromium in the wrought alloy 625 (the chromium content of the alloy 625: 20.97 wt.%, reported in Table 6-1). Accordingly, chromium is very prone to dissolution during the exposure of the alloy 625 to the molten salt (initiation stage) and the chromium-rich scale forms on the surface of the alloy (propagation stage).

The concentration of chromium is almost the same as the original composition of the alloy 625 underneath the chromium-depleted zone but the grain boundaries are rich in sulfur and oxygen in this region, which is shown in Figure 6-9 (c, d). It should be noted that chromium is the most important alloying element, protecting the wrought alloy 625 against corrosive environments at ambient temperature through the formation of the protective chromium-nickel oxide, $Ni(Cr_2O_4)$, and Cr_2O_3 layers as was confirmed by the XRD data (Figure 6-12a).

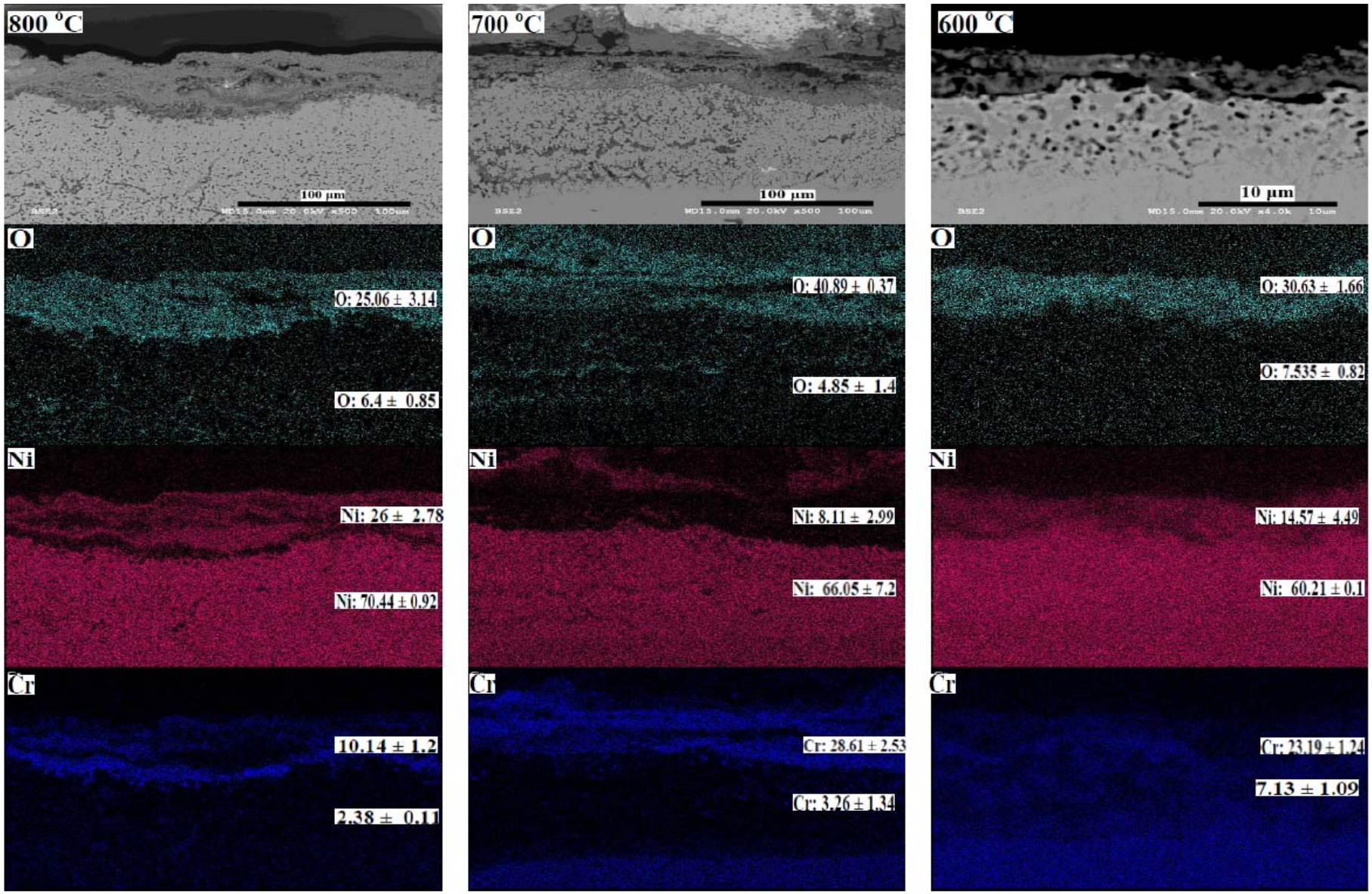

Figure 6-8- X-ray mapping of oxygen, nickel and chromium on the cross section of the attacked alloy 625 samples, exposed to the molten salt mixture (1) for 24 hr, and EDX elemental analysis of nickel, chromium and oxygen in chromium- and nickel-rich layers.

SEM photomicrographs from the cross section of the attacked alloy 625 immediately after the EIS test, can be seen in Figure 6-7 at different magnifications. Also, Figure 6-8 illustrates X-ray maps of oxygen, nickel, and chromium on the cross section of the attacked alloy, as well as EDX elemental analysis of chromium, nickel, and oxygen in nickel- and chromium-rich layers. Based on the cross-sectional SEM images, mean thickness of the scale at 600, 700 and 800°C was equal to 5.6 ± 2.3 μm, 48.1 ± 14.3 μm and 72.2 ± 20.2 μm, respectively. Upon increasing the temperature, the thickness of the oxide layers and of the chromium-depleted zone rose. The porous and non-protective nature of the chromium-rich layer/scale is obvious in Figures 6-7 and 6-8. Based on the SEM results in Figures 6-5 (b, d and f) and 6-7, general surface corrosion, intergranular corrosion, formation of voids and a network of distributed pores on the surface and the cross section, as well as internal oxidation (Figure 6-8) and internal sulfidation (Figure 6-9) were identified as different modes of corrosion attack. The high concentration of sulfur and oxygen in the grain boundaries are to blame for the occurrence of the intergranular corrosion together with the internal attack. Montgomery et al. [80] reported severe pitting and interdendritic (similar to the intergranular attack in the wrought alloy 625) corrosion of weld overlay alloy 625 at relatively low temperature of 300°C in waste incinerator and biomass plants because of high presence of heavy metals together with chlorine; it was deduced that chloride and sulfates presented as heavy metal salts in melt or semi-melt phases, were responsible for pitting and interdendritic corrosion [80].

The chromium-rich corrosion product layer, which is highly porous and detached from the substrate particularly at 700 and 800°C, shows the possible diffusion paths for the aggressive species (sulfur and oxygen) of the molten salt to reach the surface of the alloy and diffuse inward mainly through the grain boundaries. This is likely the main cause for the intergranular corrosion and the formation of the sulfur-oxygen rich regions (internal oxidation and sulfidation attack) in the internal attacked areas, as can be seen in Figure 6-9.

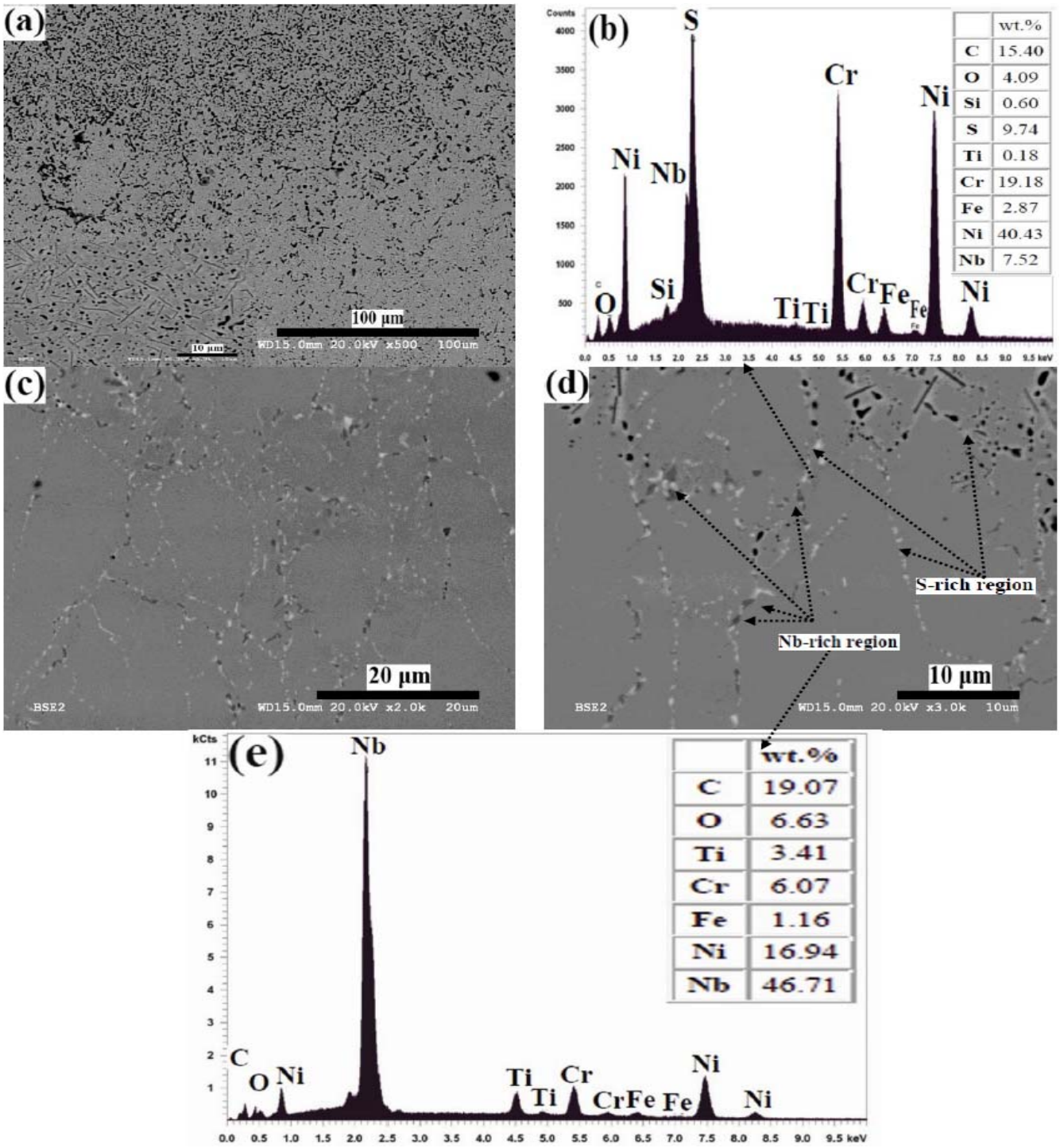

Figure 6-9- SEM photomicrographs of the alloy 625 cross section, exposed to the molten salt mixture (1) for 24 hr at 800^{o}C which show a) intergranular nature of the oxidation in the internal attacked areas, c) and d) sulfur/niobium-rich grain boundaries underneath the chromium-depleted zone as well as b) EDX spectrum of the white regions, and e) EDX spectrum of the niobium-rich regions in the grain boundaries.

Figure 6-8 confirms the selective oxidation of chromium in the internal attacked areas particularly at 700 and 800°C. In fact, because of the non-protective and porous nature of the chromium-rich scale, the corrosive species diffused towards the alloy surface during the exposure of the alloy to the molten salt, and it caused the intergranular corrosion process, which is exhibited in the internal attacked areas in Figure 6-9, followed by the pores formation. The intergranular nature of the internal attacked area can be clearly observed in Figure 6-9 (a, c, d).

At the areas close to the interface of the alloy and the molten salt in the chromium-depleted zone, in addition to the intergranular attack, formation of the pores inside the grains is also evident (Figure 6-9a). When the grain boundaries become rich in oxygen and sulfur at these areas, oxygen and sulfur diffuse into the grains; as a result, the internal attacked areas developed inside the grains. However, in Figures 6-9c and 6-9d which belong to the areas located far enough from the surface of the alloy (underneath the chromium-depleted zone), the grains boundaries are rich in sulfur and oxygen, and the pores are at the early stage of development, initiating from the grain boundaries. Based on the EDX spectrum in Figure 6-9b, the amount of chromium in the sulfur-oxygen rich grain boundaries is very close to the chromium concentration in the wrought alloy 625 because these regions are located underneath the chromium-depleted zone and the depletion of chromium did not occur in this area. The fact of the matter is that the inward diffusion of oxygen and sulfur through the grain boundaries from the interface of the alloy and the molten salt is faster than the outward diffusion of chromium from the alloy, which caused the formation of the chromium-depleted zone and the development of the chromium-rich layer on the surface. For this reason, the diffusion depth of sulfur and oxygen through the grain boundaries is higher than the thickness of the chromium-depleted zone. As a result, underneath the chromium-depleted zone, there is an area with the chromium concentration very close to the chemical composition of the wrought alloy 625 but the grain boundaries are rich in sulfur and oxygen in this area. In Figure 6-9d, a few pores in the range of 70-200 nm in size, are shown at their

early stage of formation. Moreover, the EDX analysis confirmed the presence of the niobium-rich regions in the grain boundaries, which contain 46.71 wt. % of niobium (Figure 6-9e). The presence of the niobium-rich zones confirmed the tendency of niobium for migration to the grain boundaries from the bulk of the alloy during the internal oxidation/sulfidation phenomena. The migration of the niobium to the grain boundaries causes the galvanic effect between the niobium-rich zones in the grain boundaries region and the grain core, which can accelerate the formation of the pores.

With regard to the occurrence of the internal oxidation, when chromium is selectively oxidized, particularly in the grain boundaries which act as the fast diffusion paths for the oxygen and sulfur diffusion, but cannot reach the surface quickly enough to develop a scale, the internal oxidation occurs. Initiation of the internal attack begins from the grain boundaries because activation energy for grain boundary diffusion is generally only about half that for volume diffusion [140]. Furthermore, it has been clearly established that alloy grain boundaries act as preferential paths for sulfur diffusion over a wide range of temperature leading to precipitation of sulfide in intergranular regions and consequently occurrence of internal sulfidation [141]. According to the SEM results, the internal oxidation of chromium and the external scaling occurred. Obviously, with increasing the temperature, the depth of the chromium-depleted zones and the thickness of the internal attacked area increased due to the kinetic effect (Figure 6-8). In WTE boiler environments, when the molten phase contained chlorine and sulfur, corrosion products of alloy 625 had lamellar structures and occurrence of oxidation, sulfidation, and chlorination was confirmed at the alloy/scale interface under a low partial pressure (P) of oxygen (P_{O2})-high P_{Cl2} condition [83]. Reportedly, a significant percentage of high-temperature corrosion failure involves internal oxidation [139]. The internally precipitated reaction products cause embrittlement and dilation of alloy subsurface region, which can cause affected zone to flake off. Because the process is supported by diffusion of interstitial species (for example dissolved oxygen in the current study), it is rapid and the internal oxidation is known as a very destructive process in industrial applications [139].

Table 6-3- EDX elemental analysis (wt. %) from the attacked surface of the alloy 625 corroded samples, exposed to the molten salt mixture (1) for 24 hr.

	Attacked Surface of Alloy 625			Outer Surface of Scale		
	800°C	700°C	600°C	800°C	700°C	600°C
Ni	54.80 ± 1.46	54.48 ± 3.28	59.11 ± 0.2	19.67 ± 3.53	7.42 ± 0.73	20.49 ± 2.41
Cr	3.55 ± 0.81	9.57 ± 2.2	11.56 ± 0.69	14.22 ± 1.08	43.69 ± 1.91	24.18 ± 1.70
Mo	8.37 ± 1.04	8.6 ± 0.63	8.6 ± 0.41	ND	ND	ND
Nb	2.24 ± 0.32	0.54 ± 0.16	1.24 ± 0.13	1.09 ± 0.17	2.76 ± 0.03	2.24 ± 0.24
Ti	0.1 ± 0.01	0.11 ± 0.03	0.09 ± 0.02	0.15 ± 0.01	0.34 ± 0.01	0.33 ± 0.06
O	17.83 ± 1.39	16.41 ± 4.32	10.3 ± 0.45	32.6 ± 4.68	31.06 + 0.64	28.70 ± 1.00
Fe	2.98 ± 0.26	1.07 ± 0.47	2.58 ± 0.16	3.3 ± 0.54	0.19 ± 0.01	10.1 ± 0.71
Al	0.1 ± 0.01	0.1 ± 0.02	0.1	0.89 ± 0.20	0.22 ± 0.08	0.6 ± 0.24
Si	0.25 ± 0.05	0.37 ± 0.08	0.3 ± 0.04	3.68 ± 0.35	0.42 ± 0.13	0.89 ± 0.1
Cl	0.15 ± 0.03	1.16 ± 0.1	0.12 ± 0.04	ND	0.11 ± 0.1	0.14 ± 0.03
S	ND	ND	ND	0.33 ± 0.06	3.86 ± 1.06	0.85 ± 0.20
Zn	ND	ND	ND	13.84 ± 2.84	ND	4.95 ± 0.21
Pb	ND	ND	ND	2.05 ± 1.1	ND	1.37 ± 0.17
C	8.67 ± 0.38	7.48 ± 1.97	6.05 ± 0.75	8.3 ± 0.4	5.39 ± 0.28	4.41 ± 0.23

(ND: Not Detected)

During the initiation stage of hot corrosion, alloy and deposit face with some changes including: 1) depletion of elements which are responsible for formation of protective scale on the alloy's surface (mainly chromium in alloy 625), 2) incorporation of sulfur from deposit into the alloy and, 3) dissolution of oxides into the salt and development of cracks or channels into the scale. These are to blame for making the alloy susceptible to rapid corrosion attack and degradation at the second stage of hot corrosion (propagation stage). Local penetration of the molten salt through the scale and subsequent spreading along the scale/alloy interface can occur at the end of the initiation stage. As a result, the molten salt can reach the sites with low oxygen activity and chromium-depletion when alloy is a nickel-based superalloy containing high percentage of chromium, facilitating a rapid propagation stage. At the initiation stage of hot corrosion, oxidation of alloying elements, mainly chromium, nickel, and niobium in the current study (Table 6-3), causes the electron transfer from the metallic atoms to the medium. By starting the second stage of hot corrosion (propagation stage), protective nature of oxide

scales drastically alters because the oxide scales become porous and non-protective and subsequently the alloy experiences a rapid corrosion [63, 66-68, 70].

6.6 EIS study

The impedance behavior of the alloy 625 electrode including the measured and the calculated Nyquist plots plus the Bode diagrams of the phase angle and the total impedance magnitude at 600, 700 and 800°C, are presented in Figure 6-10. Considering the extensive discussion in section 6.5 on the surface and the cross-sectional properties of the alloy 625 after 24 hr exposure to the molten salt medium, the EIS data were fit into two equivalent circuits, representing a porous and non-protective scale model. The model parameters for the equivalent circuits can be seen in Figure 6-11. The Nyquist diagrams show two depressed capacitive loops, including a loop at high frequency, relatively large at 700 and 600°C, and a loop at low frequency range, relatively large at 800°C. The capacitive loop, which is related to the dielectric properties of the chromium-rich scale, located at 50 kHz - 1.15 mHz, 4340 Hz - 39.2 mHz, and 50 kHz - 832 mHz frequency range at 600, 700 and 800°C, respectively. Based on the presented model parameters for the equivalent circuits in Figure 6-11, the charge transfer resistance of the outer chromium-rich barrier layer (R_{sl}) is relatively low at 700 and 800°C. Consequently, the barrier layer did not act as an effective protective layer, as was confirmed by the SEM, and the weight-loss measurement results. In fact, the barrier layer can be considered as a corrosion product, not an effective protective layer. In the Nyquist plots of Figure 6-10, the values of both real and imaginary impedance rose with decreasing the temperature to 600°C, resulting in an increase in the impedance modulus and the radius of the capacitive loop.

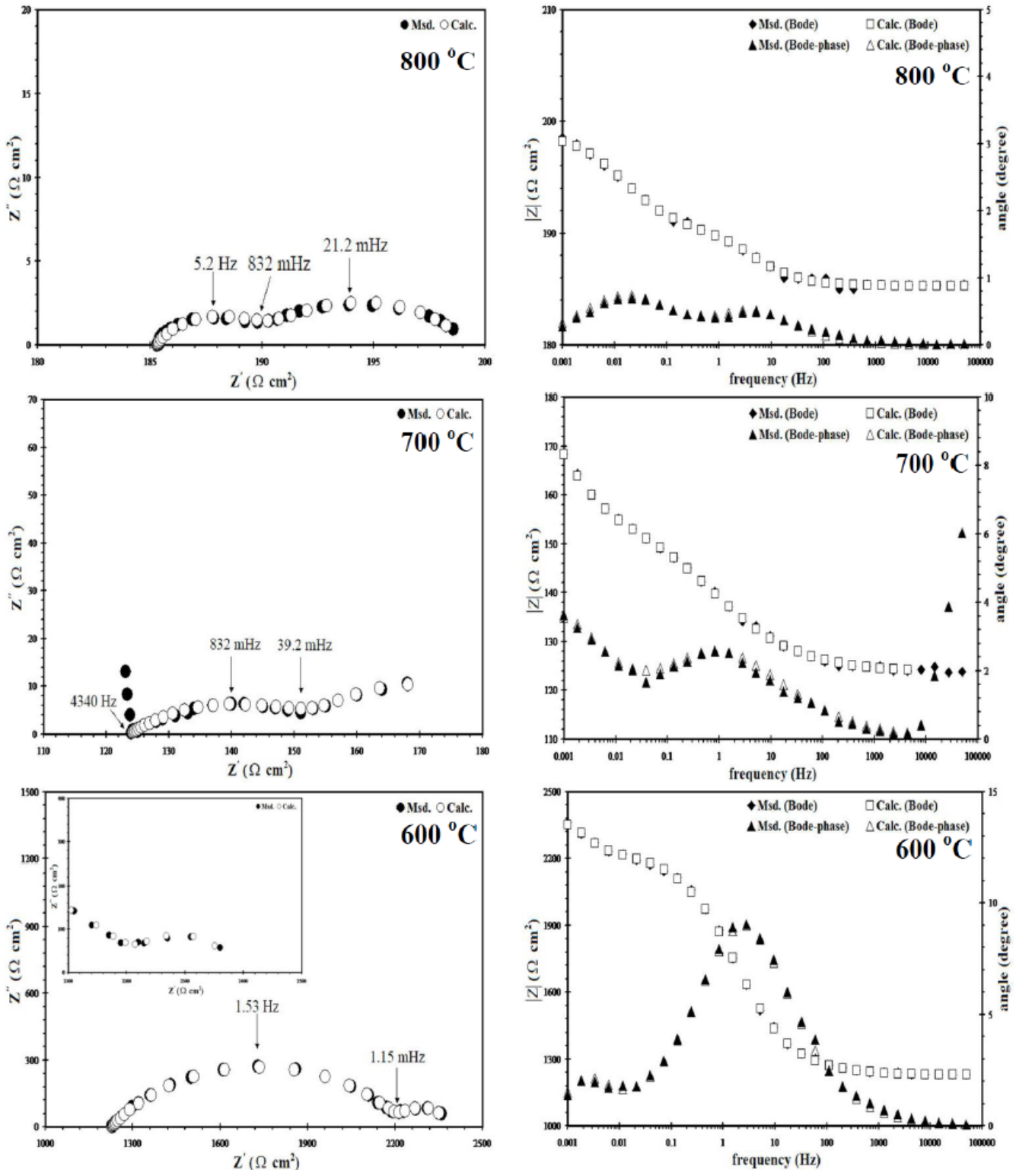

Figure 6-10- Electrochemical impedance spectroscopy (EIS) Nyquist plots response plus Bode diagrams of phase angle and total impedance magnitude for the alloy 625, exposed to the molten salt mixture (1) for 24 hr.

At 600 and 700°C, the corresponding curves of the phase angle vs. frequency have one relatively symmetrical maximum at 1.53 Hz and 832 mHz, respectively. Also, a shoulder, which has a maximum at 5.2 Hz, is identifiable in the phase angle vs. frequency curve of 800°C. These relaxation processes are related to the growth of the porous scale. According to the suggested equivalent circuits, the capacitive loop at higher frequencies (600°C: 50 kHz - 1.15 mHz; 700°C: 4340 Hz - 39.2 mHz; and 800°C: 50 kHz - 832 mHz) is attributed to the dielectric properties of the scale, formed on the electrode surface from which the chromium-rich layer resistance value ($R_{sl:}$ transfer resistance of ions in the scale) is determined. Q_{dl} and R_{dl} represent the double-layer capacitance and the charge transfer resistance along the pores in the porous scale. Also, Q_{sl} (C_{sl} at 600°C) is the representation of the capacitive behavior of the scale. Constant phase element (CPE) is utilized to account for non-uniform current distribution from the pure capacitive behavior and the deviation due to surface inconsistencies. By increasing the temperature from 600°C to 700 and 800°C, the value of R_s (solution resistance between the working and the reference electrode) decreased because viscosity of the molten salt reduced as a result of an increase in the temperature, while the mass fraction of the molten phase increased, simultaneously, based on the DTA curve in Figure 6-2. These two factors enhanced the diffusion of the aggressive species from the molten medium toward the interface of the molten phase/electrode surface and subsequently accelerated the corrosion of the alloy. A straight line, slope smaller than -1 at high frequency range of 50 KHz to 4340 Hz, is distinguishable in the Bode diagram at 700°C. This feature is related to frequency dispersion and can be attributed to solid surface inhomogeneities [142]. At all the investigated temperatures, the phase angle maxima were much smaller than 90 degrees. Carranza and Alvarez explained that surface roughness, frequency dispersion of time constants due to local inhomogeneities in dielectric material, porosity mass transport effects and relaxation effects are some reasons of this phenomenon [143]. In the current study, the main reasons for having phase angles much smaller than 90° are the porosity mass transport effects and the frequency dispersion of the time constants due to local inhomogeneities in the dielectric material.

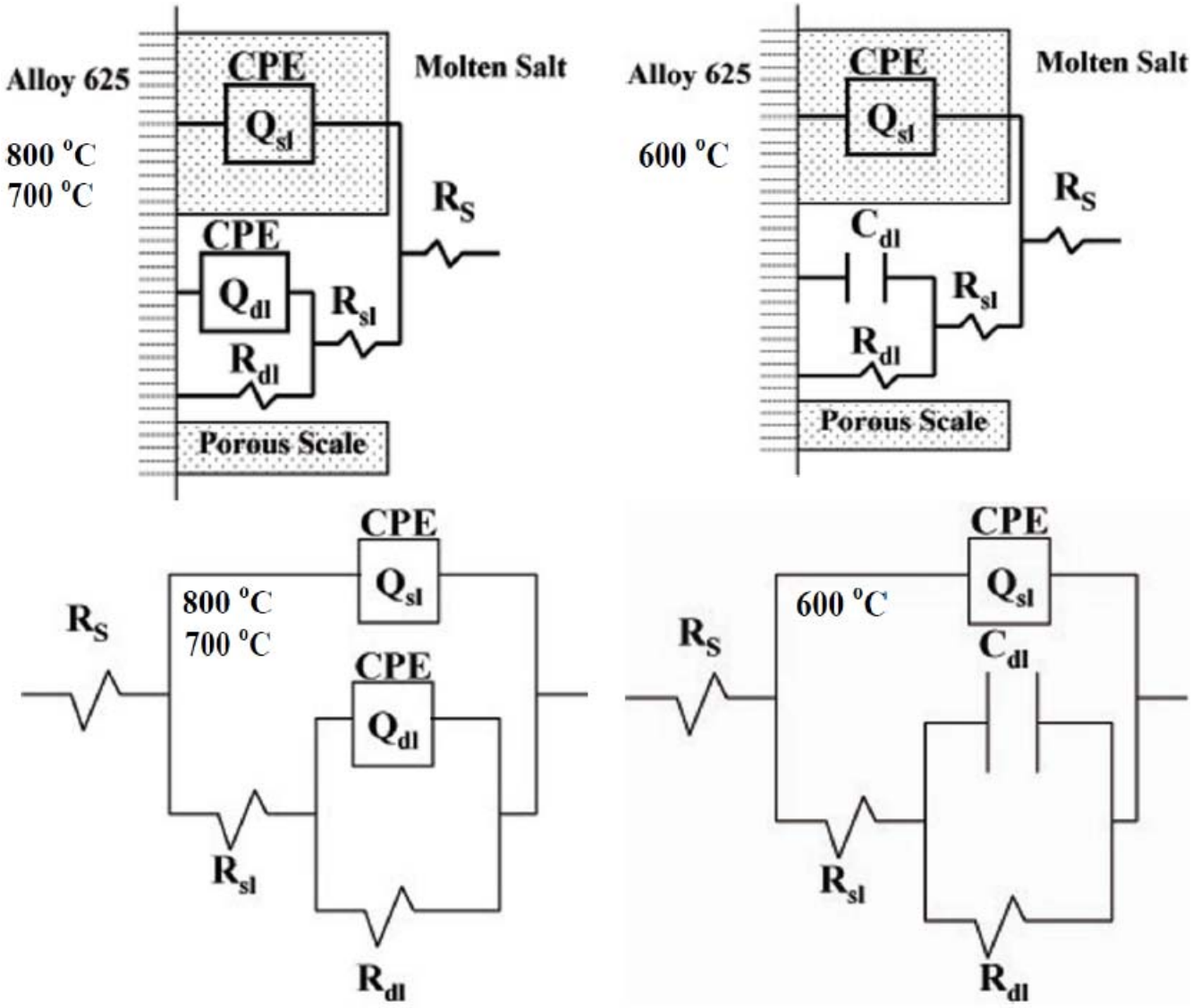

Parameter / Temperature	R_s (Ω cm^2)	R_{sl} (Ω cm^2)	Q_{sl}-Yo (S sec^n cm^{-2})	Q_{sl}-n	R_{dl} (Ω cm^2)	Q_{dl}-Yo (S sec^n cm^{-2})	Q_{dl}-n	$\chi^2 \times 10^{-6}$
800 °C	185.3	5.17	1.68×10^{-2}	0.71	8.80	0.49	0.62	2.13
700 °C	123.8	32.43	1.48×10^{-2}	0.46	32.74	1.07	0.67	13.31

Parameter / Temperature	R_s (Ω cm^2)	R_{sl} (Ω cm^2)	Q_{sl}-Yo $10^2 \times$ (S sec^n cm^{-2})	Q_{sl}-n	R_{dl} (Ω cm^2)	C_{dl} (F cm^{-2})	$\chi^2 \times 10^{-6}$
600 °C	1229	1011	2.43×10^{-2}	0.62	141.9	0.48	17.02

Figure 6-11- Equivalent electrochemical circuits (porous and non-protective scale model) plus the model's parameters of the equivalent circuits for the alloy 625, exposed to the molten salt mixture (1) for 24 hr.

It looks that the latter is due to the inhomogeneous nature of the molten salt mixture. As a result, a constant phase element (CPE) was introduced into the equivalent circuits, proposed to reproduce the results, to account for these effects. Beverskog et al. mentioned that the number of distinguishable maxima or related shoulders was an indication of the minimum number of relaxation processes (time constants) that occurred in electrochemical system, which were detectable thorough EIS [144]. A porous scale model was suggested by Perez et al. [81] to explain the corrosion of alloy 625 beneath molten $ZnCl_2$-KCl mixture at 650°C after 100 hr exposure. In this case, corrosion mechanism was controlled by diffusion of aggressive ions through alloy/melt interface and EIS profiles were fit to a protective scale model before 100 hr exposure [23, 81].

6.7 XRD analysis

After exposing the alloy to the molten salt for 24hr, the surfaces of the samples were covered by a thick layer of corrosion products (Figures 6-5 and 6-7) and the scales. In order to identify these corrosion products and the scales, formed on the surface of the alloy after the EIS test, the surfaces of the corroded specimens were studied by XRD technique. The XRD patterns of the as-received alloy 625 surface and the initial salts, in comparison with the prepared simulated salt mixture, are presented in Figure 6-12 (a, b). The XRD patterns of the attacked surface of the specimens, in comparison with the standard XRD patterns (JCPDS file) of the major identified phases, at 800, 700 and 600°C (after the EIS test) can be seen in Figures 6-13, 6-14 and 6-15, respectively. Also, list of the corrosion products extracted from the XRD patterns in Figures 6-13, 6-14, and 6-15, is presented in Table 6-4. In order to identify the observed peaks in the XRD patterns, the obtained XRD patterns compared with the standard JCPDS cards of almost 9000 phases, which were selected based on the available elements in the molten salt/alloy system. Figure 6-12a confirms that the protective layer of the wrought alloy 625 consists of $Ni(Cr_2O_4)$ (JCPDS # 01-089-6615) and Cr_2O_3 (JCPDS # 01-04-0315) phases at ambient temperature.

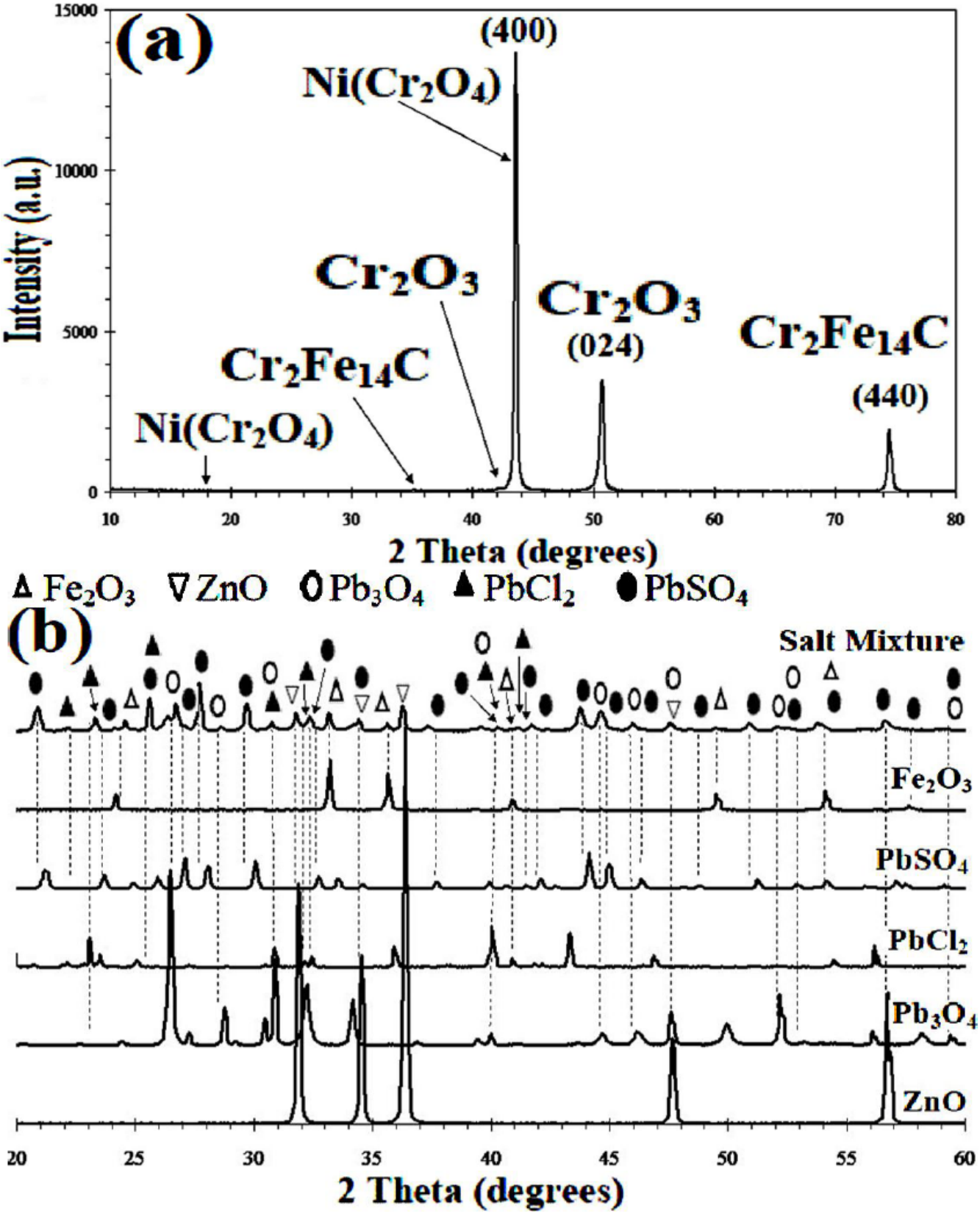

Figure 6-12- X-ray diffraction (XRD) patterns of a) surface of the as-received wrought alloy 625 after polishing, and b) the initial salts and the prepared simulated salt mixture (1).

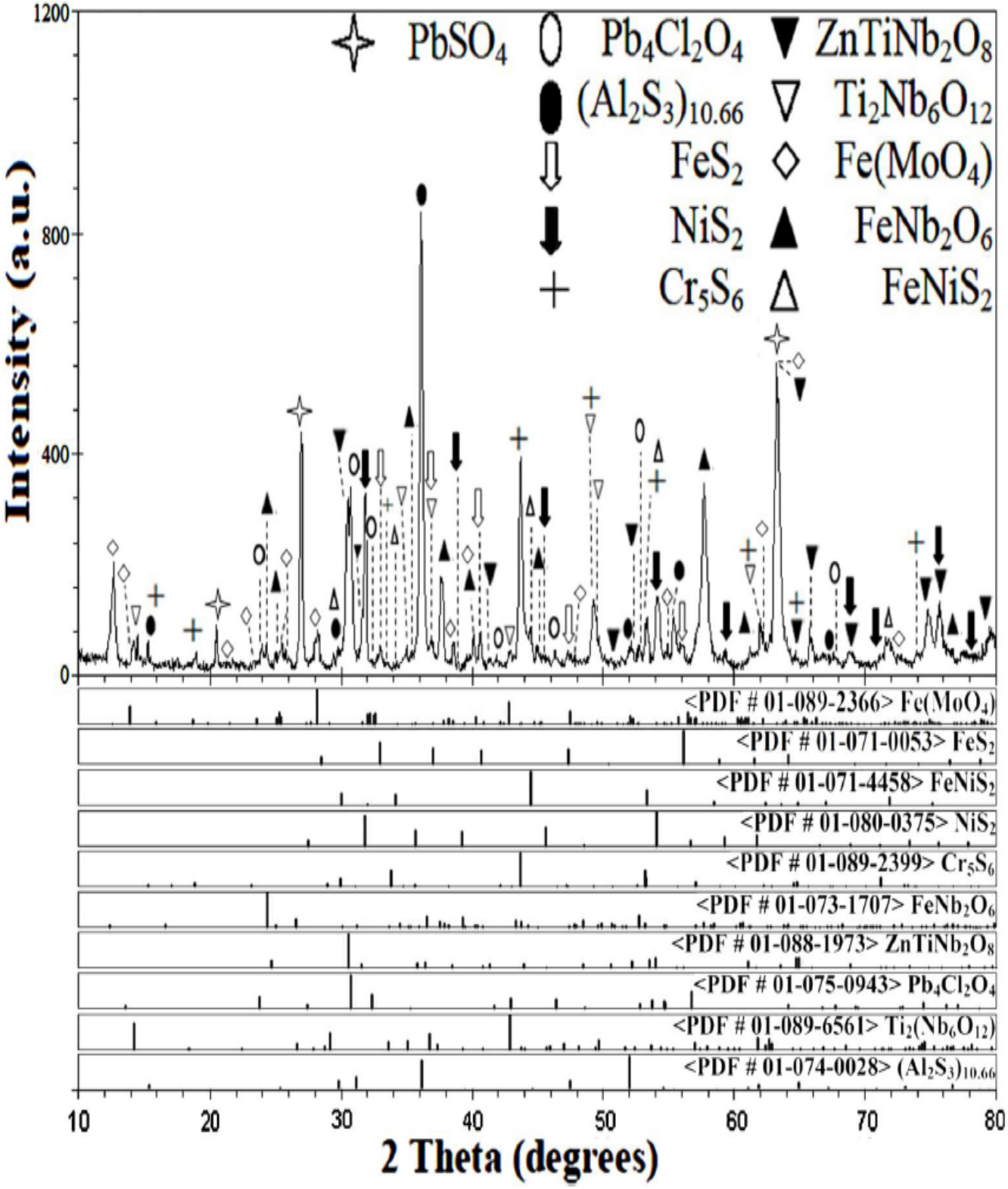

Figure 6-13- X-ray diffraction (XRD) pattern of attacked surface of the alloy 625 after the EIS test at 800°C in comparison with the standard XRD patterns of the identified components, compiled by JCPDS.

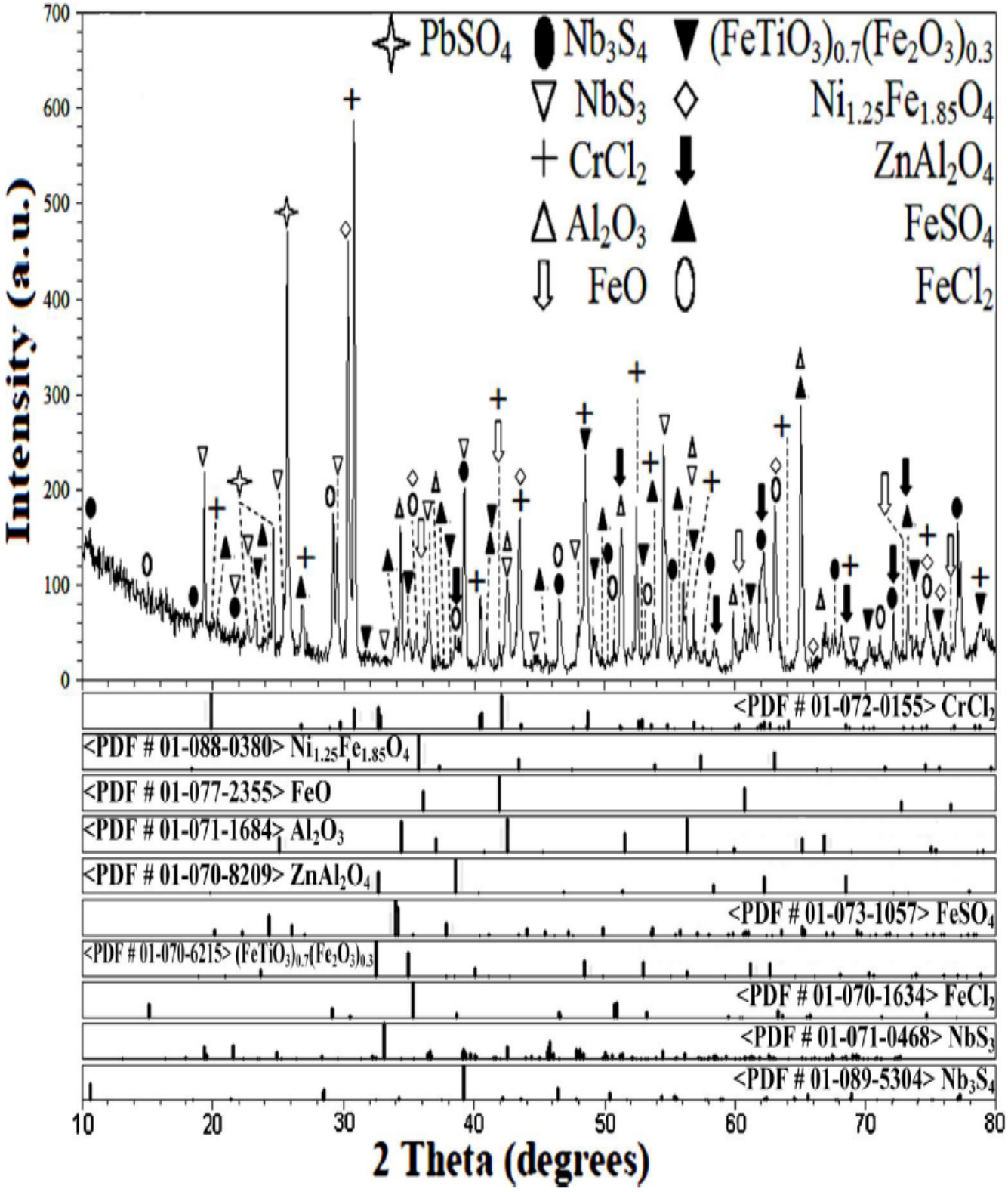

Figure 6-14- X-ray diffraction (XRD) pattern of attacked surface of the alloy 625 after the EIS test at 700°C in comparison with the standard XRD patterns of the identified components, compiled by JCPDS.

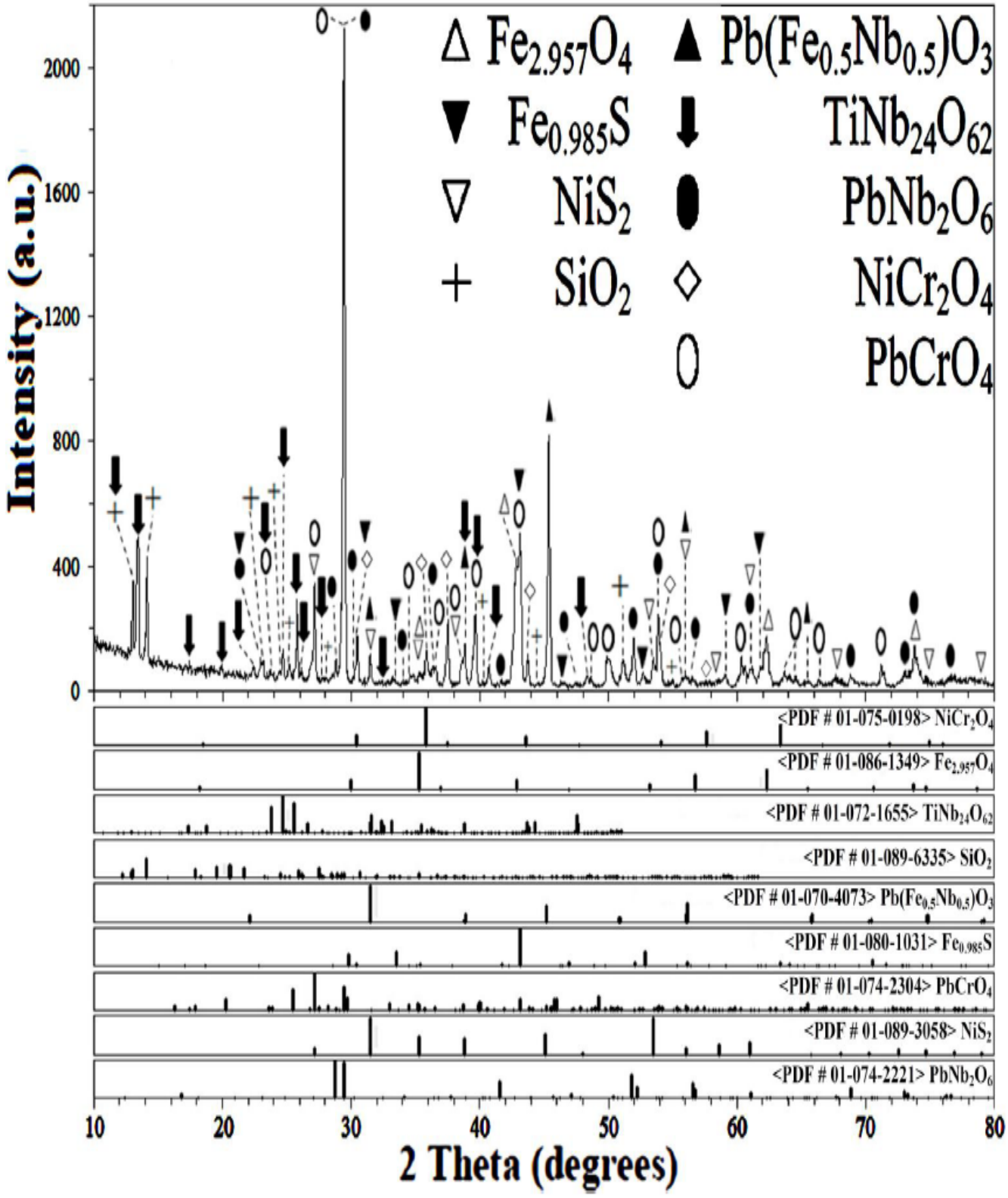

Figure 6-15- X-ray diffraction (XRD) pattern of attacked surface of the alloy 625 after the EIS test at 600°C in comparison with the standard XRD patterns of the identified components, compiled by JCPDS.

However, the characteristic peaks of the $Ni(Cr_2O_4)$ and the Cr_2O_3 protective layers completely disappeared/dissolved when the alloy was exposed to the molten salt medium at 600, 700 and 800°C. The dissolution of the protective layers justifies weak corrosion resistance/appreciable corrosion susceptibility of the alloy 625 in the molten salt medium as previously confirmed by the weigh-loss measurement technique (section 3.4). Nickel, chromium, iron, niobium, and titanium alloying elements in the chemical composition of the alloy 625 have a tendency to dissolution in the molten salt. Based on the XRD results, nickel mainly dissolved in the molten salt as Ni^{+2} at 800 and 600°C. According to Table 6-4 the dissolution of chromium in the form of Cr_5S_6 at 800°C, Cr^{+2} at 700°C and CrO_4^{2-} at 600°C caused the breakdown and the degradation of the protective layer. Weak characteristic peaks of $NiCr_2O_4$ are identifiable in the XRD pattern at 600°C (Figure 6-15). The $NiCr_2O_4$ phase was characterized as a porous layer, based on the SEM results in Figures 6-7 and 6-8. Consequently, the $NiCr_2O_4$ layer cannot act as an effective protective layer. Molybdenum showed a strong resistance to dissolution in the molten salt at 600 and 700°C, while it was dissolved in the form of $Fe(MoO_4)$ at 800°C. The concentration of the dissolved molybdenum in the molten salt mixture, measured by means of ICP technique, was equal to 153, 38 and 6 ppm at 800, 700 and 600°C, respectively. The amounts of the dissolved chromium and nickel in the molten salt mixture were determined as: Ni, 75, 26 and 11 ppm at 800, 700 and 600°C, respectively; and Cr, 630, 209 and 14 at 800, 700 and 600°C, respectively.

Formation of $CrNbO_4$ in scale was reported by Perez et al. during degradation of alloy 625 in $ZnCl_2$-KCl molten salt mixture at 650°C [81]. Ishitsuka et al. [84] reported that fast dissolution of Cr_2O_3 happened and chromium dissolved as a hexavalent chromium ion in molten chloride and chloride/sulfate mixture. In fact, in the molten chloride environments, which mainly formed in WTE boilers, the dissolution of the protective Cr_2O_3 films could occur through the chemical formation of CrO_4^{2-} [84]. In the current study, the dissolution of chromium in the form of CrO_4^{2-} occurred at 600°C (Figure 6-15 and Table 6-4). In the presence of molybdenum, vanadium or tungsten in the alloy, since

these elements have a tendency to form their oxides on the surface of the alloy, P_{O2-} of the molten salt at the interface will increase and the solubility of Cr_2O_3 will be expected to decrease [145]. Therefore, these protective oxide films can effectively assist the Cr_2O_3 layer to protect the alloy against the corrosive molten salt containing chlorine ions [145]. Obviously, these oxides could protect the substrate from the hot corrosion if they demonstrate a low solubility in a molten salt corrosive environment, which is a somewhat basic solution especially in WTE boilers. Despite the fact that Fe_3O_4 is another oxide having low solubility in such a corrosive environment, it could not play the role of a protective oxide layer because of weak protective properties [31].

Table 6-4- Identified corrosion products extracted from Figures 6-13, 6-14 and 6-15.

Temperature / Element	800°C	700°C	600°C
Ni	NiS_2, $FeNiS_2$	$Ni_{1.25}Fe_{1.85}O_4$	NiS_2, $NiCr_2O_4$
Cr	Cr_5S_6	$CrCl_2$	$PbCrO_4$, $NiCr_2O_4$
Mo	$Fe(MoO_4)$	-	-
Fe	FeS_2, $FeNiS_2$, $FeNb_2O_6$, Fe(MoO4)	FeO, $FeSO_4$, $FeCl_2$, $Ni_{1.25}Fe_{1.85}O_4$ $(FeTiO_3)_{0.7}(Fe_2O_3)_{0.3}$,	$Fe_{0.985}S$, $Pb(Fe_{0.5}Nb_{0.5})O_3$, $Fe_{2.975}O_4$
Nb	$ZnTiNb_2O_8$, $FeNb_2O_6$, $Ti_2(Nb_6O_{12})$	NbS_3, Nb_3S_4	$PbNb_2O_6$, $TiNb_{24}O_{62}$, $Pb(Fe_{0.5}Nb_{0.5})O_3$
Ti	$ZnTiNb_2O_8$, $Ti_2(Nb_6O_{12})$	$(FeTiO_3)_{0.7}(Fe_2O_3)_{0.3}$	$TiNb_{24}O_{62}$

6.8 Platinum electrodes stability

ICP/AAS was used to analyze the elemental composition of the molten salt electrolyte after the electrochemical tests at 600, 700 and 800°C. Platinum element was not detected by ICP/AAS in the chemical composition of the molten salt electrolyte. This confirms that platinum reference and counter electrodes do not react with the molten salt during the electrochemical tests and no degradation of the platinum electrode in the molten salt medium occurs. Furthermore, phase composition of the platinum

wires, in as-received condition and after exposure to the molten salt during the electrochemical tests, was studied by XRD technique and results can be seen in Figure 6-16.

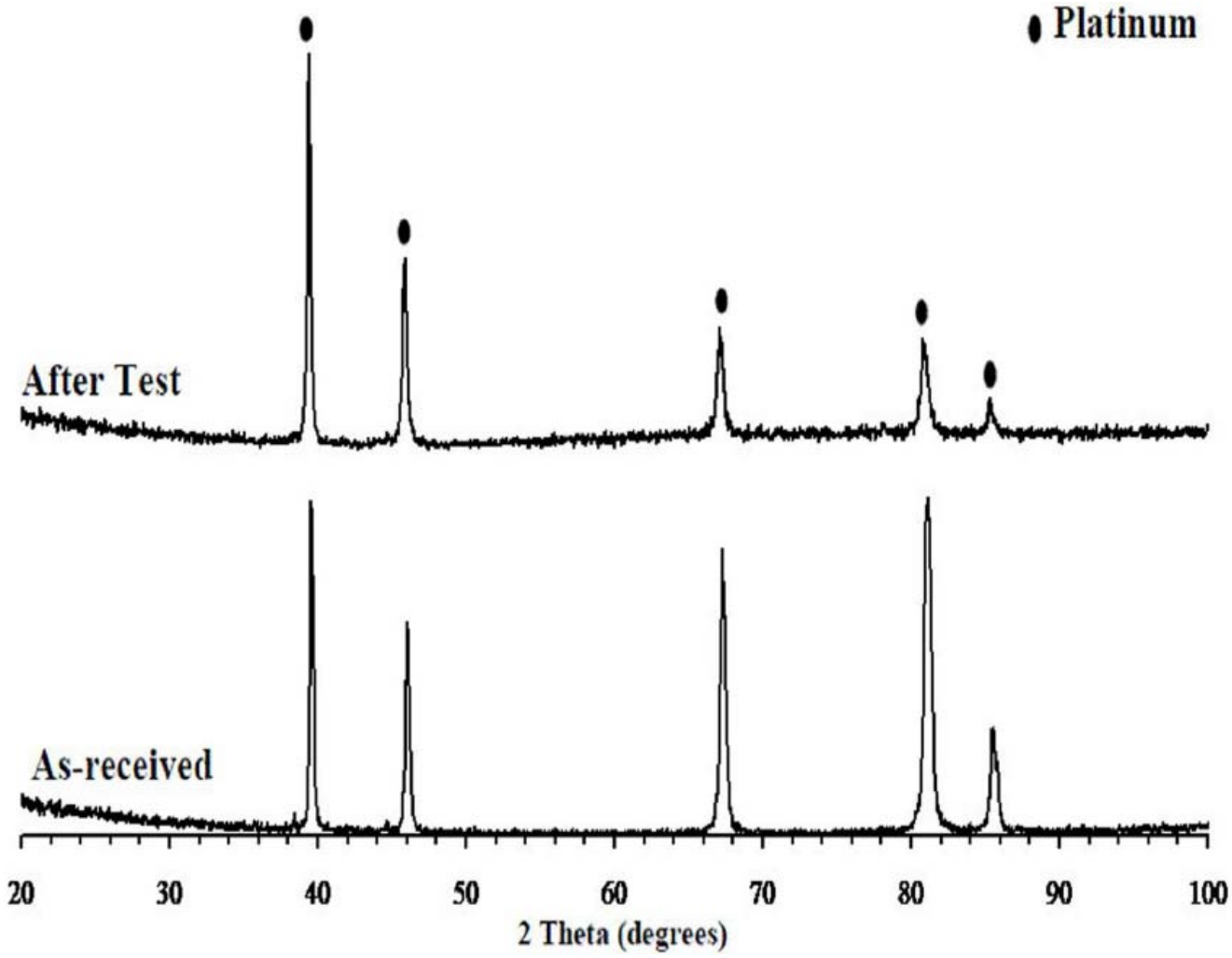

Figure 6-16- X-ray diffraction (XRD) patterns of the platinum reference electrode before and after the electrochemical tests which show the characteristic peaks of platinum.

Both patterns illustrate only the characteristic peaks of platinum (JCPDS # 00-004-0802) and no differences were noted between these two patterns. SEM photomicrographs and EDX analysis from the cross section of the platinum wire, as well as X-ray mapping of platinum in the as-received condition and after the exposure to the molten salt during the electrochemical tests can be seen in Figure 6-17.

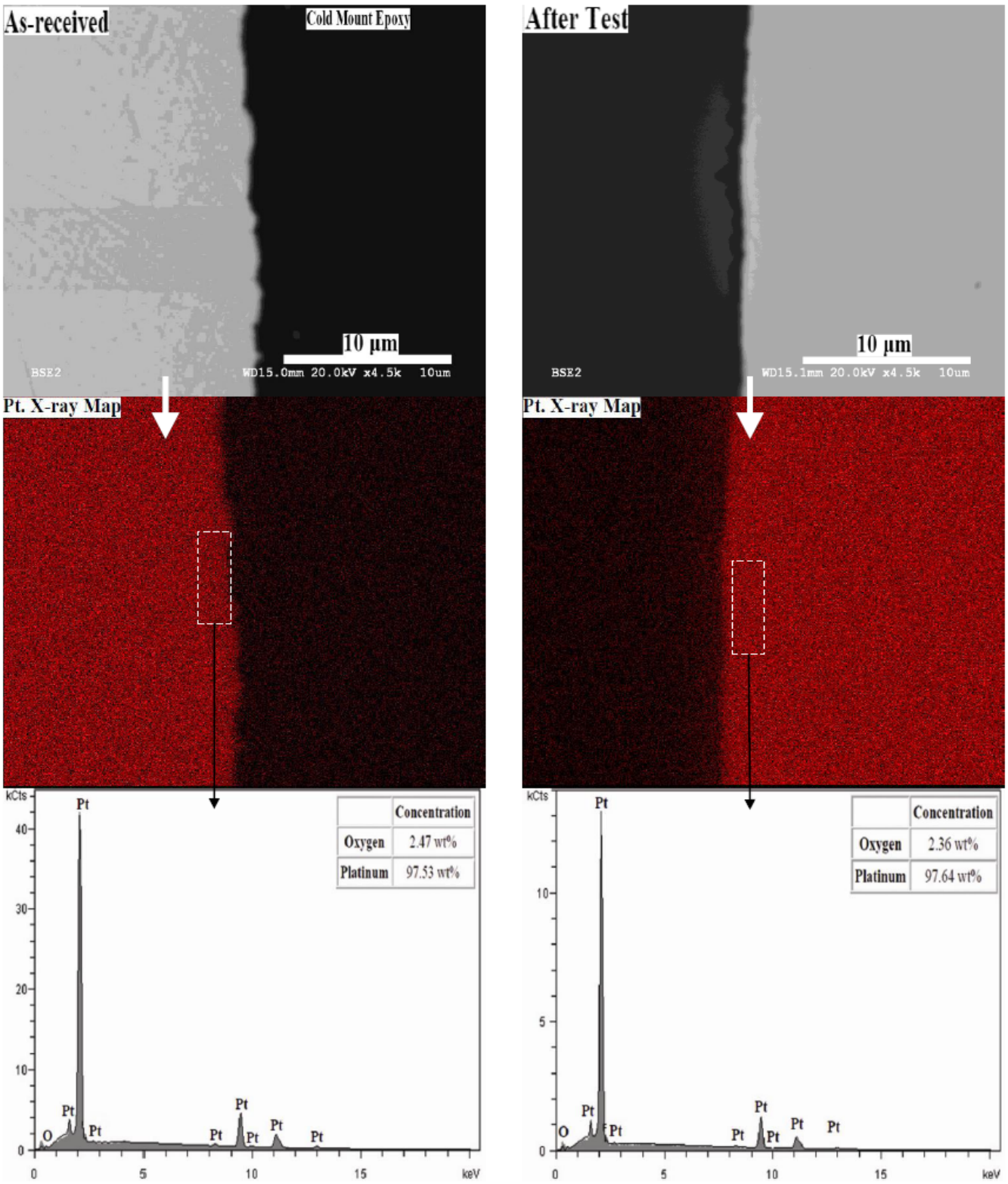

Figure 6-17- SEM photomicrographs and X-ray mapping of platinum as well as EDX analysis of the platinum wire cross section in the as-received condition and after the electrochemical tests in the molten salt medium (1).

Obviously, no considerable differences can be observed between these two conditions and no internal oxidation, pitting, surface cracking or surface degradation occurred in the platinum wire samples after the exposure to the molten salt medium. The X-ray mapping of platinum in Figure 6-17 confirms that the distribution of platinum in the surface layer of the wire remains completely uniform after the exposure to the molten salt medium and no sign of platinum-depletion/degradation can be observed. Also, results of the weight-loss measurement confirmed no weight-gain/loss of platinum after the EIS and the potentiodynamic polarization test, when the platinum electrodes were exposed to the molten salt for 24 hr at 800, 700 and 600°C. In summary, platinum exhibited strong resistance to degradation in the molten salt medium and it did not react with the molten phase, which justifies the selection of this metal as a pseudo-reference electrode in the current study.

Furthermore, successful application of platinum (melting point: 1768.3°C) as a counter and reference electrode for high temperature electrochemical studies has been widely reported in literature, particularly in molten salt environments containing high amounts of heavy metals such as Pb, Zn, and V, as well as high concentrations of Cl and S elements and at temperatures up to 900°C [86, 87, 89, 90, 94-98, 146]. This fact confirms that platinum has been known as a reliable pseudo-reference electrode for molten salt-induced corrosion studies.

6.9 Summary

OCP, potentiodynamic polarization, EIS, embedded test, weight-loss measurement method, XRD, SEM/EDX, and ICP/AAS were utilized to study electrochemical properties, corrosion behavior, and degradation mechanisms of wrought alloy 625 beneath 47 $PbSO_4$ - 23 ZnO - 13 Pb_3O_4 - 10 Fe_2O_3 - 7 $PbCl_2$ (wt. %) molten salt mixture under air atmosphere at 600, 700, and 800°C. An electrochemical model was used to explain the corrosion/electrochemical behavior of the alloy. This model fit with the obtained EIS data well because of the porous/non-protective nature of the Cr-rich anodic film.

7 Hot corrosion behavior of wrought alloy 625 in 47 $PbSO_4$-23 ZnO-13 Pb_3O_4-7 $PbCl_2$-10 CdO (wt. %) molten salt mixture[1]

Corrosion behavior of alloy 625 was studied in 47 $PbSO_4$-23 ZnO-13 Pb_3O_4-7 $PbCl_2$-10 CdO (wt. %) molten salt mixture, molten salt mixture (3), under air atmosphere at 600, 700 and 800°C. OCP measurement, potentiodynamic polarization, EIS and weight-loss measurement techniques were utilized to evaluate the degradation mechanisms and characterize the corrosion behavior of the alloy. Morphology, chemical composition and phase structure of the corrosion products and surface layers of the corroded specimens were studied by XRD and SEM/EDX.

7.1 OCP measurements

In a corrosion cell, potential of working electrode versus reference electrode when no potential or current is being applied to the cell is known as open circuit potential (OCP). The OCP is also called zero-current potential or rest potential [147]. In order to study some aspects of the kinetics and mechanism of the electrode processes, for examples passive layer or anodic film growth, stability or dissolution, monitoring the OCP vs. time can be used [148]. OCP changes as a function of time at 600, 700 and 800°C can be seen in Figure 7-1. At the beginning of the test, the potential of the electrode increased together with some variations and then reached a steady-state. This indicates that the corrosion resistance of the alloy increased with time and eventually reached a relatively stable value because of the formation of an anodic film. In the OCP curves at 600 and 700°C, the potential of the electrodes increased for 45 minutes and then reached a quasi-steady-state. This rapid increase in the potential of the electrode exposed to the molten salt at 600 and 700°C could be attributed to the spontaneous growth of an anodic film on the surface of the electrode in these two temperatures. Steady-

[1] A version of this chapter is published: E. Mohammadi Zahrani, A. Alfantazi, "Corrosion behaviour of alloy 625 in $PbSO_4$-Pb_3O_4-$PbCl_2$-ZnO-10 wt. % CdO molten salt medium", Metallurgical and Materials Transaction: A, 43 (2012) 2857-2868.

state OCP of the electrode at 700 and 600°C was found to be 7 and 12 mV, respectively. At 800°C the OCP curve fluctuated during the first 19 hr of exposing to the molten salt. Afterwards, OCP curve reached a quasi-steady-state. Steady-state OCP of the electrode was equal to 5.7 mV, very close to the steady-state OCP at 700°C. The fluctuation at the first 19 hr of exposure to the molten salt at 800°C could be attributed to the unstable nature of the film formed on the surface of the electrode.

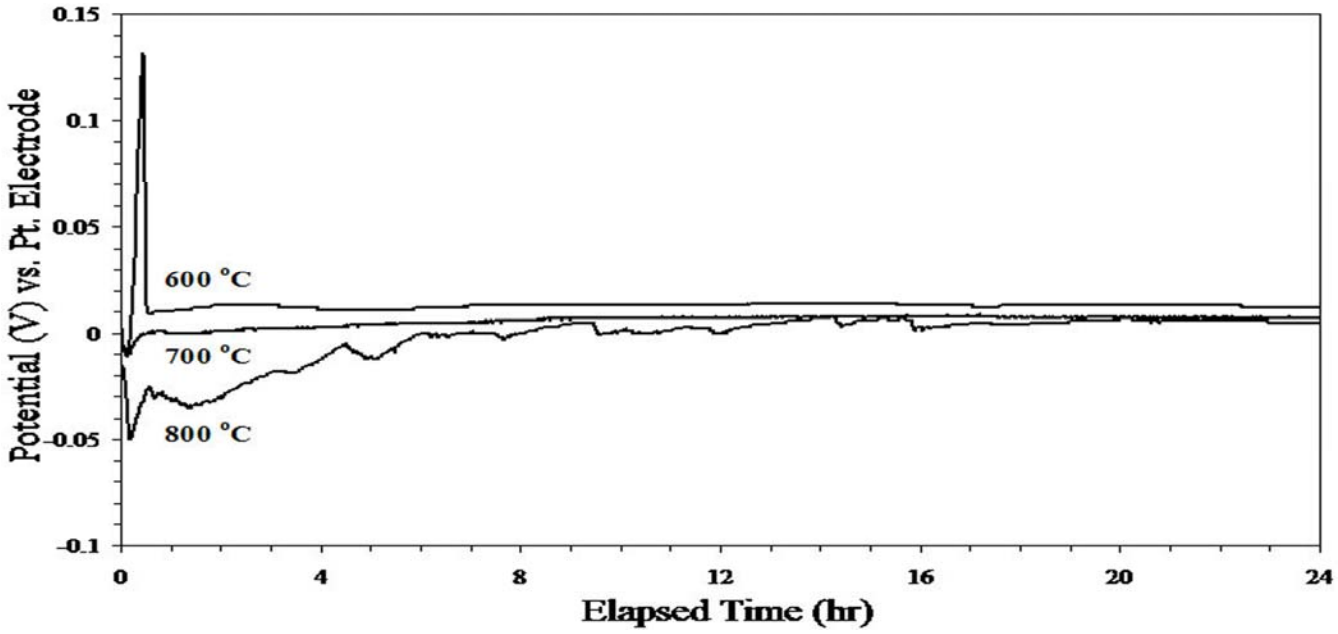

Figure 7-1- OCP of alloy 625 electrodes exposed to the molten salt mixture (3) at 600, 700 and 800°C for 24 hr.

7.2 Potentiodynamic polarization study

Potentiodynamic polarization method has been widely used as a powerful technique for general corrosion testing and measurement of corrosion rate of different alloys in molten salt medium. Figure 7-2 showed the potentiodynamic polarization curves at 600, 700 and 800°C after 24 hr of exposure, when OCP reached a stable value. Corrosion potential, extracted from potentiodynamic polarization data, and corrosion rate (mm / year), measured through weight-loss measurement technique, was tabulated in Table 7-1.

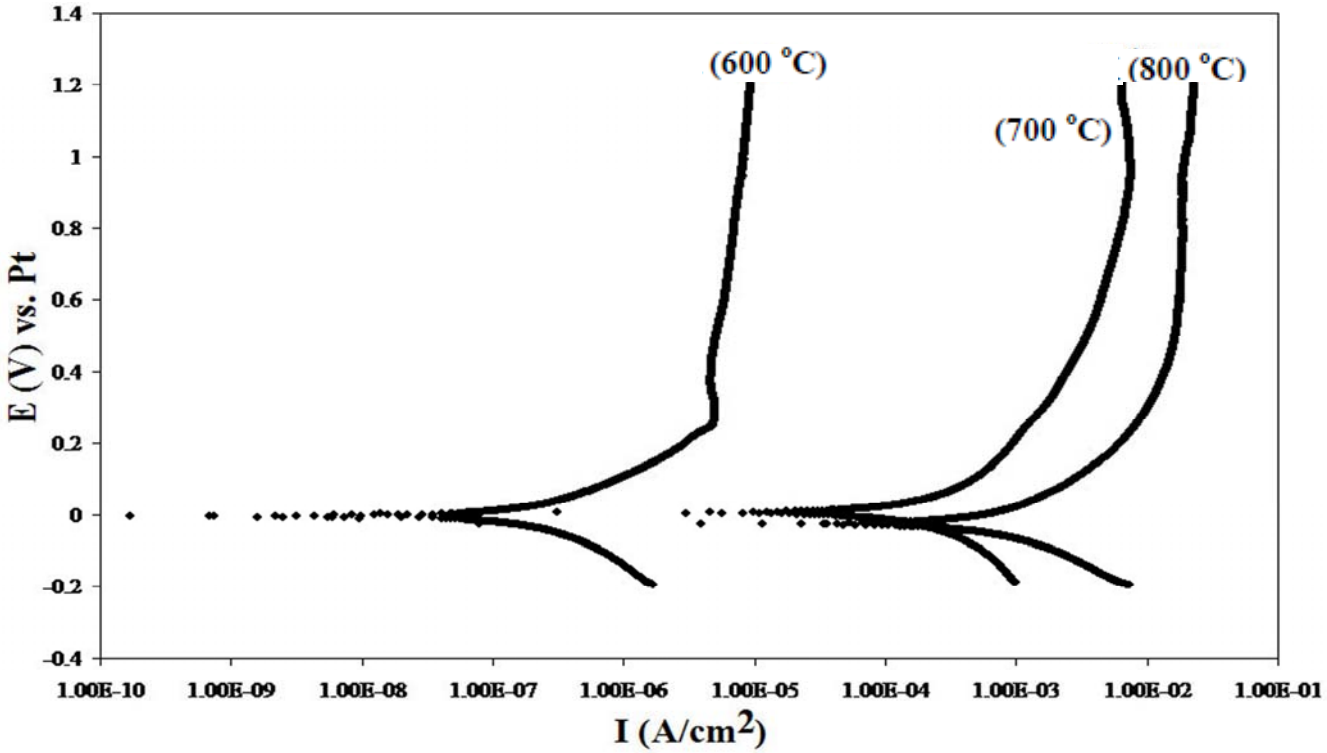

Figure 7-2- Potentiodynamic polarization curves of alloy 625, exposed to the molten salt mixture (3) at 600, 700 and 800°C for 24 hr.

Table 7-1- Obtained corrosion potential from the potentiodynamic polarization curves, and the calculated corrosion rate from the equation (4-1) for alloy 625 samples, exposed to the molten salt mixture (3) at 600, 700 and 800°C for 24 hr.

	800°C	700°C	600°C
E_{corr} (mV vs. Platium)	-26.9	5.1	-3.7
Corr. Rate (mm/year)	48.6 ± 7.20	19.5 ± 3.81	0.1 ± 0.05

The corrosion potential of alloy 625 electrode in the molten salt mixture at 600, 700 and 800°C was determined to be -3.7, 5.2 and -26.9 mV, respectively. Except for the E_{corr} value at 700°C which is positive, E_{corr} values at 600 and 800°C are negative and obviously the most active E_{corr} belongs to 800°C. In fact, it suggests that smaller driving force was required to initiate the corrosion of alloy 625 at 800°C. It was clear that by increasing the temperature, the corrosion rate of the alloy increased and the potentiodynamic polarization curves shifted toward left hand side of the diagram. In fact, the

corrosion activity increased with an increase in the temperature because of an increase in the electrical conductivity of the molten salt mixture as well as a reduction in the viscosity of the molten salt, thus favoring the diffusion of chemical active species. Considering the anodic branch of the potentiodynamic polarization curves, it could be suggested that alloy 625 could form an oxide film at all investigated temperatures. The oxide film seems to be less protective at the higher temperatures (700 and 800°C) due to a significant increase in the anodic current density by increasing the temperature [149]. At the potentiodynamic polarization curve of 600°C, in the potentials higher than +0.25 mV up to +1.2 mV, the anodic current density was almost constant in a wide potential region. Due to this relatively stable anodic current density in a wide potential range, oxide film (anodic film) can be described as a passive-like layer. The oxide layer, which formed at 600°C on the alloy surface, was more protective compared to the 700 and 800°C due to the lower corrosion rate of the alloy at 600°C.

7.3 EIS study

The electrochemical corrosion behavior of alloy 625 was modeled based on the obtained data from EIS technique and a good agreement between the model and experimental data was observed. Impedance behavior of alloy 625 electrode including measured and calculated Nyquist plots plus bode diagrams of phase angle and total impedance magnitude at 600, 700 and 800°C, are presented in Figure 7-3. Considering the surface and cross section morphology of alloy 625 after the electrochemical tests, two electrochemical models were developed and EIS data were fitted into two equivalent circuits. The electrochemical circuits of these two purposed models as well as model's parameters for equivalent circuit at each temperature can be seen in Figure 7-4.

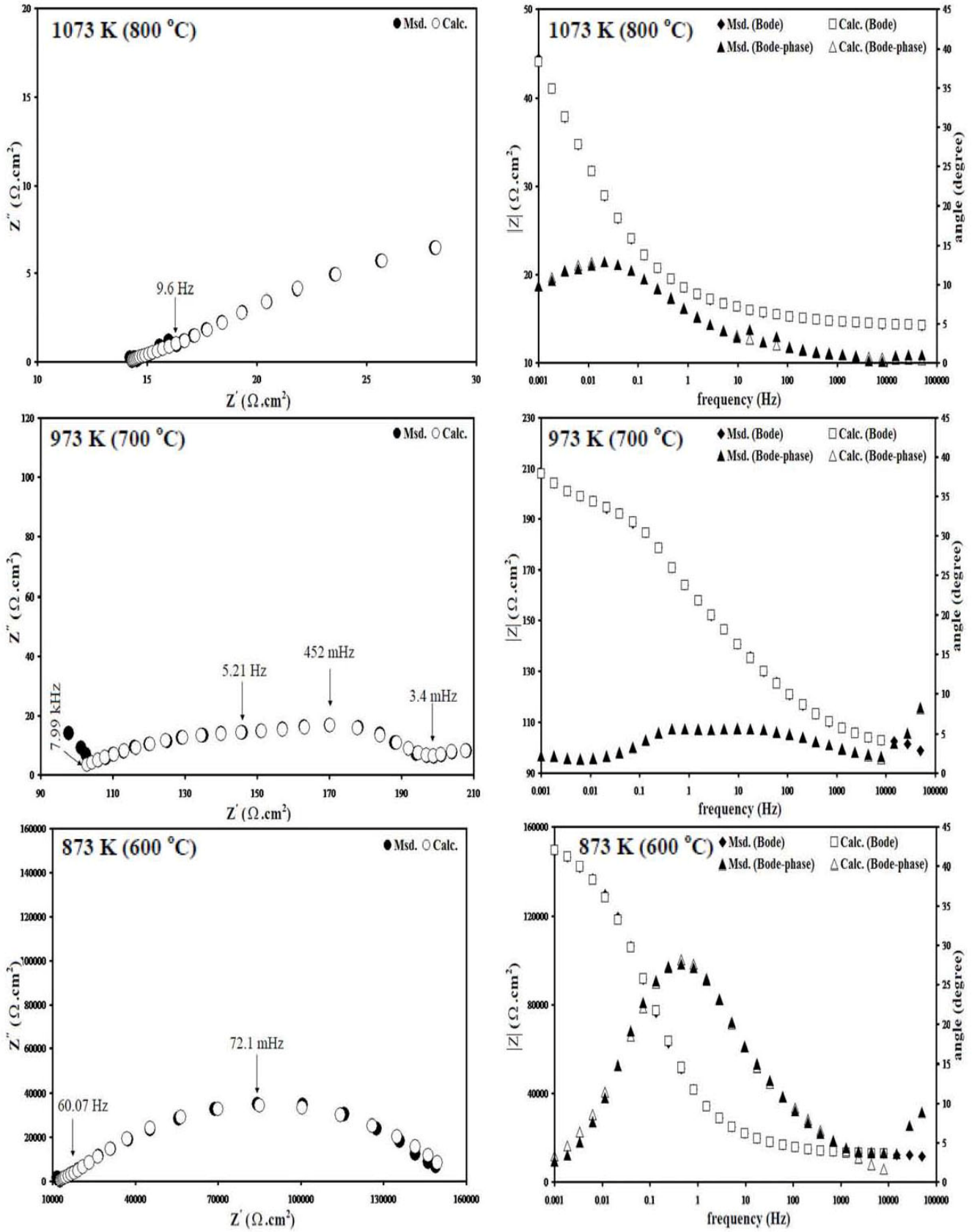

Figure 7-3- Electrochemical impedance spectroscopy (EIS) Nyquist plots response plus bode diagrams of phase angle and total impedance magnitude for alloy 625, exposed to molten salt mixture (3) for 24 hr.

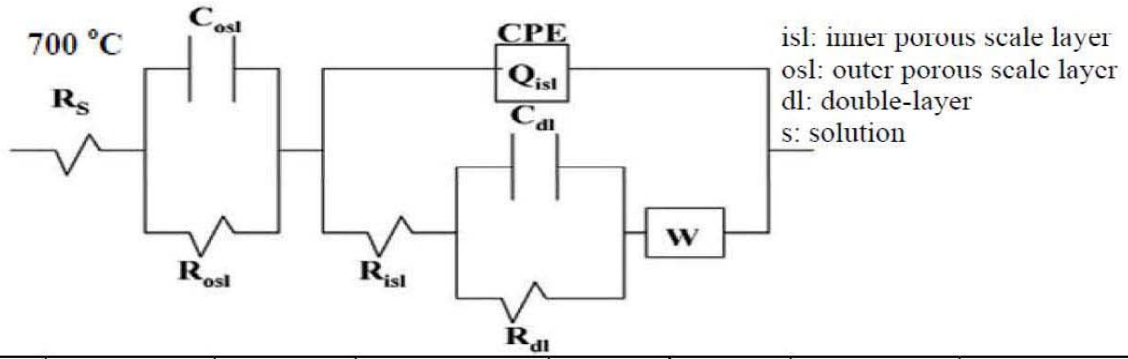

Parameter / Temperature	R_s ($\Omega.cm^2$)	R_{osl} ($\Omega.cm^2$)	C_{osl} ($F.cm^{-2}$)	R_{isl} ($\Omega.cm^2$)	Q_{isl}-Yo ($S.sec^n.cm^{-2}$)	Q_{isl}-n	R_{dl} ($\Omega.cm^2$)	C_{dl} ($F.cm^{-2}$)	W ($S.sec^{0.5}.cm^{-2}$)	χ^2
973 K (700 °C)	97.44	10.98	0.04585	99.29	0.003058	0.322	11.2	12.92	0.0002296	8.35×10^{-6}

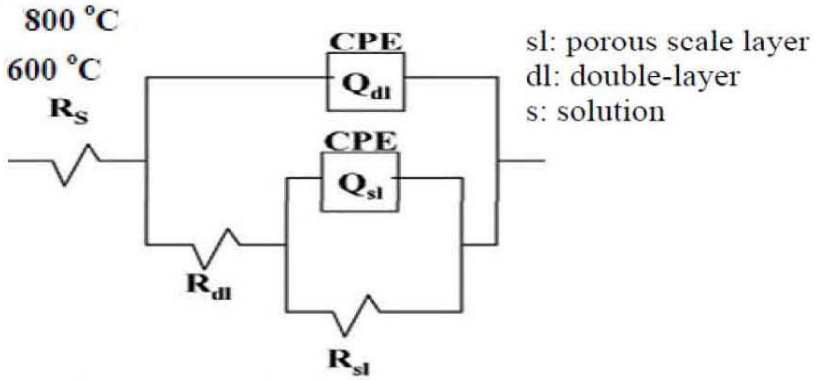

Parameter / Temperature	R_s ($\Omega.cm^2$)	R_{dl} ($\Omega.cm^2$)	Q_{dl}-Yo ($S.sec^n.cm^{-2}$)	Q_{dl}-n	R_{sl} ($\Omega.cm^2$)	Q_{sl}-Yo ($S.sec^n.cm^{-2}$)	Q_{sl}-n	χ^2
1073 K (800 °C)	14.16	7.05	0.07424	0.3438	43.83	0.04967	0.5718	7.854×10^{-5}
873 K (600 °C)	12350	11420	0.000004549	0.562	133200	0.000007669	0.5961	3.064×10^{-4}

Figure 7-4- Equivalent electrochemical circuits at 700°C (two non-protective scale layers model), 800 and 600°C (porous scale layer model) beneath molten salt mixture plus the model's parameters of equivalent circuits for alloy 625 exposed to molten salt mixture (3) for 24 hr.

At 800 and 600°C, Nyquist diagrams show two depressed capacitive loops including a small loop in high frequency range and a loop in low frequency range. Corresponding phase angle vs. frequency curves had one relatively symmetrical maximum in the low frequency range. The capacitive loops is related to the dielectric properties of the Cr-rich porous layer formed on the electrode surface at 800 and 600°C. Equivalent circuit of porous scale model at 800 and 600°C belongs to the alloy suffering from localized fast corrosion attack (pitting) in the molten salt environment as it can be seen in Figures 7-8 and 7-9. In this model, R_{dl} and R_{sl} represent charge transfer resistance along the localized corrosion zone (porous zone) and transfer resistance of ions in the scale layer, respectively.

At 700°C, two depressed semi-circles were distinguishable in the Nyquist diagram, and an obvious linear region followed the second capacitive loop. The measured EIS data were fit into a two non-protective and porous scale layers model (Figures 7-3 and 7-4). The linear region of the Nyquist diagram could be attributed to molten phase mass transfer effects and Warburg-type behavior when the frequency is lower than 3.4 mHz. This linear region diminished as the temperature decreased to 600°C; probably, the resistance of the scale layer increased at lower temperatures and masked the linear region. This linear region disappeared when the temperature increased to 800°C because diffusion of the aggressive species at the interface of the alloy and molten salt becomes faster and diffusion of the oxidants could not act as a rate-controlling step at 800°C. The phase angle vs. frequency curve (700°C) had one maximum and one shoulder at the high and low frequency ranges, respectively. According to Figure 7-4, the charge transfer resistance of the outer scale layer (R_{osl}) at 700°C and charge transfer resistance of scale layer (R_{sl}) at 800°C, both are quite low and these layers could not act as effective protective barrier layers. This fact was confirmed by high corrosion rate of the alloy 625 at 800 and 700°C. However, charge transfer resistance of scale layer (R_{sl}) at 600°C is high and it shows that scale layer of the alloy at 600°C can reasonably play the role of an effective protective barrier layer and reduce the corrosion rate of the alloy at 600°C compared to 700 and 800°C.

At all the investigated temperatures, the phase angle maxima were much smaller than 90 degree. As was mentioned for the same observation in chapter 6, Carranza and Alvarez explained that surface roughness, frequency dispersion of time constants due to local inhomogeneities in the dielectric material, porosity mass transport effects and relaxation effects could be some reasons for this phenomenon [143]. In the present study, the most probable reason for having phase angles much smaller than 90° could be the frequency dispersion of time constants due to the local inhomogeneities in the dielectric material, because of the inhomogeneous nature of the molten salt mixture. Also, for bode plots of 700 and 600°C, the diagrams showed straight lines with slopes smaller than -1 at high frequency range. This feature could be related to the frequency dispersion and it can be attributed to the solid surface inhomogeneities [100]. Beverskog et al. mentioned that the number of distinguishable maxima or related shoulders was an indication of the minimum number of relaxation processes (time constants) that occurred in the electrochemical system, which were detectable through the EIS technique [144].

Therefore, the EIS results exhibited a minimum of one time constant at 800 and 600°C, but a minimum of two relaxation processes and time constants at 700°C. At 700°C, the relaxation process at the high frequency range may be attributed to the growth of the outer porous scale layer and, at the same time, the relaxation process at the low frequency range may be related to the growth of the inner porous scale layer [150, 151]. In Figure 7-3, the values of both real and imaginary impedance rose with decreasing temperature in the molten salt, resulting in an increase of the impedance modulus and the radius of the capacitive loop. This agreed with the decrease of corrosion rates observed in Table 7-1. R_s, the solution resistance between the working and reference electrode, and R_{ct} (R_{dl}), the charge transfer resistance of the diffusion controlled reaction, both values significantly increased by decreasing the temperature. This phenomenon may be explained considering the fact that the viscosity of the molten salt significantly decreased as a result of an increase in temperature, while the mass fraction of the molten

phase increased, simultaneously. These two factors could enhance the diffusion of the aggressive species from the molten environment toward the molten phase / electrode surface interface and subsequently accelerate the corrosion of the alloy.

7.4 XRD analysis

In order to develop an understanding of the corrosion products and scale layer phase structure, formed on the surface of the alloy after electrochemical studies, the surface of the alloy 625 corroded samples was studied by XRD technique. The obtained XRD patterns from the scale layers exposed at 600, 700 and 800°C are presented in Figure 7-5. Also, the XRD patterns of the initial salts as well as prepared salt mixture can be seen in Figure 7-6 for comparison. In the XRD pattern of 800°C, in addition to the residue salts such as $PbSO_4$ (JCPDS # 01-089-7356), $PbCl_2$ (JCPDS # 01-084-1177) , ZnO (JCPDS # 01-075-1526) and $(Cd_{0.2}Zn_{0.8})S$ (JCPDS # 01-071-4155), which deposited on the surface of the electrode, Cr_2O_3 (JCPDS # 01-084-0315), CrO_3 (JCPDS # 01-072-0634), $FeSO_3$ (JCPDS # 01-071-2014), $CrNbO_4$ (JCPDS # 01-074-1941), NiO (JCPDS # 01-071-1179)and $(Cr_{0.045}Fe_{0.955})S$ (JCPDS # 01-070-2914) phases were detectable in the scale layer. In Figure 7-7, the XRD pattern at 800°C was compared with the standard XRD patterns (JCPDS file) of the major corrosion products. By decreasing the temperature, major peaks of CrO_3 and Cr_2O_3 disappeared and the others became significantly weak. Ultimately, no obvious and well-developed characteristic peaks of Cr_2O_3 phase were detectable in the XRD pattern of 600°C. Meanwhile, the characteristic peaks of the NiO became more intense at decreasing temperatures. Another important observation was the detection of $FeSO_3$ and $(Cr_{0.045}Fe_{0.955})S$ in the scale layer as a result of iron sulfidation process during corrosion in molten salt.

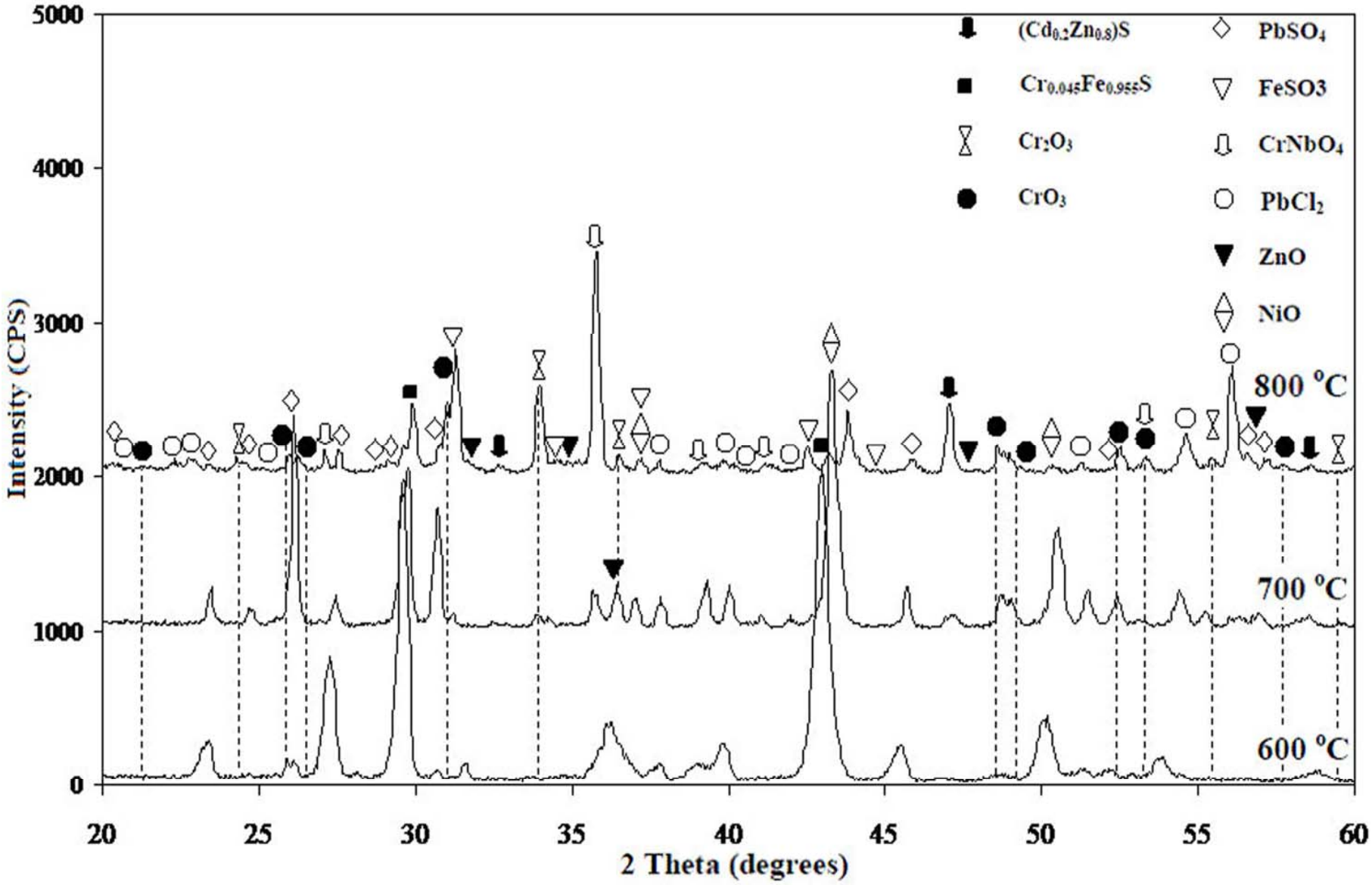

Figure 7-5- X-ray diffraction (XRD) patterns of corrosion products formed on the surface of alloy 625 after electrochemical tests at 600, 700 and 800°C.

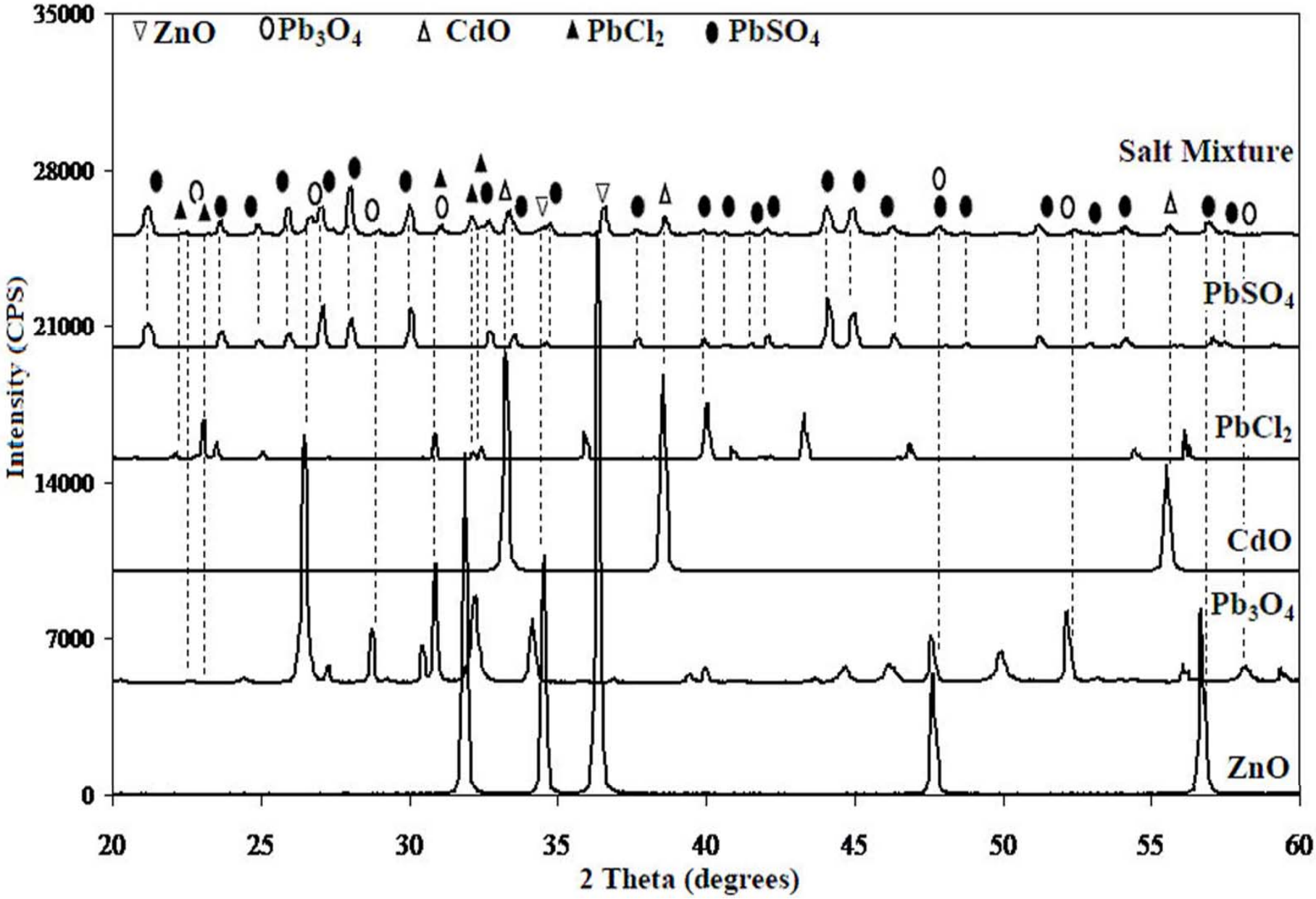

Figure 7-6- X-ray diffraction (XRD) patterns of initial salts and prepared salt mixture.

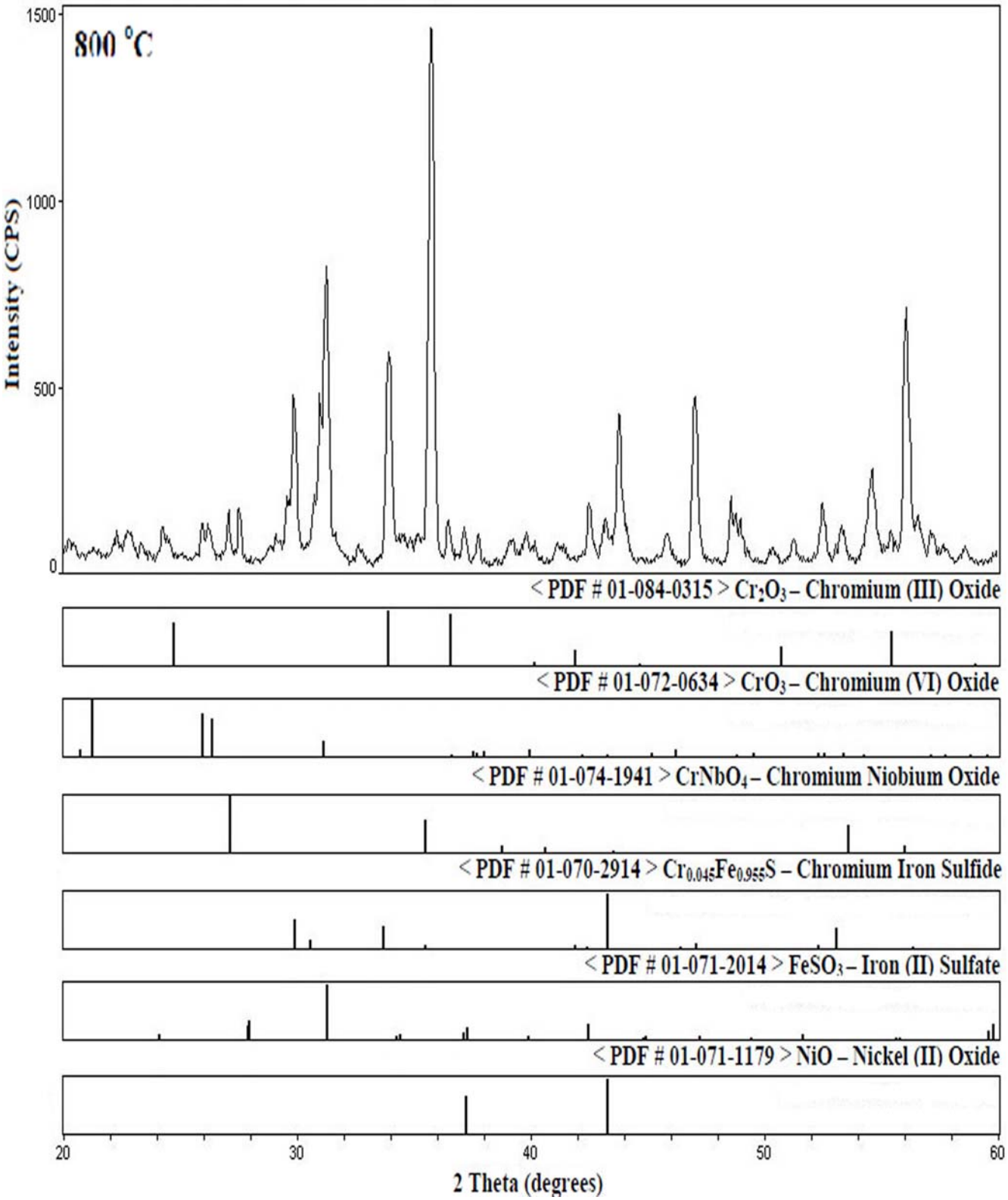

Figure 7-7- Corrosion products formed on the surface of alloy 625 after electrochemical tests at 800°C in comparison with standard XRD patterns of the components, compiled by JCPDS.

The formation of these two phases confirmed that iron, an available element in the chemical composition of alloy 625, could be dissolved in the molten salt through sulfidation reaction. However, active oxidation of Cr and Ni, two major alloying elements in alloy 625, appeared to be the main degradation mechanism. Formation of $(Cr_{0.045}Fe_{0.955})S$ phase indicated that a sulfidation reaction also could have contributed to the Cr dissolution. Niobium is another alloying element in the chemical composition the alloy 625, with a tendency for participation in the active oxidation reactions because of the presence of $CrNbO_4$ in the XRD patterns. However, the presence of MoO_2 was not identified by XRD. Hence, active oxidation and sulfidation appeared to be the two major phenomena occurring at the substrate / melt interface to selectively dissolve the substrate alloying elements and cause the corrosion attack [70]. Based on the phase composition of the scale layer formed on the surface of the alloy after the tests, the active oxidation is the main degradation mechanism in alloy 625 under the molten salt system of the present study. XRD results confirmed that the metal ions Fe^{+2}, Ni^{+2}, Cr^{+3} and Cr^{+6} react with the oxide ions to form metal oxides. Because of the occurrence of such oxidation reactions, the oxygen concentration increased near the surface of the alloy, which could enhance oxygen diffusion into the alloy from the atmosphere through the molten salt to form oxide.

7.5 SEM/EDX analysis

Figures 7-8 and 7-9 present SEM photomicrographs from the surface and cross section of alloy 625 at different magnifications and SEM imaging modes (backscattered electron (BSE) and secondary electron (SE)) after exposure to the molten salt mixture in corrosion tests at 600, 700 and 800°C. Corrosion products and a thick Cr-rich oxide layer, together with some pores and pits under the Cr-rich layer (internal attacked area), were formed at the surface of the substrate at 800 and 700°C. Based on the SEM results, there appeared to be two types of attack for Inconel 625 including general surface corrosion and pitting.

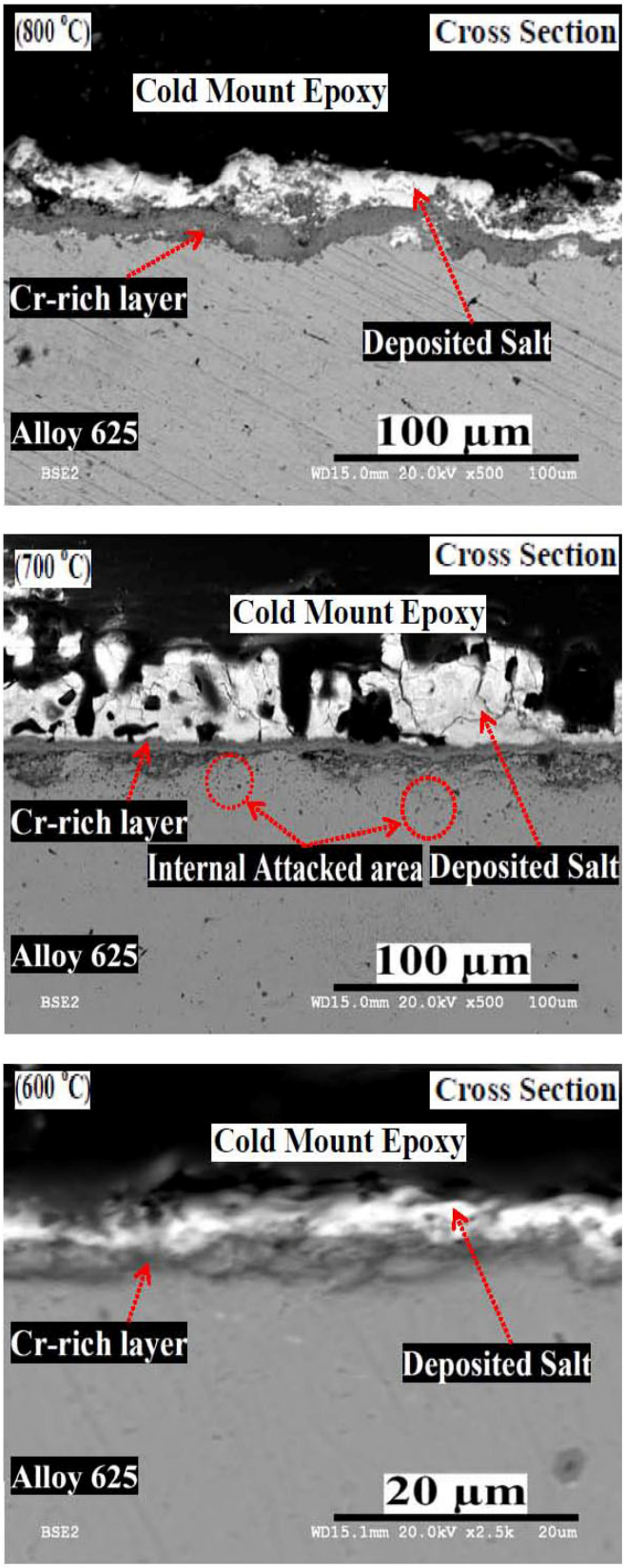

Figure 7-8- SEM photomicrographs of alloy 625 substrates, exposed to the molten salt mixture (3), which show the surface and cross section of the corroded samples.

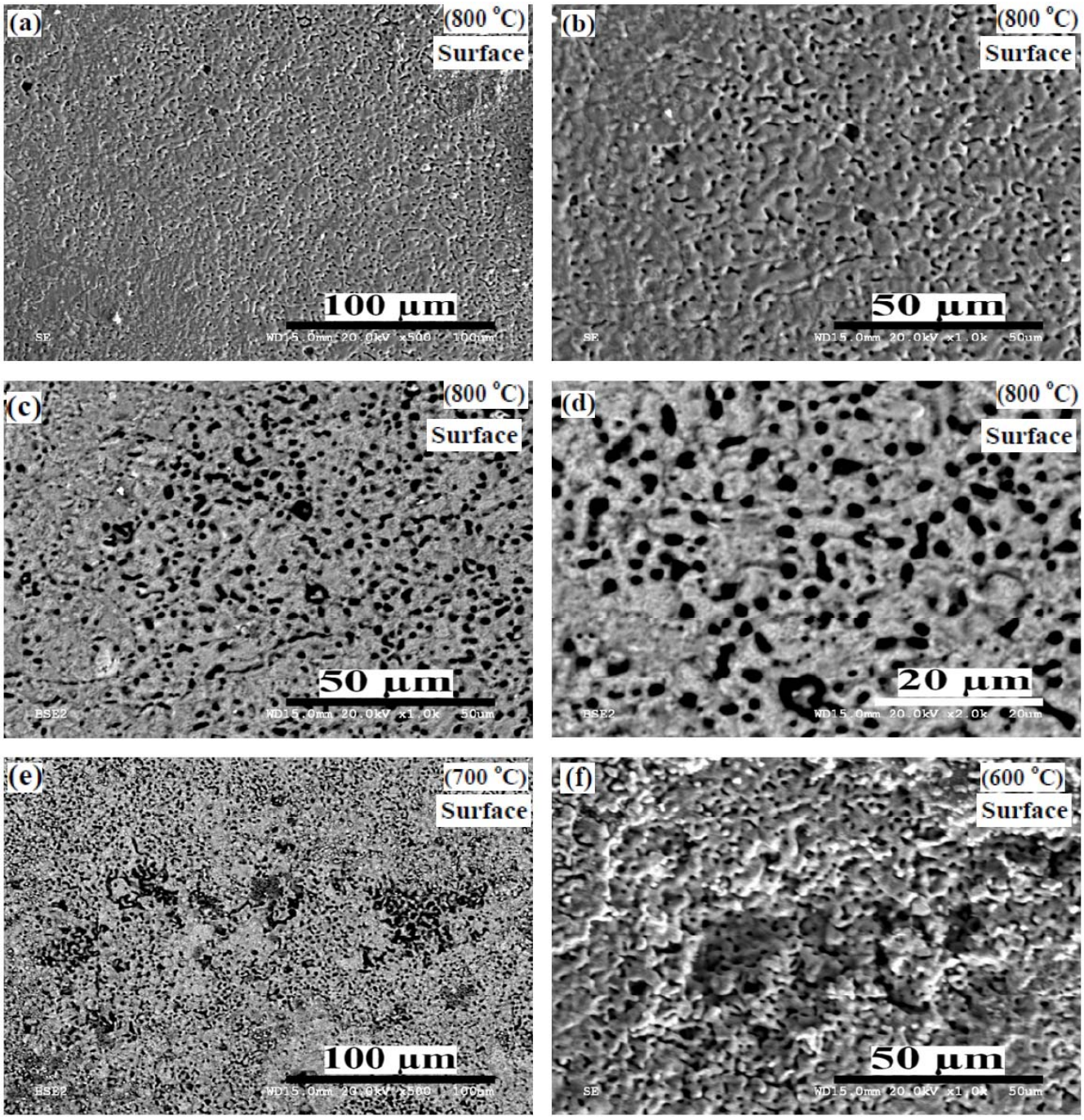

Figure 7-9- SEM photomicrographs of the surface of alloy 625 substrates, exposed to the molten salt mixture (3), which illustrate secondary electron (SE) images at a) 500x, and b) 1000x magnification, c) Backscattered electron (BSE) mode of image (b) at the same magnification for comparison purpose, d) BSE image at 2000x magnification, e) BSE image at 500x magnification, and f) SE image at 1000x magnification. General surface corrosion and pitting, as two main modes of corrosion attack, are obvious in these images.

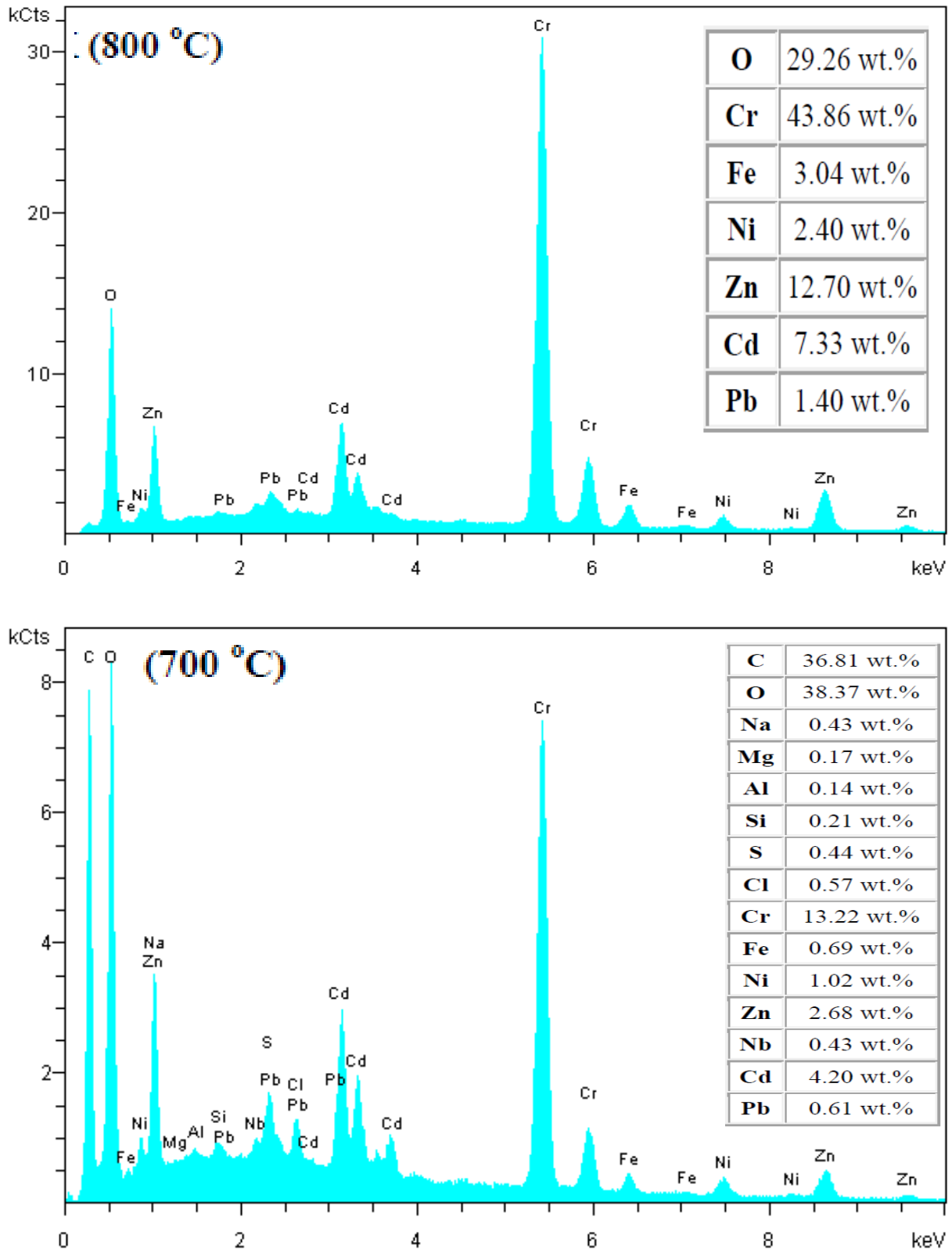

Figure 7-10- EDX analysis from the outer surface of the scale layer formed on the surface of alloy 625 substrate, exposed to the molten salt mixture.

A comparison, which was made between SE and BSE modes of an image in Figure 7-9b and Figure 7-9c, is an obvious evidence of the presence of pores and pits on the attacked surfaces after exposure to the molten salt medium. Pitting corrosion occurred due to the breakdown of the initial protective oxide layer by molten salt dissolution of the oxide or crack formation in the oxide layer. Montgomery et al. mentioned that chloride and sulphates present as heavy metal salts in the melt or semi-melt phase could be responsible for pitting corrosion [80]. It seems that because of the non-protective nature of the Cr-rich oxide layer which was formed on the surface of alloy at 700 and 800°C, corrosive species diffused in the alloy from surface during exposure to the molten salt and caused the intergranular corrosion process (internal attacked area). The internal attacked area was not formed under the interface of the Cr-rich oxide layer and alloy at 600°C, so the oxide layer formed on the surface of the substrate at 600°C could be considered as an effective protective oxide layer, not a corrosion product layer. The mean thickness of the oxide layers at 600, 700 and 800°C, measured by using SEM photomicrographs, was equal to 2.46 ± 0.50 µm, 7.88 ± 2.96 µm and 10.00 ± 2.61 µm, respectively. As it can be seen by increasing the temperature, the thickness of the oxide layers rose. EDX analysis from the outer surface of the scale layer, formed on the surface of the substrate at 700 and 800°C, can be seen in Figure 7-10. Cr content (dissolved from the substrate) of this layer was equal to 43.9 and 13.2 wt. % at 800 and 700°C, respectively. This result was in a good agreement with the higher corrosion rate of the alloy 625 in the molten salt environment at 800°C than at 700°C. Because of the significant amount of oxygen in the chemical composition, it is plausible to claim that Cr was dissolved into the molten phase during the active oxidation reactions at the interface of the substrate and the molten salt, which was in a good agreement with the results of XRD analysis. X-ray maps for Cr, Ni and O at the interface of the substrate and molten phase at 700 and 800°C were presented in Figure 7-11. Ni and Cr mapping showed that Ni-rich layer, formed on top of the Cr-rich layer was denser and thicker at 700°C than at 800°C.

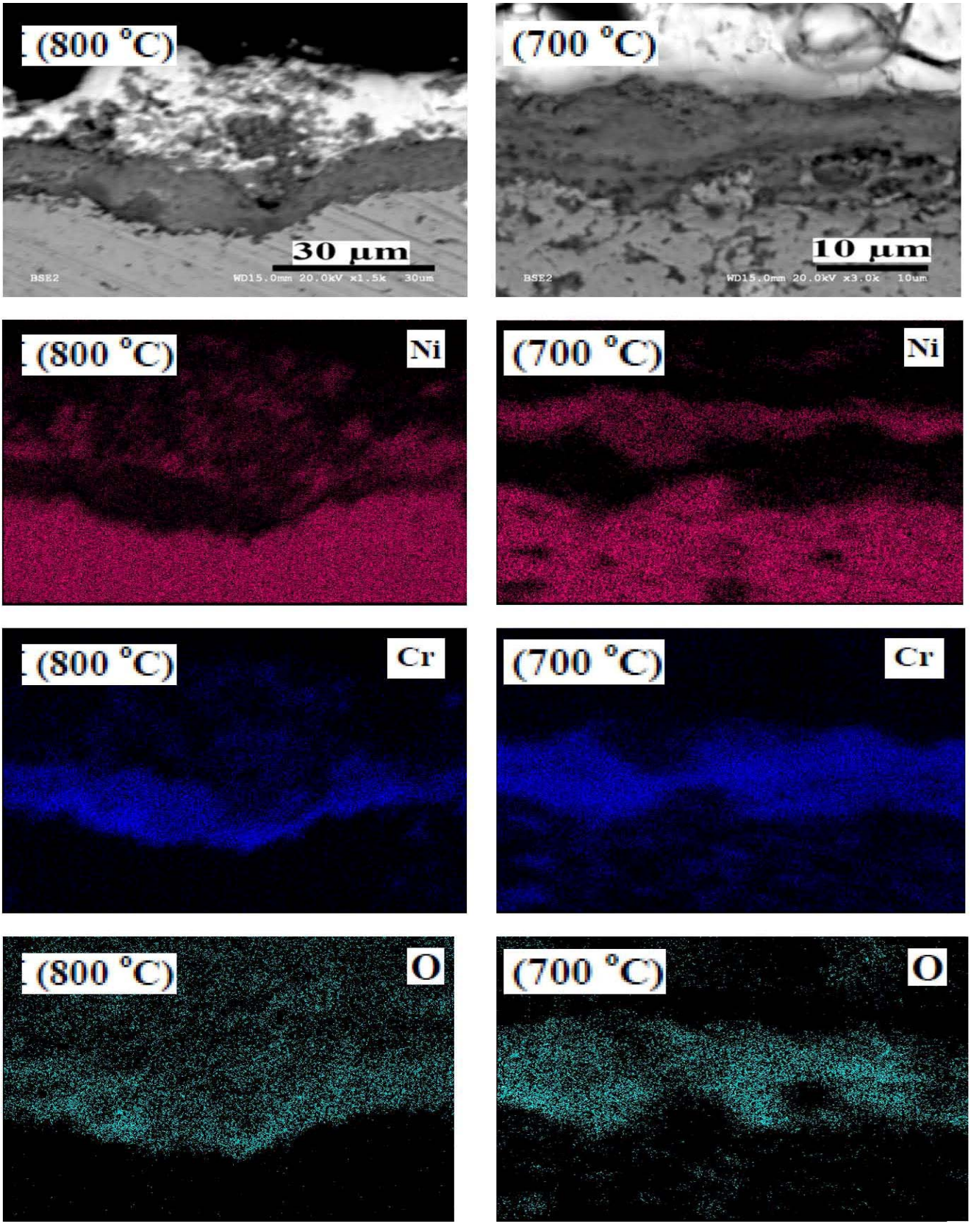

Figure 7-11- X-ray mapping of Cr and Ni and EDX analysis of the cross section of the alloy 625 substrate, exposed to the molten salt mixtures.

The formation of two Ni- and Cr-rich oxide layer on the surface of the alloy at 700°C was in a good agreement with the results of the EIS plots, which showed two depressed semi-circle capacitive loops in the Nyquist diagram of 700°C. Based on the Ni, Cr and O mapping in Figure 7-11, it was clear that in the bode plot of the sample at 700°C, the relaxation process at the high frequency range was attributed to the growth of the outer Ni-rich oxide barrier layer and the simultaneous relaxation process at low frequency range was related to the growth of the inner Cr- rich oxide barrier layer. Ni, Cr and O mapping confirmed the presence of dissolved Cr and Ni in the molten salt composition in the form of oxide, in the areas which were away from the substrate / molten salt interface. EDX analysis of the Cr-rich layer (area close to the Cr-rich layer / alloy interface) confirmed that at 800°C, the concentration of Cr (46.5 wt. %) was higher compared to that at 700°C (34.6 wt. %), while the concentration of the Ni was higher (8.2 wt. %) at the 700°C. It means that at 800°C, the tendency of Cr for participation in the active oxidation reaction at the interface of the alloy and molten salt was higher, which was in a good agreement with the XRD results.

7.6 Summary

Corrosion behavior and degradation mechanisms of alloy 625 beneath 47 $PbSO_4$ - 23 ZnO - 13 Pb_3O_4 - 10 CdO - 7 $PbCl_2$ (wt. %) molten salt mixture under air atmosphere were studied at 600, 700, and 800°C by EIS, OCP, and potentiodynamic polarization techniques. Alloy 625 could form an anodic film after 24 hours exposure to the molten salt. XRD and SEM/EDX techniques were utilized to study the morphology, chemical composition and phase structure of the corrosion products and surface layers of the corroded specimens. The anodic film was a protective layer at 600°C, while it should be regarded as a corrosion product film with decreased resistance at temperatures of 700 and 800°C. The formation of a porous and non-protective oxide layer with decreased resistance was responsible for the weak protective properties of the barrier layer at high temperatures of 700 and 800°C.

8 Conclusions

8.1 Failure analysis of the weld overlay alloy 625 in the KIVCET radiant boiler

Solidification cracks were found to be associated with the interdendritic regions due to the presence of the Laves constituent. The dilution and, consequently the presence of a significant amount of Fe in the weldment composition were the key issues in the alloy 625 weld overlay. The high heat input and the dilution were also reasons for the formation of Fe-rich inclusions in the welding structure. As confirmed by the laboratory-scale hot corrosion study, the Fe-rich inclusions were susceptible to the hot corrosion attack, when the weld overlay was exposed to the corrosive environment of the boiler. Consequently, these inclusions reduced the resistance of the weld overlay alloy 625 to the molten salt-induced corrosion. SEM analysis confirmed the presence of a network of well-developed circumferential cracks across the surface of the weld overlay. SEM/EDX results, together with the laboratory-scale hot corrosion study indicated that a combination of defects, such as cracks and porosities, and the molten salt penetration into the weld overlay through the cracks/defects, led to the degradation of the weld overlay.

It was confirmed that Cr, Nb, and Fe elements in the weld overlay alloy 625 have the highest tendency to be dissolved in the molten salt medium, compared to other alloying elements in the weld alloy 625 (particularly Ni), when the weld overlay was exposed to the molten phase. This caused the formation of Cr- and Nb-depleted zones in the weld overlay. Internal sulfidation and oxidation were identified as two modes of hot corrosion attack in the weld overlay alloy 625.

As confirmed by SEM and optical microscope results, the deep and branched cracks acted as pathways for the molten phase to penetrate inside the weld overlay, reach the underlying carbon steel substrate, and spread along the weld layer/tube interface. SEM/EDX results showed that the dendrite cores acted as the preferential pathways for the molten salt penetration and diffusion of the aggressive species (O,

S). Consequently, the penetration of the molten phase into the cracks accelerated the propagation of the cracks, and it facilitated further crack branching. Pitting corrosion in the carbon steel tube was a direct consequence of the molten salt penetration into the weld/tube interface and subsequent hot corrosion attack. Oxidation and sulfidation of Fe were identified as the main mechanisms of the carbon steel tube hot corrosion.

The cracks mainly initiated from the preferentially corroded and (Mo, Nb)-depleted dendritic cores on the HSS. The solidification cracks, which are open to the surface, can also act as potential sites for penetration of the molten phase into the weld layer and gradual development of the cracks which intersect the weld layer/tube interface. The hot corrosion study confirmed that after 24 hr of exposure to the molten salt, (Cr, Fe)-rich scales formed on the surface of the weld overlay alloy 625. The scales are considered as corrosion products, not effective barrier layers. Channels and discontinuities, as well as pores in the structure of the scales, acted as effective pathways for corrosive species (O, S, Cl) to reach the surface of the weld overlay. XRD results confirmed that nickel, chromium, molybdenum, niobium, titanium, and iron were the major elements in the chemical composition of the corrosion products and scales, which shows the susceptibility of these elements to be dissolved in the molten salt mixture.

8.2 Hot corrosion of wrought alloy 625 in 47 $PbSO_4$-23 ZnO-13 Pb_3O_4-10 Fe_2O_3-7 $PbCl_2$ (wt. %)

The alloy 625 presented the active dissolution behavior and an anodic film was formed on the surface of the alloy, which was characterized as a non-protective porous corrosion product layer. Underneath the chromium-rich corrosion product layer, a chromium-depleted zone formed. The corrosion product layer mainly consists of chromium, oxygen, and nickel. General surface corrosion, intergranular corrosion, formation of voids, and a network of distributed pores on the surface and the cross-section, as well as internal oxidation and sulfidation were identified as different modes of corrosion attack.

Based on the XRD data, the characteristic peaks of Ni(Cr_2O_4) and Cr_2O_3 layers, which protected the alloy against aqueous corrosive environments at ambient temperature, completely disappeared/dissolved when the alloy was exposed to the molten salt medium at 600, 700, and 800°C. The dissolution of the protective layers correlates with the weak corrosion resistance/appreciable corrosion susceptibility of alloy 625 in the molten salt environment. High concentrations of sulfur and oxygen in the grain boundaries are evidences of intergranular corrosion together with the internal attack.

An electrochemical model (a porous and non-protective barrier layer model) was used to explain the corrosion/electrochemical behavior of the alloy which fit with the obtained EIS data well. The highly porous and chromium-rich corrosion product layer acts as a possible diffusion path for the aggressive species of the molten salt to reach the surface of the alloy and diffuse inward mainly through the grain boundaries. This causes the intergranular corrosion process, observed as the internal attacked areas. The reaction of the sulfur from the molten salt with the alloy can be considered an important factor in the propagation mode of corrosion of the alloy 625.

8.3 Hot corrosion of wrought alloy 625 in 47 $PbSO_4$-23 ZnO-13 Pb_3O_4-10 CdO-7 $PbCl_2$ (wt. %)

The EIS analyses showed a relaxation process in the low frequency range at 800 and 600°C, while it showed two relaxation processes at 700°C. The relaxation process at the high frequency range was attributed to the growth of the outer Ni-rich oxide barrier layer and, at the same time, the relaxation process at low frequency range was related to the growth of the inner Cr- rich oxide barrier layer. During the corrosion process, Cr was mainly dissolved in an active oxidation process as CrO_3, Cr_2O_3, and $CrNbO_4$ while Ni dissolved only as NiO in the system. Fe and a small portion of Cr also participated in a sulfidation reaction at the molten salt/metal interface. There were two types of attack

for Inconel 625, general surface corrosion and pitting. Pitting corrosion occurred due to the breakdown of the initial oxide layer by molten salt dissolution of the oxide or oxide cracking.

References

1. The World Bank Group (1998). Pollution Prevention and Abatement Handbook: Lead and Zinc Smelting. 332-336.
2. Sannikov, Y.I., Liamina, M.A.; Shumskij, V.A.; Radashin, M.V. (1998). A physical and chemical description of the Kivcet lead flash smelting process. *CIM Magazine*, 91 (1022), 76-81.
3. Walker, M.J. (1998). Kivcet smelter on stream at Tail. (Cominco Ltd.'s Trail integrated lead-zinc plant). *Mining Magazine*, April 1998, 256-263.
4. Asham, D.W. (1998). Pilot plant and commercial scale test work on the KIVCET process for Camino's new lead smelter. *Zinc and Lead Processing Conference*, The Metallurgical Society of CIM, Montreal, QC, Canada, 783-794.
5. Mohammadi Zahrani, E.; Alfantazi, A. (2013). Hot corrosion failure of overlay weld cladding in radiant boiler of a KIVCET flash lead smelter", *Metallurgical and Materials Transaction: A*, DOI: 10.1007/s11661-013-1803-y, In press.
6. Lai, G. Y.; Blogg, N. (2004). Unifuse® overlay cladding for surface protection against corrosion and erosion/corrosion in power boilers and waste heat recovery systems. *OMMI*, 3, 1-19.
7. Lai, G.; Hulsizer, P. Corrosion control by modern weld overlay technology. Technical Report of Metserve International Inc., 1-11 (homepage: http://www.metserve.co.za).
8. DuPont, J.N. (1996). Solidification of an alloy 625 weld overlay. *Metallurgical and Materials Transaction: A*, 27, 3612-3620.
9. Nugent, R.M. (1986). Alloy 625 surfacing of tool and die steels. Welding Journal, 65(6), 33-39.
10. Levin, B.F.; DuPont, J.N.; Marder, A.R. (1994). Weld overlay coatings for erosion control. *Proceedings of the TMS Symposium on High Temperature Coatings*, Chicago, Illinois, October 2-6, 325-340.

11. Dimbylow, C.S. (1985). Bead geometry and properties of Inconel 625 overlays on steel. *Metal construction***,** 35-39 (http://ammtiac.alionscience.com/ammt/iacdocs.do?B126064).

12. Williams, J. C.; Starke, E. A. (2003). Progress in structural materials for aerospace systems, *Acta Materials*, 52, 5775-99.

13. Smith, G.; Shoemaker, L. (2004). Advanced Nickel Alloys for Coal-Fired Boiler Tubing. *Advanced Materials and Process*, 162, 23-26.

14. Sims, C. T.; Stoloff, N. S.; Hagel, W. C. (1987). Superalloys II: High Temperature Materials for Aerospace and Industrial Power. John Wiley and Sons, New York, NY.

15. Reed, R.C. (2006). The Superalloys: Fundamentals and Applications. Cambridge University Press, New York, NY.

16. Askeland, D. R. (1990). The Science and Engineering of Materials. Second Edition, Chapman and Hall, London.

17. Chattopadhyay, R. (2001). Surface Wear: Analysis, Treatment and Prevention. ASM International, Materials Park, OH.

18. Dieter, G. E. (1986). Mechanical Metallurgy. Third Edition, McGraw-Hill, New York, NY.

19. McLean, M. (1995). Nickel-based alloys: recent developments for the aero-gas turbine. in H.M. Flower, ed., High Performance Materials For Aerospace, Chapman & Hall, London.

20. Durand-Charre, M. (1997). The Microstructure of Superalloys. Gordon & Breach Science Publishers, Amsterdam.

21. Ricks, R. A.; Porter, A.J.; Ecob, R.C. (1983). The growth of gamma prime precipitates in nickel-base superalloys. *Acta Metallurgica*, 31, 43-53.

22. Karunaratne, M.S.A.; Reed, R.C. (2003). Interdiffusion of the platinum group metals in nickel at elevated temperatures. *Acta Materialia*, 51, 2905-2919.

23. Perez, F.J.; Hierro, M.P.; Nieto, J. (2008). Waste incineration corrosion processes: oxidation mechanisms by electrochemical impedance spectroscopy. *Materials and Corrosion*, 59, 566-572.

24. Spiegel, M. (1999). Salt melt induced corrosion of metallic materials in waste incineration plants. *Materials and corrosion*, 50, 373-393.

25. Sidhu, T.S.; Agrawal, R.D.; Prakash, S. (2005). Hot corrosion of some superalloys and role of high-velocity oxy-fuel spray coatings-a review. *Surface and Coating Technology*, 198, 441-446.

26. Otero, E.; Pardo, A.; Hernaez, J.; Perez, F.J. (1991). The hot corrosion of in-657 superalloy in Na_2SO_4-V_2O_5 melt eutectic. Corrosion Science, 32, 677-832.

27. Nylof, L.; Haggblom, E. (1997). Corrosion of experimental superheater alloys in waste fuel combustion. CORROSION/97. NACE International, Houston, TX, Paper No. 154.

28. Mohammadi Zahrani, E.; Cuevas-Arteaga, C; Alfantazi, A.; Verhelst, D. (2010). High temperature corrosion of 625 supperalloy under iron-zinc-lead oxide / sulfate / chloride salt mixtures. *Electrochemical Society Transaction*, 28, 171-185.

29. Philip, A.; Schweitzer, P.E. (2007). Fundamentals of Metallic Corrosion: Atmospheric and Media Corrosion of Metals. CRC Press, New York, NY

30. Wang, F.; Shu, Y. (2003). Influence of Cr content on the corrosion of Fe-Cr alloys: the synergistic effect of NaCl and water vapour. *Oxidation of Metals*, 59, 201-214.

31. Grabke, H.J.; Spiegel, M.; Zhas, A. (2004). The role of alloying elements and carbides in the chloride-induced corrosion of steels and alloys. *Materials Research*, 7, 89-95.

32. Martin, F.J.; Natishan, P.M.; Lucas, K.E.; Hogan, E.A.; Grolleau, A.M.; Thomas, E.D. (2003). Crevice corrosion of alloy 625 in natural seawater. *Corrosion*, 59, 498-504.

33. Smith, G.D.; Tillack, D.J.; Patel, S.J. (2001). Alloy 625 – impressive past / significant presence / awesome future. Superalloys 718, 625, 706 and Various Derivatives, Edited By: E.A. Loria, TMS, 35-46.

34. Tedmon, C.S.; Vermilyea, D.A. (1971). Carbide sensitization and intergranular corrosion of nickel base alloys. *Corrosion*, 27, 376-381.

35. Zhao, S.; Dong, J.; Xie, X.; Smith, G.D.; Patel, S.J. (2004). Thermal stability study on a new Ni-Cr-Co-Mo-Nb-Ti-Al superalloy. Superalloy 2004, TMS, Champion, PA, 63-72.

36. Xie, X.; Zhao, S.; Dong, J.; Smith, G.D.; Baker, B.A.; Patel, S.J. (2008). A new improvement of Inconel 740 for USC power plants. *Proceeding of the 5th International Conference on Advances in Materials Technology for Fossil Power Plants*, Marco Island, Florida, 220-230.

37. Kawahara, Y. (2007). Application of high temperature corrosion-resistant materials and coatings under sever corrosive environment in waste-to-energy boilers. *Journal of Thermal Spray Technology*, 16, 202-213.

38. Kalivodova, J.; Baxter, D.; Schultze, M.; Rohr, V. (2008). Corrosion behaviour of boiler steels, coatings and welds in flue gas environments. *Materials and Corrosion*, 59, 367-373.

39. Uusitalo, M.A.; Vuoristo, P.M.J.; Mantyla. T.A. (2004). High temperature corrosion of coatings and boiler steels below chlorine-containing salt deposits. *Corrosion Science*, 46, 1311–1331.

40. Zhang, D.; Harris, S.J.; McCartney, D.G. (2003). Microstructure formation and corrosion behaviour in HVOF-sprayed Inconel 625 coatings. *Materials Science and Engineering: A*, 344, 45-56.

41. Ahmed, N.; Bakare, M.S.; McCartney, D.G.; Voisey, K.T. (2010). The effects of microstructural features on the performance gap in corrosion resistance between bulk and HVOF sprayed Inconel 625. *Surface & Coatings Technology*, 204, 2294-2301.

42. Parker, D.W.; Kutner, G.L. (1991). HVOF-spray technology poised for growth. *Advanced Materials and Processes*, 4, 68-72.

43. Kawahara, Y; Kira, M. (1994). Corrosion prevention of waterwall tube by field metal spraying in municipal waste incineration plants. *Corrosion*, 53, 241-246.

44. Herman, H.; Sampath; S.; McCune, R.; (2000). Thermal spray: current status and future trends. *MRS Bulletin*, 25, 17-25.

45. Al-Fadhli, H.Y.; Stokes, J.; Hashmi, M.S.J.; Yilbas, B.S. (2006). HVOF coating of welded surfaces: fatigue and corrosion behaviour of stainless steel coated with Inconel-625 alloy. *Surface & Coatings Technology*, 200, 4904-4908.

46. Uusitalo, M.A.; Vuoristo, P.M.J.; Mantula, T.A. (2002). Elevated temperature errosion-corrosion of thermal sprayed coatings in chlorine containing environments. *Wear*, 252, 586-594.

47. Al-Fadhli, H.Y.; Stokes, J.; Hashmi, M.S.J.; Yilbas, B.S. (2006). The erosion-corrosion behaviour of high velocity oxy-fuel (HVOF) thermally sprayed Inconel-625 coating on different metallic surfaces. *Surface & Coatings Technology*, 200, 5782-5788.

48. Uusitalo, M.A.; Vuoristo, P.M.J.; Mantula, T.A. (2002). High temperature corrosion of coatings and boiler steels in reducing chlorine-containing atmosphere. *Surface & Coatings Technology*, 161**,** 275-285.

49. Higuera, V.; Belzunce, F.J.; Carriles, A.; Poveda, S. (2002). Influence of the thermal-spray procedure on the properties of a nickel-chromium coating. *Journal of Materials Science*, 37, 649-654.

50. Gil, L.E.; Staia, M.H. (2002). Effects of HVOF parameters on adhesion and microstructure of thermal sprayed NiWCrBSi coatings. *Surface Engineering*, 18, 309-315.

51. Rademarkers, P.; Hesseling, W.; Wetering, J. (2002). Review on corrosion in waste incinerators, and possible effect of bromine. TNO Industrial Technology.

52. Lee, S.; Themelis, N.J.; Castaldi, M.J. (2007). High-temperature corrosion in waste-to-energy boilers. *Journal of Thermal Spray Technology*, 16, 104-110.

53. Solomon, N.G. (1998). Erosion-resistant coatings for fluidized bed boilers. *Materials Performance*, 37, 38-43.

54. Cieslak, M.J.; Headley, T.J.; Kollie, T.; Romig, A.D. (1988). A melting and solidification study of alloy 625. *Metallurgical and Materials Transaction: A*, 19, 2319-2331.

55. Cieslak, M.J. (1991). The welding and solidification metallurgy of alloy 625. *Welding Journal*, 70, 49s-56s.

56. Borland, J.C. (1960). Generalized theory of super-solidus cracking in welds and casting. *British Welding Journal*, 7, 508-512.

57. Arata, Y.; Inoue, K. (1973). Automatic control of arc welding (report II): optical sensing of joint configuration. *Transaction of Japanese Welding Research Institute*, 2(1), 87-101.

58. Brooks, J.A. (1990). Proceedings of Weldability of Materials. ed. Patterson, R.A.; Mahin, K.W.; October 8–12, ASM International, Materials Park, OH, 41-48.

59. Dupont, J. N.; Banovic, S. W.; Marder, A. R. (2003). Microstructural evolution and weldability of dissimilar welds between a super austenitic stainless steel and nickel base alloys. *Welding Journal*, 82(6), 125s-135s.

60. Banovic, S. W.; Dupont, J. N.; Marder, A. R. (2001). Dilution control in gas-tungsten-arc welds involving superaustenitic stainless steels and nickel-based alloys. *Metallurgical and Materials Transaction: B*, 32, 1171-1176.

61. Sidhu, T.S.; Prakash, S.; Agrawal, R.D. (2006). Hot corrosion and performance of nickel-based coatings. *Current Science*, 90, 41-47.

62. Stringer, J. (1983). High Temperature Corrosion. NACE-6, ed. R.A. Rapp, Houston, TX, National Association of Corrosion Engineers, 389.

63. Pettit, F.S.; Giggins, C.S. (1987). Hot Corrosion. In Superalloys II, eds. Sims, C.T.; Stoloff, N.S.; Hagel, W.C., John Wiley & Sons, New York, NY.

64. Rapp, R.A.; Zhang, Y.S. (1994). Hot corrosion of materials: fundamental studies. *JOM*, 46, 47-55.

65. Zwaher, H. (2003). Ways to Improve the Efficiency of Waste to Energy Plants for the Production of Electricity and Reusable Materials. 11th North America WTE conference, Florida, Tampa.

66. Pettit, F.S.; Meier, G.H. (1984). Oxidation and Hot Corrosion of Superalloys. In Superalloys, ed. Gell, M.; Kartovich, C.S.; Bricknel, R.H.; Kent, W.B.; Radovich, J.F., The Metals Society of AIME, Warrendale, PA, 651.

67. Saunders, S.R.J. (1995). Corrosion in the presence of melts and solids., In: Guidelines for Methods of Testing and Research in High Temperature Corrosion, eds. H.J. Grabke and D.B. Meadowcroft, The Institute of Materials, London.

68. Bircks, N.; Meier, G.H.; Pettit, F.S. (2006). Introduction to the High Temperature Oxidation of Metals. Second Edition, Cambridge University Press, New York, NY.

69. Singh, H.; Puri, D.; Prakash, S. (2007). An overview of Na_2SO_4 and/or V_2O_5 induced hot corrosion of Fe- and Ni-based superalloys. *Review on Advanced Materials Science*, 16, 27-50.

70. Rapp, R.A. (2002). Hot corrosion of materials: a fluxing mechanism?. *Corrosion Science*, 44, 209-221.

71. Singh, H.; Sidhu, B.S.; Puri, D.; Prakash, S. (2007). Use of plasma spray technology for deposition of high temperature oxidation/corrosion resistant coatings – a review. *Materials and Corrosion*, 58, 92-102.

72. Edris, H.; McCartney, D.G.; Sturgeon, A.J. (1997). Microstructural characterization of high velocity oxy-fuel sprayed coating of Inconel 625. *Journal of Materials Science*, 32, 863-868.

73. Meier, G.H. (1989). A review of advances in high-temperature corrosion, *Materials Science and Engineering: A*, 120-121, 1-11.

74. Khanna, A.S.; Jha, S.K. (1988). Degradation of materials under hot corrosion conditions. *Transaction of Indian Institute of Metals*, 51, 279-290.

75. Hancock, P. (1987). Vanadic and chloride attack of superalloys. *Materials Science and Technology*, 3, 536-544.

76. Wright, I.G. (1987). High-temperature corrosion. Metals Handbook, Materials Park, ASM, 9th Edition, 13, 97-103.

77. Meier, G.H. (1989). A review of advances in high-temperature corrosion, *Materials Science and Engineering: A*, 120-121, 1-11.

78. Nicholls, J.R.; Stephenson, D.J. (1992). A life prediction model for coatings based on the statistical analysis of hot salt corrosion performance. *Corrosion Science*, 31, 1313-1325.

79. Luer, K., DuPont, J.; Mardar, A.; Skelonis, C. (2001). Corrosion fatigue of alloy 625 weld cladding in combustion environments. *Materials at High Temperature*, 18(1), 11-19.

80. Montgomery, M.; Biede, O.; Larson, O. H. (2006). Experiences with Inconel 625 in biomass and waste incineration plants. *Materials Science Forum*, 522-523, 523-530.

81. Perez, F.J.; Nieto, J.; Trilleros, J.A.; Hierro, M.P. (2006). Hot corrosion monitoring of waste incineration corrosion processes using electrochemical techniques. *Materials Science Forum*, 522-523, 531-538.

82. Kawahara, Y. (2006). Evaluation of high-temperature corrosion life using temperature gradient corrosion test with thermal cycle component in waste combustion environment. *Materials and Corrosion*, 57(1), 60-72.

83. Kawahara, Y. (2002). High temperature corrosion mechanisms and effect of alloying elements for materials used in waste incineration environment. *Corrosion Science*, 44, 223-245.

84. Ishitsuka, T., Nose, K. (2002). Stability of protective oxide films in waste incineration environment-solubility measurement of oxide in molten chloride. *Corrosion Science*, 44, 247-263.

85. Wright, I.G.; Krause, H.H.; Dooley, R.B. (1995). A review of materials problem and solution in U.S. waste fired steam boilers. Corrosion/95, NACE International, Paper No. 562.

86. Barraza-Fierro, J.I.; Espinosa-Medina, M.A.; Hernandez-Hernandez, M.; Liu, H.B.; Sosa-Hernandez, E. (2012) Effect of Li and Cu addition on corrosion of Fe–40 at.% Al intermetallics in molten LiCl–KCl eutectic salt. *Corrosion Science*, 59, 119-126.

87. Zeng, C.L.; Wang, W.; Wu, W.T. (2001). Electrochemical impedance models for molten salt corrosion. *Corrosion Science*, 43, 787-801.

88. Tristancho-Reyes, J.L.; Chacon-Nava, J.G.; Pena-Ballesteros, D.Y.; Gaona-Tiburcio, C.; Gonzalez-Rodriguez, J.G.; Martinez-Villafane, A.; Almeraya-Calderon, F. (2011). Hot corrosion behaviour of NiCrFeNbMoTiAl coating in molten salts at 700^{o}C by electrochemical techniques. *International Journal of Electrochemical Science*, 6, 432-441.

89. Otero, A.; Pardo, A.; Perez, F.J.; Utrilla, M.V.; Levi, T. (1998). Corrosion behaviour of 12CrMoV steel in waste incineration environments: hot corrosion by molten chloride. Oxidation of Metals, 49, 467-483.

90. Espinosa-Medina, M.A.; Carbajal-De la Torre, G.; Liu, H.B.; Martinez-Villafane, A.; Gonzalez-Rodriguez, J.G. (2009). Hot corrosion behaviour of Fe-Al based intermetallic in molten $NaVO_3$ salt. *Corrosion Science*, 52, 1420-1427.

91. Gonzalez-Rodriguez, J.G.; Mejia, E.; Lucio-Garcia, M. A.; Salinas-Bravo, V.M.; Pprcayo-Calderon, J.; Martinez-Villafane, A. (2009). An electrochemical study of the effect of Li on the corrosion behavior of Ni_3Al intermetallic alloy in molten (Li+K) carbonate. *Corrosion Science*, 51, 1619-1627.

92. Martinez-Villafane, A.; Almeraya-Calderon, F.; Gaona-Tiburcio, C.; Chacon-Nava, J.; Gonzalez-Rodriguez, J.G. (2003). Evaluation of corrosion resistance of two engineering alloys in molten salts by electrochemical techniques. *Materials and Corrosion*, 54, 32-36.

93. Cuevas-Arteaga, C.; Porcayo-Calderon, J.; Izquierdo, G.; Martinez-Villafane, A.; Gonzalez-Rodriguez, J.G. (2001). Study of hot corrosion of alloy 800 using linear polarization resistance and weight loss measurement. *Materials Science and Technology*, 17, 880-885.

94. Cuevas-Arteaga, C.; Uruchurtu-Chavarin, J.; Gonzalez, J.; Izquierdo-Montalvo, G.; Procayo-Calderon, J.; Cano-Castillo, U. (2004). Corrosion evaluation of alloy 800 in sulfate/vanadate molten salts. *Corrosion*, 60, 548-560.

95. Cuevas-Arteaga, C. (2008). Corrosion study of HK-40m alloy exposed to molten sulfate/vanadate mixtures using the electrochemical noise technique. *Corrosion Science*, 50, 650-663.

96. Cuevas-Arteaga, C.; Uruchurtu-Chavarín, J.; Porcayo-Calderon, J.; Izquierdo Montalvo, G.; Gonzalez, J. (2004). Study of molten salt corrosion of HK-40m alloy applying linear polarization resistance and conventional weight loss techniques. *Corrosion Science*, 46, 2663-2679.

97. Espinosa, M. A.; Carbajal De la Torre, G.; Parcayo-Calderon, J.; Martinez-Villafane, A.; Chacon-Nava, J. G.; Casales, M.; Gonzalez-Rodriguez, J.G. (2003). Corrosion of atomized Fe40Al based intermetallics in molten Na_2SO_4. *Materials and Corrosion*, 54, 304-310.

98. Espinosa-Medina, M.A.; Casales, M.; Martinez-Villafañe, A.; Porcayo-Calderon, J.; Martinez, L.; Gonzalez-Rodriguez, J.G. (2001). Hot corrosion of atomized iron aluminides doped with boron and reinforced with alumina. *Materials Science and Engineering: A*, 300, 183-189.

99. Martinez, L.; Amaya, M.; Porcayo-Calderon, J. (1998). High-temperature electrochemical testing of spray atomized and deposited iron aluminides alloyed with boron and reinforced with alumina particulate, *Materials Science and Engineering: A*, 258, 306-312.

100. Gao, G.; Stott, F.H.; Dawson, J.L.; Farrell, D.M. (1990). Electrochemical monitoring of high-temperature molten-salt corrosion. *Oxidation of Metals*, 33, 79-94.

101. Farrell, D.M.; Cox, W.M.; Stott, F.H.; Eden, D.A.; Dawson, J.L.; Wood, C.C. (1985). High Temperature Technology, 15-21.

102. Farrell, D.M.; Stott, F.H.; Rocchini, G.; Colombo, A. (1991). Electrochemical aspects of high temperature corrosion reactions in combustion systems. *U.K. Corrosion 91*, Manchester: European Federation of Corrosion, 2, 1-14.

103. American Society for Testing and Materials (2011). Standard Guide for Preparation of Metallographic Specimens. *ASTM E3-11*, 1-13.

104. International Organization for Standardization. Corrosion of Metals and Alloys - Method for Metallographic Examination of Samples after Exposure to High-Temperature Corrosive Environments. ISO/DIS 26146.

105. Davis, J.R. (2000). ASM Specialty Hand Book: Nickel, Cobalt and their Alloys. ASM International, Materials Park, OH, 301.

106. American Society for Testing and Materials (2010). Standard Test Method for Determining Average Grain Size. *ASTM E112-10*, 1-26.

107. Lu, W.M.; Pan, T.J.; Zhang, K.; Niu, Y. (2008). Accelerated corrosion of five commercial steels under $ZnCl_2$ – KCl deposit in a reducing environment typical of waste gasification at 673-773 K. Corrosion Science, 50, 1900-1906.

108. Di Martino, J.; Rapin, C.; Berthod, P.; Podor, R.; Steinmetz, P. (2004). Corrosion of metals and alloys in molten glasses. Part 1: glass electrochemical properties and pure metal (Fe, Co, Ni, Cr) behaviours. *Corrosion Science*, 46, 1849-1864.

109. Zhu, B.; Lindbergh, G.; Simonsson, D. (1999). Comparison of electrochemical and surface characterization methods for investigation of corrosion of bipolar plate materials in molten carbonate fuel cell: Part I. Electrochemical study. *Corrosion Science*, 41, 1497-1513.

110. Niu, Y.; Wang, S.; Gao, F.; Zhang, Z.G.; Gesmundo, F. (2008). The nature of the third-element effect in the oxidation of Fe–*x*Cr–3 at. % Al alloys in 1 atm O_2 at 1000 °C, Corrosion Science, 50, 345-356.

111. Ruh, A.; Spiegel, M. (2006). Thermodynamic and kinetic consideration on the corrosion of Fe, Ni and Cr beneath a molten KCl–$ZnCl_2$ mixture. *Corrosion Science*, 48, 679-695.

112. Tanaka, M.; Kashiwagi, K.; Kawashima, N.; Kitaoka, S.; Sakurada, O.; Ohya, Y. (2012). Effect of grain boundary cracks on the corrosion behaviour of aluminum titanate ceramics in a molten aluminum alloy. *Corrosion Science*, 54, 90-96.

113. Sequeira, C.A.C. (2003). High Temperature Corrosion in Molten Salts. Trans Tech Publications Ltd., London, 3–40.

114. American Society for Testing and Materials (2009). Standard Test Method for Conducting Potentiodynamic Polarization Resistance Measurements. *ASTM G59-97*, 1-4.

115. American Society for Testing and Materials (2004). Standard Reference Test Method for Making Potentiostatic and Potentiodynamic Anodic Polarization Measurements. *ASTM G5-94*, 1-12.

116. Zou, Y.; Wang, J.; Zheng, Y. Y. (2011). Electrochemical techniques for determining corrosion rate of rusted steel in seawater, *Corrosion Science*, 53, 208-216.

117. American Society for Testing and Materials (2011). Standard Practice for Preparing, Cleaning, and Evaluating Corrosion Test Specimens. *ASTM G1-03*, 1-9.

118. American Society for Testing and Materials (2004). Standard Practice for Laboratory Immersion Corrosion Testing of Metals. *ASTM G31-72*, 1-8.

119. Firouzi, A.; Shirvani, K. (2010). The structure and high temperature corrosion performance of medium-thickness aluminide coatings on nickel-based superalloy GTD-111, *Corrosion Science*, 52, 3579-3585.

120. Pires, J. N.; Loureiro, A.; Bolmsjo, G. (2006). Welding Robots: Technology, System Issues and Applications. Springer, London.

121. Dupont, J. N.; Robino, C. V.; Michael, J. R.; Notis, M. R.; Marder, A. R. (1998). Solidification of Nb-bearing superalloys: part I. reaction sequences. *Metallurgical and Material Transactions: A*, 29, 2785-2796.

122. Chandrasekaran, K. N.; Tiedje, S.; Hald, J. (2009). Solidification paths in modified Inconel 625 weld overlay material. *International Journal of Cast Metals Research*, 22, 306-310.

123. Adamiec, J. (2009). High temperature corrosion of power boiler components cladded with nickel alloys. *Materials Characterization*, 60, 1093-1099.

124. Maguire, M.C.; Michael, J.R. (1994). Weldability of alloy 718, 625 and variants. Third International Special Emphasis Symposium on Superalloys 718, 625, 706 and Various Derivatives, TMS, Pittsburgh, PA, 881-892.

125. Hanninen, H.; Brederholm, A.; Saukkonen, T. (2008). Hot Cracking Phenomena in Welds II, Springer, Berlin, 171-191.

126. Lai, G. (1998). The properties and characteristics of alloy 625 overlay tubing for recovery boiler applications. *TAPPI Engineering & Papermaking Conference Proceedings*, TAPPI Press, Miami, FL, 417-430.

127. Kieser, J. R.; Taljat, B.; Wang, X.-L.; Swinderman, R.; Maziasz, P.; Thomas, R.; Payzant, E.; Singbeil, D.; Prescott, R. (1997). Analysis of cracking of co-extruded recovery boiler floor tubes. *TAPPI Engineering & Papermaking Conference Proceedings*, TAPPI Press, Atlanta, GA, 1025-1041.

128. Radhakrishna, C. H.; Prasad Rao, K. (1984). The formation and control of Laves phase in Superalloy 718 welds. *Journal of Materials Science*, 32, 1977-1984.

129. Cieslak, M. J.; Knorovski, G. A.; Headley, T. J.; Roming, A. D. (1986). The use of new PHACOMP in understanding the solidification microstructure of nickel base alloy weld metal. *Metallurgical and Materials Transaction: A*, 17, 2107-2116.

130. Dupont, J. N. (1999). Microstructural development and solidification cracking susceptibility in the fusion zone of a stabilized stainless steel. *Welding Journal*, 78(7), 253s-263s.

131. Knorovsky, G. A.; Cieslak, M. J.; Headley, T. J.; Romig, A. D.; Hammetter, W. F. (1989). INCONEL 718: A solidification diagram. *Metallurgical and Materials Transaction: A*, 29, 2149-2158.

132. Mohammadi Zahrani, E.; Alfantazi, A. (2012). Molten Salt Induced Corrosion of Inconel 625 Superalloy in $PbSO_4$-Pb_3O_4-$PbCl_2$-Fe_2O_3-ZnO Environment. *Corrosion Science*, 65, 340-359.

133. Cortial, F.; Corrieu, J. M.; Vernot-loier, C. (1995). Influence of heat treatments on microstructure, mechanical properties, and corrosion resistance of weld alloy 625. *Metallurgical and Materials Transaction: A*, 26, 1273-1286.

134. Dupont, J. N.; Marder, A. R. (1996). Dilution in single pass arc welds. *Metallurgical and Materials Transaction: B*, 27, 481-489.

135. Karunakaran, N.; Balasubramanian, V. (2011). Effect of pulsed current on temperature distribution, weld bead profiles and characteristics of gas tungsten arc welded aluminum alloy joints. Transaction of Nonferrous Metals Society of China, 21, 278-286.

136. Schirra, J. J.; Caless, R. H.; Hatala, R. W. (1991). Superalloys 718, 625 and Various Derivatives, E. A. Loria (Ed.), TMS, Pittsburgh, PA, 375-388.

137. Singbeil, D.; Prescott, B.; Keiser, J.; Swindeman, B. (1997). Composite tube cracking in craft recovery boilers – a state-of-the-art review, *TAPPI Engineering & Papermaking Conference Proceedings*, TAPPI Press, Nashville, TN, 1001-1024.

138. Hojerslev, C.; Tiedje, N.; Hald, J. (2005). Understanding local limited performance of nickel based weld clad material in terms of segregation effects. *Proceeding of Danish Metallurgical Society*, Winter Meeting, Kolding, Denmark.

139. John, R. C. (1996). Engineering assessment of oxidation of engineering alloys. *NACE Corrosion Conference*, NACE International, Houston, TX,171.

140. Reed-Heel, R.E.; Abbaschian, R. (1994). Physical Metallurgy Principles, Third Edition, PWS Publishing Company, Boston, MA.

141. Young, D. J. (2008). High Temperature Oxidation and Corrosion of Metals, First Edition, Elsevier Corrosion Series, London.

142. Hladky, K.; Callow, L.M.; Dawson, J.L. (1980). Corrosion rates from impedance measurements: an introduction, *British Corrosion Journal*, 15, 20-25.

143. Carranza, R.M.; Alvarez, M.G. (2009). The effect of temperature on the passive film properties and pitting behaviour of a Fe-Cr-Ni alloy. *Corrosion Science*, 38, 909-925.

144. Beverskog, B.; Bojinov, M.; Englund, A.; Kinnunen, P.; Laitinen, T.; Mäkelä, K.; Saario, T.; Sirkiä, P. (2002). A mixed-conduction model for oxide films on Fe, Cr and Fe-Cr alloys in high-temperature aqueous electrolytes-I. Comparison of the electrochemical behaviour at room temperature and at 200°C. *Corrosion Science*, 44, 1901-1921.

145. Montany, B.P.; Shores, D.A. (2004). Role of chlorides in hot corrosion of a cast Fe–Cr–Ni alloy. Part I: Experimental studies, *Corrosion Science*, 46, 2893-2907.

146. Mohammadi Zahrani, E.; Alfantazi, A. (2012). Corrosion behavior of alloy 625 in $PbSO_4$-Pb_3O_4-$PbCl_2$-ZnO-10 wt. % CdO molten salt medium. *Metallurgical and Materials Transaction: A*, 43, 2857-2868.

147. Bard, A. J.; Faulkner, L. A. (2001). Electrochemical Methods: Fundamentals and Applications. Second Edition, John Wiley and Sons Inc., New York, NY, 5-9.

148. Zelinsky, A.G.; Pirogov, B.Y.; Yurjev, O.A. (2004). Open circuit potential transients and electrochemical quartz crystal microgravimetry measurements of dissolution of copper in acidic sulfate solutions. *Corrosion Science*, 46, 1083-1093.

149. Sun, H.; Wu, X.; Han, E-H. (2009). Effects of temperature on the protective property, structure and composition of the oxide film on Alloy 625. *Corrosion Science*, 51, 2565-2572.

150. Park, J. J.; Pyun, S.I.; Lee, S. B. (2004). Growth kinetics of passivating oxide film of Inconel alloy 600 in 0.1 M Na_2SO_4 solution at 25–300 °C using the abrading electrode technique and ac impedance spectroscopy. *Electrochimica Acta*, 49, 281-292.

151. Rosborg, B.; Pan J. (2008). An electrochemical impedance spectroscopy study of copper in a bentonite/saline groundwater environment. *Electrochimica Acta*, 53, 7556-7564.